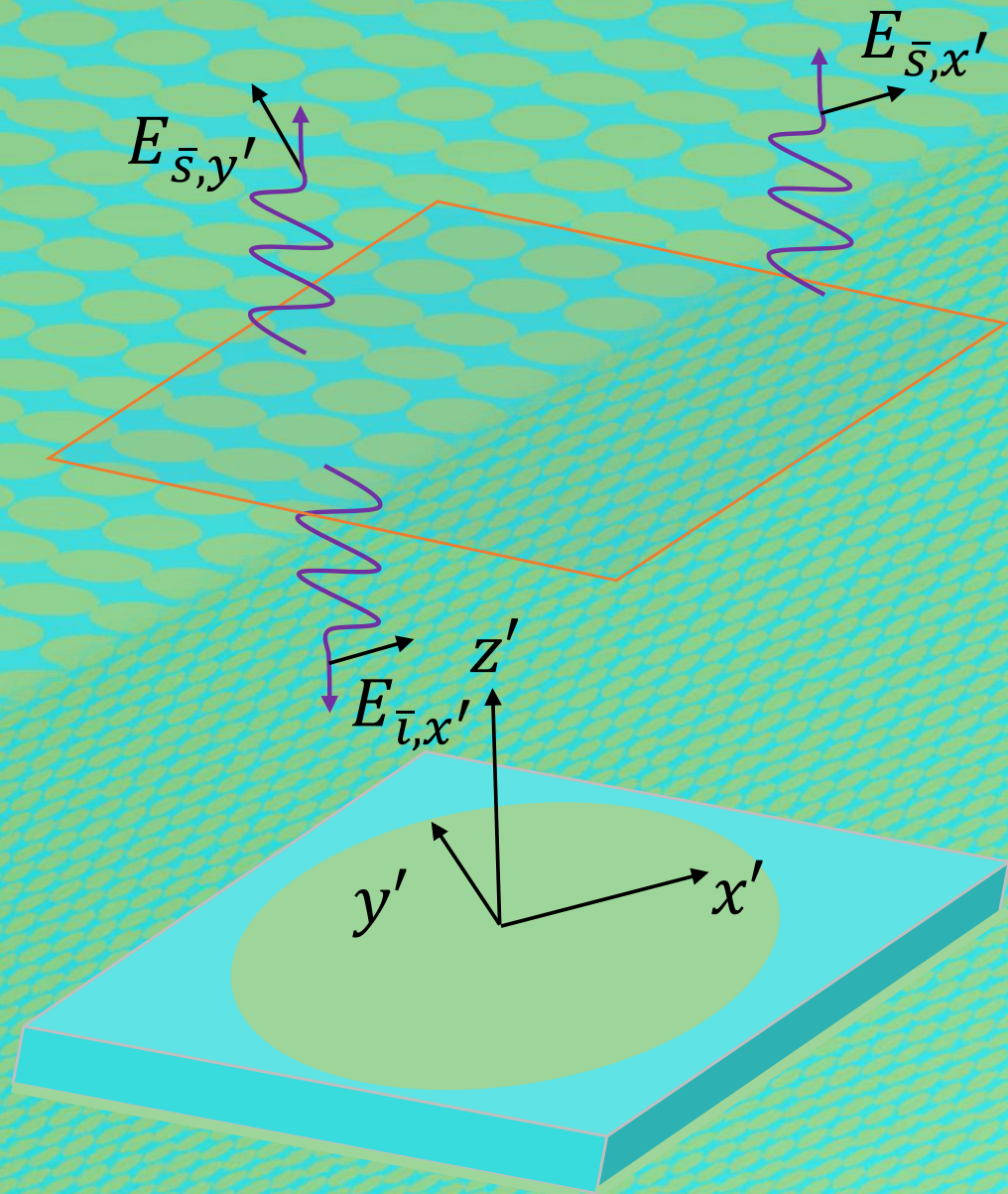


Metasurface Antenna for Space-based SAR

Master Thesis | Aerospace Engineering

Sebastian Falckenheiner

Delft University of Technology



Metasurface Antenna for Space-based SAR

by

Sebastian Falckenheiner

to obtain the degree of Master of Science in Aerospace Engineering
at the Delft University of Technology,
to be defended publicly on Wednesday December 21, 2022 at 14:00.

Student number: 4563387
Project duration: March 2022 - November 2022
Supervisors: Dr. ir. J.M. Kuiper, TU Delft
Prof. Dr. G. Gerini, TNO
Thesis committee: Dr. A. Cervone, TU Delft
Dr. J.J.D. Loicq, TU Delft

This thesis is confidential and cannot be made public until December 21, 2024.

An electronic version of this thesis is available at <http://repository.tudelft.nl/>.

Preface

It is amazing how fast five years, between the start of my BSc and the end of my MSc, can go through. I have experienced so many meaningful experiences at TU Delft that remembering all of them and thanking to the people that made them possible would need a separate work package within this assignment. Therefore, I would try to keep this short and structured, just like the rest of this report. I would like to start first by addressing the possible reader of this project, which is one important reason why we do research in the first place. If you are an aerospace engineering student looking for a thesis project and you encountered this report, please do not be discouraged by the amount of things that you may encounter new. The most important principles behind this can be learned by taking two extra courses, which can be used to apply this technology not only for antennas, but for many other radio and even optical devices. If you are outside this group, I hope that you find what you are looking in this report and please do not hesitate to contact the author if you want to discuss further any part.

On an academic and professional level I would like to thank Hans Kuiper and Giampiero Gerini, which were my direct supervisors at TU Delft and at TNO respectively. Their guidance helped me not only to produce the results contained in this report, but also to review sources in a critical way, learn from my mistakes, and explain very complex topics in a simple manner. I am extremely grateful with the opportunity they gave me because, even though there was a big knowledge gap, they trusted that I could fill it within the duration of this assignment. Subsequently, conducting most of the thesis work at TNO was a great experience. I had the opportunity to learn not only about my topic, but also about what others do and the societal relevance of the work conducted there. Special thanks to Thomas, Anthony, Jeroen, Tiberiu, Dave, Leyi, Yining, Marie, Alberto, Sanne, Ronald and Quentin for all the interesting talks that we had, moments shared, and activities done after work.

During my time at TU Delft I had wonderful experiences that helped me to develop in a professional and personal level. Therefore, I would like to thank to all the people that make that possible. Not only the academic staff, but the people that support every process that a student has to go through from the start to the end of any degree. To them, my deepest and most sincere recognition. Also, it would not be exaggerated for me to say that I could not have finished this degree without the support of my friends here in Delft. An special thanks to Eneko, Quim, Adrián, Diego, Roberto, Jander, Pablo, Luis, Carlos, Alfonso, Gabriel, Mariano, Shashruth, and the others that I may be forgetting. All the study sessions have finally paid off. Furthermore, I would like to thank the current and previous introduction programme members from the university, that are in charge of welcoming new students and make them acquainted to the student life in Delft. An special thanks to Marjo, Rianne and Sophie, who taught me important lessons about multiculturalism and acculturation.

On a more personal level, I would like to thank the immense support that I got from my family. It is usually not easy being away from the place where you lived for so long, specially in the middle of a pandemic. The endless talks that I had with my parents and brothers made me genuinely happy and gave me the required energy to continue working every day. However, I cannot say that I did not feel at home here. For that, I would like to thank my girlfriend Raquel who was always there, specially in the difficult times during the hardest lock-downs, and when the problems and stress feelings would overshadow any possible future glimpse of joy. Also, an special thanks to all my current and ex housemates, which contributed to the “gezelligheid” that I got from Delft. Last but not least, I would like to thank to all the people from Peru with whom I do not talk that much, but always have hope to get together and have meaningful conversations like we did in the past. Not only to my friends of school, neighbourhood, previous working locations and university, but also to my high school teachers who were one of the first ones guiding my learning process.

Sebastian Falckenheiner
Delft, December 2022

Summary

Synthetic Aperture Radars (SAR) have demonstrated to be great instruments for space-based Earth observation in the microwave frequency, with applications from biomass observation to oil spill detecting. On the other side, metasurface antennas are a new type of planar antennas with a great potential for space applications, as they are compact and easy to produce. These antennas, also called printed antennas, are manufactured using Printed Circuit Board technology where scattering elements with predetermined shapes are printed on top of the dielectric layer, producing modulated far-field radiation patterns when excited at its centre by a dipole source. Several methods have been developed in the past years addressing one or many parts of the design and applications of these antennas, which rely in more or less measure in locally developed tools. However, some parts of these methods can take a great amount of time to implement, making this process more difficult than it should especially if the user has commercial electromagnetic simulation tools available that could accelerate this process. On the other side, the possibility of using these antennas in SAR applications has been limitedly explored, especially for the metasurface antennas capable of generating single radiation patterns. In this work, different procedures have been adapted to the design of a high-gain SAR metasurface antenna (36 dB directivity and 3.2° first-null beam-width) for a multi-static Earth observation mission within the S-band (3.2 GHz), showing that the proposed methodology produces accurate results. Furthermore, the final design shows that the antenna requirements can be easily achieved, but in terms of mass the proposed antenna performs worse than other low-mass concepts, such as folded antenna arrays, which adapt better to the stringent mass requirement proposed in this mission. However, the antenna mass can be reduced by either operating in a higher frequency, reducing the dielectric slab thickness, or by using lighter materials for this part of the antenna.

The developed method consists on four steps: Obtaining the initial antenna parameters (thickness, permittivity, unit cell size and shape), producing a reactance database associated to the unit cell shape, synthesising the desired radiation pattern in a reactance distribution, and match the aforementioned distribution with particular unit cells shape. The initial antenna parameters were obtained by adjusting these to allow only the propagation of the fundamental Floquet mode when the unit cells are modelled with periodic boundary conditions, simulating an infinite structure. The patch shape chosen was the elliptical, and the parameters varied to generate the database were its inclination angle and the ratio of the minor axis to major axis. Next, the reactance database was produced by using the electromagnetic simulation software Lumerical® Finite-Difference Time-Domain to obtain the anisotropic scattering response of these unit cells to an incident plane wave, which was verified with a reactance database generated by other researchers using a Method of Moments formulation, obtaining a maximum 4.5 % deviation within the range of database shapes used later for the design. Following, the antenna synthesis was performed using an adiabatic Floquet-wave expansion suggested in [40] obtaining extremely low differences between the objective and the resulting far-field patterns in term of gain and cross polarization. Finally, the reactance distribution in the antenna was matched to the patch shapes from the reactance database, obtaining a maximum reactance deviation in the final design less than 4.5 % in a small number of patches in the antenna. The main antenna characteristics are summarized in table 1.

Table 1: Summary of SAR metasurface antenna characteristics.

Parameters	Values
Frequency	3.2 GHz
Antenna Radius	1 m
Dielectric layer material	AR-1000
Relative permittivity	9.8
Unit cell length and width	10 mm
Patch shape	Elliptical
Antenna thickness	4 mm
Directivity	35.28 dB
Half-Power Beam-Width	3.41°
Mass range	53 kg - 81 kg

The presented work can be regarded as an additional step to make the metasurface technology more accessible. These antennas can not only be used for SAR, but also for satellite communications where different radiation patterns can be obtained by changing only the printed patches on top, making them easily adaptable for multiple mission scenarios as the development times are reduced. Furthermore, making this antenna deployable would facilitate its accessibility for CubeSat, opening a wider range of new applications.

Contents

List of symbols	x
List of abbreviations	xv
1 Introduction	1
1.1 Motivation	1
1.2 Research design	3
1.3 Report overview	3
2 Synthetic Aperture Radar	4
2.1 General principles of SAR satellites	4
2.2 SwarmSAR mission	5
2.2.1 Mission description	6
2.2.2 Antenna requirements	7
2.3 SAR antenna used for comparison	8
3 Theoretical background	10
3.1 General electromagnetic theory	10
3.1.1 EM wave propagation	11
3.1.2 Transmission line theory	15
3.1.3 Antenna theory	20
3.1.4 Floquet series	24
3.2 Metasurface antennas	28
3.2.1 Basic principles	28
3.2.2 Design methodology	29
3.2.3 Unit cell modelling	30
3.2.4 Modulation technique: Adiabatic Floquet analysis	35
3.3 FDTD simulations	42
3.3.1 Basic principles	42
3.3.2 Yee cell	43
3.3.3 Boundary conditions	44
4 Metasurface antenna design	46
4.1 Unit cell impedance database	46
4.1.1 Physical properties of the unit cell	46
4.1.2 Scattering method	48
4.2 Antenna synthesis	65
4.2.1 Target field	65
4.2.2 Adiabatic Floquet analysis implementation	66
4.3 Patch matching	74
4.3.1 Method description	74
4.3.2 Verification	77
4.3.3 Results	77
5 Results and discussion	84
5.1 Design results	84
5.2 Conclusion and recommended further work	86
References	88
A Reciprocity theorem	92
B Method of stationary phase	93

C Method of Moments (MoM) impedance representation**96**

List of Figures

1.1	Stripmap and Spotlight SAR modes, where ROI represents Region Of Interest. Source: [4].	1
1.2	Example of metasurface antenna. Source: [36].	2
1.3	Metasurface and SAR SDGs	3
2.1	Radar airborne imaging acquisition. Source: [51]	5
2.2	Image ambiguities when sampling independently at different locations. Source: [47, p. 182]	6
2.3	SwarmSAR concept formation. The same ROI would be observed by multiple satellites with different Tx (transmission) frequency, but all of them will be capable of receive the emitted signal of their peers. Source: [17].	6
2.4	Deployment procedure of the antenna used for comparison [54].	9
3.1	Incident and transmitted plane waves in dielectric media	13
3.2	Transmission line resonator. Source: [18]	20
3.3	Transmission line resonator at arbitrary reference plane R . Source: [18]	20
3.4	Floquet spectral points for a two-dimensional array. Figure retrieved from Bhattacharyya [3, p. 70]	26
3.5	Metasurface patch and aperture antennas examples found in literature. At the left, the patch type metasurfaces are shown where the metal cladding is represented in red, whereas at the right an aperture type metasurface design is shown with the metal cladding represented in yellow.	28
3.6	Example of metasurface unit cell layout. At the left, the patch-type unit cell is shown with the representation of its electric currents in a discretised mesh. At the right, the aperture-type unit cell is shown with the representation of its magnetic currents in a discretised mesh. Source: [24]	29
3.7	Metasurface analysis regions separated by sizes. Source: [40]	29
3.8	Block diagram of the process to design a metasurface antenna. Source: [40]	30
3.9	Metasurface unit cell reference coordinate system.	31
3.10	Transmission line representation of a metasurface with the polarization definition.	33
3.11	Opaque and transparent reactances for anisotropic metasurfaces. Figures taken from Martini et.al. [28, p. 6]	34
3.12	Construction of Yee cell in a three-dimensional mesh. Source: [7, p. 748]	43
3.13	Electric field when using periodic boundary conditions in a 2D simulation	45
4.1	Patch shapes performances in metasurface antennas. Source: [9, p. 4]	47
4.2	Elliptical patch configuration for the unit cell.	49
4.3	Mesh (orange squares) in the unit cell planes for $\eta = 0.8$, $a'/d = 0.9$ and $\delta = 20^\circ$. The green arrow represents the magnetic field, the blue arrow the electric field and the purple the propagation direction. The lightblue region indicates the dielectric substrate slab, the green ellipse the patch and the dark region free-space. The thick orange lines represent the simulation region, the darker blue lines the periodic boundary conditions, the yellow lines the monitor where the data is recorded, and the transparent grey area the plane where the plane wave is injected.	50
4.4	Unit cell mesh after implementing the adaptive mesh refinement for two different η values, $\delta = 10^\circ$ and $a'/d = 0.9$. Thick orange lines surround the region where the mesh is refined.	51
4.5	Incident and reflected TM and TE plane waves in the rotated unit cell reference system.	52
4.6	Mesh size refinement for $a'/d = 0.9$, $\eta = 0.95$, $\alpha_{sw} = \delta = 0^\circ$, $\epsilon_r = 9.8$, $d = 3$ mm, $h = 1$ mm, and $f = 11$ GHz.	54

4.7 Reflected far-field projection of cross-polarized electric field component for different mesh refinements.	54
4.8 Incident surface wave for different δ patch orientations. The smaller angle between the symmetric axis of the square lattice and the patch is shown when this is different than zero.	55
4.9 Evaluation of the reciprocal network condition ($\Gamma_{12} - \Gamma_{21} = 0$) for $(\Delta x_0, \Delta y_0) = \lambda/1,300$. Thick red lines in figure 4.9b represent δ -values at which the cross-polarization is close to zero.	55
4.10 Conditions for lossless network obtained from equation (4.6) for $(\Delta x_0, \Delta y_0) = \lambda/1,300$	57
4.11 Obtained resistance matrix components $Re(\underline{\mathbf{Z}})$ (or $\underline{\mathbf{R}}$) after processing the reflection matrix $\underline{\mathbf{\Gamma}}$ for an incident surface wave with $k_\rho = 0$ and the simulation mesh $(\Delta x_0, \Delta y_0) = \lambda/1,300$	58
4.12 Opaque reactance matrix components considering $k_\rho = 0$ obtained from the simulation mesh $(\Delta x_0, \Delta y_0) = \lambda/1,300$	59
4.13 Cross-diagonal resistance evaluated in terms of the magnitude of the cross-diagonal impedance for the simulation mesh $(\Delta x_0, \Delta y_0) = \lambda/1,300$	59
4.14 Obtained transparent reactance database $\underline{\mathbf{X}}_s$ from the simulation mesh $(\Delta x_0, \Delta y_0) = \lambda/1,300$. The values for $\eta = 1$ have been added.	60
4.15 Equivalent impenetrable metasurface reactance linearly interpolated from simulations compared to the verification plot. The ψ angle is used in the vertical axis keeping $\alpha_{sw} = 0$ and $\psi = \delta$	60
4.16 Dispersion curves for different values of α_{sw} keeping $\delta = 0^\circ$ (top row), and for different values of δ keeping $\alpha_{sw} = 0$ (bottom plot). For all cases $\eta = 0.5$. Example data used from Mencagli et.al. [32].	61
4.17 IDC for two different patch configurations obtained with the presented simulation method (left) compared against results in literature (right). The color bar on the plots of the right represent the frequency in GHz.	62
4.18 Resulting database for the patch configuration specified in table 4.1 for $\alpha_{sw} = \delta$, $a/d = 0.9$ and $f = 3.2$ GHz.	63
4.19 Transparent reactance matrix components of the verification dataset for $\alpha_{sw} = 0$, 3.2 GHz, $a/d = 0.9$, and varying δ (figures 4.19a to 4.19c). Next, figures 4.19d to 4.19f show the relative difference between the obtained values in figure 4.18 with the verification database. The insets focus on the ambiguous image sections.	64
4.20 Difference between the numerically and analytically obtained α in step 8 of the modulation algorithm.	69
4.21 Difference between the numerically and analytically obtained radial modulation coefficient in step 13 of the algorithm.	69
4.22 α/k and β_Δ/k as a function of the modulation parameters for different values of \bar{X}/ζ considering $N = 1$ for a circularly-polarized antenna radiating a broadside beam. Example data obtained from Minatti et.al. [37].	71
4.23 Convergence of the modulation index \mathbf{m} as a function of the number of iterations in the algorithm for the verification antenna parameters.	71
4.24 Comparison of leakage parameters and Poynting vector magnitudes from the verification research publication [40, p. 3914] and the results after the implementation of this algorithm.	72
4.25 Comparison between the normalized total current density aligned with the x-axis $ J_x $ obtained from the implementation of this algorithm and the one resulting from the implementation of a MoM algorithm in the consulted research publication [40]. Right inset shows the x-aligned current distribution in the verification example, whereas the one on the left shows this same parameter for this implementation.	72
4.26 Main part: comparison between the resulting far-field CP pattern with the CP verification example (red solid line) and the XP (dotted line), obtained from Minatti et.al. [40, p. 3916]. Left inset: Difference between the resulting and the objective CP far-fields. Right inset: XP results. All the results are in the plane $\varphi = 45^\circ$	73
4.27 Directivity evaluated in the (u, v) -plane for the verification case.	73

4.28 Main part: CP far-field radiation pattern of SAR antenna design. Left inset: Difference between the resulting and the objective CP far-fields. Right inset: XP results. All the results are in the plane $\varphi = 45^\circ$	74
4.29 Directivity of SAR antenna evaluated in the (u, v) -plane.	74
4.30 Final transparent reactance dyad in the metasurface antenna.	75
4.31 Transparent reactance at $\phi = 0^\circ$ and $\phi = 90^\circ$ for the metasurface SAR antenna.	75
4.32 Discretisation results of objective transparent reactance and propagating angle of unit cells in the metasurface antenna.	77
4.33 Absolute and percentage difference of the partial results between $\tilde{\underline{\underline{\mathbf{X}}}}_s(x, y)$ and $\hat{\underline{\underline{\mathbf{X}}}}_s(x, y)$ aligned with α_{sw}	78
4.34 Absolute and percentage difference of the partial results between the dyadic components of $\tilde{\underline{\underline{\mathbf{X}}}}_s(x, y)$ and $\hat{\underline{\underline{\mathbf{X}}}}_s(x, y)$ aligned with α_{sw}	78
4.35 Reactance difference per dyadic component of the partial results compared with shape parameters η and $\frac{a'}{d}$ for a surface wave propagating approximately in vertical direction.	80
4.36 Reactance database $\underline{\underline{\mathbf{X}}}_s$ for $\psi = 45^\circ$. The black lines indicate the reactance values for maximum amplitude at $\phi = 90^\circ$	80
4.37 Patch orientation angle δ of the partial results with respect to the x -axis in the metasurface antenna.	80
4.38 Absolute and percentage difference of final results between $\tilde{\underline{\underline{\mathbf{X}}}}_s(x, y)$ and $\hat{\underline{\underline{\mathbf{X}}}}_s(x, y)$ aligned with α_{sw}	81
4.39 Absolute and percentage difference of final results between the dyadic components of $\tilde{\underline{\underline{\mathbf{X}}}}_s(x, y)$ and $\hat{\underline{\underline{\mathbf{X}}}}_s(x, y)$ aligned with α_{sw}	81
4.40 Reactance difference per dyadic component of final results compared with shape parameters η and $\frac{a'}{d}$ for a surface wave propagating approximately in vertical direction.	81
4.41 Final shape parameters in the metasurface antenna.	82
4.42 Final SAR metasurface antenna layout in the xy -plane. Areas 1 and 2 are shown in more detail in figure 4.43.	83
4.43 Metasurface SAR antenna detail views of figure 4.42.	83
5.1 Metasurface antenna mounting configuration. Source: [38]	85

List of Tables

1	Summary of SAR metasurface antenna characteristics.	iii
2.1	Desired antenna characteristics for every node of the SwarmSAR mission extracted from [17].	7
2.2	Reference antenna main characteristics [54] compared against SwarmSAR from table 2.1.	8
3.1	Synthesis process of metasurface antennas using adiabatic Floquet analysis. Table obtained from Minatti et. al. [40, p. 3913]	37
4.1	Literature examples of unit cell physical properties compared with chosen design (grey).	48
4.2	Antenna parameters for different aperture distributions. Formulas obtained from [1].	65
4.3	Elliptical patch shapes simulated for the database expansion. Gray cells show the shape simulated as a function of δ (rows) and $\frac{a'}{a}$ (columns) for $\eta \in [0.72, 0.8]$	79
5.1	Metasurface SAR antenna design main characteristics.	85
B.1	Sign of \bar{A}' and \bar{B}' considering the values of \bar{A} and \bar{B}	95

List of symbols

Symbol	Meaning
\perp	Perpendicular
\dagger	Hermitian conjugate
\top	Transpose
∇_t	Gradient of the transverse components
\mathcal{O}	Higher order terms
α	Attenuation parameter
α_{sw}	Surface wave propagation angle
β	Propagation constant
$\beta^{(q)}$	Propagation constant vector of the q Floquet mode
β_{Δ}	Propagation constant local variation
β_{sw}	Surface wave propagation constant
Γ	Reflection coefficient
$\underline{\underline{\Gamma}}$	Reflection matrix
$\Delta(\cdot)$	Variation of (\cdot) parameter
δ	Patch inclination angle
δ'	Dirac delta function
δ_c	Discrete constant
Δx_0	Reference Yee-cell length in x -direction
Δy_0	Reference Yee-cell length in y -direction
Δz_0	Reference Yee-cell length in z -direction
ϵ	Permittivity
ϵ_r	Relative permittivity
ζ	Impedance of free-space
η	Ratio between minor and major axes
η_{eff}	Antenna efficiency
θ	Elevation or inclination angle in the spherical space
θ_c	Critical angle
θ_i	Angle of incidence
θ_t	Angle of transmission
ϑ	Arbitrary value
ι	Arbitrary value
κ	Arbitrary value
λ	Wavelength
μ	Permeability
μ_0	Permeability of free-space
ξ	Arbitrary value
ρ	Position vector
$\hat{\rho}$	Radial unit vector
$\rho\rho$	Dyadic term aligned with ρ
$\rho\phi$	Cross-diagonal dyadic term
ρ_e	Electric source
ρ_m	Magnetic source
ρ	Radial position
$\bar{\rho}_\epsilon$	Dielectric density
$\bar{\rho}_r$	Supporting structure surface density

Symbol	Meaning
$\tilde{\sigma}$	Grouping of scalar terms in the modulation equation
σ	Electric conductivity
σ^*	Equivalent magnetic loss
τ	Arbitrary function
ϕ	Azimuthal angle in the antenna
$\hat{\phi}$	Azimuthal unit vector in the antenna
Φ'	Electric scalar potential
Φ	Slow-varying phase factor
$\phi\phi$	Dyadic term aligned with ϕ
$\tilde{\varphi}$	Phase shift
$\hat{\varphi}$	Azimuthal unit vector in the spherical space
φ	Azimuthal angle in the spherical space
$\underline{\chi}$	Adiabatic dispersion term
ψ	Angle between δ and α_{sw}
ω	Angular frequency
\bar{a}	Periodicity of antenna array along x-axis
\bar{A}	Arbitrary function
\mathbf{A}	Magnetic vector potential
\bar{a}	Feeding mechanism radius
a	Antenna radius
A	Reference area
\bar{A}'	Arbitrary function
a'	Ellipse major axis length
<i>avg</i>	Average
\mathbf{B}	Magnetic flux density
\bar{B}	Arbitrary function
\tilde{b}	Periodicity of antenna array along y-axis
\bar{B}'	Arbitrary function
b'	Ellipse minor axis length
$B_{\tilde{n}}$	Bessel function of order \tilde{n}
\bar{C}	Arbitrary function
c	Light speed
<i>cp</i>	Co-polarized
\mathbf{D}	Electric flux density
D	Directivity
d	Span of square lattice
<i>dyn</i>	Dynamic
\mathcal{E}	Electric field vector in the time domain
\mathbf{E}	Electric field vector
\hat{e}	Eigenvector
e	Weak electric field components
$\mathbf{E}^{(q)}$	Electric field corresponding to the q Floquet mode
E_0	Electric field amplitude
\mathbf{E}_A	Aperture field distribution
<i>ee</i>	TM mode
<i>eh</i>	Cross-polarization from TM to TE mode
\mathbf{E}_t	Tangential electric field
\mathbf{e}_t	Surface tangential components of the total surface electric field
\mathbf{f}	Vector amplitude function
f	Frequency
F	Slowly-varying function
$f(x)$	Electric field amplitude function of single antenna
F_p	p -solution of the magnetic vector potential

Symbol	Meaning
\tilde{g}	Fourier transform of the field of single antenna without phase shift
$g(x)$	Field of single antenna without phase shift
h	Dielectric thickness
\mathbf{H}	Magnetic field vector
$H_p^{(q)}$	Hankel function of the q kind and p order
\mathbf{H}_t	Tangential magnetic field
\mathbf{h}_t	Surface tangential components of the total surface magnetic field
$h(x)$	Electric field amplitude function of infinite antenna array
$\tilde{h}(k_x)$	Fourier transform of the field of an infinite antenna array
h'	Arbitrary periodic function
he	Cross -polarization TE to TM mode
hh	TE mode
\mathbf{I}	Surface current
I	Current
\bar{i}	Incident
\mathbf{J}	Electric current density
j	Imaginary number
$\mathbf{J}^{(q)}$	Current density of the q Floquet mode
$\mathbf{j}^{(q)}$	Basis function of the current density of the q Floquet mode
J_0	Current density magnitude of a purely propagating TM surface wave
\mathbf{k}	Wavevector
k	Free-space wavenumber
$k^{(q)}$	Wavenumber of the q mode
$\mathbf{k}^{(q)}$	Wavevector of the q mode
$\tilde{k}^{(0)}(\boldsymbol{\rho})\rho$	Global phase
k_ρ	Transverse wavenumber magnitude
$k_{\rho sw}$	Transverse wavenumber of the surface wave
k_c	Cut-off wavenumber
$Ks(\boldsymbol{\rho})$	Fast-varying phase factor
\mathbf{k}_t	Transverse wavevector
\mathbf{K}_t	Wavenumber times the gradient of the average phasing factor
K_z	Square root of the difference between k^2 and \mathbf{K}_t^2
\mathbf{L}	Arbitrary vector
L	Arbitrary function
$l(\boldsymbol{\rho})$	Average phasing factor
l	Arbitrary line
LF	Low-frequency
\mathbf{M}	Magnetic current density
\mathbf{m}	Modulation index vector
\bar{m}_ϵ	Dielectric mass
\tilde{n}	Constant term
n	Refractive index
N	Number of elements used
N_Y	Number of Yee-cells
obj	Objective
$\underline{\underline{\mathbf{P}}}$	Grouping matrix
p	Index variable
P_{rad}	Radiated power
P_{sw}	Surface wave power
p_{sw}	Surface wave power density per unit azimuthal angle

Symbol	Meaning
q	Index variable
$\underline{\underline{Q}}$	Average reactance matrix for iterative solving
\mathbf{r}	Space coordinate vector
r	Radial direction in spherical space
$\underline{\underline{R}}(\alpha_{sw})$	Rotation matrix as a function of α_{sw}
rot	Rotated matrix
$\underline{\underline{S}}$	Scattering matrix
$\underline{\underline{S}}$	Poynting vector
\bar{s}	Reflected
$S(\rho)$	Radiated power density per unit surface of the aperture
S_{pq}	Scattering parameter pq
t	Time
T	Transmission coefficient
t_s	Time step
$\underline{\underline{U}}$	Unitary matrix
U	Radiation intensity
u	Coordinate in the (u, v) -plane
U_A	Step function for the antenna aperture
V	Voltage
V'	Volume
v	Coordinate in the (u, v) -plane
w	Index variable
X	Reactance
x	Horizontal Cartesian coordinate
\mathbf{x}	Coefficient vector of the representation basis
$\underline{\underline{X}}$	Opaque reactance
$\hat{\mathbf{x}}$	Unit vector in Cartesian coordinates directed along the x -axis
$\underline{\underline{X}}^{(q)}$	Reactance of Floquet mode q
$\underline{\underline{X}}$	Average reactance
x_0	Arbitrary point at arbitrary plane
$\underline{\underline{X}}_0$	Transmission line reactance of free-space
$\underline{\underline{X}}_{cc}$	Transmission line reactance of the dielectric substrate
$\underline{\underline{X}}_{GF}^{(n)}$	Spectral Green function of the reactance of the grounded dielectric slab
x_p	Cross-polarized
X_{ps}	p -eigenvalue of the transparent reactance
$\tilde{\underline{\underline{X}}}_s$	Objective reactance distribution
$\hat{\underline{\underline{X}}}_s$	Estimated reactance distribution
$\underline{\underline{X}}_s$	Transparent reactance
$\underline{\underline{X}}_s^{\curvearrowright}$	Rotated transparent reactance matrix
x_s	Stationary x -coordinate
$X_{s,eq}$	Equivalent impenetrable metasurface reactance

Symbol	Meaning
y	Vertical Cartesian coordinate
\hat{y}	Unit vector in Cartesian coordinates directed along the y -axis
y_s	Stationary y -coordinate
z	Out-of-plane Cartesian or cylindrical coordinate
\vec{Z}	Impedance seen from right
\overleftarrow{Z}	Impedance seen from left
\hat{z}	Unit vector in Cartesian coordinates directed along the z -axis
$\underline{\underline{Z}}$	Impedance matrix
$\underline{\underline{z}}^{(\pm 1)}$	Slow-varying terms in the adiabatic expression
Z_∞	Asymptotic impedance
Z_0	Characteristic impedance
Z_1	Transmission line impedance of the dielectric substrate
$\underline{\underline{Z}}_G^{(q)}$	Spectral Green function of the q Floquet mode of the impedance
$\underline{\underline{Z}}_{MoM}$	MoM impedance matrix
$\underline{\underline{Z}}_s$	Transparent impedance

List of abbreviations

Abbreviation	Meaning
Ant	Antenna
cELC	Complementary Electric-Inductive-Capacitive
CRR	Cross Range Resolution
CP	Co-polarized
EM	Electromagnetic
ESA	European Space Agency
FDM	Frequency Division Multiplexing
FDTD	Finite-Differences Time-Domain
FNBW	First-Null Beam-Width
FSLM	First side lobe maximum
GF	Green's Function
HPBW	Half-Power Beam-Width
InSAR	Interferometric Synthetic Aperture Radar
IDC	Isofrequency Dispersion Curves
MIMO	Multiple Input Multiple Output
MoM	Method of Moments
PEC	Perfect Electric Conductor
PL	Payload
PML	Perfectly Matched Layer
PRF	Pulse Repetition Frequency
ROI	Region of Interest
RWG	Rao-Wilton-Gilsson
SAR	Synthetic Aperture Radar
SIMO	Single Input Multiple Output
SDG	Sustainable Development Goal
Sub	Subsystem
TE	Transverse Electric
TEM	Transverse Electromagnetic
TM	Transverse Magnetic
TNO	Netherlands Organisation for Applied Scientific Research
TRL	Technology Readiness Level
XP	Cross-polarized

Introduction

The introduction to this report consists of a brief motivation that summarizes separately the topics of Synthetic Aperture Radars (SAR) and metasurface antennas, and contextualizes the idea of using them together in space-based applications. Next, the research design is treated, containing the research objective and research questions. Finally, the overview of this report is presented.

1.1. Motivation

Antenna engineering has been an active field of research for more than a century. Its usefulness for wireless communication and imaging has made the improvement of this component a constant goal in systems design. This is also the case for space systems. They are found in the communication subsystem, which is a vital part in every space mission, and occasionally in the payload for imaging purposes. It is in this second application that this research project will focus, specifically in SAR imaging, which works at the radio frequency and has been used in numerous space missions not only for Earth observation, but also for other celestial bodies like in the Magellan mission which scanned the surface of Venus or the Cassini mission that scanned Titan.

SAR systems in space-based applications are used to obtain high resolution images of celestial bodies in three dimensions. One of the main advantages of this system is that images are less affected by atmospheric conditions and, as the light source is generated by the SAR system itself, it operates in day and night conditions. On the other side, SAR systems use antennas that are usually either phased-array antennas which are expensive, heavy and inefficient, or a mechanically actuated gimbal dishes, which are bulky, slow and require moving parts [4]. Three basic modes are used in SAR systems: stripmap, spotlight and scan. Stripmap mode uses a fixed beam radiation pattern to scan a large region of interest, resulting in a relatively low resolution. On the other side, spotlight mode steers the radiation beam to focus it in one region of interest, achieving a higher resolution at the expense of scanning a smaller region. Scan mode, in contrast, steers the beam over an even larger observable region that can be achieved with stripmap mode, but obtaining the worst image resolution. Examples of stripmap and spotlight modes are shown in figure 1.1 where the fixed and the steerable characteristic beams are clearly shown for both modes.

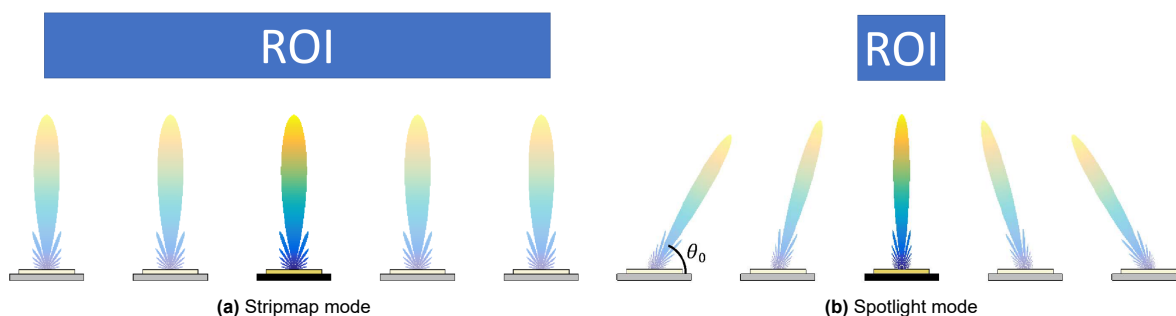


Figure 1.1: Stripmap and Spotlight SAR modes, where ROI represents Region Of Interest. Source: [4].

One new type of antenna that is being heavily researched during the past two decades is one based on modulated impenetrable metasurfaces, which is made up of an electrically thin metamaterial layer with a perfect electric conductor (PEC) ground plane at the bottom. Metamaterials are engineered-type materials which consist of an electrically thick dielectric substrate with sub-wavelength electromagnetic (EM) scatterers that, when modulated correctly, possess EM properties that are not found in natural homogeneous materials like negative refractive index, permeability and permittivity [31]. Further developments in this area made possible to control phase, amplitude, polarization and leakage of the propagating radiation with an electrically thin metamaterial layer, called metasurface. Due to these properties, metasurfaces have gained a lot of attention in the past two decades ranging from novel applications like cloaking to more conventional like antennas. In these two applications, a modulated impenetrable metasurface is used because it is desired that the radiation would propagate in the region above the metasurface in a controlled manner. Consequently, the radiation cannot penetrate what is underneath the metasurface (therefore impenetrable) and the scatterers are modulated so the radiation can be emitted in a pre-defined pattern. In the case of space missions and in the radio spectrum, many research papers have been devoted to the antenna applications of metasurfaces for satellite communication and imaging due to the wide range of radiating patterns that they can produce, their low-mass design, the ease to reproduce them and low manufacturing cost [38]. Currently, metasurfaces antennas have a Technology Readiness Level (TRL) of six for Earth observation¹, which makes them a promising technology for future space missions. An example of such antenna is shown in figure 1.2 which has been produced for a satellite with an isoflux radiation pattern [36]. Even though a disadvantage that is commonly cited is its dispersive nature, which would make them only suitable to function in a narrow bandwidth [38], new modulation methods show that they can achieve a bandwidth up to 30 % [8].

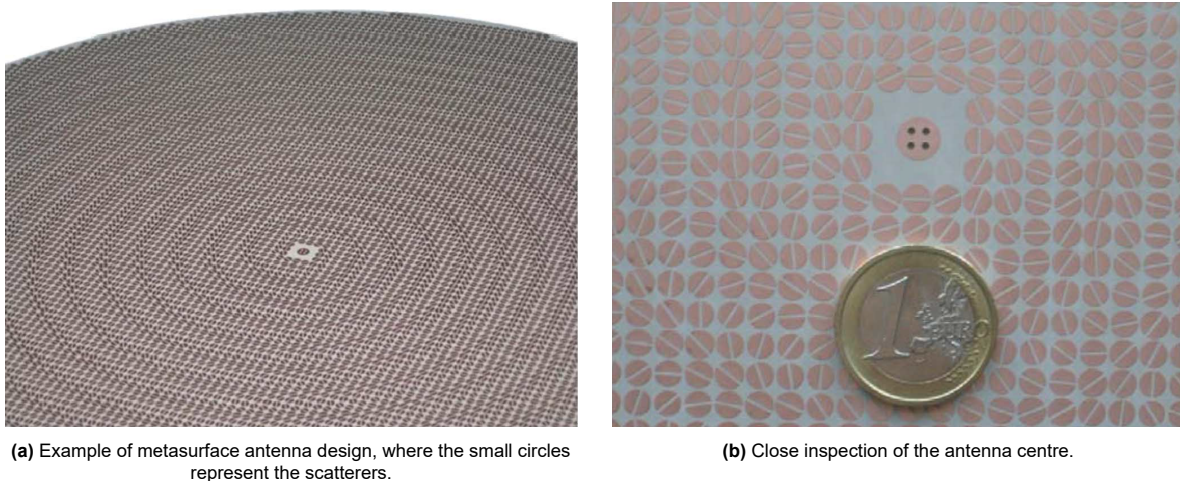


Figure 1.2: Example of metasurface antenna. Source: [36].

These two applications have an enormous potential when used together. Metasurface antennas, apart of being characterized by a flat design, are easy to manufacture because regular printed circuit board technology is used to produce them. “The qualification and acceptance process required for each new (*satellite antenna*) design constitutes a significant part of the development time and cost” [38, p. 1298], which can be reduced by just changing a thin layer on top of the antenna when different designs are required. On the other side, SAR are usually restricted to heavy and bulky systems to handle multiple imaging modes. However, there are new approaches directed to use them in a multi-static configuration composed by simple nodes with only high-gain antennas capable of realising interferometric measurements [17]. Joining these two concepts together could not only lower the entry barriers of these these type of missions, but could make earth observation more accessible.

In the context of the Sustainable Development Goals (SDG), SAR missions, depending on their nature, address *13 Climate action*, *14 Life below water*, and *15 Life on land*. The capability of these satellites to observe the movements of ice bodies and water currents has been proved for a long time,

¹Wave Up R & D. Available on <http://www.wave-up.it/rd/> Consulted on 06-11-2022

which affect primarily goals 13 and 14. Some examples are the characterization of ocean wave parameters [21] and oil spill characterization [55]. Furthermore, polarimetric SAR can be used to obtain indications of soil moisture [51], and biomass and carbon deposition in forests with the Biomass mission from the European Space Agency (ESA), which is expected to launch in 2024². On the other side, metasurface antennas, as it is an emerging field, are more related to *9 Industry, innovation and infrastructure* because of their still innovative nature that could make antenna production for satellite applications more affordable. The aforementioned SDGs are summarized in figure 1.3.



Figure 1.3: Metasurface and SAR SDGs

1.2. Research design

When consulting the available literature, some concepts have been developed in the scope of metasurface antennas with local-developed methods that are sometimes challenging to implement. For example, in [4] a method is shown particularly in the scope of SAR space missions with multiple imaging modes using dynamic metasurfaces, which in contrast with regular metasurfaces, have diodes in its unit cells that make possible controlling each one of these individually and obtain multiple radiation patterns. On the other side, in [40] a method to design metasurface antennas is presented which again relies on local-developed approach to retrieve the impedance of each unit cell configuration. Therefore, it was desired to use a different technique to arrive to a final design using more widely available tools for simulation, such as commercial software for EM.

The main research objective of this thesis is then to obtain a methodology to design an efficient metasurface antenna for SAR stripmap imaging mode by using efficient and widely available design methods and tools, and compare their performance with other antenna configurations. To achieve this objective, the following research questions can be formulated:

1. Given the antenna requirements for a space-based SAR satellite, how can it be arrived to an antenna design that, based on metasurface technology, would efficiently work in stripmap mode?
2. What are the main advantages and disadvantages of this design when compared to a reference antenna for SAR imaging systems with similar requirements?

The first research question focus on the development of a methodology to design metasurface antennas for space-based SAR imaging, which would fall into a design type of practice oriented research, as described by [53], where the research value would be on obtaining a different method that uses different tools for designing metasurface antennas. Subsequently, the research value of the second question relies on how well this type of antenna can be used for space-based SAR imaging when compared to another type of antenna which characteristics would fall within the mission requirements.

1.3. Report overview

This thesis report is structured as follows. Chapter 2 treats SAR systems. In there, a general explanation of these systems is given, followed by the example mission used for the antenna design, the SwarmSAR mission, and the antenna used for comparison. Next, chapter 3 explains the theoretical background necessary to understand metasurface antennas. It starts treating general electromagnetic theory, followed by antenna theory and ending in Finite-Difference Time-Domain (FDTD) EM simulations. Afterwards, chapter 4 goes over the developed methodology, in which the first part calculates the reactance database, the second part implements an existing methodology for the antenna synthesis [40], and the last part matches the required antenna pattern with the patches in the database. Finally, chapter 5 shows the final results and conclusions.

²Biomass - Earth Online. Available on <https://earth.esa.int/eogateway/missions/biomass?text=biomass> Consulted on 06-11-2022.

2

Synthetic Aperture Radar

Synthetic Aperture Radars (SAR) in space are used primarily for remote sensing applications. By using interferometric and polarimetric principles, they can achieve high resolutions and identify the main contribution to the back-scattered signal. In this chapter, the basics of SAR satellites is explained in section 2.1. Next, in section 2.2 the SwarmSAR mission, which is a multi-node SAR mission and its antenna requirements are used to test the robustness of the metasurface methodology in chapter 4, is introduced. Finally, to compare the resulting antenna design with existing concepts, an example of a folded antenna found in literature is presented in section 2.3 and its performance is evaluated with the requirements presented in section 2.2.

2.1. General principles of SAR satellites

Satellites capable of performing radio-imaging are used in the vicinity of a celestial body to obtain images in the microwave region. The main advantage of using this frequency band is that there is almost no atmospheric interference because microwaves can penetrate clouds and other atmospheric gases. Furthermore, there is no need to image only during the day, as the satellite itself generates its own source that is backscattered from the celestial body. Therefore, these type of satellites are regarded as “all-weather instruments” [51].

Airborne radio-imaging in stripmap mode is performed as shown in figure 2.1. Other modes exist, such as the scan and spotlight, but they require a steerable antenna and will not be discussed in this work. The spacecraft (it can also be an aircraft, but this thesis is centred in space applications) points a highly-directed beam from its antenna, which is slightly deviated from the nadir direction to the cross-track direction, to get an elliptical illumination shape of the terrain. The signal sent by the satellite consists on a chirped pulse, that is, a short pulse with a linear frequency variation [51, p. 8]. Then, the same satellite receives the backscattered signal and reconstructs the image.

In the cross-track (range) direction, the amplitude of the received signal from this elliptical surface has a time-delay between the scattering that results from the area that is closer to the antenna and the ones that are further away, which permits to differentiate the objects that are in the cross-track direction. It is therefore important that the beam is not pointing exactly pointing in nadir direction, because there would be ambiguities in the obtained image between positive and negative cross-track direction. Furthermore, the resolution in this direction is determined by the bandwidth of the chirped pulse because, as the frequency is being changed, the received signal can be filtered to associate each frequency to the cross-track location of the scatterer [51]. Therefore, the cross-track resolution is independent of the satellite’s distance to the target.

In case of the along-track (azimuthal) direction, two general techniques are easily recognizable. The first one is used by real aperture radars, which consists of employing the angular resolution of the antenna to obtain each pixel in this direction [51]. This is the same principle as a normal lens: the distance resolution is determined by the Half-Power Beam-Width (HPBW) and the satellite’s orbital altitude. The resulting imaging method is comparable with the so-called pushbroom imaging system, where the satellite obtains multiple pixels in the cross-track direction, but only one in the azimuthal direction for each snapshot taken.

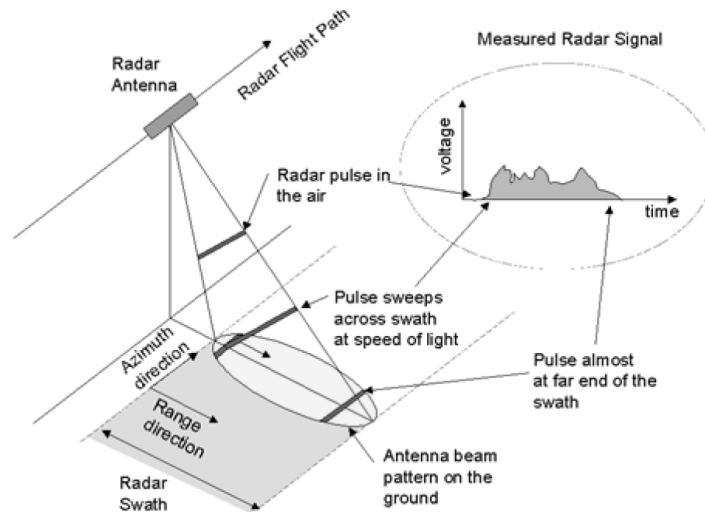


Figure 2.1: Radar airborne imaging acquisition. Source: [51]

The second technique is used by SAR and consists on using the Doppler effect of the reflected signal to increase the along-track resolution. As the satellite is approaching to a scatterer, the frequency starts increasing until the satellite is at broadside direction, when then it starts to decrease until the scatterer is out of sight. Then, the satellite can post-process the information received from the scatterer at different frequencies to increase the resolution in the along-track direction. Ultimately, the final resolution in this direction is determined by the amount of time the scatterer was observable by the satellite [51]. However, the Nyquist sampling criterion has to be considered to obtain the Pulse Repetition Frequency (PRF), which affects the achievable swath size [51]. Therefore, a compromise has to be made between the azimuthal resolution and this parameter.

Multiple SAR images of the same Region Of Interest (ROI) at different angles can be used to obtain a three-dimensional mapping of the area. This is achieved by the so-called Interferometric Synthetic Aperture Radar (InSAR), which uses phase information of receivers at different locations to resolve the three-dimensional ambiguities that may be encountered. Consider as an example figure 2.2 where four points are sampled with radars at different locations. It results clear that, due to phase differences, the points *a*, *b* and *d* are distinguishable in figure 2.2a due to its phase difference. However, points *a* and *c* cannot be distinguished because the same phase difference will be backscattered from both. If the information of the second radar in figure 2.2b is combined, where *a* and *c* can be differentiated, all the points could be differentiated and a three-dimensional image of the ROI can be achieved, which is the general principle of InSAR.

On the other side, the polarization of the emitted radiation from the SAR instrument can be predetermined to measure the surface response to different polarization types. Considering the case of linear polarization, the SAR instrument can send the signal with a referent linear polarization and measure the reflected signal with the same polarization and the one with a polarization shifted by 90° . This same procedure can be repeated for a signal emitted with an orthogonal polarization, and again the response can be measured in both polarizations. Instead of obtaining one value per pixel, four values are obtained which can be used to characterize different surface elements such as ocean currents [21], oil [55], soil moisture [51] and other surface elements.

2.2. SwarmSAR mission

In this section, the SwarmSAR mission is presented. In section 2.2.1 the mission is presented and the main characteristics of the composing nodes are described. In section 2.2.2 the desired antenna characteristics are presented and transformed into antenna requirements.

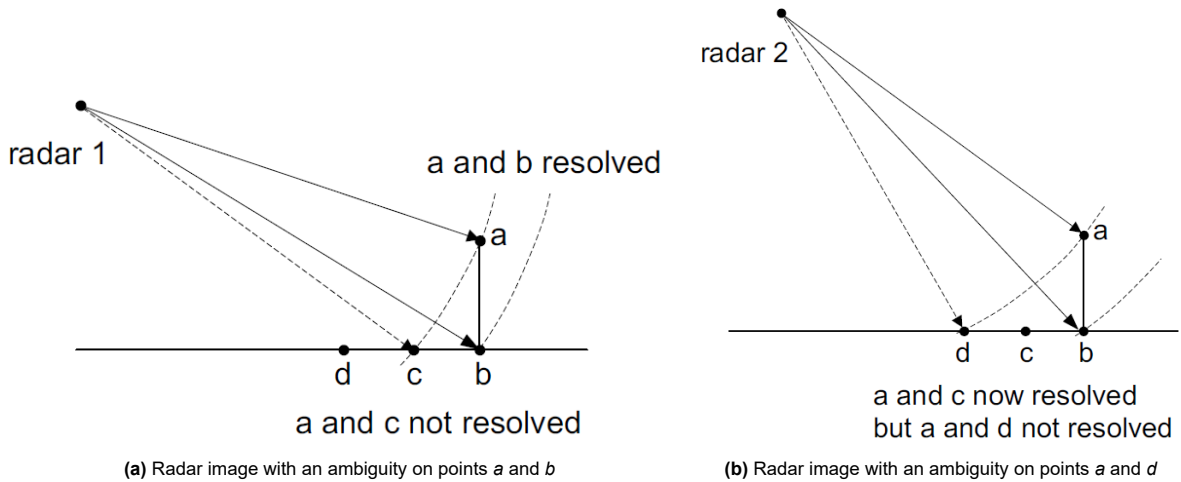


Figure 2.2: Image ambiguities when sampling independently at different locations. Source: [47, p. 182]

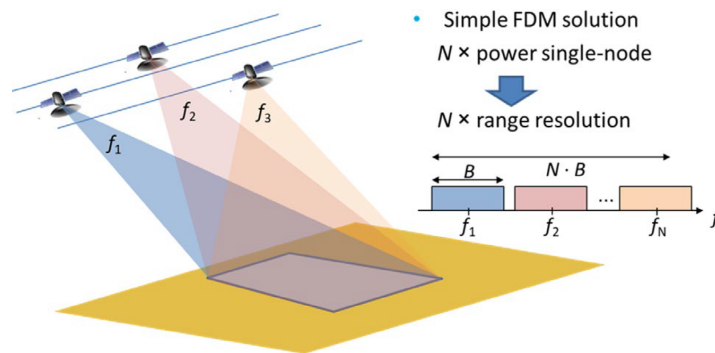


Figure 2.3: SwarmSAR concept formation. The same ROI would be observed by multiple satellites with different Tx (transmission) frequency, but all of them will be capable of receive the emitted signal of their peers. Source: [17].

2.2.1. Mission description

The SwarmSAR is a conceptual Earth-observation mission that would use multiple satellites working either individually as SAR satellites in stripmap mode, or as a constellation of Multiple Input Multiple Output (MIMO) satellites with the additional abilities to perform high-resolution imaging, along-track and cross-track interferometry [17]. In the high-resolution imaging acquisition, all the satellites would be pointing at the same ROI and would emit a pulse in a different section of the antenna bandwidth, using a Frequency Division Multiplexing (FDM) strategy simulating N Single Input Multiple Output (SIMO) systems, where N is the numbers of satellites in the constellation [17]. The nodes separation in cross-track direction allows to perform an InSAR image acquisition scheme that can resolve three-dimensional surfaces, as it was explained in section 2.1. Using a satellite constellation to perform InSAR has an important advantage: the temporal change of the mapped surface is negligible for one scan of the N imaging satellites [17]. The along-track separation between individual nodes gives the further possibility to perform ground moving target identification [17], detecting the relative velocity of moving targets in the ground. An example of this image acquisition scheme is shown in figure 2.3.

In this conceptual mission, each satellite is referred as a "node" which can be characterized as follows:

1. "The nodes are extremely simple in terms of illumination capabilities" [17].
2. "The nodes are all equal" [17].
3. "The nodes are self-sufficient" [17].

The first point indicates that a simple antenna with no beam-steering capabilities is required [17]. A pencil-beam antenna that radiates in broadside direction would fulfil this condition. The second point gives the constellation the interchangeability option whenever a node stops working. Finally, the third part emphasizes that each node can work independently to obtain SAR imaging in stripmap mode.

Compared to SAR satellites of medium (between 100 kg and 1000 kg) and large (>1000 kg) sizes, the SwarmSAR constellation does not have advanced beam-forming capabilities and does not support multiple SAR mode imaging. Therefore, the main purpose is not to compete with those platforms in terms of versatility nor image quality, but to provide "... competitive imaging at affordable costs and fast temporal revisit in a limited number of spots" [17]. Furthermore, for the interferometric mode, it benefits from a MIMO system with satellites separated in the along-track direction, delivering fast results with small temporal differences when compared to single-platform SAR systems, where the satellite has to pass at least two times over the same location to perform interferometric measurements, or have a big size to use two antennas sufficiently separated from each other to perform interferometric measurements. An example of the second case is the Shuttle Radar Topography Mission (SRTM) which used a main radar with transmission and receiving capabilities in the Shuttle cargo bay, and a receiver radar in a mast that would be deployed from the cargo bay, separated 60 m from the Shuttle [10].

2.2.2. Antenna requirements

The desired antenna characteristics of the SwarmSAR mission are retrieved from [17] and presented in table 2.1.

Table 2.1: Desired antenna characteristics for every node of the SwarmSAR mission extracted from [17].

Parameter	Value
Frequency	3.2 GHz
Average Tx power	20 W
Pulse length	20 μ s
Radius	1 m
Directivity	36 dB
HPBW	3.2°
Bandwidth	20 MHz
Surface weight ratio	1 m ² /kg

The characteristics from table 2.1 are subsequently translated into antenna requirements, where "SYS" represents system, "Sub" subsystem, "PL" payload, and "Ant" antenna. As in the source [17] there is no tolerance in the pulse length nor in the central frequency, the author assigned arbitrarily a value of 1 μ s and ± 1 MHz respectively for the completeness and robustness of the requirements.

- **SwarmSAR-SYS-Sub-PL-Ant-01:** The antenna shall perform its measurements on a central frequency of 3.2 GHz with a maximum deviation of ± 1 MHz.
- **SwarmSAR-SYS-Sub-PL-Ant-02:** The antenna bandwidth shall not be smaller than 20 MHz.
- **SwarmSAR-SYS-Sub-PL-Ant-03:** The maximum radius of the antenna shall not exceed 1 m.
- **SwarmSAR-SYS-Sub-PL-Ant-04:** The directivity shall not be smaller than 36 dB in the whole antenna bandwidth.
- **SwarmSAR-SYS-Sub-PL-Ant-05:** The HPBW shall not be greater than 3.2° in the whole antenna bandwidth.
- **SwarmSAR-SYS-Sub-PL-Ant-06:** The transmission power shall not be smaller than 20 W.
- **SwarmSAR-SYS-Sub-PL-Ant-07:** The pulse length shall not deviate by more than 1 μ s from 20 μ s.
- **SwarmSAR-SYS-Sub-PL-Ant-08:** The antenna surface weight ratio shall not be smaller than 1 m²/kg.

Particularly for this antenna design exercise, as research question focuses in obtaining a methodology for a metasurface antenna design, *SwarmSAR-SYS-Sub-PL-Ant-07* is not relevant because it constraints the precision of the system that sends the signal to the feeding point, which is out of the scope of the presented methodology. Furthermore, *SwarmSAR-SYS-Sub-PL-Ant-06* is also not evaluated because it constraints the design of the feeding system which is not included in the scope of

Table 2.2: Reference antenna main characteristics [54] compared against SwarmSAR from table 2.1.

Parameter	Value	SwarmSAR required value
Frequency	3.6 GHz	3.2 GHz
Stowed volume	2U (20 cm×10 cm×11.35 cm)	Not specified
Deployed area	1.7 m ²	3.14 m ²
Directivity	34 dB	36 dB
XP level	0 dB	Not specified
HPBW	3.4°	3.2°
Side lobe level	24 dB	Not specified
Directivity loss at ±100 MHz	0.5 dB	20 MHz bandwidth
Polarization	Linear	Not specified
Membrane mass	336 g	Not applicable
Total mass	1.5 kg	3.14 kg
Surface weight ratio	1.13 m ² /kg	1 m ² /kg

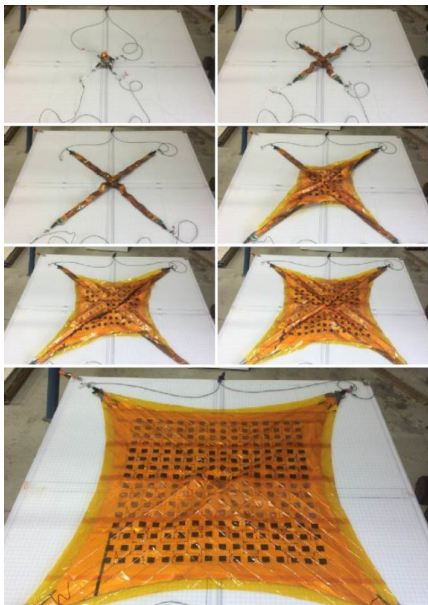
this methodology. The rest of the requirements are relevant and should be addressed in such a design. However, due to limitations in the capacity to simulate such a structure, the requirements that demand broadband simulations are not considered or only evaluated at the central frequency. That is the case for *SwarmSAR-SYS-Sub-PL-Ant-02*, which is not considered, and *SwarmSAR-SYS-Sub-PL-Ant-04* and *SwarmSAR-SYS-Sub-PL-Ant-05*, which are only evaluated at their central frequency of 3.2 GHz.

2.3. SAR antenna used for comparison

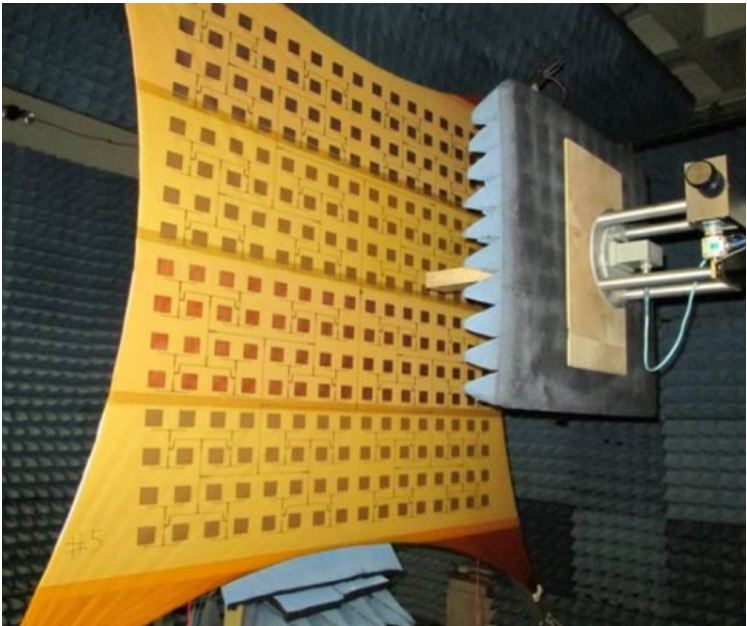
The antenna chosen for comparison is the one presented by Warren, Steinbeck, Minelli, and Mueller in [54]. This is a folded phased array antenna which consists of 16×16 patch antennas on a thin membrane that is deployed once the satellite is in orbit. Table 2.2 shows the main specifications of this antenna, which has been chosen because it is developed for space applications and has a similar central frequency as the one required in table 2.1, which is compared in the gray column.

Figure 2.4 shows the antenna used for comparison when it is folded, its unfolding procedure and when it is fully deployed. This antenna has been designed specifically to fit in a 6U CubeSat and, even though it is a phased array antenna, no electronic beam steering have been shown in the consulted literature, however the authors report that this capability has been tested [54].

With the presented antenna characteristics in table 2.2 and, comparing them with the antenna requirements presented before, some insights can be obtained from the suitability of this antenna design. First, the central frequency would have to be shifted to 3.2 GHz, which would increase the antenna size and its weight. However, it is expected that the new surface weight ratio would have a similar value to the current one of 1.13 m²/kg, which considers the complete antenna system and meets *SwarmSAR-SYS-Sub-PL-Ant-08*. Next, the HPBW of 3.4° does not meet *SwarmSAR-SYS-Sub-PL-Ant-05* because it is above the required value of 3.2°. Subsequently, the maximum directivity of 34 dB is below the requirement of 36 dB and therefore fails to meet *SwarmSAR-SYS-Sub-PL-Ant-04*, affecting *SwarmSAR-SYS-Sub-PL-Ant-02* too as the loss of 0.5 dB at ±100 MHz from the maximum directivity makes this requirement unrealisable with the current design. To meet all of these requirements, the antenna area and the number of patches should be increased, but *SwarmSAR-SYS-Sub-PL-Ant-03* constraints the antenna radius to 1 m, which can be interpreted as an antenna area constraint of 3.14 m². Currently, an area of 1.7 m² is used, but considering the shift to a bigger wavelength, the needed increase in gain and HPBW, a bigger antenna would result from subsequent iterations and an extra assessment would be needed to evaluate if the resulting design meets the antenna requirements. Nevertheless, this comparison case is useful due to the similarity with the SwarmSAR frequency band and gain, and would be used to compare against the resulting design from the methodology developed in chapter 4.



(a) Deployment procedure of antenna used for comparison.



(b) Fully deployed antenna used for comparison

Figure 2.4: Deployment procedure of the antenna used for comparison [54]

3

Theoretical background

In this chapter, the theoretical background is presented which consists on a brief explanation of general electromagnetic concepts that are subsequently applied in the metasurface design. This explanation should not be considered as sufficient to profoundly understand these topics, but as a comprehensive list of tools with its own derivations, and presented to facilitate their application and serve as a support for further discussion. This chapter is based on Maxwell's equations, and the derivations presented are expected to be traceable to that set of concepts.

This chapter is presented as follows. The first section contains the general electromagnetic theory, which is formed by the explanation of EM wave propagation, transmission line theory, antenna theory, and Floquet series. The section of Floquet series is based on solid knowledge of Fourier transforms and the properties of operators and functions in time and in the frequency domain. Furthermore, although it is not essential, that section contains an application to antenna theory which uses electric potential functions which explanation can be consulted in [1, p. 127-143]. These applications are oriented to antenna arrays but, for a continuous source as a metasurface, the array can be evaluated with an integral over the area instead of a summation of individual antennas to recreate their properties, ignoring coupling effects between elements.

The section of metasurface antennas contains an explanation oriented to the design of such structure. The concepts presented therein are simplified to be as concise as possible for their application. Most of these methods are based in a Galerkin spectral Method of Moments (MoM) used to obtain a solution that represents the weighted influence of a set of basis functions that describes the current density on the metasurface, which is characterized by a set of spectral Green's functions (GF) in terms of Floquet modes. This topic is partially treated in appendix C, but the reader is encouraged to review [24] if the interest in this part persists.

Finally, the section of FDTD simulations gives a brief introduction to this method, stating how the meshing works and the concept of Yee cells. As there are entire books treating this subject, it was decided to only explain the basics about this topic. The book of Yang and Mittra [15] provides a good explanation of this method applied to the simulation of metamaterials.

3.1. General electromagnetic theory

In this section the theoretical background of EM that is needed to properly analyse metasurface antennas in the microwave region and in spectral domain is explained. The first subsection explains wave propagation in the context of metasurface antennas. This is divided in three parts, where the first one derives the plane wave equations and their EM properties. Subsequently surface waves are treated, which are more closely related to metasurfaces because it is the main form in which EM waves propagate within them. Finally, the derivation of cylindrical EM waves is presented, which describes the direction in which surface waves propagate from a central feeding point to the boundaries of the metasurface antenna.

Subsequently, transmission line theory is treated with special emphasis on impedance calculation with scattering parameters (or S-parameters), and the transverse resonance method principles to obtain the impedance in transmission lines.

In the next subsection, a brief explanation of the spectral techniques used to calculate far-field patterns is given, together with the derivation of basic antenna parameters used to compare their performance.

Finally Floquet series are explained, which treat propagation of EM waves in periodic structures and in the spectral domain. They give a comprehensive idea of conditions for the propagation of fundamental and higher order modes in terms of wavenumber and elements size, which is subsequently applied in metasurface analysis to model unit cells and their periodicities, using their properties to obtain leaky-wave radiation.

3.1.1. EM wave propagation

EM wave propagation can be derived from Maxwell's equations. Their classical derivation in the phasor domain is presented in equation (3.1) where equation (3.1a) and equation (3.1b) describe the Gauss law, and equation (3.1c) and equation (3.1d) the Faraday's and Ampere-Maxwell's law respectively. In these equations, \mathbf{E} represents the electric field, \mathbf{r} the space coordinate vector, ρ_e the electric charge density per unit volume, ϵ the permittivity, \mathbf{H} the magnetic field, ρ_m the magnetic charge per unit volume, μ the permeability, j is the imaginary number, ω the angular velocity of the periodic signal, \mathbf{M} the magnetic current density, and \mathbf{J} the electric current density. It is important to note that the terms of magnetic charge $\rho_m(\mathbf{r})$ and magnetic current $\mathbf{M}(\mathbf{r})$ do not exist in reality, but are used as reciprocal terms of their electric counterparts, which is useful in multiple derivations.

$$\nabla \cdot \mathbf{E}(\mathbf{r}) = \frac{\rho_e(\mathbf{r})}{\epsilon} \quad (3.1a) \quad \nabla \cdot \mathbf{H}(\mathbf{r}) = \frac{\rho_m(\mathbf{r})}{\mu} \quad (3.1b)$$

$$\nabla \times \mathbf{E}(\mathbf{r}) = -j\omega\mu\mathbf{H}(\mathbf{r}) - \mathbf{M}(\mathbf{r}) \quad (3.1c) \quad \nabla \times \mathbf{H}(\mathbf{r}) = j\omega\epsilon\mathbf{E}(\mathbf{r}) + \mathbf{J}(\mathbf{r}) \quad (3.1d)$$

The phasor domain is used to analyse harmonic variables in a steady-state system, which are represented as in equation (3.2) for a time- and space-dependent variable [44, p. 8], where \mathcal{E} is the electric field in time domain, and t is the time. In the rest of this report, the phasor domain is assumed in all the notation except when explicitly stated.

$$\mathcal{E}(\mathbf{r}, t) = \text{Re}\{\mathbf{E}(\mathbf{r})e^{j\omega t}\} \quad (3.2)$$

It is important to note that the permittivity and permeability can be defined also in relative terms. That is, the one of free space, with sub-index zero, is taken as reference and a relative term multiplies it to obtain the permittivity and permeability of the medium. This is shown in equation (3.3) where a dependency on the frequency is obtained because this material property can change with different frequencies. However, in this report this dependency is implicitly assumed.

$$\epsilon_r(\omega)\epsilon_0 = \epsilon(\omega) \quad (3.3a) \quad \mu_r(\omega)\mu_0 = \mu(\omega) \quad (3.3b)$$

The EM power transferred by the electric and magnetic fields is represented by the Poynting vector $\mathbf{S}(\mathbf{r})$, defined in equation (3.4a) where the asterisk represents the complex conjugate. The Poynting vector represents the direction in which the energy is transferred and it is expressed in Watts per meter square. Its real part represents the actual power that is transferred either in Ohmic losses or in radiated energy, whereas its imaginary part is the energy that is in its vicinity in terms of capacitance and inductance. The average of the Poynting vector can be obtained with the half of the real part of equation (3.4a) in equation (3.4b), which is aligned with the propagation direction.

$$\mathbf{S}(\mathbf{r}) = \mathbf{E}(\mathbf{r}) \times \mathbf{H}^*(\mathbf{r}) \quad (3.4a) \quad \mathbf{S}_{avg}(\mathbf{r}) = \frac{1}{2}\text{Re}[\mathbf{E}(\mathbf{r}) \times \mathbf{H}^*(\mathbf{r})] \quad (3.4b)$$

It is widely known that the equation of a wave propagating in three dimensions can be represented in the time domain by equation (3.5a) where c is the propagation velocity, which in EM waves is the speed of light. In the phasor domain, the derivative notation can be taken away, resulting in equation (3.5b) where k is the wavenumber, measured in radians per meter. This last equation is known as the Helmholtz equation, which is widely used in EM theory.

$$\nabla^2 \mathcal{E}(\mathbf{r}, t) - \frac{1}{c^2} \frac{\partial^2 \mathcal{E}(\mathbf{r}, t)}{\partial t^2} = 0 \quad (3.5a) \quad \nabla^2 \mathbf{E} + \frac{\omega^2}{c^2} \mathbf{E} = \nabla^2 \mathbf{E} + k^2 \mathbf{E} = 0 \quad (3.5b)$$

This can be applied to the Maxwell's equations by considering a charge-free medium, that is, $\rho_e(\mathbf{r}) = \rho_m(\mathbf{r}) = 0$ and $\mathbf{J}(\mathbf{r}) = \mathbf{M}(\mathbf{r}) = 0$. Consequently, the Maxwell's equations described in equation (3.1)

take the form of equation (3.6).

$$\nabla \cdot \mathbf{E}(\mathbf{r}) = 0 \quad (3.6a) \quad \nabla \cdot \mathbf{H}(\mathbf{r}) = 0 \quad (3.6b)$$

$$\nabla \times \mathbf{E}(\mathbf{r}) = -j\omega\mu\mathbf{H}(\mathbf{r}) \quad (3.6c) \quad \nabla \times \mathbf{H}(\mathbf{r}) = j\omega\epsilon\mathbf{E}(\mathbf{r}) \quad (3.6d)$$

Following, the curl of equation (3.6b) is taken and the expression in the right-hand-side is replaced with equation (3.6d) in equation (3.7a). By using the property of the curl operator $\mathbf{L}_1 \times \mathbf{L}_2 \times \mathbf{L}_3 = \mathbf{L}_2(\mathbf{L}_1 \cdot \mathbf{L}_3) - \mathbf{L}_3(\mathbf{L}_1 \cdot \mathbf{L}_2)$ and equation (3.6a), the final expression results in the Helmholtz equation for the electric field, analogous to equation (3.5b). The same procedure can be repeated for the magnetic field, obtaining equation (3.7b). It is important to note that the wavenumber k results from these expressions, and is defined as $k = \omega\sqrt{\epsilon\mu}$.

$$\begin{aligned} \nabla \times \nabla \times \mathbf{E}(\mathbf{r}) &= -j\omega\mu [\nabla \times \mathbf{H}(\mathbf{r})] & \nabla \times \nabla \times \mathbf{H}(\mathbf{r}) &= j\omega\epsilon [\nabla \times \mathbf{E}(\mathbf{r})] \\ \nabla \times \nabla \times \mathbf{E}(\mathbf{r}) &= -j\omega\mu [j\omega\epsilon\mathbf{E}(\mathbf{r})] & \nabla \times \nabla \times \mathbf{H}(\mathbf{r}) &= -j\omega\epsilon [j\omega\mu\mathbf{H}(\mathbf{r})] \\ \nabla [\nabla \cdot \mathbf{E}(\mathbf{r})] - \nabla^2 \mathbf{E}(\mathbf{r}) &= \omega^2 \epsilon \mu \mathbf{E}(\mathbf{r}) & \nabla [\nabla \cdot \mathbf{H}(\mathbf{r})] - \nabla^2 \mathbf{H}(\mathbf{r}) &= \omega^2 \epsilon \mu \mathbf{H}(\mathbf{r}) \\ \nabla^2 \mathbf{E}(\mathbf{r}) + k^2 \mathbf{E}(\mathbf{r}) &= 0 & \nabla^2 \mathbf{H}(\mathbf{r}) + k^2 \mathbf{H}(\mathbf{r}) &= 0 \end{aligned} \quad (3.7a) \quad (3.7b)$$

Plane waves

Considering a uniform plane wave propagating in positive z-direction, that is, an EM wave where the electric and magnetic fields have uniform properties on the xy-plane. This makes the electric and magnetic fields lose their dependency with the in-plane components, resulting in $\mathbf{E}(\mathbf{r}) = \mathbf{E}(z)$ and $\mathbf{H}(\mathbf{r}) = \mathbf{H}(z)$. The general solution to equation (3.7a) becomes equation (3.8a) for the electric and equation (3.8b) for the magnetic fields, where H^+ and E^+ indicate a progressive and E^- and H^- a regressive wave respectively, which values can be obtained by using specific boundary and initial conditions for the evaluated problem. As the values of the electric and magnetic fields only depend on the z-component, the curl in z-direction is zero, making the electric and magnetic field to only have components perpendicular to the propagation direction.

$$E_x(z) = E_x^+ e^{-jkz} + E_x^- e^{jkz} \quad (3.8a) \quad H_x(z) = H_x^+ e^{-jkz} + H_x^- e^{jkz} \quad (3.8b)$$

Following, it can be shown that the electric and magnetic fields are orthogonal to each other. This can be obtained by evaluating equation (3.6c) and equation (3.6d) for each Cartesian component. The final result is shown in equation (3.9), where $\zeta = \sqrt{\mu/\epsilon}$ is the intrinsic impedance of the medium where the plane wave propagates, and $\hat{\mathbf{k}}$ is the unit vector of the wavevector which orientation denotes the direction of propagation of the plane wave and its magnitude the wavenumber. The direction of propagation of the wavevector is the same as the direction of the average Poynting vector $\mathbf{S}_{avg} = S_{avg} \hat{\mathbf{k}}$, which average magnitude is shown in equation (3.10).

$$\mathbf{E}(z) = -\zeta \hat{\mathbf{k}} \times \mathbf{H}(z) \quad (3.9a) \quad \mathbf{H}(z) = \frac{1}{\zeta} \hat{\mathbf{k}} \times \mathbf{E}(z) \quad (3.9b)$$

$$S_{avg} = \frac{|\mathbf{E}(z)|^2}{2\zeta} \quad (3.10)$$

Finally, consider the case of a plane wave propagating in positive z-direction with an incident angle θ_i between the z- and x-axes as shown in figure 3.1. When the electric field is oriented such that all of its components are contained in the propagation plane (aligned only with the z- and x-axes), and the magnetic field is aligned to the axis perpendicular to the propagation plane (in this case the y-axis), the plane wave is said to be vertical, parallel or P polarized. On the contrary, when the magnetic field components can be represented in the propagation plane and the electric field components are perpendicular to this plane, the plane wave is said to be horizontal, perpendicular, or S polarized. It is important to note that any arbitrary direction of the electric and magnetic field perpendicular to the propagation direction in the plane wave case is possible and can be represented as a linear combination of the P and S polarizations [44, p. 35].

Surface waves

Consider Snell's refraction law $n_1 \sin \theta_i = n_2 \sin \theta_t$ for a plane wave in 2D as in figure 3.1 going from a high to a low permittivity medium $n_1 > n_2$ with same electrical permeability $\mu_1 = \mu_2$, where n is

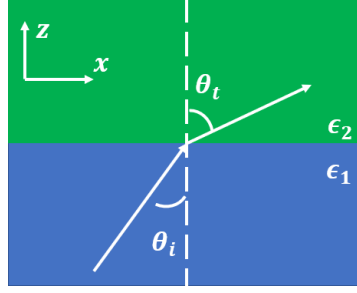


Figure 3.1: Incident and transmitted plane waves in dielectric media

the refractive coefficient defined as $n = \sqrt{\epsilon\mu}$, and θ_i and θ_t are the incident and transmitted angles respectively. For this configuration, the critical angle θ_c is the incidence angle for which $\theta_t = 90^\circ$, reducing Snell's law to $\sin \theta_c = \sqrt{\epsilon_2/\epsilon_1}$. Any incident plane wave with an incident angle higher than the critical angle "will be totally reflected and the transmitted wave will not propagate into region 2" [44, p. 38]. This case would result in $\sin \theta_t > 1$ and $\cos \theta_t = \sqrt{1 - \sin^2 \theta_t}$ where $\theta_t \in \text{Im}$. It results convenient to use the example of a P polarized wave transmitted from the interface given by Pozar [44, p. 38-41] as described in figure 3.1, which electric and magnetic fields are given by equation (3.11) where E_0 is the electric field amplitude, $T \in [0, 1]$ is the transmission coefficient, $\epsilon_{2,r}$ is the relative permittivity of medium 2, and k_2 is the wavenumber in medium 2.

$$\mathbf{E} = E_0 T (\cos \theta_t \hat{\mathbf{x}} - \sin \theta_t \hat{\mathbf{z}}) e^{-jk_2(x \sin \theta_t + z \cos \theta_t)} \quad (3.11a)$$

$$\mathbf{H} = \frac{E_0 T \sqrt{\epsilon_{2,r}}}{\zeta} \hat{\mathbf{y}} e^{-jk_2(x \sin \theta_t + z \cos \theta_t)} \quad (3.11b)$$

Considering that $\sin \theta_t$ is real and $\cos \theta_t$ imaginary, they can be replaced by $k_2 \sin \theta_t = \beta$ and $k_2 \cos \theta_t = -j\alpha$ where $(\beta, \alpha) \in \mathbb{R}$. The results are shown in equation (3.12) which clearly shows that the electric and magnetic field decay exponentially in z -direction and propagate in x -direction, which are main characteristics of surface waves, because the exponential function has a real negative component being multiplied by the z -distance.

$$\mathbf{E} = E_0 T \left(\frac{-j\alpha}{k_2} \hat{\mathbf{x}} - \frac{\beta}{k_2} \hat{\mathbf{z}} \right) e^{-j\beta x - \alpha z} \quad (3.12a)$$

$$\mathbf{H} = \frac{E_0 T \sqrt{\epsilon_{2,r}}}{\zeta} \hat{\mathbf{y}} e^{-j\beta x - \alpha z} \quad (3.12b)$$

The Poynting vector of a surface wave is shown in equation (3.13) where it can be interpreted that no real power flow occurs for the transmitted wave in z -direction, as the unit vector is multiplied by an imaginary term. Therefore, all the real power that the incident wave had before impinging the interface is reflected back [44].

$$\mathbf{S} = \mathbf{E} \times \mathbf{H}^* = \frac{E_0^2 T^2 \sqrt{\epsilon_{2,r}}}{\zeta k_2} (-j\alpha \hat{\mathbf{z}} + \beta \hat{\mathbf{x}}) e^{-2\alpha z} \quad (3.13)$$

Cylindrical waves

The following derivation is based on the work of Harrington described in [16, p. 198-204]. The Helmholtz equation presented in equation (3.5b) can be expressed in cylindrical coordinates as in equation (3.14) where the electric field in radial direction E_ρ is used to represent an arbitrary wave function.

$$\frac{1}{\rho} \frac{\partial}{\partial \rho} \left(\rho \frac{\partial E_\rho}{\partial \rho} \right) + \frac{1}{\rho^2} \frac{\partial^2 E_\rho}{\partial \phi^2} + \frac{\partial^2 E_\rho}{\partial z^2} + k^2 E_\rho = 0 \quad (3.14)$$

Solving equation (3.14) by separation of variables with the wave function in the form of $E_\rho = L_1(\rho)L_2(\phi)L_3(z)$ and dividing by E_ρ , equation (3.15) can be obtained.

$$\frac{1}{\rho L_1} \frac{d}{d\rho} \left(\rho \frac{dL_1}{d\rho} \right) + \frac{1}{\rho^2 L_2} \frac{d^2 L_2}{d\phi^2} + \frac{1}{L_3} \frac{d^2 L_3}{dz^2} + k^2 = 0 \quad (3.15)$$

The third term in equation (3.15) could be the only one that would depend of z . However, as no other term depend on that variable and this term is explicitly independent of ρ and ϕ , the third term must be explicitly independent on z to assure that the left-hand part of equation (3.15) gives always zero. Therefore, this term is replaced by the constant k_z in equation (3.16).

$$\frac{1}{L_3} \frac{d^2 L_3}{dz^2} = -k_z^2 \quad (3.16)$$

Then, equation (3.16) can be used in equation (3.15), which results in equation (3.17) after multiplying by ρ^2 .

$$\frac{\rho}{L_1} \frac{d}{d\rho} \left(\rho \frac{dL_1}{d\rho} \right) + \frac{1}{L_2} \frac{d^2 L_2}{d\phi^2} + (k^2 - k_z^2) \rho^2 = 0 \quad (3.17)$$

Now, the second term is independent on ρ and z , while the rest do not depend on ϕ . Therefore, it can be reached to the same conclusion as in equation (3.16) but for ϕ . That is, equation (3.18) where \tilde{n} is a constant.

$$\frac{1}{L_2} \frac{d^2 L_2}{d\phi^2} = -\tilde{n}^2 \quad (3.18)$$

Then, considering equation (3.18), equation (3.17) becomes equation (3.19), which depends only of ρ .

$$\frac{\rho}{L_1} \frac{d}{d\rho} \left(\rho \frac{dL_1}{d\rho} \right) - \tilde{n}^2 + (k^2 - k_z^2) \rho^2 = 0 \quad (3.19)$$

Finally, k_ρ is defined as $k_\rho^2 + k_z^2 = k^2$ and replaced in equation (3.19) to form equation (3.20a), which is part of a more general system of equations defined in equation (3.20).

$$\rho \frac{d}{d\rho} \left(\rho \frac{dL_1}{d\rho} \right) + [(k_\rho \rho)^2 - \tilde{n}^2] L_1 = 0 \quad (3.20a)$$

$$\frac{d^2 L_2}{d\phi^2} + \tilde{n}^2 L_2 = 0 \quad (3.20b) \quad \frac{d^2 L_3}{dz^2} + k_z^2 L_3 = 0 \quad (3.20c)$$

In this equation system, equations (3.20b) and (3.20c) represent harmonic functions which are analogous to the regular Helmholtz equation defined in equation (3.5b). Equation (3.20a), however, is a well-known differential equation which solutions are called Bessel functions. It is not the intention of this chapter to go into the details of the mathematical derivation of these functions. However, their implications in electromagnetic waves will be described.

The general solution of the harmonic equations in equation (3.20) can be expressed as in equation (3.8) by a function of the periodic elements, $h'(\tilde{n}\phi)$ and $h'(k_z z)$. Then, the solution to the Helmholtz equation in cylindrical coordinates can be expressed as the multiplication of the functions with the form of equation (3.21) where $B_{\tilde{n}}$ represents a Bessel's function of order \tilde{n} .

$$E_\rho(k_\rho, \tilde{n}, k_z) = B_{\tilde{n}}(k_\rho \rho) h'(\tilde{n}\phi) h'(k_z z) \quad (3.21)$$

In contrast to equation (3.8) and $h'(k_z z)$, $h'(\tilde{n}\phi)$ describes the contribution of an azimuthal variables with $E_\rho(\varphi) = E_\rho(\phi + 2\pi)$. Therefore " $h'(\tilde{n}\phi)$ must be periodic in ϕ , in which case \tilde{n} must be an integer" [16, p. 200]. In EM and in general in wave theory, $J_{\tilde{n}}(k_\rho \rho)$ represents the notation used for a Bessel function of order \tilde{n} which is non-singular at $\rho = 0$ and represents a cylindrical standing wave. On the other side, $H_{\tilde{n}}^{(1)}(k_\rho \rho)$, called a Hankel function of order \tilde{n} and of first kind, represents an inward travelling wave, whereas $H_{\tilde{n}}^{(2)}(k_\rho \rho)$ is a Hankel function of order \tilde{n} and second kind, denotes an outward travelling wave. In the Hankel functions the propagating wave can be attenuated if the wavenumber is complex.

3.1.2. Transmission line theory

A transmission line can be interpreted as a circuit representation that is used whenever the voltages and currents have non-negligible variations in magnitude and phase over the length of the circuit. In the traditional circuit model, the electrical properties are modelled considering ideal elements, also called lumped elements, such as capacitors, inductors and resistors. However, in microwaves “the phase of the voltage or current changes significantly over the physical extent of the device because the device dimensions are on the order of the electrical wavelength” [44, p. 1]. When analysing metasurfaces in the microwave regime, a transmission line representation is used to consider the effects of each of its element’s physical dimensions in terms of phase shifts of the incoming wave, which can later be analysed in terms of surface reactance distribution for the propagating waves.

EM modes

The electric and magnetic field can be represented by the sum of independent terms, denoted by the sub-index q in equation (3.22) defined as modes propagating in z -direction. One form of representing these modes is by separating the amplitude, $V_q(z)$ for electric and $I_q(z)$ for magnetic field respectively, and modal functions, $\mathbf{E}_q(x, y)$ and $\mathbf{H}_q(x, y)$.

$$\mathbf{E}(\mathbf{r}) = \sum_q V_q(z) \mathbf{E}_q(x, y) \quad (3.22a) \quad \mathbf{H}(\mathbf{r}) = \sum_q I_q(z) \mathbf{H}_q(x, y) \quad (3.22b)$$

Contrary to the plane wave case, the dependency on the in-plane components is preserved in this case, leading to the solution defined in equation (3.23) for a progressive wave where β is defined as the propagation constant, which is a positive real number.

$$\mathbf{E}(x, y, z) = \mathbf{E}(x, y) e^{-j\beta z} \quad (3.23a) \quad \mathbf{H}(x, y, z) = \mathbf{H}(x, y) e^{-j\beta z} \quad (3.23b)$$

Combining the expressions obtained in equation (3.23) with the Helmholtz equation in equation (3.7), equation (3.24) is obtained, where k_c is the cut-off wavenumber defined as $k_c^2 = k^2 - \beta^2$.

$$\left(\frac{\partial^2}{\partial x^2} + \frac{\partial^2}{\partial y^2} - \beta^2 + k^2 \right) \mathbf{E}(x, y) = \left(\frac{\partial^2}{\partial x^2} + \frac{\partial^2}{\partial y^2} + k_c^2 \right) \mathbf{E}(x, y) = 0 \quad (3.24a)$$

$$\left(\frac{\partial^2}{\partial x^2} + \frac{\partial^2}{\partial y^2} - \beta^2 + k^2 \right) \mathbf{H}(x, y) = \left(\frac{\partial^2}{\partial x^2} + \frac{\partial^2}{\partial y^2} + k_c^2 \right) \mathbf{H}(x, y) = 0 \quad (3.24b)$$

Furthermore, using equation (3.23) in Maxwell’s equations for source-free EM fields specified in equation (3.6), equation (3.25) is obtained. Solving this equation leaving the terms E_z and H_z as independent variables leads to the expressions in equation (3.26) for the field transverse components. The longitudinal components, on the other side, can be derived from the third element of the vector given in equation (3.24).

$$\begin{bmatrix} \frac{\partial E_z}{\partial y} + j\beta E_y \\ -j\beta E_x - \frac{\partial E_z}{\partial x} \\ \frac{\partial E_y}{\partial x} - \frac{\partial E_x}{\partial y} \end{bmatrix} = -j\omega\mu \mathbf{H}(x, y, z) \quad (3.25a) \quad \begin{bmatrix} \frac{\partial H_z}{\partial y} + j\beta H_y \\ -j\beta H_x - \frac{\partial H_z}{\partial x} \\ \frac{\partial H_y}{\partial x} - \frac{\partial H_x}{\partial y} \end{bmatrix} = -j\omega\mu \mathbf{E}(x, y, z) \quad (3.25b)$$

$$E_x = -\frac{j}{k_c^2} \left(\beta \frac{\partial E_z}{\partial x} + \omega\mu \frac{\partial H_z}{\partial y} \right) \quad (3.26a) \quad H_x = \frac{j}{k_c^2} \left(\omega\epsilon \frac{\partial E_z}{\partial y} - \beta \frac{\partial H_z}{\partial x} \right) \quad (3.26b)$$

$$E_y = \frac{j}{k_c^2} \left(-\beta \frac{\partial E_z}{\partial y} + \omega\mu \frac{\partial H_z}{\partial x} \right) \quad (3.26c) \quad H_y = -\frac{j}{k_c^2} \left(\omega\epsilon \frac{\partial E_z}{\partial x} + \beta \frac{\partial H_z}{\partial y} \right) \quad (3.26d)$$

Solutions to equation (3.24) and equation (3.26) can be classified as follows according to the values of E_z and H_z :

- Transverse electromagnetic (TEM): Both the components of the electric and magnetic fields that are aligned with the propagation direction are zero ($E_z = H_z = 0$).
- Transverse electric (TE): The electric field component aligned with the propagation direction is zero, but the one of the magnetic field is not ($E_z = 0$ and $H_z \neq 0$).

- Transverse magnetic (TM): Only the magnetic field is orthogonal to the propagation ($H_z = 0$ and $E_z \neq 0$).
- Hybrid mode: The electric and magnetic fields can have components aligned with the propagation direction ($E_z \neq 0$ and $H_z \neq 0$).

In the case of TEM waves, non-trivial solutions exist for equation (3.26) if $k = \beta$ and $k_c = 0$. When the field components parallel to the propagation direction are set equal to zero, the ratio between field perpendicular components results in equation (3.27) which is the equation of the wave impedance for the TEM mode. It is important to note that this equation is frequency-independent, that is, the impedance value does not vary with varying frequency. Furthermore, TEM waves can only exist when two conductors are separated from each other, originating a difference in electric potential [44, p. 99]. This can be obtained by considering $E_z = H_z = 0$ in the Helmholtz equation, which results in the Laplace equation given in equation (3.28). A solution to this equation is given in equation (3.29) where $\Phi'(x, y)$ is the electric scalar potential function, which is the same as in electrostatics. Following from electrostatics theory, the voltage and currents can be defined as in equation (3.30) where the voltage is calculated by integrating the electric field through two points with different electric potential p_1 and p_2 , and the current is obtained by integrating along one of the magnetic field lines defined as \vec{l}_c . It is important to note that the characteristic impedance (Z_0) in the TEM case can be defined as the ratio of current and voltages in the progressive and regressive wave cases as in equation (3.31). The progressive and regressive solutions are obtained because equation (3.29) satisfies Laplace equation, which as in the Helmholtz case in equation (3.8), results in equation (3.32). Finally, the average power P_{avg} leaving an area A can be obtained from equation (3.4) as shown in equation (3.33) which contains the real power in the real term and the reactive power in the imaginary term.

$$Z_{TEM} = \frac{E_x}{H_y} = -\frac{E_y}{H_x} = \sqrt{\frac{\mu}{\epsilon}} = \zeta \quad (3.27)$$

$$\left(\frac{\partial^2}{\partial x^2} + \frac{\partial^2}{\partial y^2}\right) E_{x,y} = \nabla_t^2 \mathbf{E}_t(x, y) = 0 \quad (3.28a) \quad \left(\frac{\partial^2}{\partial x^2} + \frac{\partial^2}{\partial y^2}\right) H_{x,y} = \nabla_t^2 \mathbf{H}_t(x, y) = 0 \quad (3.28b)$$

$$\mathbf{E}_t = -\nabla_t \Phi'(x, y) \quad (3.29)$$

$$V = \Phi'_1 - \Phi'_2 = \int_{p_2}^{p_1} \mathbf{E} \cdot d\mathbf{l}_{1,2} \quad (3.30a) \quad I = \oint \mathbf{H} \cdot d\mathbf{l} \quad (3.30b)$$

$$Z_0 = \frac{V^+}{I^+} = -\frac{V^-}{I^-} \quad (3.31)$$

$$V(z) = V^+ e^{-jkz} + V^- e^{jkz} \quad (3.32a) \quad I(z) = I^+ e^{-jkz} + I^- e^{jkz} \quad (3.32b)$$

$$P_{avg} = \frac{1}{2} \iint_A (\mathbf{E} \times \mathbf{H}^*)^\top \cdot d\mathbf{A} = \frac{1}{2} (VI^*) \quad (3.33)$$

In the case of TE waves, the result of replacing $E_z = 0$ in equation (3.26) is given in equation (3.34). In this case, the cut-off frequency is different from zero as non-trivial solutions can be obtained. Therefore, the TE wave impedance can be derived as in equation (3.35), which is frequency-dependent. Furthermore, the solutions for the longitudinal component of the magnetic fields are defined by equation (3.36), which are subjected to the boundary conditions given by the specific geometry of the system. As many of these solutions can arise with different cut-off frequencies, H_z can be expressed as a linear combination of these as in equation (3.37), where the individual elements in the sum are referred as modes. Whenever the excited frequency is greater than the cut-off frequency, the mode is referred as a propagating mode. Otherwise, it is evanescent as its amplitude decreases exponentially in the guiding structure.

$$E_x = -\frac{j\omega\mu}{k_c^2} \frac{\partial H_z}{\partial y} \quad (3.34a) \quad H_x = -\frac{j\beta}{k_c^2} \frac{\partial H_z}{\partial x} \quad (3.34b)$$

$$E_y = \frac{j\omega\mu}{k_c^2} \frac{\partial H_z}{\partial x} \quad (3.34c) \quad H_y = -\frac{j\beta}{k_c^2} \frac{\partial H_z}{\partial y} \quad (3.34d)$$

$$Z_{TE} = \frac{E_x}{H_y} = -\frac{E_y}{H_x} = \frac{k\zeta}{\beta} \quad (3.35)$$

$$\left(\frac{\partial^2}{\partial x^2} + \frac{\partial^2}{\partial y^2} - \beta^2 + k^2 \right) H_z(x, y) = 0 \quad (3.36)$$

$$H_z(x, y, z) = \sum_q H_{z,q}(x, y) e^{-j\beta_q z} \quad (3.37)$$

The TM waves, on the other side, arise when $H_z = 0$. Equation (3.38) gives the field's transverse components, which results in a frequency-dependent wave impedance of the form of equation (3.39). The longitudinal component given in equation (3.40) is subjected to the boundary conditions defined by the specific geometry of the problem. As in the TE case, the cut-off frequency is greater than zero and is different for each mode arising in the structure. These define the longitudinal component of the electric field defined as in equation (3.41). There are propagating and evanescent modes which arise when the exciting frequency is greater or less than the cut-off frequency respectively, as in the TE case.

$$E_x = -\frac{j\beta}{k_c^2} \frac{\partial E_z}{\partial x} \quad (3.38a) \quad H_x = \frac{j\omega\epsilon}{k_c^2} \frac{\partial E_z}{\partial y} \quad (3.38b)$$

$$E_y = -\frac{j\beta}{k_c^2} \frac{\partial E_z}{\partial y} \quad (3.38c) \quad H_y = -\frac{j\omega\epsilon}{k_c^2} \frac{\partial E_z}{\partial x} \quad (3.38d)$$

$$Z_{TM} = \frac{E_x}{H_y} = -\frac{E_y}{H_x} = \frac{\beta\zeta}{k} \quad (3.39)$$

$$\left(\frac{\partial^2}{\partial x^2} + \frac{\partial^2}{\partial y^2} - \beta^2 + k^2 \right) E_z(x, y) = 0 \quad (3.40)$$

$$E_z(x, y, z) = \sum_q E_{z,q}(x, y) e^{-j\beta_q z} \quad (3.41)$$

When the excitation frequency is increased in a waveguide, the region of interest is close to a source, or discontinuities are present, additional modes may arise forming a discrete spectrum of propagating signals [16, p. 63]. Furthermore, these signals can be either TM, TE or TEM, which is how hybrid modes originate.

Port model

Although port models are used to analyse microwave circuits, they can also serve in grounded meta-surface design by representing each incident and reflected mode as a port. In a two-port model, that is two incident and two transmitted waves on a device, the scattering matrix ($\underline{\mathbf{S}}$) that relates the transmitted and reflected equivalent voltages can be represented as in equation (3.42) where V_p^+ and V_p^- are the equivalent incident and reflected voltages respectively [44, p. 174]. The parameter S_{pp} in $\underline{\mathbf{S}}$ represents, in absence of sources, the reflection coefficient when the incident wave starts propagating in transmission line p and all the other transmission lines are matched at their ends to avoid reflections. Then, the parameter S_{pq} where $p \neq q$ represents the transmission coefficient of an incident excitation in transmission line q that propagates into transmission line p when all the other transmission lines are again matched.

$$\begin{bmatrix} V_1^- \\ V_2^- \end{bmatrix} = \begin{bmatrix} S_{11} & S_{12} \\ S_{21} & S_{22} \end{bmatrix} \cdot \begin{bmatrix} V_1^+ \\ V_2^+ \end{bmatrix} \quad (3.42)$$

It is important to note that the term equivalent voltage is used to include, apart from the TEM, the TM and TE polarized waves which do not have a unique voltage value defined throughout their cross-section. The equivalent voltage is defined as the voltage needed to maintain all the properties of

currents, impedance and power for TEM modes in TE and TM modes. That is, the calculation of the characteristic impedance as in equation (3.31), the definition of progressive and regressive voltages and currents as in equation (3.32), the fact that their conjugated product is proportional to the average power as in equation (3.33), and the proportionality of voltage to transverse electric field, and current to transverse magnetic field as in equation (3.30) [44, p. 168]. Analogous to the equivalent voltage, the equivalent current for TE and TM modes can be defined considering all the previously presented requirements.

The impedance matrix can be defined in a similar manner as the scattering matrix. Equation (3.43) shows the matrix equation that defines the impedance matrix \underline{Z} for a two-port system.

$$\begin{bmatrix} V_1 \\ V_2 \end{bmatrix} = \begin{bmatrix} Z_{11} & Z_{12} \\ Z_{21} & Z_{22} \end{bmatrix} \cdot \begin{bmatrix} I_1 \\ I_2 \end{bmatrix} \quad (3.43)$$

There are important properties that can be derived from equation (3.43). Consider the case of a reciprocal two-port network, that is, a network without active devices. Then, the fields at the termination ports 1 and 2 of the transmission lines caused by two independent sources \hat{a} and \hat{b} in the network are related by equation (3.44) due to the reciprocity theorem, explained in appendix A. It is only considered the surface defined by the termination ports because, if the device has metal boundaries then $\mathbf{E}_t = 0$, or if it has infinite boundaries (free-space) then the tangential fields can also be approximated to zero [44, p. 176].

$$\iint_{A_1} (\mathbf{E}_{\hat{a}1} \times \mathbf{H}_{\hat{b}2})^\top \cdot d\mathbf{A}_1 + \iint_{A_2} (\mathbf{E}_{\hat{a}2} \times \mathbf{H}_{\hat{b}2})^\top \cdot d\mathbf{A}_2 = \iint_{A_1} (\mathbf{E}_{\hat{b}2} \times \mathbf{H}_{\hat{a}1})^\top \cdot d\mathbf{A}_1 + \iint_{A_2} (\mathbf{E}_{\hat{b}2} \times \mathbf{H}_{\hat{a}2})^\top \cdot d\mathbf{A}_2 \quad (3.44)$$

Considering the condition for tangential fields in transmission lines defined previously to obtain equivalent voltages and currents, the fields present in equation (3.44) can be expressed as in equation (3.45) with their equivalent voltages and currents, and the terms $\mathbf{E}_{t,p}$ and $\mathbf{H}_{t,p}$ which represent the transverse modal electric and magnetic field respectively for port p [44, p. 176]. These modal fields are normalized such that equation (3.46) holds at the defined boundaries.

$$\mathbf{E}_{\hat{a}1} = V_{\hat{a}1} \mathbf{E}_{t,1} \quad (3.45a) \quad \mathbf{H}_{\hat{a}1} = I_{\hat{a}1} \mathbf{H}_{t,1} \quad (3.45b) \quad \mathbf{E}_{\hat{b}1} = V_{\hat{b}1} \mathbf{E}_{t,1} \quad (3.45c) \quad \mathbf{H}_{\hat{b}1} = I_{\hat{b}1} \mathbf{H}_{t,1} \quad (3.45d)$$

$$\mathbf{E}_{\hat{a}2} = V_{\hat{a}2} \mathbf{E}_{t,2} \quad (3.45e) \quad \mathbf{H}_{\hat{a}2} = I_{\hat{a}2} \mathbf{H}_{t,2} \quad (3.45f) \quad \mathbf{E}_{\hat{b}2} = V_{\hat{b}2} \mathbf{E}_{t,2} \quad (3.45g) \quad \mathbf{H}_{\hat{b}2} = I_{\hat{b}2} \mathbf{H}_{t,2} \quad (3.45h)$$

$$\iint_{A_1} (\mathbf{E}_{t,1} \times \mathbf{H}_{t,1})^\top \cdot d\mathbf{A}_1 = \iint_{A_2} (\mathbf{E}_{t,2} \times \mathbf{H}_{t,2})^\top \cdot d\mathbf{A}_2 = 1 \quad (3.46)$$

Including equation (3.45) and equation (3.46) in equation (3.44), equation (3.47) can be obtained, which leads to the conclusion that $Z_{12} = Z_{21}$ making the impedance matrix symmetric for a reciprocal network.

$$\begin{aligned} V_{\hat{a}1} I_{\hat{b}1} - V_{\hat{b}1} I_{\hat{a}1} + V_{\hat{a}2} I_{\hat{b}2} - V_{\hat{b}2} I_{\hat{a}2} &= 0 \\ (Z_{11} I_{\hat{a}1} + Z_{12} I_{\hat{a}2}) I_{\hat{b}1} - (Z_{11} I_{\hat{b}1} + Z_{12} I_{\hat{b}2}) I_{\hat{a}1} + (Z_{21} I_{\hat{a}1} + Z_{22} I_{\hat{a}2}) I_{\hat{b}2} - (Z_{21} I_{\hat{b}1} + Z_{22} I_{\hat{b}2}) I_{\hat{a}2} &= 0 \\ (Z_{12} - Z_{21})(I_{\hat{a}2} I_{\hat{b}1} - I_{\hat{b}2} I_{\hat{a}1}) &= 0 \\ Z_{12} &= Z_{21} \end{aligned} \quad (3.47)$$

The same property can be derived for the scattering matrix. From equations (3.32) and (3.43), equation (3.48) is obtained, which gives an explicit expression of the scattering matrix in terms of the impedance matrix. Then, considering a reciprocal network where $\underline{Z} = \underline{Z}^\top$, it can be shown with the last expression in equation (3.48) that the scattering matrix is also symmetric in a reciprocal system. Equation (3.49) shows this last step where \underline{U} is the unitary matrix.

$$\begin{aligned}
\mathbf{V}^+ + \mathbf{V}^- &= \underline{\mathbf{Z}} \cdot (\mathbf{I}^+ + \mathbf{I}^-) \\
\mathbf{V}^+ + \mathbf{V}^- &= \underline{\mathbf{Z}} \cdot \left(\frac{1}{Z_0} \mathbf{V}^+ - \frac{1}{Z_0} \mathbf{V}^- \right) \\
Z_0(\mathbf{V}^+ + \mathbf{V}^-) &= \underline{\mathbf{Z}} \cdot (\mathbf{V}^+ - \mathbf{V}^-) \\
(\underline{\mathbf{Z}} - Z_0 \underline{\mathbf{U}}) \cdot \mathbf{V}^+ &= (\underline{\mathbf{Z}} + Z_0 \underline{\mathbf{U}}) \cdot \mathbf{V}^- \\
\mathbf{V}^- &= (\underline{\mathbf{Z}} + Z_0 \underline{\mathbf{U}})^{-1} \cdot (\underline{\mathbf{Z}} - Z_0 \underline{\mathbf{U}}) \cdot \mathbf{V}^+ \\
\underline{\mathbf{S}} &= (\underline{\mathbf{Z}} + Z_0 \underline{\mathbf{U}})^{-1} \cdot (\underline{\mathbf{Z}} - Z_0 \underline{\mathbf{U}})
\end{aligned} \tag{3.48}$$

$$\underline{\mathbf{S}}^\top = (\underline{\mathbf{Z}} - Z_0 \underline{\mathbf{U}})^\top \cdot [(Z_0 \underline{\mathbf{U}} + \underline{\mathbf{Z}})^{-1}]^\top = (\underline{\mathbf{Z}} - Z_0 \underline{\mathbf{U}}) \cdot (Z_0 \underline{\mathbf{U}} + \underline{\mathbf{Z}})^{-1} = \underline{\mathbf{S}} \tag{3.49}$$

Furthermore, an explicit equation of $\underline{\mathbf{Z}}$ is reached in terms of $\underline{\mathbf{S}}$ by replacing $\mathbf{V}^- = \underline{\mathbf{S}} \cdot \mathbf{V}^+$ in the third line of equation (3.48). Then equation (3.50) is obtained which relates the scattering and impedance matrices.

$$\underline{\mathbf{Z}} = Z_0(\underline{\mathbf{U}} + \underline{\mathbf{S}}) \cdot (\underline{\mathbf{U}} - \underline{\mathbf{S}})^{-1} \tag{3.50}$$

Apart from reciprocal networks, there can also be networks that do not dissipate any of the input power, called lossless networks which requirement is $\text{Re}\{P_{av}\} = 0$ from equation (3.33) which can also be applied to TM and TE modes. First, equation (3.51) is obtained by using equation (3.33) for the entire network. Then, evaluating the case where $p = q$, equation (3.52) is reached which shows that $\text{Re}\{Z_{pp}\} = 0$. Then, for cases where $p \neq q$, it can be assumed that all the other currents that do not pass through ports p or q are set to zero, which results in the condition given by equation (3.53). It results necessary that $\text{Re}\{I_p I_q^* + I_q I_p^*\} \text{Re}\{Z_{pq}\} = 0$ to fulfil equation (3.53), which results in equation (3.54) and $\text{Re}\{Z_{pq}\} = 0$. Therefore, to obtain a lossless network the impedance matrix has to be purely imaginary [44, p. 177].

$$P_{avg} = \frac{1}{2} \mathbf{V}^\top \cdot \mathbf{I}^* = \frac{1}{2} (\underline{\mathbf{Z}} \cdot \mathbf{I})^\top \cdot \mathbf{I}^* = \frac{1}{2} \mathbf{I}^\top \cdot \underline{\mathbf{Z}} \cdot \mathbf{I}^* = \frac{1}{2} \sum_{p=1}^N \sum_{q=1}^N I_p Z_{pq} I_q^* \tag{3.51}$$

$$\text{Re}\{I_p Z_{pp} I_p^*\} = |I_p|^2 \text{Re}\{Z_{pp}\} = 0 \quad \text{where} \quad \text{Re}\{Z_{pp}\} = 0 \tag{3.52}$$

$$\text{Re}\{(I_p I_q^* + I_q I_p^*) Z_{pq}\} = 0 \tag{3.53}$$

$$[\text{Re}\{I_p I_q^*\} + \text{Re}\{I_q I_p^*\}] \text{Re}\{Z_{pq}\} = 2 [\text{Re}\{I_p\} \text{Re}\{I_q\} + \text{Im}\{I_p\} \text{Im}\{I_q\}] \text{Re}\{Z_{pq}\} = 0 \tag{3.54}$$

where $\text{Re}\{Z_{pq}\} = 0$

In the case of the scattering matrix, the real average power can be derived from equation (3.55). The real part of last two terms inside the curly brackets equals to zero, as shown in equation (3.56). Then, the first two terms are completely real, which means that they must be equal to have no losses in the network. From this condition equation (3.57) can be derived, which shows that the scattering matrix must be unitary to have no losses in the network [44, p. 182-183].

$$\text{Re}\{P_{av}\} = \text{Re}\left\{ \frac{1}{2} \mathbf{V}^\top \cdot \mathbf{I}^* \right\} = \frac{1}{2Z_0} \text{Re}\{(\mathbf{V}^+ + \mathbf{V}^-)^\top \cdot (\mathbf{V}^+ - \mathbf{V}^-)^*\} \tag{3.55}$$

$$\text{Re}\{P_{av}\} = \frac{1}{2Z_0} \text{Re}\{(\mathbf{V}^+)^\top \cdot (\mathbf{V}^+)^* - (\mathbf{V}^-)^\top \cdot (\mathbf{V}^-)^* + (\mathbf{V}^-)^\top \cdot (\mathbf{V}^+)^* - (\mathbf{V}^+)^\top \cdot (\mathbf{V}^-)^*\}$$

$$\begin{aligned}
&\text{Re}\left\{ \sum_{p=1}^N V_p^- (V_p^+)^* - \sum_{p=1}^N V_p^+ (V_p^-)^* \right\} \\
&= \sum_{p=1}^N \text{Re}\{V_p^-\} \text{Re}\{V_p^+\} + \sum_{p=1}^N \text{Im}\{V_p^+\} \text{Im}\{V_p^-\} - \sum_{p=1}^N \text{Re}\{V_p^+\} \text{Re}\{V_p^-\} - \sum_{p=1}^N \text{Im}\{V_p^+\} \text{Im}\{V_p^-\} = 0
\end{aligned} \tag{3.56}$$

$$(\mathbf{V}^+)^T \cdot (\mathbf{V}^+)^* = (\mathbf{V}^-)^T \cdot (\mathbf{V}^-)^* = (\underline{\mathbf{S}} \cdot \mathbf{V}^+)^T \cdot (\underline{\mathbf{S}} \cdot \mathbf{V}^+)^* = (\mathbf{V}^+)^T \cdot \underline{\mathbf{S}}^T \cdot \underline{\mathbf{S}}^* \cdot (\mathbf{V}^+)^* \quad (3.57)$$

$$\underline{\mathbf{S}}^T \cdot \underline{\mathbf{S}}^* = \underline{\mathbf{U}}$$

Transverse resonance condition

The transverse resonance condition is a method used to calculate the resonance frequencies of structures with resonating properties. In metasurface design, they are applied to unit cells to find the dispersion function which relates the surface wave wavenumber with the free-space wavenumber. This subsection is based on the work of David R. Jackson which lecture materials can be accessed online [18].

A diagram of a lossless resonator is shown in figure 3.2 which serves as an example to summarize this method. In this one-dimensional diagram, two impedance values jX_{L1} and jX_{L2} are defined at $x = 0$ and at $x = L$ respectively in a transmission line with characteristic impedance Z_0 .

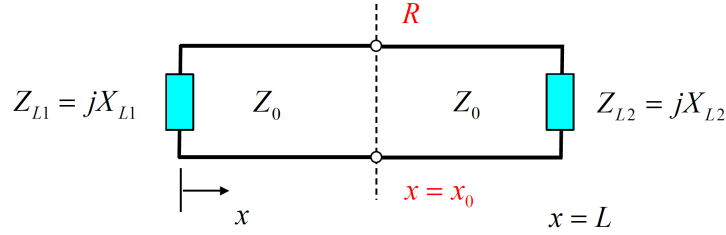


Figure 3.2: Transmission line resonator. Source: [18]

At an arbitrary plane R where $x = x_0$, an imaginary cut can be made such that the currents and voltages seen from the right are equivalent to the ones seen from the left, resulting in figure 3.3 where $V^r = V^l$ and $I^r = I^l$, and the superscripts r and l indicate right and left respectively. Then, the impedance can be calculated by obtaining the ratio of voltage and current for left and right directions, but considering that the positive direction is right, so a minus sign must be added to the impedance on the left, resulting in $\vec{Z} + \vec{Z} = 0$ in equation (3.58c) at $x = x_0$ where the arrow on top means the direction relative to R instead of the traditional vector notation.

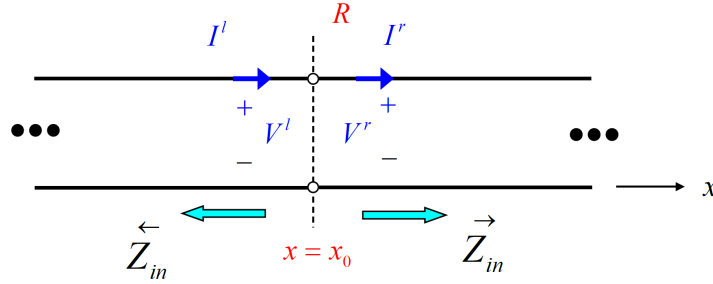


Figure 3.3: Transmission line resonator at arbitrary reference plane R . Source: [18]

$$\vec{Z} = \frac{V^r}{I^r} \quad (3.58a) \quad \vec{Z} = \frac{V^l}{-I^l} \quad (3.58b) \quad \vec{Z} = -\vec{Z} \quad (3.58c)$$

This method is used in metasurfaces to obtain the resonating surface wave wavenumber for a particular free-space wavenumber by assuming this same resonator configuration where the plane division is in the interface of the metasurface with free space. When using this method for a broadband frequency range, the dispersion curve for a unit cell configuration can be obtained which relates the propagation constant with the excitation frequency.

3.1.3. Antenna theory

This subsection explains in generalized terms the antenna figures of merit that are used throughout this report and how to calculate them from the near-field parameters. The first part of this subsection, based

on the work of Balanis [1, p. 684-702], explains how the near-field calculations can be extrapolated to the far-field by using a series of assumptions and techniques in the spectral plane. Next, the second part based on the work of the same author [1, p. 37-47], explains the basic figures of merit of antennas, how to calculate them and what do they represent.

Near- to far-field conversion

Antennas are devices which main objective is to emit or receive a particular far-field radiation pattern. The effect of the radiation in its vicinity (near-field) can be extrapolated over large distances (far-field) in the spherical plane to measure its performance in different directions. To this end, spectral techniques, which are used for aperture-type antennas, can be used to obtain the far-field radiation pattern from the near-field radiation. First, considering an antenna that radiates in the positive z-direction. The electric field in the source-free region ($z > 0$) can be represented as a Fourier transform of its spectral components as in equation (3.59) where $\mathbf{f}(k_x, k_y)$ is an amplitude function of these spectral components on a Cartesian plane.

$$\mathbf{E}(x, y, z) = \frac{1}{4\pi^2} \int_{-\infty}^{+\infty} \int_{-\infty}^{+\infty} \mathbf{f}(k_x, k_y) e^{-j\mathbf{k}\cdot\mathbf{r}} dk_x dk_y \quad (3.59)$$

The effect of the z-component can be decoupled from the exponential function of equation (3.59) because of its dependency with k_x and with k_y . Then, equation (3.59) takes the form of equation (3.60) which resembles a two-dimensional Fourier transform, with the term that represents the frequency domain inside the square brackets.

$$\mathbf{E}(x, y, z) = \frac{1}{4\pi^2} \int_{-\infty}^{+\infty} \int_{-\infty}^{+\infty} [\mathbf{f}(k_x, k_y) e^{-jk_z z}] e^{-j(k_x x + k_y y)} dk_x dk_y \quad (3.60)$$

The dependency of k_z on the tangential wavevector $\mathbf{k}_t = \hat{\mathbf{x}}k_x + \hat{\mathbf{y}}k_y$ can be expressed as in equation (3.61), where $k^2 \geq k_x^2 + k_y^2$, so the fields do not decay exponentially from the surface as it was explained on section 3.1.1 when the Poynting vector was defined in equation (3.4).

$$k_z = k^2 - k_x^2 - k_y^2 \quad \longrightarrow \quad k_z = \sqrt{k^2 - k_x^2 - k_y^2} \quad (3.61)$$

Next, a closed-form expression of f_z can be obtained. Using equation (3.6a) for the source-free region on equation (3.59) leads to equation (3.62). Interchanging the divergence by the double integral, and considering a solenoidal field in the spectral domain defined as $\nabla \cdot \mathbf{f}(k_x, k_y) = 0$ leads to equation (3.63) and to the relation of f_z with f_x and f_y .

$$\nabla \cdot \mathbf{E}(x, y, z) = \nabla \cdot \left[\frac{1}{4\pi^2} \int_{-\infty}^{+\infty} \int_{-\infty}^{+\infty} \mathbf{f}(k_x, k_y) e^{-j\mathbf{k}\cdot\mathbf{r}} dk_x dk_y \right] = 0 \quad (3.62)$$

$$\begin{aligned} \mathbf{f} \cdot \nabla e^{-j\mathbf{k}\cdot\mathbf{r}} &= -j\mathbf{f} \cdot \mathbf{k} e^{-j\mathbf{k}\cdot\mathbf{r}} = 0 \\ \mathbf{f} \cdot \mathbf{k} &= (\mathbf{f}_t + \hat{\mathbf{z}}f_z) \cdot \mathbf{k} = 0 \\ f_z &= -\frac{f_x k_x + f_y k_y}{k_z} \end{aligned} \quad (3.63)$$

Next, the method of stationary phase explained in appendix B will be used to evaluate equation (3.59). First, the expression within the exponential function is evaluated in equation (3.64a), where \mathbf{k} is expressed in the Cartesian coordinate system and \mathbf{r} in the spherical coordinate system, where φ indicates the azimuthal angle and θ the inclination or elevation angle. Using the conversion from one system to another, \mathbf{r} can be transformed to the Cartesian coordinate system, and the dot product of equation (3.64a) is expressed in equation (3.64b). Finally, equation (3.61) can be used to replace k_z and have a final expression as a function of k_x and k_y in equation (3.64c).

$$\mathbf{k} \cdot \mathbf{r} = (k_x \hat{\mathbf{x}} + k_y \hat{\mathbf{y}} + k_z \hat{\mathbf{z}}) \cdot \hat{\mathbf{r}} r \quad (3.64a)$$

$$\mathbf{k} \cdot \mathbf{r} = r(k_x \sin \theta \cos \varphi + k_y \sin \theta \sin \varphi + k_z \cos \theta) \quad (3.64b)$$

$$\mathbf{k} \cdot \mathbf{r} = r \left(k_x \sin \theta \cos \varphi + k_y \sin \theta \sin \varphi + \sqrt{k^2 - k_x^2 - k_y^2} \cos \theta \right) \quad (3.64c)$$

From equation (3.64c) the stationary points can be evaluated. These are given by the partial derivatives of k_x and k_y as in equation (3.65), where additional relations between k_x , k_y and k_z are found on these stationary points.

$$\begin{aligned} \frac{\partial(\mathbf{k} \cdot \mathbf{r})}{\partial k_x} = r \left(\sin \theta \cos \varphi - \frac{k_x}{k_z} \cos \theta \right) = 0 & \quad \frac{\partial(\mathbf{k} \cdot \mathbf{r})}{\partial k_y} = r \left(\sin \theta \cos \varphi - \frac{k_y}{k_z} \cos \theta \right) = 0 \\ k_x = k_z \frac{\sin \theta \cos \varphi}{\cos \theta} & \quad k_y = k_z \frac{\sin \theta \sin \varphi}{\cos \theta} \end{aligned} \quad (3.65a) \quad (3.65b)$$

Using the relations obtained on equation (3.65) and the wavenumber expression in equation (3.61), equation (3.66) can be obtained, which shows an independent expression of k_z from k_x and k_y which is used on the stationary point. Next, equations (3.65a) and (3.65b) can be used with equation (3.66) to obtain equations (3.67a) and (3.67b) respectively, which show closed forms expressions of k_x and k_y at these locations, named k_1 and k_2 respectively.

$$k^2 = k_z^2 + k_x^2 + k_y^2 = k_z^2 \left(1 + \frac{\sin^2 \theta}{\cos^2 \theta} \right) \quad (3.66)$$

$$k_z = k \cos \theta$$

$$k_x = k \sin \theta \cos \varphi = k_1 \quad (3.67a) \quad k_y = k \sin \theta \sin \varphi = k_2 \quad (3.67b)$$

Following, equation (3.67) can be used in equation (3.64c) to obtain an expression for $\mathbf{k} \cdot \mathbf{r}$ at the stationary points.

$$\mathbf{k} \cdot \mathbf{r} \Big|_{\substack{k_y=k_2 \\ k_x=k_1}} = r \left(k \sin^2 \theta \cos^2 \varphi + k \sin^2 \theta \sin^2 \varphi + k \cos^2 \theta \right) = kr \quad (3.68)$$

Subsequently, a Taylor series expansion to the second order can be used for $\mathbf{k} \cdot \mathbf{r}$ considering that the first derivatives are zero. This expansion can be expressed as a second-degree polynomial in equation (3.70a), where equations (3.70b) to (3.70f) show what the coefficients and variables therein represent.

$$\begin{aligned} \mathbf{k} \cdot \mathbf{r} \approx \mathbf{k} \cdot \mathbf{r} \Big|_{\substack{k_y=k_2 \\ k_x=k_1}} + \frac{1}{2} \frac{\partial^2(\mathbf{k} \cdot \mathbf{r})}{\partial k_x^2} \Big|_{\substack{k_y=k_2 \\ k_x=k_1}} (k_x - k_1)^2 + \frac{1}{2} \frac{\partial^2(\mathbf{k} \cdot \mathbf{r})}{\partial k_y^2} \Big|_{\substack{k_y=k_2 \\ k_x=k_1}} (k_y - k_2)^2 \\ + \frac{\partial^2(\mathbf{k} \cdot \mathbf{r})}{\partial k_x \partial k_y} \Big|_{\substack{k_y=k_2 \\ k_x=k_1}} (k_x - k_1)(k_y - k_2) \end{aligned} \quad (3.69)$$

$$\mathbf{k} \cdot \mathbf{r} \approx kr - \bar{A}\xi^2 - \bar{B}\kappa^2 - \bar{C}\xi\kappa \quad (3.70a)$$

$$\bar{A} = -\frac{1}{2} \frac{\partial^2(\mathbf{k} \cdot \mathbf{r})}{\partial k_x^2} \Big|_{\substack{k_y=k_2 \\ k_x=k_1}} \quad (3.70b) \quad \bar{B} = -\frac{1}{2} \frac{\partial^2(\mathbf{k} \cdot \mathbf{r})}{\partial k_y^2} \Big|_{\substack{k_y=k_2 \\ k_x=k_1}} \quad (3.70c) \quad \bar{C} = -\frac{1}{2} \frac{\partial^2(\mathbf{k} \cdot \mathbf{r})}{\partial k_x \partial k_y} \Big|_{\substack{k_y=k_2 \\ k_x=k_1}} \quad (3.70d)$$

$$\xi = k_x - k_1 \quad (3.70e) \quad \kappa = k_y - k_2 \quad (3.70f)$$

Following, the expressions in equation (3.65) can be used to obtain the second derivatives defined by \bar{A} , \bar{B} and \bar{C} in equations (3.71a) to (3.71c), which depend only on the spherical coordinates and the wavenumber.

$$\bar{A} = \frac{r}{2k} \left(1 + \frac{\sin^2 \theta \cos^2 \varphi}{\cos^2 \theta} \right) \quad (3.71a)$$

$$\bar{B} = \frac{r}{2k} \left(1 + \frac{\sin^2 \theta \sin^2 \varphi}{\cos^2 \theta} \right) \quad (3.71b)$$

$$\bar{C} = \frac{r}{k} \frac{\sin^2 \theta}{\cos^2 \theta} \cos \varphi \sin \varphi \quad (3.71c)$$

$$4\bar{A}\bar{B} - \bar{C}^2 = \left(\frac{r}{k \cos \theta} \right)^2 \quad (3.71d)$$

Next, equations (3.70e), (3.70f) and (3.71) can be used to evaluate equation (3.59) on its stationary points. Using the same assumptions as in appendix B, $\mathbf{f}(k_x, k_y)$ can be assumed to be a slowly-varying function, which effect within the integral can be considered negligible and therefore it can be evaluated outside. This results in equation (3.72) where $A_{1,2}$ is the surface area in the stationary points.

$$\begin{aligned}\mathbf{E}(x, y, z) &\approx \frac{1}{4\pi^2} \iint_{A_{1,2}} \mathbf{f}(k_x = k_1, k_y = k_2) e^{-j(kr - \bar{A}\xi^2 - \bar{B}\kappa^2 - \bar{C}\xi\kappa)} d\xi d\kappa \\ \mathbf{E}(x, y, z) &\approx \frac{1}{4\pi^2} \mathbf{f}(k_1, k_2) e^{-jkr} \iint_{A_{1,2}} e^{j(\bar{A}\xi^2 + \bar{B}\kappa^2 + \bar{C}\xi\kappa)} d\xi d\kappa\end{aligned}\quad (3.72)$$

As the stationary phase method is used, the integral in equation (3.72) resembles the one in equation (B.5). Therefore, this can be approximated as in equation (B.13) considering that this integral does not have the term k in the exponential part because its effect has already been included when evaluating $\mathbf{k} \cdot \mathbf{r}$. Equation (3.71d) shows that $4\bar{A}\bar{B} > \bar{C}^2$ and from equation (3.71a) it can be noted that $\bar{A} > 0$. This results in $\delta_c = 1$ from equation (B.13), and the final expression for this integral can be obtained in equation (3.73).

$$\iint_{A_{1,2}} e^{j(\bar{A}\xi^2 + \bar{B}\kappa^2 + \bar{C}\xi\kappa)} d\xi d\kappa = \frac{j2\pi\delta_c}{\sqrt{4\bar{A}\bar{B} - \bar{C}^2}} = j\frac{2\pi k}{r} \cos\theta \quad (3.73)$$

The approximation of the double integral by using the stationary phase method in equation (3.73) can be used in equation (3.72), resulting in equation (3.74). The only term that still needs to be expressed in spherical coordinates is $\mathbf{f}(k_1, k_2)$.

$$\mathbf{E}(r, \theta, \varphi) \approx j\frac{k \cos\theta}{2\pi r} e^{-jkr} \mathbf{f}(k_1 = k \sin\theta \cos\varphi, k_2 = k \sin\theta \sin\varphi) \quad (3.74)$$

First, equation (3.63) can be used to obtain an expression of \mathbf{f} only in terms of f_x and f_y as in equation (3.75a). Next, this is evaluated in k_1 and k_2 by using equation (3.67) to replace k_x and k_y , which is shown in equation (3.75b). Finally, equation (3.75b) is transformed from Cartesian to spherical coordinates in equation (3.75c), considering that the radial electric field amplitude is zero because of the far-field assumption.

$$\mathbf{f} = \hat{\mathbf{x}}f_x + \hat{\mathbf{y}}f_y - \hat{\mathbf{z}}\frac{f_x k_x + f_y k_y}{k_z} \quad (3.75a)$$

$$\mathbf{f}(k_1, k_2) = \hat{\mathbf{x}}f_x + \hat{\mathbf{y}}f_y - \hat{\mathbf{z}}\frac{\sin\theta}{\cos\theta}(f_x \cos\varphi + f_y \sin\varphi) \quad (3.75b)$$

$$\mathbf{f}(k_1, k_2) = \hat{\boldsymbol{\theta}}\frac{f_x \cos\varphi + f_y \sin\varphi}{\cos\theta} - \hat{\boldsymbol{\phi}}(f_x \sin\varphi - f_y \cos\varphi) \quad (3.75c)$$

Using equation (3.75c) in equation (3.74) results in equation (3.76), which is the final expression for the electric field in the far-field as a function of its amplitude evaluated in its stationary points. The amplitude function components, f_x and f_y , are expressed in equation (3.77) and can be obtained by using an inverse Fourier transform of equation (3.60) evaluated with equation (3.67) at $z = 0$, and assuming that the radiation comes only from the antenna aperture.

$$\mathbf{E}(r, \theta, \varphi) \approx \frac{jk}{2\pi r} e^{-jkr} \left[\hat{\boldsymbol{\theta}}(f_x \cos\varphi + f_y \sin\varphi) - \hat{\boldsymbol{\phi}} \cos\theta (f_x \sin\varphi - f_y \cos\varphi) \right] \quad (3.76)$$

$$f_x(k_x = k_1, k_y = k_2) = \iint_A E_x(x', y', z' = 0) e^{jk(x' \sin\theta \cos\varphi + y' \sin\theta \sin\varphi)} dA \quad (3.77a)$$

$$f_y(k_x = k_1, k_y = k_2) = \iint_A E_y(x', y', z' = 0) e^{jk(x' \sin\theta \cos\varphi + y' \sin\theta \sin\varphi)} dA \quad (3.77b)$$

Basic antenna parameters

To measure the antenna's performance, some basic parameters are used. First, the radiation pattern of two-dimensional antennas, such as aperture antennas, can be plotted in the so-called (u, v) -plane, which is a conversion of one of the spherical coordinates hemisphere into a planar coordinate system.

Equation (3.78) shows this coordinate transformation, which can be used to change the spherical coordinate system of parameters in the far-field to one easier to plot and interpret. The resulting plot when using the (u, v) -plane will have at its centre the broadside direction, and at the boundaries where $\sqrt{u^2 + v^2} = 1$ values at which $\theta = 90^\circ$.

$$u(\theta, \varphi) = \sin \theta \cos \varphi \quad (3.78a) \quad v(\theta, \varphi) = \sin \theta \sin \varphi \quad (3.78b)$$

The radiation intensity $U(\theta, \varphi)$ can be defined as the ‘‘Power radiated from an antenna per unit of solid angle’’ [1, p. 37], which is given by equation (3.79) considering the far-field approximation, where the radiation propagates as plane waves. As the average Poynting vector that was defined in equation (3.10) is in Cartesian coordinates, this is now changed to the spherical coordinates reference frame to keep consistency with the far-field notation.

$$U(\theta, \varphi) = r^2 S_{avg}(\theta, \varphi) = \frac{r^2}{2\zeta} \mathbf{E}^\top(\theta, \varphi) \cdot \mathbf{E}^*(\theta, \varphi) \quad (3.79)$$

Next, the radiated power P_{rad} can be obtained by integrating $U(\theta, \varphi)$ over the spherical coordinate system as shown in equation (3.80). As this project is centred in the application of metasurface antennas, which can be approximated to aperture antennas, only the north hemisphere is considered. This is because in equation (3.77) it has only been considered that the radiation area is delimited by the antenna area, making not possible the evaluation of back lobes due to phenomena such as fringing fields on the boundaries. Therefore, the upper integration boundary of θ set to $\pi/2$ to evaluate only the north hemisphere.

$$P_{rad} = \int_0^{2\pi} \int_0^{\pi/2} U(\theta, \varphi) \sin \theta d\theta d\varphi \quad (3.80)$$

Following, the directivity can be defined as ‘‘the ratio of the radiation intensity in a given direction from the antenna to the radiation intensity averaged over all directions’’ [1, p. 41]. This is shown in equation (3.81) which illustrates the radiation intensity divided by the radiated power per solid angle unit (4π).

$$D(\theta, \varphi) = \frac{4\pi U(\theta, \varphi)}{P_{rad}} \quad (3.81)$$

Subsequently, it is possible to obtain the directivity for the co-polarized (CP) D_{cp} and cross-polarized (XP) D_{xp} radiation patterns using the third Ludwig definition of cross polarization [22]. To this end, consider an aperture antenna with an electric field directed along the x-axis. Then, the CP radiation will be the one that is also aligned with this same axis, which can be evaluated as in equation (3.82) where the matrix that multiplies $\mathbf{E}(\theta, \varphi)$ can be obtained by aligning these vectors with the x- and y-axes, which represent the CP and XP respectively.

$$\begin{bmatrix} E_{cp} \\ E_{xp} \end{bmatrix} = \begin{bmatrix} \cos \varphi & -\sin \varphi \\ \sin \varphi & \cos \varphi \end{bmatrix} \cdot \begin{bmatrix} E_\theta \\ E_\varphi \end{bmatrix} \quad (3.82)$$

Finally, equation (3.82) can be included in the directivity calculation as in equation (3.83) [6, p. 48].

$$D_{cp} = \frac{4\pi |E_\theta \cos \varphi - E_\varphi \sin \varphi|^2}{2\zeta P_{rad}} \quad (3.83a) \quad D_{xp} = \frac{4\pi |E_\theta \sin \varphi + E_\varphi \cos \varphi|^2}{2\zeta P_{rad}} \quad (3.83b)$$

3.1.4. Floquet series

Floquet series are employed to solve Maxwell equations for periodic structures because they allow to model just one element of the periodic array and apply periodic boundary conditions to model the rest of the elements. Furthermore, a decoupled solution set is obtained in terms of fundamental and higher-order modes. They are a generalization of Fourier series whenever the magnitude and the phase of a function have different periodicities, which is the case for the analysis of scanning beam arrays [3, p. 65]. This is extrapolated to work with metasurfaces because both metasurfaces and antenna arrays are composed by periodic structures that influence the incident electric and magnetic fields.

Periodic lattice

Floquet series are explained in the book of Arun K. Bhattacharyya for a rectangular grid [3, p. 61-76] as the one in metasurfaces configurations and, in this subsection, the derivations are based entirely on its book. First, consider the amplitude function of a single antenna element in a linear antenna array $f(x)$. Then, the amplitude function of an infinite antenna array for this one-dimensional parameter is $h(x)$ and is specified in equation (3.84) where p is the index of the array element, \tilde{a} is the amplitude periodicity and $\tilde{\varphi}$ is a real number that modifies the phase periodicity.

$$h(x) = \sum_{p=-\infty}^{\infty} f(x - p\tilde{a})e^{-jp\tilde{\varphi}} \quad (3.84)$$

The Fourier transform of $h(x)$ is given by equation (3.85) where k_x is the wavenumber directed along x -direction in rad m^{-1} .

$$\tilde{h}(k_x) = \frac{1}{2\pi} \sum_{p=-\infty}^{\infty} e^{-jp\tilde{\varphi}} \int_{-\infty}^{\infty} f(x - p\tilde{a})e^{jk_x x} dx \quad (3.85)$$

This expression can be simplified by considering $g(x)$ as the function of this antenna array without the influence of $\tilde{\varphi}$ ($\tilde{\varphi} = 0$) and its Fourier transform specified in equation (3.86). In this expression, the equation (3.86a) includes the statement of the Fourier transform as a function of the infinite sum of $f(x - p\tilde{a})$, and equation (3.86b) shows a solution by using the shift theorem and then replacing the infinite sum of exponential terms by an infinite sum of Dirac delta functions.

$$\tilde{g}(k_x) = \frac{1}{2\pi} \int_{-\infty}^{\infty} g(x)e^{jk_x x} dx = \frac{1}{2\pi} \sum_{p=-\infty}^{\infty} \int_{-\infty}^{\infty} f(x - p\tilde{a})e^{jk_x x} dx \quad (3.86a)$$

$$\tilde{g}(k_x) = \tilde{f}(k_x) \sum_{p=-\infty}^{\infty} e^{jp\tilde{\varphi}} = \frac{2\pi}{\tilde{a}} \tilde{f}(k_x) \sum_{p=-\infty}^{\infty} \delta' \left(k_x - \frac{2p\pi}{\tilde{a}} \right) \quad (3.86b)$$

This can be applied to $h(x)$ by considering the term $\tilde{\varphi}$ as shown in equation (3.87) where the only difference between this last expression and the one without $\tilde{\varphi}$ is the term $\tilde{\varphi}/\tilde{a}$ which represents the phase shift applied to the spectral function $\tilde{h}(k_x)$.

$$\tilde{h}(k_x) = \tilde{f}(k_x) \sum_{p=-\infty}^{\infty} e^{jp(k_x \tilde{a} - \tilde{\varphi})} = \frac{2\pi}{\tilde{a}} \tilde{f}(k_x) \sum_{p=-\infty}^{\infty} \delta' \left(k_x - \frac{2p\pi}{\tilde{a}} - \frac{\tilde{\varphi}}{\tilde{a}} \right) \quad (3.87)$$

When expanding this last element into its series representation, the Floquet series expansion of $h(x)$ is obtained, which is shown in equation (3.88) and is the analogous case of the Fourier series expansion when the phase has a different period as the function's magnitude.

$$h(x) = \frac{2\pi}{\tilde{a}} \sum_{p=-\infty}^{\infty} \tilde{f} \left(\frac{2p\pi + \tilde{\varphi}}{\tilde{a}} \right) e^{-\frac{j}{\tilde{a}}(2p\pi + \tilde{\varphi})x} \quad (3.88)$$

The generalization for a 2D case can be done by considering periods of \tilde{a} and \tilde{b} along the x - and y -axes respectively for the magnitude, and k_{x0} and k_{y0} along x - and y -axes respectively that determine the phase shift (equivalent to $\tilde{\varphi}/\tilde{a}$). This is shown in equation (3.89) where $x_p = p\tilde{a}$ and $y_q = q\tilde{b}$ represent the discrete points where, for example, an antenna element would be located in a rectangular grid.

$$h(x, y) = \sum_{p=-\infty}^{\infty} \sum_{q=-\infty}^{\infty} f(x - x_p, y - y_q) e^{-jk_{x0}x_p - jk_{y0}y_q} \quad (3.89)$$

Then, by using an equivalent 2D expression as the one in equation (3.85), equation (3.90) is obtained where k_y is the wavenumber along the y -axis.

$$\tilde{h}(k_x, k_y) = \frac{1}{4\pi^2} \sum_{p=-\infty}^{\infty} \sum_{q=-\infty}^{\infty} e^{-jk_{x0}x_p - jk_{y0}y_q} \int_{-\infty}^{\infty} \int_{-\infty}^{\infty} f(x - x_p, y - y_q) e^{jk_x x + jk_y y} dx dy \quad (3.90)$$

Using the Fourier shift theorem and the Dirac delta equivalence for an infinite sum of periodic functions as in equation (3.87), the expression in equation (3.91) is obtained, showing that “the Fourier spectrum for $h(x, y)$ exists only at discrete points in the $k_x k_y$ -plane” [3, p. 69]. The spectrum of the different Floquet points defined in equation (3.91) is shown in figure 3.4 as a periodic lattice where each of the points is a Floquet mode, being the one centred at the origin the fundamental one with $p = q = 0$.

$$\tilde{h}(k_x, k_y) = \tilde{f}(k_x, k_y) \sum_p \sum_q e^{jx_p(k_x - k_{x0}) + jy_q(k_y - k_{y0})} \quad (3.91a)$$

$$\tilde{h}(k_x, k_y) = \frac{4\pi^2}{\tilde{a}\tilde{b}} \tilde{f}(k_x, k_y) \sum_p \sum_q \delta' \left(k_x - k_{x0} - \frac{2p\pi}{\tilde{a}} \right) \delta' \left(k_y - k_{y0} - \frac{2q\pi}{\tilde{b}} \right) \quad (3.91b)$$

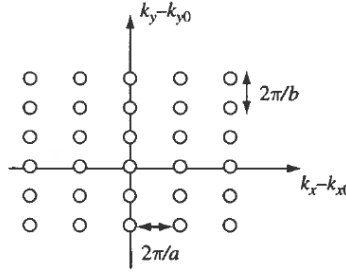


Figure 3.4: Floquet spectral points for a two-dimensional array. Figure retrieved from Bhattacharyya [3, p. 70]

To conclude the theoretical part on Floquet series, the series representation of $h(x, y)$ is given in equation (3.92) where the elements k_{xp} and k_{yq} are defined in equation (3.93).

$$h(x, y) = \frac{4\pi^2}{\tilde{a}\tilde{b}} \sum_p \sum_q \tilde{f}(k_{xp}, k_{yq}) e^{-jk_{xp}x - jk_{yq}y} \quad (3.92)$$

$$k_{xp} = k_{x0} + \frac{2p\pi}{\tilde{a}} \quad k_{yq} = k_{y0} + \frac{2q\pi}{\tilde{b}} \quad (3.93)$$

Antenna array application

Floquet series can be applied to an antenna array as follows. Consider a linear array composed by infinite dipoles oriented parallel to the y -axis in the xy -plane at $z = 0$ with surface current excitation \mathbf{I} defined by equation (3.94).

$$\mathbf{I} = \hat{\mathbf{y}} \sum_{p=-\infty}^{\infty} f(x - p\tilde{a}) e^{-jp\tilde{\varphi}} \quad (3.94)$$

Disregarding any coupling between the dipole antennas, a TM_y field is produced and, using the Lorentz gauge condition, the current density along the y -axis J_y is obtained as a function of the magnetic vector potential $\mathbf{A} = \hat{\mathbf{y}}A_y$, together with its representation as a function of the current excitation \mathbf{I} from equation (3.94) in equation (3.95a). Furthermore, this can also be expressed in terms of Floquet series by using equation (3.88) in equation (3.95a) as shown in equation (3.95b).

$$\nabla^2 A_y + k^2 A_y = -J_y = -\delta'(z) \sum_{p=-\infty}^{\infty} f(x - p\tilde{a}) e^{-jp\tilde{\varphi}} \quad (3.95a)$$

$$\nabla^2 A_y + k^2 A_y = -J_y = -\delta'(z) \frac{2\pi}{\tilde{a}} \sum_{p=-\infty}^{\infty} \tilde{f} \left(\frac{2p\pi + \tilde{\varphi}}{\tilde{a}} \right) e^{-\frac{j}{\tilde{a}}(2p\pi + \tilde{\varphi})x} \quad (3.95b)$$

After an inspection of the right-hand side of equation (3.95b), a solution of A_y can have the form of equation (3.96) where $F_p(z)$ is the p -solution of A_y .

$$A_y = \sum_{p=-\infty}^{\infty} F_p(z) e^{-\frac{j}{a}(2p\pi + \tilde{\varphi})x} \quad (3.96)$$

For each term p of $F_p(z)$, the solution of equation (3.95b) can have the form specified in equation (3.97) where the terms k_{xp} and k_{zp} are specified in equation (3.98).

$$\frac{\partial^2 F_p(z)}{\partial z^2} + k_{zp}^2 F_p(z) = -\delta'(z) \frac{2\pi}{\tilde{a}} \tilde{f}(k_{xp}) \quad (3.97)$$

$$k_{xp} = \frac{2p\pi + \tilde{\varphi}}{\tilde{a}} \quad k_{zp}^2 = k^2 - k_{xp}^2 \quad (3.98)$$

A solution of $F_p(z)$ that satisfies equation (3.97) is given in equation (3.99) for positive values of z .

$$F_p(z) = \frac{\pi}{j\tilde{a}k_{zp}} \tilde{f}(k_{xp}) e^{-jk_{zp}z} \quad \forall \quad z > 0 \quad (3.99)$$

Equation (3.99) can be replaced in equation (3.96) to obtain the final expression for the magnetic vector potential in equation (3.100).

$$A_y = \frac{\pi}{j\tilde{a}} \sum_{p=-\infty}^{\infty} \frac{\tilde{f}(k_{xp})}{k_{zp}} e^{-jk_{xp}x - jk_{zp}z} \quad \forall \quad z > 0 \quad (3.100)$$

By using Maxwell's equations and the definition of magnetic vector potential as in equation (3.101), the electric field is obtained where $E_x = E_z = 0$ and its y -component is specified in equation (3.102) where the time dependency has been added. The exponential term in the summation is the Floquet modal function, which is associated to a plane wave. The propagation direction of the Floquet mode \mathbf{k} is shown in equation (3.103).

$$\mathbf{H} = \nabla \times (\hat{\mathbf{y}}A_y) \quad \mathbf{E} = \frac{1}{j\omega\epsilon_0} \nabla \times \mathbf{H} \quad (3.101)$$

$$E_y(x, y, z, t) = -\frac{\pi\omega\mu_0}{\tilde{a}} \sum_{p=-\infty}^{\infty} \frac{\tilde{f}(k_{xp})}{k_{zp}} e^{j\omega t - jk_{xp}x - jk_{zp}z} \quad \forall \quad z > 0 \quad (3.102)$$

$$\mathbf{k}^{(p)} = \hat{\mathbf{x}}k_{xp} + \hat{\mathbf{z}}k_{zp} \quad (3.103)$$

For the case in which the surface current varies in two dimensions with the x and y -axes, the derivation results more complicated, but the result is similar to the one obtained in equation (3.103) and it is given by equation (3.104) where k_{xpq} and k_{ypq} have been already defined in equation (3.93) and $k_{zpq}^2 = k^2 - k_{xpq}^2 - k_{ypq}^2$.

$$\mathbf{k}^{(pq)} = \hat{\mathbf{x}}k_{xpq} + \hat{\mathbf{y}}k_{ypq} + \hat{\mathbf{z}}k_{zpq} \quad (3.104)$$

These results show that the direction of propagation of a Floquet mode is determined by the value of $\mathbf{k}^{(pq)}$. The Floquet mode corresponding to $p = 0$ is defined as the dominant mode because it radiates in the direction that the array's antennas are oriented according to their phase shift k_{x0} and k_{y0} . Furthermore, an evanescent Floquet mode arises when k_{zpq} is imaginary. That is, when $k_{xpq}^2 + k_{ypq}^2 > k^2$ which produces an evanescent wave that decays along the z -direction.

It was already referred in the surface waves subsection that, whenever there is a transition between a relatively high refractive media to a low refractive one in angles beyond the critical angles, a surface wave would appear characterized by an exponential decaying electric field along z -direction as shown in equation (3.12). This is analogous to having an imaginary k_{zp} value in equation (3.102) because the electric field would also decay in positive z -direction. Therefore, it can be concluded that, if a Floquet mode that is exponentially decaying in z -direction arises in an antenna array plane with higher refractive index than the one in free-space, it will produce a surface wave along its plane. This can occur in an array of microstrip antennas or in a metasurface antenna.

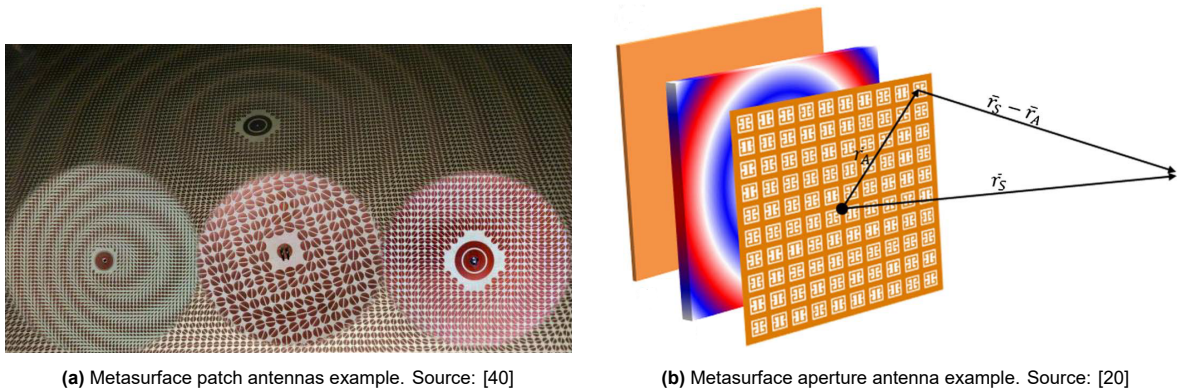


Figure 3.5: Metasurface patch and aperture antennas examples found in literature. At the left, the patch type metasurfaces are shown where the metal cladding is represented in red, whereas at the right an aperture type metasurface design is shown with the metal cladding represented in yellow.

3.2. Metasurface antennas

In this section, the needed theory regarding metasurfaces to design an antenna is treated. The basic principles of metasurfaces are explained, followed by a proposed procedure in [40] to design a metasurface antenna starting with an objective current distribution. Next, the unit cell concept is described together with all the assumptions and the most relevant methods used to model them. Finally, the modulation technique that uses adiabatic Floquet waves is explained in a practical step-by-step form to apply it to the antenna design.

3.2.1. Basic principles

Metasurfaces are composed of sub-wavelength elements arranged in a 1D- or 2D-arrays which collectively are capable of changing the phase, amplitude, polarization and leakage parameters of the propagating radiation throughout the structure. Some examples of applications are polarizers, cloaking devices, lenses and antennas [19]. As this last application is the one that is most useful for this research project, it will be discussed thoroughly, with particular emphasis in examples with frequencies between 2 GHz and 27 GHz.

A metasurface antenna can have either a linear, rectangular or circular shape, composed of smaller unit cell elements. Examples of circular and rectangular arrays are shown in figure 3.5. The central feeding system can always be assumed to launch an azimuthally symmetric surface wave [23] which is either converted into leaky-wave radiation by using patch-type sub-wavelength unit cells, or radiated by small apertures by using aperture-type sub-wavelength unit cells. Both layouts are shown in figure 3.6 with the representation of the electric and magnetic currents in the left and right bottom images respectively. In the first case, a surface wave propagates throughout the structure with a wavefront that is modulated by the patches on top. In the second, electrical modes propagate within the metasurface in a similar manner as in a parallel-plate waveguide for a two-dimensional metasurface, and as in a microstrip for a one-dimensional metasurface in which the apertures on top scatter the incident radiation. Properties of these unit cells such as resonance, given by the Q -number, and impedance are dependent on the orientation of the axes of symmetry of the unit cell with respect to the incident wave, the shape of the metal patch or aperture on top, the thickness and the electric permittivity of the substrate laying underneath. Different shapes of unit cell patches or apertures have been tested by many authors with satisfactory results [35, 9, 43]. As an example, in figure 3.5a, the first two antennas on the right represent a “coffee beam” patch consisting of a circular patch with a “thin slit cut along their diameter” [36], the one on the left has elliptical patches, and in figure 3.5b the aperture shape is called complementary electric-inductive-capacitive (cELC) resonator and is mainly found in aperture-type patches. In the presented work, all the simulations and models have been performed with patch-type unit cells because the used methods were based on this type of configuration.

Furthermore, it is important to classify the size of the analysis region in terms of wavelength λ because, for each different domain size, a different analysis method would be used either for simulations, impedance/resonance calculations or antenna modulation. A good example is indicated in figure 3.7

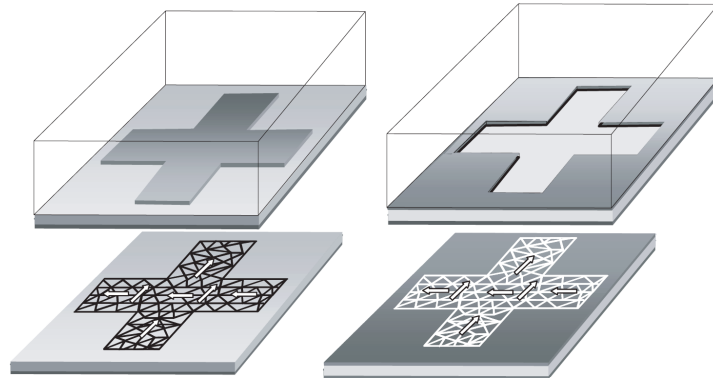


Figure 3.6: Example of metasurface unit cell layout. At the left, the patch-type unit cell is shown with the representation of its electric currents in a discretised mesh. At the right, the aperture-type unit cell is shown with the representation of its magnetic currents in a discretised mesh. Source: [24]

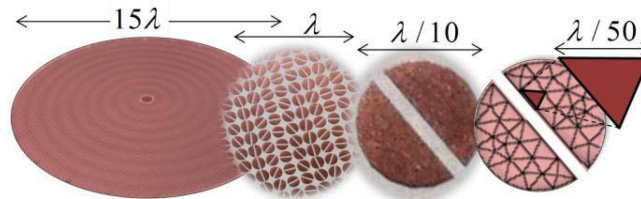


Figure 3.7: Metasurface analysis regions separated by sizes. Source: [40]

where the scales from left to right are the macroscopic, mesoscopic, molecular and atomic [40]. The atomic scale has an approximate size of $\lambda/50$ and is regularly used as a basic unit in numerical simulations. That is, numerical simulations often calculate the electric and magnetic fields in each of these units. Following, the molecular scale ($\lambda/10$) contains the unit cell, which impedance or resonance values are obtained through numerical simulations by evaluating the aggregate effects of the electric and magnetic fields of the contained atomic units. Next, the mesoscopic level (λ) has the dimensions of the wavelength propagating in the structure and is used to modulate the emitted radiation by using the impedance/resonance values obtained from the molecular level. Results from this level usually come from antenna modulation, but in more simple cases, like in a one-dimensional antenna, a full-wave simulation with commercial software can still be made. Finally, the macroscopic level contains the whole antenna structure and is usually prohibitive for full-wave simulations. Therefore, analytical models have been made that manage to capture all the relevant phenomena by making assumptions that reduce the computational efforts when inserted again in a numerical model [30].

3.2.2. Design methodology

A general methodology that synthesizes all the parts of a metasurface antenna design is given in figure 3.8 [40], which is the first step to answer the first research question of this thesis project. Therefore, its general steps are followed in chapter 4, but using in some parts alternative methods which reasoning is explained in that same chapter. The design starts with obtaining the aperture field that would result in a desired far-field pattern. There are several methods to perform this part, but the authors suggest to use the approach in [5] which is based on phased arrays antennas. Ideally, the discrete results from this synthesis process would be interpolated to obtain the electric field distribution in the metasurface. Other alternative is to use the inverse Fourier transform of the desired far-field pattern to obtain the field distribution in the aperture, which is documented in [1] specifically for continuous sources. Prior this procedure, the desired antenna pattern, the excitation frequency and the antenna size are needed.

The next part is the continuous reactance synthesis, which method is explained in section 3.2.4. This consists on using the electric field in the aperture obtained in the previous step to get a continuous reactance distribution. Other metasurface antenna parameters must be selected prior this procedure, such as the dielectric thickness and relative permittivity, as the resulting reactance is the one of the patch cladding at the metasurface interface. This part is followed by a check of the continuous impedance

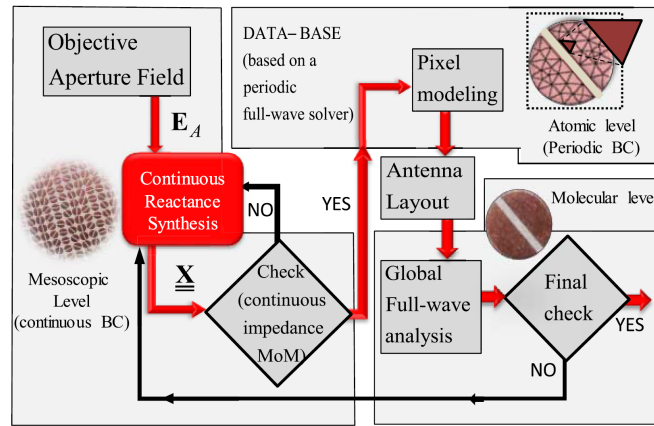


Figure 3.8: Block diagram of the process to design a metasurface antenna. Source: [40]

using a technique based on the MoM and basis functions that drastically reduce the computation effort [13].

Following, the pixel (or unit cell) modelling is performed which consists on obtaining the reactance values of each unit cell configuration with a full-wave simulation of each individual term. The reactance is a function of the patch shape, its size relative to the unit cell, the input frequency, the propagation direction of the surface wave, and the patch angle in the unit cell. Because a discrete number of simulations are performed, as a last step an interpolation can be applied to the obtained results to have a continuous distribution of these values. It is important to note that this process is performed after the synthesis because the range of reactance values are known, and the patches dimensions can be easily tuned to enclose the whole range. Section 3.2.3 provides a general description on how this part is performed.

Next, once the desired impedance distribution is known (section 3.2.4) and the relation of each unit cell shape with impedance values is also known (section 3.2.3), these two are matched to produce an antenna layout. As it is difficult that the database contains all the required impedance values, an optimization process is performed that minimizes the difference between the reactance of the chosen patch geometry and the one required from the synthesis process.

Finally, a full-wave simulation is performed of the antenna with all of its unit cells in place to verify that it gives actually the desired pattern. This process can be time-consuming for commercial software, therefore other methods can be used to approach this problem in an efficient manner. The author in [40] suggests “grouping Rao-Wilton-Glisson functions on singular value decomposition basis and incorporating them in an adaptive integral method” [40, p. 3908].

3.2.3. Unit cell modelling

As it was described on previous lines, a metasurface antenna is composed by unit cell elements that modify the wavefront of propagating waves. This is possible because an impedance or resonance value can be associated to each unit cell configuration that would either facilitate or hinder the propagation of surface waves within the structure. It then results necessary to know in detail how design choices at a macroscopic, mesoscopic, molecular and atomic scales would affect the impedance associated to these unit cells. Therefore, the objective of this subsection is to describe the available methods to calculate the reactance of different unit cell configurations (molecular and atomic levels) of the patch-type metasurface while explaining the assumptions and the theoretical background in which these are based. It is important to note that all of these methods rely in a big or small measure in software capable of performing full-wave simulations.

Macroscopic assumptions

Macroscopic assumptions are considered to simplify the analysis of a unit cell structure and to generalize it to the entire antenna. In most of the literature reviewed, the relative permittivity and the thickness of the dielectric is constant throughout the whole structure. The impedance, on the other side, is expressed as a function of the position vector in a two-dimensional metasurface antenna as $\rho = \rho \cos \phi \hat{x} + \rho \sin \phi \hat{y}$ where ρ is the position radius, ϕ is the azimuthal angle in the antenna, and \hat{x}, \hat{y}

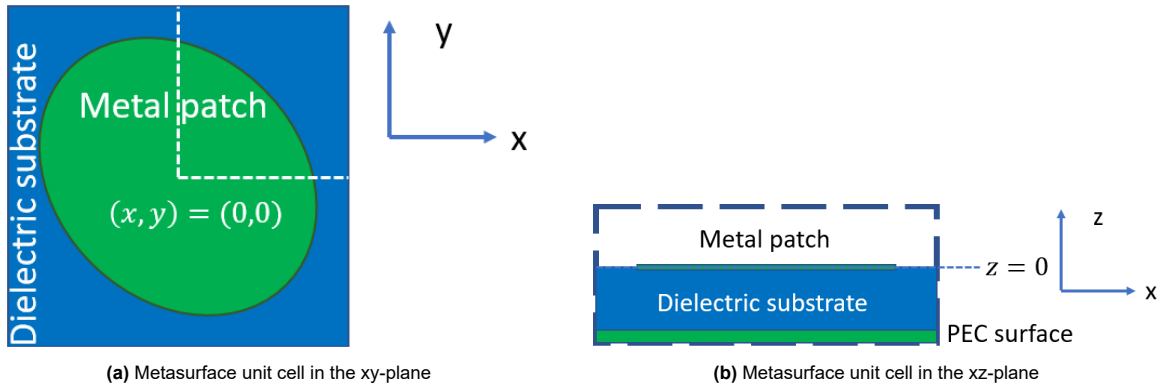


Figure 3.9: Metasurface unit cell reference coordinate system.

are the unit vectors of the Cartesian coordinates within the metasurface antenna. The relation of the patch shape and orientation with the previously defined constant parameters and the frequency of the incident wave results in the impedance value for that specific unit cell configuration.

In the context of the holographic principle, which main ideas are carefully explained in the next subsection, unit cells are assumed to be arranged to the incident electromagnetic radiation such that the difference between the scattering from two consecutive unit cells does not vary drastically. If there would be sudden variations in the shape of consecutive unit cells, additional modes could be generated that would undermine the antenna performance. As a consequence of this unit cell placement restriction, small changes in terms of shape and orientation in consecutive unit cells can be observed in the designs that are based on the holographic principle. Another reason to avoid sudden changes in consecutive unit cells is because they are sub-wavelength elements which impedance for a specific configuration is calculated by using periodic boundary conditions in one unit cell to simulate EM radiation incident to an infinite array of unit cells. The obtained impedance value is subsequently associated to the unit cell characterized by its shape parameters and orientations but, as its impedance is calculated by simulating an infinite structure, similar conditions must be present in the resulting metasurface to ensure consistency between measurements and the final design. Therefore, as stated before, the impedance of a metasurface can be precisely modulated provided that small changes in shape parameters in consecutive unit cells are present. One important effect of this choice is that all unit cells will have the same length and width (d) in both x and y -axes, which results convenient for subsequent parts to fit in the antenna.

It is often found in literature that the relative permittivity and the thickness (h) is constant throughout the metasurface. Considering this assumption facilitates the simulation procedure, as two additional degrees of freedom are limited. However, as modulation is possible by changing the orientation and size of the metal patch on top of the unit cell, it could be also possible by changing the dielectric constant and the thickness of the metasurface, with the consequences of possibly introducing additional modes and increasing the dispersion of the propagating waves, which are similar to the consequences of varying the shape parameters of the top metallic patch. The problem of using a metasurface antenna entirely based on one of these parameters is that the polarization control is limited. An example in literature is found in one of the first papers dedicated to design a metasurface antenna where the thickness of the grounded dielectric slab is varied to obtain a beam-shaped radiation pattern [39].

Next, it is assumed that no ohmic losses are present in the unit cell. Therefore, its impedance can be modelled directly with the unit cell's reactance value which is equal to the impedance's imaginary part. This is an accurate assumption because, even though dielectric losses are dominant in the metasurface for the analysed frequency range, these are relatively small compared to the propagating wave [34, p. 1538].

Finally, the coordinate system is defined. Square unit cells are used because these are the most common in literature and they give a smooth spatial variation between them. Their length and width is represented by d and they are presented in figure 3.9 in both the xy - and xz -planes.

Transmission line representation

Considering the spectral lattice defined in figure 3.4 and the reference system used in unit cell analysis, the wavevector in terms of Floquet modes propagating through an infinite array of unit cells can be defined as a variation of equation (3.104) for a surface wave propagating in the xy -plane where \mathbf{k}_t represents the fundamental Floquet mode, as it is shown in equation (3.105).

$$\mathbf{k}_q = \mathbf{k}_t + \frac{2\pi q_x}{d} \hat{\mathbf{x}} + \frac{2\pi q_y}{d} \hat{\mathbf{y}} \quad \forall \quad q_x, q_y = 0, \pm 1, \pm 2, \dots \quad (3.105)$$

Then, the average tangential fields on the metasurface at $z = 0^+$ are defined using the fundamental Floquet mode as a phasing term in the spectral plane as shown in equation (3.106) where \mathbf{E}_t and \mathbf{H}_t are the average tangential electric and magnetic fields, \mathbf{e}_t and \mathbf{h}_t are the “surface tangential components of the total electric and magnetic fields on the surface”, $\boldsymbol{\rho} = x\hat{\mathbf{x}} + y\hat{\mathbf{y}}$ is the position vector in Cartesian coordinates, and $\mathbf{k}_t = k_x\hat{\mathbf{x}} + k_y\hat{\mathbf{y}}$ is the transverse wavevector [28, p. 5]. Furthermore, as stated in section 3.1.4, $|\mathbf{k}_t|^2 > k^2$ to ensure an exponentially decaying propagation in z -direction and a surface wave propagating in the xy -plane.

$$\begin{bmatrix} \mathbf{E}_t \\ \mathbf{H}_t \end{bmatrix} = \frac{1}{d^2} \int_{-d/2}^{d/2} \int_{-d/2}^{d/2} \begin{bmatrix} \mathbf{e}_t(\boldsymbol{\rho}', \mathbf{k}_t) \\ \mathbf{h}_t(\boldsymbol{\rho}', \mathbf{k}_t) \end{bmatrix} e^{j\mathbf{k}_t \cdot \boldsymbol{\rho}'} dx' dy' \quad (3.106)$$

The Floquet modes representation in equation (3.105) can be expressed in a multiple port model. In theory, this model would consist of an infinite number of Floquet modes which could be represented by a network with an infinite number of ports. However, due to the thickness of the dielectric substrate, only the fundamental TM and TE modes are accessible to the ground plane while the other modes are evanescent, as they decay exponentially from the metasurface interface with free-space [28, p. 7]. This makes possible to simplify the analysis of an infinite-port network to a two-port network containing only the fundamental modes.

Furthermore, it is important to make the distinction between isotropic and anisotropic patches for the metasurface unit cell structure. An isotropic patch is defined as a type of patch with regular shape such as a circle or square, whereas an anisotropic patch has additional features like slots or grooves and two orthogonal symmetry axes [28, p. 2].

The isotropic metasurface was treated in detail in the research paper of Maci, Minatti, Casaletti and Bosiljevac [25] where the unit cell was approximated to a TM polarized transmission line, which is the dominant polarization at big and medium wavelength sizes. In this definition of the TM mode, the electric field is aligned with the direction of propagation of the surface wave, and the magnetic field is perpendicular to it, as shown in figure 3.10b. Regarding the transmission line representation of the unit cell, a diagram is shown in figure 3.10a where it is illustrated that patches in a metasurface change the wavefront of a propagating surface wave with wavevector \mathbf{k}_t to go from one point $\boldsymbol{\rho}_1$ to $\boldsymbol{\rho}_2$ while emitting leaky radiation. Furthermore, the transmission line model on top is illustrated, where the TM impedance of the free-space transmission line Z_0^{TM} with characteristic impedance ζ ends in a reactive load $jX(\boldsymbol{\rho})$ where $X(\boldsymbol{\rho})$ is the metasurface reactance.

The plot in figure 3.10a represents the reactance in the metasurface at macroscopic dimensions, as this varies as a function of the position within the metasurface $\boldsymbol{\rho}$, which is the result of the modulation procedure. However, in this section the interest lies in the reactance at a molecular level, which is dependent on both the frequency ω and on the transverse wavevector \mathbf{k}_t that is incident to the unit cell. Nevertheless, in the isotropic case, the direction of the wavevector is not important due to the symmetry of the surface patch, so the transverse wavenumber $k_\rho = \sqrt{\mathbf{k}_t^\top \cdot \mathbf{k}_t}$ is used instead of the wavevector. Furthermore, the impedance is represented only by a reactance scalar term due to the small periodicity of the unit cell with respect to the incident surface wave wavelength, as “Larger periodicities may instead cause transfer of energy to higher order Floquet modes that may be effectively interpreted as a loss” [27, p. 85]. Also it is assumed that neither the dielectric nor the metal in the metasurface cause ohmic losses, which is an acceptable assumption for the employed frequency range, and allows to represent the impedance of the metasurface as a pure reactance.

The transverse resonance condition described in section 3.1.2 is used for the unit cell impedance $jX(\omega, k_\rho)$ and the free-space TM impedance $Z_0^{TM}(\omega, k_\rho)$. This can be done by considering that the structure’s impedance matches the one of free-space, so there are only reactances at both sides of the transmission line and there are no active power sources, as it was shown in figure 3.2. The result

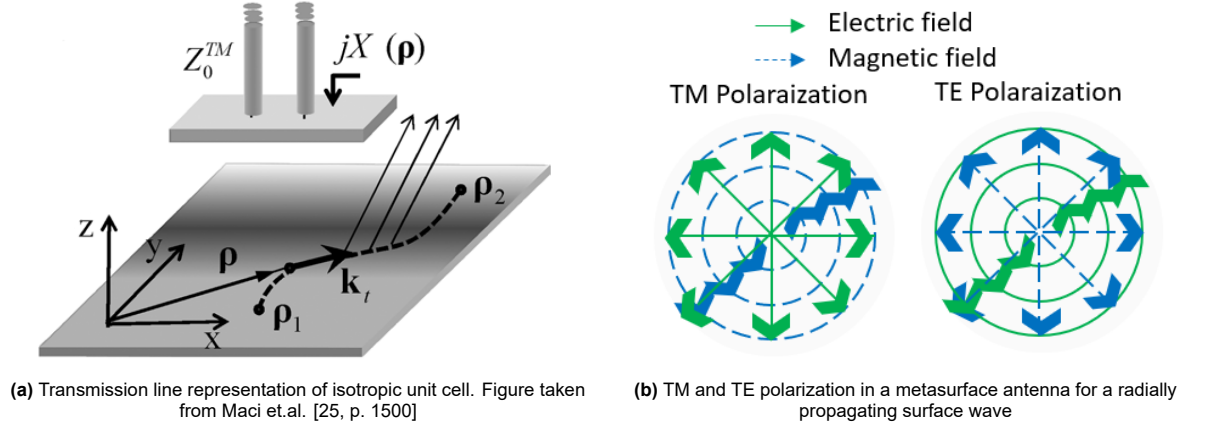


Figure 3.10: Transmission line representation of a metasurface with the polarization definition.

is shown in equation (3.107) where the transverse wavenumber is expressed as a function of the unit cell reactance.

$$X(\omega, k_\rho) = \frac{\zeta}{k} \sqrt{k_\rho^2 - k^2} \quad \Rightarrow \quad k_\rho = k \sqrt{1 + \left(\frac{X(\omega, k_\rho)}{\zeta} \right)^2} \quad (3.107)$$

The metasurface reactance can be also expressed in terms of average tangential electric and magnetic fields, which results in the impedance boundary condition. Consider \mathbf{E}_t and \mathbf{H}_t from equation (3.106). The metasurface impedance can then be expressed in terms of these values as stated in equation (3.108) at the interface of the top layer with free-space. This representation is helpful to illustrate the relation between electric field, magnetic field and the unit cell reactance just derived.

$$\mathbf{E}_t|_{z=0^+} = jX(\omega, k_t) [\hat{\mathbf{z}} \times \mathbf{H}_t]_{z=0^+} \quad (3.108)$$

Although the impedance of isotropic metasurfaces looks very simple to calculate, its disadvantage is that it exhibits a rather high circular cross-polarization level when used for metasurface antennas [38, p. 1294]. Therefore, many recent papers are devoted to expand on the theory of anisotropic metasurfaces. Martini, Mencagli and Maci proposed using a representation similar to a two-port model, and therefore treating the reactance value in equation (3.108) as a matrix with components indicating the reactance relative to TM ($\hat{\mathbf{k}}_t \hat{\mathbf{k}}_t$) and TE ($\hat{\mathbf{k}}_t^\perp \hat{\mathbf{k}}_t^\perp$) electromagnetic waves, and the cross-diagonal reactance term ($\hat{\mathbf{k}}_t \hat{\mathbf{k}}_t^\perp$) in dyadic form [28].

Figure 3.11a shows this transmission line model with reactance $\underline{\mathbf{X}}$ defined as the opaque reactance, which represents a parallel circuit between the reactance of the patch cladding, also called transparent reactance, $\underline{\mathbf{X}}_s$ and the one of the short circuit ground connection $\underline{\mathbf{X}}_{cc}$ [28, p. 6]. On the other side, figure 3.11b shows the equivalent transmission line network model when decomposing the parallel circuit representation of the opaque reactance into the transparent metasurface reactance and the short circuit reactance, which contains the effect of the dielectric under the patch cladding, the finite length and the perfect electric conductor (PEC) at the ground plane.

It can also be assumed that losses are not present in the anisotropic unit cell, making the impedance purely imaginary ($\underline{\mathbf{Z}} = j\underline{\mathbf{X}}$ and $\underline{\mathbf{Z}}_s = j\underline{\mathbf{X}}_s$). Furthermore, when the metal patch has two symmetry axes, the reactance matrices $\underline{\mathbf{X}}$ and $\underline{\mathbf{X}}_s$ are real, symmetric, and possess real eigenvalues and orthogonal eigenvectors [28, p. 6].

As stated before, all reactances in the anisotropic model are composed by matrices representing dyads. The opaque reactance is shown in equation (3.109) where X^{ee} is the reactance when the source is TM polarized, X^{hh} is the reactance when the source is TE polarized and X^{eh} is the cross-diagonal reactance. That is, when the source is either TE or TM polarized and the scattered wave is TM or TE polarized respectively. In equation (3.110) the transparent reactance is also expressed in dyad notation, where the components ee , hh and eh are TM, TE and cross-diagonal reactances respectively.

$$\underline{\mathbf{X}}(\omega, \mathbf{k}_t) = X^{ee} \hat{\mathbf{k}}_t \hat{\mathbf{k}}_t + X^{hh} \hat{\mathbf{k}}_t^\perp \hat{\mathbf{k}}_t^\perp + X^{eh} (\hat{\mathbf{k}}_t \hat{\mathbf{k}}_t^\perp + \hat{\mathbf{k}}_t^\perp \hat{\mathbf{k}}_t) \quad (3.109)$$

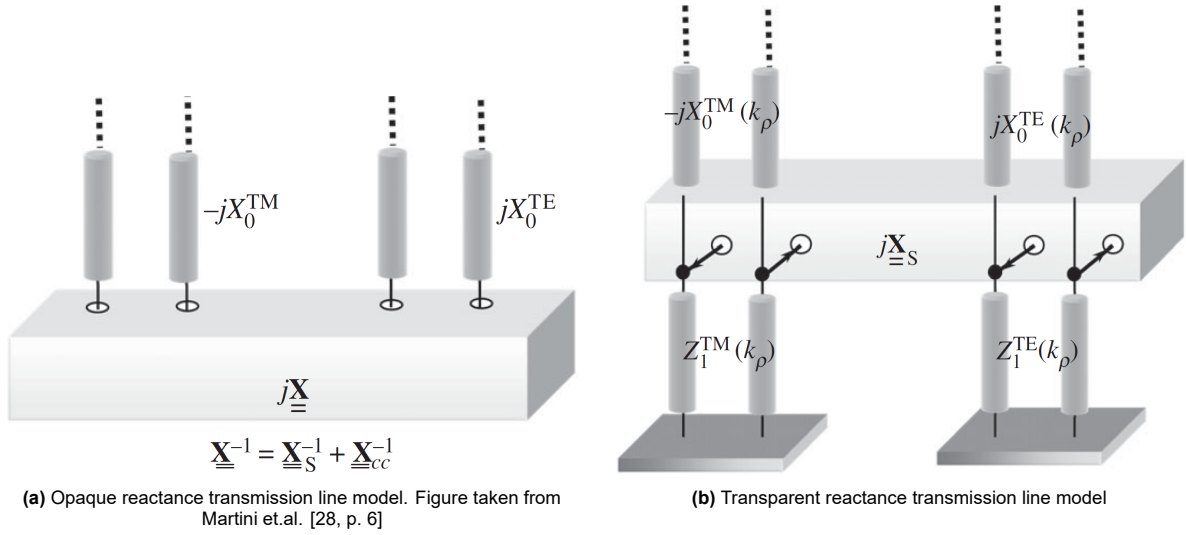


Figure 3.11: Opaque and transparent reactances for anisotropic metasurfaces. Figures taken from Martini et.al. [28, p. 6]

$$\underline{\underline{\mathbf{X}}}_s(\omega, \mathbf{k}_t) = X_s^{ee} \hat{\mathbf{k}}_t \hat{\mathbf{k}}_t + X_s^{hh} \hat{\mathbf{k}}_t^\perp \hat{\mathbf{k}}_t^\perp + X_s^{eh} (\hat{\mathbf{k}}_t \hat{\mathbf{k}}_t^\perp + \hat{\mathbf{k}}_t^\perp \hat{\mathbf{k}}_t) \quad (3.110)$$

The use of anisotropic patches affects the impedance boundary conditions. For both the TM and TE polarizations, the cross-diagonal terms from one mode has to be considered in the other. Therefore, a matrix representation is adopted for the opaque reactance in equation (3.111) with a similar fashion as in equation (3.108).

$$\mathbf{E}_t|_{z=0^+} = j\underline{\underline{\mathbf{X}}}(\omega, \mathbf{k}_t) \cdot [\hat{\mathbf{z}} \times \mathbf{H}_t]_{z=0^+} \quad (3.111)$$

As stated before, the transparent reactance is interpreted as the reactance of the patch cladding in the interface between the metasurface and free-space. This causes a discontinuity in the average tangential magnetic field in the interface of the metasurface with free-space ($z = 0$) [24, p. 363] that can be expressed in terms of the impedance boundary conditions as in equation (3.112).

$$\mathbf{E}_t|_{z=0^+} = j\underline{\underline{\mathbf{X}}}_s(\omega, \mathbf{k}_t) \cdot [\hat{\mathbf{z}} \times \mathbf{H}_t|_{z=0^+} - \hat{\mathbf{z}} \times \mathbf{H}_t|_{z=0^-}] \quad (3.112)$$

The transmission line impedance of free-space is characterized by $-jX_0^{TM}$ and jX_0^{TE} for TM and TE polarizations respectively, as it was shown in figure 3.11. These components can be analytically calculated as stated in equation (3.113) and subsequently represented in dyad form as is shown in equation (3.114).

$$X_0^{TM}(\omega, \mathbf{k}_t) = \frac{\zeta \sqrt{k_\rho^2 - k^2}}{k} \quad (3.113a) \quad X_0^{TE}(\omega, \mathbf{k}_t) = \frac{k\zeta}{\sqrt{k_\rho^2 - k^2}} \quad (3.113b)$$

$$\underline{\underline{\mathbf{X}}}_0(\omega, \mathbf{k}_t) = -X_0^{TM} \hat{\mathbf{k}}_t \hat{\mathbf{k}}_t + X_0^{TE} \hat{\mathbf{k}}_t^\perp \hat{\mathbf{k}}_t^\perp \quad (3.114)$$

The transmission line impedance of the dielectric substrate is characterized by $Z_1^{TM}(k_\rho)$ and $Z_1^{TE}(k_\rho)$ for the TM and TE modes respectively, and are given in equation (3.115). Then, considering the short circuit at the ground plane caused by the PEC, the short circuit reactance $\underline{\underline{\mathbf{X}}}_{cc}$ can be represented as in equation (3.116).

$$Z_1^{TM}(\omega, \mathbf{k}_t) = \frac{\zeta \sqrt{\epsilon_r k^2 - k_\rho^2}}{\epsilon_r k} \quad (3.115a) \quad Z_1^{TE}(\omega, \mathbf{k}_t) = \frac{\zeta k}{\sqrt{\epsilon_r k^2 - k_\rho^2}} \quad (3.115b)$$

$$\underline{\underline{\mathbf{X}}}_{cc}(\omega, \mathbf{k}_t) = (Z_1^{TM} \hat{\mathbf{k}}_t \hat{\mathbf{k}}_t + Z_1^{TE} \hat{\mathbf{k}}_t^\perp \hat{\mathbf{k}}_t^\perp) \tan \left(h \sqrt{\epsilon_r k^2 - k_\rho^2} \right) \quad (3.116)$$

This system can be solved by using the same method than in the isotropic case, that is, applying the transverse resonance condition to the free-space and opaque reactances. As both terms are in matrix form, the system has to be solved for a zero determinant to obtain the non-trivial solution, shown in equation (3.117). The term $k_{\rho sw}$ is the wavenumber of the surface wave, which is parallel to the transverse wavenumber, and is the variable for which this equation system is solved. The surface wave wavenumber is used to obtain the dispersion curves that compares this parameter with the excitation frequency to illustrate the effect of the unit cell on the wavefront.

$$\det \left[\underline{\underline{\mathbf{X}}}(\omega, \mathbf{k}_t) + \underline{\underline{\mathbf{X}}}_0(\omega, \mathbf{k}_t) \right]_{\mathbf{k}_t = \hat{\mathbf{k}}_t k_{\rho sw}} = 0$$

$$\det \left\{ \left[\underline{\underline{\mathbf{X}}}_s(\omega, \mathbf{k}_t)^{-1} + \underline{\underline{\mathbf{X}}}_{cc}^{-1}(\omega, \mathbf{k}_t) \right]^{-1} + \underline{\underline{\mathbf{X}}}_0(\omega, \mathbf{k}_t) \right\}_{\mathbf{k}_t = \hat{\mathbf{k}}_t k_{\rho sw}} = 0 \quad (3.117)$$

The values of $\underline{\underline{\mathbf{X}}}_s$ depend on the shape and size of the patch, orientation in the unit cell, the excitation frequency and the direction at which the surface wave propagates. This last relation of $\underline{\underline{\mathbf{X}}}_s$ with the propagation angle α_{sw} , determined by $\hat{\mathbf{k}}_t$, can be analytically obtained by applying rotation matrices $\underline{\underline{\mathbf{R}}}$ as stated in the work of Patel and Grbic [43] to the reactance matrix as shown in equation (3.118) such that the rotation angle is the difference between the desired angle $\alpha_{sw,2}$ with the angle at which the surface wave was oriented in the first place $\alpha_{sw,1}$. As $\underline{\underline{\mathbf{X}}}_s$ and $\underline{\underline{\mathbf{X}}}$ are symmetric matrices, they can be diagonalized to find their eigenvalues and eigenvectors, which are orthogonal to each other, and can be used to decouple equation (3.117). The diagonalized transparent reactance, that is, when the surface wave is aligned with the eigenvector of the transparent reactance $\hat{\mathbf{e}}_{1s}$ is shown in equation (3.119) where $\hat{\mathbf{e}}_{2s}$ is the second eigenvector perpendicular to $\hat{\mathbf{e}}_{1s}$, and X_{1s} and X_{2s} are the eigenvalues associated to the eigenvectors, which represent the TM and TE reactance [28, p. 7]. In this same research paper, it was stated that on the transition region the eigenvectors coincide with the direction at which the patch symmetry axes are oriented [28, p. 11].

$$\underline{\underline{\mathbf{X}}}' = \underline{\underline{\mathbf{R}}}^\top (\alpha_{sw,2} - \alpha_{sw,1}) \cdot \underline{\underline{\mathbf{X}}}_s \cdot \underline{\underline{\mathbf{R}}}(\alpha_{sw,2} - \alpha_{sw,1}) \quad (3.118a)$$

$$\underline{\underline{\mathbf{R}}}(\alpha_{sw,2} - \alpha_{sw,1}) = \begin{bmatrix} \cos(\alpha_{sw,2} - \alpha_{sw,1}) & -\sin(\alpha_{sw,2} - \alpha_{sw,1}) \\ \sin(\alpha_{sw,2} - \alpha_{sw,1}) & \cos(\alpha_{sw,2} - \alpha_{sw,1}) \end{bmatrix} \quad (3.118b)$$

$$\underline{\underline{\mathbf{X}}}_s = \hat{\mathbf{e}}_{1s} \hat{\mathbf{e}}_{1s} X_{1s} + \hat{\mathbf{e}}_{2s} \hat{\mathbf{e}}_{2s} X_{2s} \quad (3.119)$$

The excitation frequency plays an important role in determining the practical aspects of a metasurface antenna. As the reader may have already noted, the size of the unit cell depends on the frequency range in which the antenna will be used. Considering an infinite array of unit cells with a given size, three frequency bands can be identified for the excitation frequency as presented in [28, p. 10-12].

1. **Low-frequency band:** In this band the eigenvalues of $\underline{\underline{\mathbf{X}}}_s$ are approximately equal ($X_{1s} \approx X_{2s} \approx X$) [28, p. 10]. In practical terms, it means that the incident wave perceives an isotropic patch shape even though they are anisotropic and that the wave is purely TM polarized.
2. **Transition band:** At these frequencies $X_{1s} \neq X_{2s}$, which means that the patch anisotropy starts playing a role in the impedance matrix. The TM wave has a small TE contribution and the eigenvectors are aligned with the patch symmetry axes. However, the decoupled system of equation (3.117) can still only find a solution for the TM polarization.
3. **Dynamic band:** At these frequencies TM and TE solutions of equation (3.117) exist, meaning that a dual-mode regime can arise or that a TM mode can switch to a TE abruptly because of being close to the resonance condition [28, p. 12].

There is an important link between the size of the unit cell and the propagation of higher-order Floquet modes. This size is chosen to ensure that only the fundamental Floquet mode propagates in the infinite unit cell array and the others are evanescent. To achieve this, the unit cell has to fulfil the condition given in equation (C.9) and which derivation is detailed in appendix C and in the references therein.

3.2.4. Modulation technique: Adiabatic Floquet analysis

The adiabatic Floquet analysis, as most modulation techniques used for metasurfaces, has its origin in the holographic principle. The holographic principle can be shortly defined as "... an interference

pattern using two waves, and then using the interference pattern to scatter one wave to produce the other" [11, p. 3214]. In the case of a metasurface antenna, this could be understood as the result of an interference pattern between the electric current of a cylindrically-excited surface wave and the desired current in its aperture, being the metasurface impedance distribution the result of this interference. Therefore, to generate this electric field capable of emitting a particular far-field distribution, a surface wave has to excite the metasurface with the same electric distribution as it was modelled in the first place. This shows why excitations with surface waves of different frequencies would generate different radiation distributions in a metasurface with passive unit cells, which explains their dispersive nature.

In the method presented in this subsection, adiabatic Floquet modes are used. This term is referred as a "locally periodic interpretation of non-uniform boundary conditions" [37, p. 3897]. To explain why boundary conditions are non-uniform, it is important to first describe the impedance distribution along the metasurface antenna. This is semi-periodic and excites more than one Floquet mode to allow propagation and radiation of surface waves, using the same principles as leaky-wave antennas. This produces a well-defined radiation pattern in the far field caused by the electric field in the aperture, which can be calculated with the impedance distribution in the antenna. However, to achieve far-field radiation patterns different to the pencil beam, the impedance within the metasurface antenna must have different periodicities as a function of both the azimuthal angle and the radial distance to the centre, which makes the impedance distribution semi-periodic and imposes the need of using non-uniform boundary conditions.

This method is developed in the publications of Minatti, Caminita, Martini, Sabbadini and Maci [37, 40]. Flat optics refers to a relatively new theoretical framework for "... light-wave manipulations through a general type of penetrable or impenetrable metasurfaces" [29, p. 155] which consists on changing the local boundary conditions to obtain a deformation of the surface wave wavefront [29]. In the aforementioned research papers where the modulation method is explained [37, 40], it is stated that the difference with the previous methods, which adapt the holographic principle to obtain different antenna radiation patterns [36, 38], is that the metasurface is described in terms of transparent impedance boundary conditions, which are known to be less dispersive, rather than using opaque impedance boundary conditions [40, p. 3909]. The modulation methods explained in the consulted research act at a macroscopic scale, that is at the antenna scale, by interpreting non-uniform boundary conditions of the propagating surface waves as locally periodic in a mesoscopic scale, which is named as adiabatic Floquet-wave analysis [37, p. 3896].

As a summary, the synthesis process will be presented in this subsection, which is completely based on the work of Minatti et. al. [37, 40]. This is summarized in table 3.1 and it will be explained step by step. The main requirement is to have the desired electric field aperture distribution $\mathbf{E}_A(\rho)$ because the impedance distribution in the antenna is, according to the holographic principle, a direct consequence of this parameter.

1. The working frequency f , the permittivity of the dielectric substrate ϵ_r , and the thickness of the dielectric slab h is also a requirement for the following antenna synthesis. The radius a is also a requirement which depends on the required antenna gain. The free-space wavenumber is determined from the frequency f .
2. The surface wave propagation constant β_{sw} is set in between the values of $1.3 - 1.4k$ across the whole antenna as a first initial guess.
3. At this step, it is important to introduce the reactance representation across the antenna. This is first stated, as in the unit cell case, by the transparent impedance boundary condition representation in equation (3.120) which is the same condition as in equation (3.112).

$$\mathbf{E}_t = j\mathbf{X}_s \cdot \hat{\mathbf{z}} \times (\mathbf{H}_t|_{0^+} - \mathbf{H}_t|_{0^-}) = j\mathbf{X}_s \cdot \mathbf{J} \quad (3.120)$$

The reactance is given by equation (3.121a) in dyad form where the unit vectors $\hat{\rho}$ and $\hat{\phi}$ represent the radial and azimuthal directions respectively. Each of the transparent reactance components is subsequently defined in equations (3.121b) to (3.121d) where $m_{\rho,\phi}$ is the modulation index, $K_s(\rho)$ is a fast-varying phase factor that provides the majority of the interaction with the surface wave and $\Phi_{\rho,\phi}$ is a slow-varying phase factor which impacts the polarization control.

$$\mathbf{X}_s = \hat{\rho}\hat{\rho}X_{s,\rho\rho} + (\hat{\rho}\hat{\phi} + \hat{\phi}\hat{\rho})X_{s,\rho\phi} + \hat{\phi}\hat{\phi}X_{s,\phi\phi} \quad (3.121a)$$

Table 3.1: Synthesis process of metasurface antennas using adiabatic Floquet analysis. Table obtained from Minatti et. al. [40, p. 3913]

#	Input	Step Description	Output	Eq.
Setting the initial values				
1	f, ϵ_r, h	Set k and the radius a of the antenna on the basis of the operating frequency	k, a	-
2	k	Set β_{sw} randomly in the range $\beta_{sw}/k \in [1.1, 1.8]$. It is easy to synthesize β_{sw} through patches in this range. The suggested initial value for β_{sw} is therefore $1.3 - 1.4k$	β_{sw}	-
3	β_{sw}	Find $\bar{X}_{s,\rho}$	$\bar{X}_{s,\rho}$	3.123
4	$\bar{X}_{s,\rho}$	Set the initial value of $\bar{X}_{s,\phi}$ equal to $\bar{X}_{s,\rho}$	$\bar{X}_{s,\phi}$	-
5	-	Set $\eta_{eff} = P_{rad}/P_{sw}(0)$ (initial values can be 80%-90%)	η_{eff}	-
6	$\Delta\beta = 0$	Set $\Delta\beta = 0$ and find $Ks(\rho)$	$Ks(\rho)$	3.126
7	\mathbf{e}_A	Evaluate $S(\rho)$	$S(\rho)$	3.127
8	$S(\rho)$	Set $\alpha(\rho)$	$\alpha(\rho)$	3.130
9	$Ks(\rho)$	Find (-1) wavenumber as $\beta^{(-1)} = \beta_{sw}\hat{\rho} - K\nabla_t s(\rho)$	$\beta^{(-1)}$	3.134
10	$k, \epsilon_r, h, \beta_{sw}, P_{sw}(0)$	Set the initial value of $\mathbf{j}^{(0)} = J_\rho^{(0)}\hat{\rho} + J_\phi^{(0)}\hat{\phi}$ equal to $J_0\hat{\rho}$	$\mathbf{j}^{(0)}$	3.136
Iterative loop				
11	\mathbf{E}_A	Impose $\mathbf{E}_A = \mathbf{E}^{(-1)}$ through its equivalent form and then find the solution \mathbf{m} at the iterative step 0	\mathbf{m}	3.148 3.149 3.150
12	\mathbf{m}	Find an updated value of $J_\phi^{(0)}$ with the obtained value of \mathbf{m} to update the ratio $\chi_{\phi\rho}/\chi_{\phi\phi}$ and then $\mathbf{j}^{(0)}$	$J_\phi^{(0)}$	3.144 3.147
13	$\underline{\chi}$	Solve for $\det(\underline{\chi}) = 0$, update the values of α and $\Delta\beta$	$\alpha, \Delta\beta$	3.146
14	α	Update the value of $J_\rho^{(0)}$ (and therefore of $\mathbf{j}^{(0)}$) using α found at step #13 as a preset value, update $\tilde{k}^{(0)}$ and $\tilde{\sigma}$ using $\beta_{sw} + \Delta\beta$ in place of β_{sw} , update the value of $\underline{\mathbf{Q}}$	$J_\rho^{(0)}, \tilde{k}^{(0)}, \tilde{\sigma}, \underline{\mathbf{Q}}$	3.123 3.131 3.154
15	Iterate steps #11-14 until the value of \mathbf{m} does not change any more			

$$X_{s,\rho\rho} = \bar{X}_{s,\rho}[1 + m_\rho(\rho) \cos(Ks(\rho) + \Phi_\rho(\rho))] \quad (3.121b)$$

$$X_{s,\rho\phi} = \bar{X}_{s,\rho}m_\phi(\rho) \cos(Ks(\rho) + \Phi_\phi(\rho)) \quad (3.121c)$$

$$X_{s,\phi\phi} = \bar{X}_{s,\phi}[1 + m_\phi(\rho) \cos(Ks(\rho) + \Phi_\rho(\rho))] \quad (3.121d)$$

For convenience, these equations can be arranged in terms of three contributions as shown in equation (3.122). In these expressions, the reactance matrix $\underline{\mathbf{X}}_s$ is assumed to have an average value $\underline{\mathbf{X}}_s^{(0)}$ throughout the whole metasurface, whereas the elements $\underline{\mathbf{X}}_s^{(\mp 1)}$ represent the reactance variation as a function of the modulation indices, the slow- and fast-varying parameters.

$$\underline{\mathbf{X}}_s = \underline{\mathbf{X}}_s^{(0)} + \underline{\mathbf{X}}_s^{(-1)} + \underline{\mathbf{X}}_s^{(+1)} \quad (3.122a) \quad \underline{\mathbf{X}}_s^{(0)} = \bar{X}_{s,\rho}\hat{\rho}\hat{\rho} + \bar{X}_{s,\phi}\hat{\phi}\hat{\phi} \quad (3.122b)$$

$$\underline{\mathbf{X}}_s^{(\mp 1)} = \frac{e^{\pm jKs}}{2} [m_\rho(\bar{X}_{s,\rho}\hat{\rho}\hat{\rho} - \bar{X}_{s,\phi}\hat{\phi}\hat{\phi})e^{\pm j\Phi_\rho} + m_\phi\bar{X}_{s,\rho}(\hat{\rho}\hat{\phi} + \hat{\phi}\hat{\rho})e^{\pm j\Phi_\phi}] \quad (3.122c)$$

From these equations, the interest in this step is to calculate $\bar{X}_{s,\rho}$. As a first approximation, this value can be assumed to be the average reactance because the surface wave propagates namely in radial direction. Then, when using the transverse resonant condition from equation (3.117) but for an isotropic metasurface and solving for the transparent reactance, equation (3.123) is obtained as an initial value of $\bar{X}_{s,\rho}$.

$$\bar{X}_{s,\rho} = \zeta \left[\frac{1}{\sqrt{\beta_{sw}^2/k^2 - 1}} - \frac{\epsilon_r \cot(kh\sqrt{\epsilon_r - \beta_{sw}^2/k^2})}{\sqrt{\epsilon_r - \beta_{sw}^2/k^2}} \right]^{-1} \quad (3.123)$$

4. The initial value of $\bar{X}_{s,\phi}$ is set to $\bar{X}_{s,\rho}$ also as an initial approximation as the previously calculated value is associated with the average reactance value.
5. The efficiency η_{eff} , which is equal to the ratio of the power radiated P_{rad} to the power delivered by the feeder in the form of a surface wave at the antenna origin $P_{sw}(0)$, is set as a pre-defined value. Initial estimations can be between 80%-90%.
6. The wavenumber equation throughout the entire metasurface of the zero-mode is given by equation (3.124) where β_{sw} is the previously calculated propagation constant or average wavenumber, $\Delta\beta(\rho)$ is its variation throughout the metasurface, and $\alpha(\rho)$ is the attenuation parameter, which accounts for the energy transfer between the 0- and the -1- mode during propagation, being this last mode related to the leaky-wave radiation. This assumes that the wavefront related to the 0-mode is cylindrical, as the value is assumed to be aligned in $\hat{\rho}$.

$$k^{(0)}(\rho) = \beta_{sw} + \Delta\beta(\rho) - j\alpha(\rho) \quad (3.124)$$

On the other side, the electric field aperture, which is a requirement for the modulation process, can be expressed as in equation (3.125) where E_0 is the amplitude of the electric field, $l(\rho)$ is the average phasing factor, U_A is the step function equal to one for values within the antenna aperture and otherwise, and $e_\rho(\rho)$, $e_\phi(\rho)$, $\gamma_\rho(\rho)$ and $\gamma_\phi(\rho)$ are weak variables that determine the electric field local variations in radial and azimuthal directions.

$$\mathbf{E}_A = E_0 e^{-jkl(\rho)} \left[e_\rho(\rho) e^{j\gamma_\rho(\rho)} \hat{\rho} + e_\phi(\rho) e^{j\gamma_\phi(\rho)} \hat{\phi} \right] U_A \quad (3.125)$$

The electric field in the aperture \mathbf{E}_A can be identified with the radiation mode of the transverse electric field $\mathbf{E}^{(-)}$. By considering what has been described until now and other equations and explanations given in [37, 40], an expression for a first estimation of the fast-varying parameter $K_s(\rho)$ can be obtained as shown in equation (3.126). More details about this derivation are explained in section 4.2.2.

$$K_s(\rho) = \beta_{sw} + \int_0^\rho \Delta\beta(\rho') d\rho' - kl(\rho) \quad (3.126)$$

7. The radiated power density per unit surface of the aperture $S(\rho)$ can be approximated by “interpreting the local phase in equation (3.125) as the local transverse wavevector” [40, p. 3912] given by \mathbf{K}_t . This approximation is given in equation (3.127), which presents a first estimate for this parameter.

$$S(\rho) \approx \frac{E_0^2}{2k\zeta} \left[K_z |\mathbf{e}_A|^2 + \frac{|\mathbf{K}_t \cdot \mathbf{e}_A|^2}{K_z} \right] \quad (3.127a)$$

$$\mathbf{K}_t = k\nabla l(\rho) \quad (3.127b) \quad \mathbf{e}_A = \frac{\mathbf{E}_A}{E_0} \quad (3.127c) \quad K_z = \sqrt{k^2 - \mathbf{K}_t \cdot \mathbf{K}_t} \quad (3.127d)$$

8. A first estimation of $\alpha(\rho)$ can be obtained by using the radiation per unit area obtained in the previous step and other derivations that are detailed next. These start by first considering the surface wave power density per unit azimuthal angle p_{sw} , which is related to the radiation per unit area shown in equation (3.128) in both integral and differential forms.

$$p_{sw}(0) - p_{sw}(\rho) = \int_0^\rho S(\rho') \rho' d\rho' \quad (3.128a) \quad -\frac{d}{d\rho} p_{sw}(\rho) = \rho S(\rho) \quad (3.128b)$$

Following, it is assumed that “the power radiated by an increment $d\rho$ is proportional to the local power density through $2\alpha(\rho)$ ” [40, p. 3917], as the value 2α is contained in the Poynting vector in

the electric and magnetic fields. This results ultimately in equation (3.129) also in both differential and integral forms.

$$\frac{d}{d\rho} p_{sw}(\rho) = -2\alpha(\rho)p_{sw}(\rho) \quad \Rightarrow \quad p_{sw}(\rho) = p_{sw}(0)e^{-2\int_0^\rho \alpha(\rho')d\rho'} \quad (3.129)$$

When solving for $\alpha(\rho)$, equation (3.130) is obtained, which is the approximate expression for α at this synthesis stage.

$$\alpha(\rho) = \frac{\pi\rho S(\rho)\eta_{eff}}{\int_0^a \int_0^{2\pi} S(\rho')\rho'd\rho'd\phi' - 2\pi \int_0^\rho S(\rho')\rho'd\rho'} \quad (3.130)$$

9. To obtain the propagation constant vector β with index -1 , the global phase $\tilde{k}^{(0)}(\rho)\rho$, the phase shift from the origin to the reference point ρ , has to be obtained. This is defined as in equation (3.131).

$$\tilde{k}^{(0)}(\rho)\rho = \int_0^\rho k^{(0)}(\rho')d\rho' = \beta_{sw}\rho + \int_0^\rho [\Delta\beta(\rho') - j\alpha(\rho')]d\rho' \quad (3.131)$$

Following, the current density $\mathbf{J}^{(q)}$ can be decomposed in the adiabatic Floquet wave current basis as stated in equation (3.132). Furthermore, "it has been seen that only three terms of the expansion are sufficient when only the -1 mode falls in the radiation (visible) region" [40, p. 3910]. Each of these elements can be subsequently expressed as a function of their basis function $\mathbf{j}^{(q)} = J_\rho^{(q)}\hat{\rho} + J_\phi^{(q)}\hat{\phi}$ which denotes the slowly-varying part of the q current mode, and the Hankel function of the second kind and first order $H_1^{(2)}$. This is show in equation (3.133), which contains too the fast-varying part in $Ks(\rho)$.

$$\mathbf{J} \approx \mathbf{J}^{(0)} + \mathbf{J}^{(-1)} + \mathbf{J}^{(+1)} \quad (3.132)$$

$$\mathbf{J}^{(q)} = \mathbf{j}^{(q)}e^{-jqKs(\rho)}H_1^{(2)}(\tilde{k}^{(0)}\rho) = (J_\rho^{(q)}\hat{\rho} + J_\phi^{(q)}\hat{\phi})e^{-jqKs(\rho)}H_1^{(2)}(\tilde{k}^{(0)}\rho) \quad q = 0, \pm 1 \quad (3.133)$$

Then, considering the dependency of the adiabatic current density with the mode number, each of these modes should have an independent curvilinear wavefront $\beta^{(q)}$ when the asymptotic form of the Hankel function is used, which is valid for distances greater than a wavelength. Then, $\beta^{(q)}$ is given by equation (3.134) considering the cylindrical wavefront for the 0-mode and the dependency on the fast-varying term in the higher-order modes.

$$\beta^{(q)} = \text{Re}\nabla_t[\tilde{k}^{(0)}\rho + qKs(\rho)] = (\beta_{sw} + \Delta\beta)\hat{\rho} + qK\nabla_t s(\rho) \quad (3.134)$$

It is important to note that, in order to make only the -1 mode radiate, the propagation constants for the presented modes have to satisfy equation (3.135).

$$|\beta^{(q)}| > k \quad \forall i = \{0, 1\} \quad \text{and} \quad |\beta^{(-1)}| < k \quad (3.135)$$

10. A first estimation of the current fundamental basis is required. As stated before, as the current is directed in radial positive direction, this initial approximation can be directed parallel to $\hat{\rho}$ which would yield $\mathbf{j}^{(0)} = J_0\hat{\rho}$ where J_0 is the current density magnitude associated with a purely propagating TM surface wave. This value can be approximated with equation (3.136) to obtain a first estimation of this parameter.

$$J_0 = \sqrt{\frac{P_{sw}(0)\zeta}{\bar{X}_\rho^2 k} \left[\frac{2\epsilon_r}{h(\epsilon_r k^2 - \beta_{sw}^2)^2} + \frac{1}{(\beta_{sw}^2 - k^2)^{3/2}} \right]^{-1}} \quad (3.136)$$

11. In this step a first approximation of the modulation vector \mathbf{m} is obtained. To understand how this is done, the adiabatic Floquet wave expression of the current density \mathbf{J} has to be used to calculate the electric field in terms of the Floquet modes relevant to this problem. To obtain this expression, the spectral GF $\underline{\underline{\mathbf{Z}}}_{GF}^{(q)}$ of the grounded slab at the local wavevector $\beta^{(q)}$ is used as in equation (3.137).

$$\mathbf{E}_t(\boldsymbol{\rho}) = \sum_{q=-1}^1 \mathbf{E}^{(q)} \approx \sum_{q=-1}^1 \underline{\underline{\mathbf{Z}}}_{GF}^{(q)} \cdot \mathbf{J}^{(q)} \quad \text{where} \quad \mathbf{E}^{(q)} \approx \underline{\underline{\mathbf{Z}}}_{GF}^{(q)} \cdot \mathbf{J}^{(q)} \quad (3.137)$$

The spectral GF is composed by the elements $\underline{\underline{\mathbf{X}}}_0(\beta^{(q)})$ and $\underline{\underline{\mathbf{X}}}_{cc}(\beta^{(q)})$, which are analogous to equation (3.113) and to equation (3.115), but for multiple Floquet modes and they do not necessarily have to be aligned with the transverse wavevector. They can be obtained as a function of $\beta^{(q)}$ as shown in equation (3.138) which states that the spectral GF represents the metasurface impedance for each evaluated mode in terms of the one of free-space $\underline{\underline{\mathbf{X}}}_0$ and the dielectric slab $\underline{\underline{\mathbf{X}}}_{cc}$.

$$\underline{\underline{\mathbf{Z}}}_{GF}^{(q)} = j\underline{\underline{\mathbf{X}}}_{GF}(\beta^{(q)}) = -j[\underline{\underline{\mathbf{X}}}_0^{-1}(\beta^{(q)}) + \underline{\underline{\mathbf{X}}}_G^{-1}(\beta^{(q)})]^{-1} \quad (3.138)$$

Equations (3.139) and (3.140) show how to calculate these reactance terms, which is the same as the approach shown in equations (3.113) to (3.116). These dyads are aligned with the transverse wavevector $\beta^{(q)}$, while all the previous equations are expressed in cylindrical coordinates. Therefore, if necessary a matrix rotation should be performed when changing from one reference frame to the other. It is important to note that, if only the mode -1 is radiating, the term $\underline{\underline{\mathbf{Z}}}_{GF}^{(q)}$ will be real for $q = [0, 1]$ and it will be complex for $q = -1$.

$$\underline{\underline{\mathbf{X}}}_0(\mathbf{k}_t) = X_0^{TM} \hat{\mathbf{k}}_t \hat{\mathbf{k}}_t + X_0^{TE} \hat{\mathbf{k}}_t^\perp \hat{\mathbf{k}}_t^\perp \quad (3.139)$$

$$\underline{\underline{\mathbf{X}}}_{cc}(\mathbf{k}_t) = [Z_1^{TM} \hat{\mathbf{k}}_t \hat{\mathbf{k}}_t + Z_1^{TE} \hat{\mathbf{k}}_t^\perp \hat{\mathbf{k}}_t^\perp] \tan \left(h \sqrt{\epsilon_r k^2 - k_\rho^2} \right) \quad (3.140)$$

By using equations (3.120), (3.122a), (3.132) and (3.137), equation (3.141) can be obtained, which relates Green's function with the transparent boundary conditions for every Floquet mode.

$$\mathbf{E}_t(\boldsymbol{\rho}) = \sum_{q=-1}^1 \underline{\underline{\mathbf{Z}}}_{GF}^{(q)} \cdot \mathbf{J}^{(q)} = j(\underline{\underline{\mathbf{X}}}_s^{(0)} + \underline{\underline{\mathbf{X}}}_s^{(-1)} + \underline{\underline{\mathbf{X}}}_s^{(+1)}) \cdot (\mathbf{J}^{(+1)} + \mathbf{J}^{(0)} + \mathbf{J}^{(-1)}) \quad (3.141)$$

Following, it can be proven that equation (3.141) can be split into equations (3.142) and (3.143). This can be concluded by equating the fast-varying terms of $\underline{\underline{\mathbf{X}}}_s^{(q)}$ and $\mathbf{J}^{(q)}$. More details about how this is obtained are found in section 4.2.2. $\underline{\underline{\chi}}$ is obtained as shown in equation (3.144) where the term $\underline{\underline{\mathbf{z}}}^{(\pm 1)}$ is detailed in equation (3.145).

$$\mathbf{J}^{(\pm 1)} = j[\underline{\underline{\mathbf{Z}}}_{GF}^{(\pm 1)} - j\underline{\underline{\mathbf{X}}}_s^{(0)}]^{-1} \cdot \underline{\underline{\mathbf{X}}}_s^{(\pm 1)} \cdot \mathbf{J}^{(0)} \quad (3.142)$$

$$j\underline{\underline{\chi}} \cdot \mathbf{J}^{(0)} = 0 \quad (3.143)$$

$$j\underline{\underline{\chi}} = (\underline{\underline{\mathbf{Z}}}_{GF}^{(0)} - j\underline{\underline{\mathbf{X}}}_s^{(0)}) + \underline{\underline{\mathbf{z}}}^{(+1)} + \underline{\underline{\mathbf{z}}}^{(-1)} \quad (3.144)$$

$$\underline{\underline{\mathbf{z}}}^{(\pm 1)} = \underline{\underline{\mathbf{X}}}_s^{(\mp 1)} \cdot [\underline{\underline{\mathbf{Z}}}_{GF}^{(\pm 1)} - j\underline{\underline{\mathbf{X}}}_s^{(0)}]^{-1} \cdot \underline{\underline{\mathbf{X}}}_s^{(\pm 1)} \quad (3.145)$$

Equation (3.143) admits non-trivial solutions if and only if a complex value of $k^{(0)}$ can be found that satisfies equation (3.146).

$$\det[\underline{\chi}(\boldsymbol{\rho})] = 0 \quad (3.146)$$

Equation (3.146) is the local $\boldsymbol{\rho}$ -dependent adiabatic dispersion equation that relates the local wavenumber with the adiabatic expansion in Floquet modes. By solving the second row in equation (3.143) for $\mathbf{j}^{(0)} = J_\rho^{(0)} \hat{\boldsymbol{\rho}} + J_\phi^{(0)} \hat{\boldsymbol{\phi}}$, equation (3.147) can be obtained. It is important to note that, for initial modulation values, $J_\rho^{(0)}$ can be approximated to J_0 , which is specified in equation (3.136).

$$\mathbf{j}^{(0)} = J_\rho^{(0)} \left(\hat{\boldsymbol{\rho}} - \frac{\chi_{\phi\rho}}{\chi_{\phi\phi}} \hat{\boldsymbol{\phi}} \right) \quad (3.147)$$

Furthermore, when using equations (3.137) and (3.142), equation (3.148) is obtained, which is also equivalent with the electric field on the aperture in equation (3.125), as the -1 mode is the only one that radiates.

$$\mathbf{E}^{(-1)}(\boldsymbol{\rho}) = j \underline{\mathbf{Z}}_{GF}^{(-1)} \cdot [\underline{\mathbf{Z}}_{GF}^{(-1)} - j \underline{\mathbf{X}}_s^{(0)}]^{-1} \cdot \underline{\mathbf{X}}_s^{(-1)} \cdot \mathbf{j}^{(0)} H_1^{(2)}(\tilde{k}^{(0)} \rho) = \mathbf{E}_A(\boldsymbol{\rho}) \quad (3.148)$$

When solving equation (3.148) for the modulation variables, equation (3.149) is obtained, where the coefficient term $\tilde{\sigma}$ is shown in equation (3.150a), the one that links GF with the average reactance is in equation (3.150b), the components of the modulation vector are in equation (3.150c), the components of the electric field in the aperture are in equation (3.150d) and the \mathbf{Q} -matrix is shown in equation (3.150e). In this step, as a summary, equation (3.149) is solved for \mathbf{m} by using equation (3.150) where, subsequently, all of its elements have been discussed in this step.

$$\mathbf{m} = \tilde{\sigma} \underline{\mathbf{Q}}^{-1} \cdot \underline{\mathbf{P}} \cdot \mathbf{e} \quad (3.149)$$

$$\tilde{\sigma} = \frac{2E_0}{j J_\rho^{(0)} |H_1^{(2)}(\tilde{k}^{(0)} \rho)|} \quad (3.150a) \quad \underline{\mathbf{P}} = \underline{\mathbf{1}} - j \underline{\mathbf{X}}_s^{(0)} \cdot (\underline{\mathbf{Z}}_{GF}^{(-1)})^{-1} \quad (3.150b)$$

$$\mathbf{m} = m_\rho e^{j\Phi_\rho} \hat{\boldsymbol{\rho}} + m_\phi e^{j\Phi_\phi} \hat{\boldsymbol{\phi}} \quad (3.150c) \quad \mathbf{e} = e_\rho e^{j\gamma_\rho} \hat{\boldsymbol{\rho}} + e_\phi e^{j\gamma_\phi} \hat{\boldsymbol{\phi}} \quad (3.150d)$$

$$\underline{\mathbf{Q}} = \bar{X}_{s,\rho} (\hat{\boldsymbol{\rho}} \hat{\boldsymbol{\rho}} + \hat{\boldsymbol{\phi}} \hat{\boldsymbol{\phi}}) - \frac{\chi_{\rho\phi}}{\chi_{\phi\phi}} (\bar{X}_{s,\rho} \hat{\boldsymbol{\rho}} \hat{\boldsymbol{\phi}} - \bar{X}_{s,\phi} \hat{\boldsymbol{\phi}} \hat{\boldsymbol{\rho}}) \quad (3.150e)$$

12. In this step, the new value of \mathbf{m} is used to obtain the values of $\underline{\chi}$ by using equation (3.144). Subsequently, the azimuthal term of equation (3.147) can be obtained, which is equal to $J_\phi^{(0)}$ as shown in equation (3.133).
13. Solve equation (3.146) for $k^{(0)}$ to obtain updated values of $\Delta\beta$ and α . This expression is replaced only in $\underline{\mathbf{Z}}_{GF}^{(q)}$ to define $\underline{\chi}$ as in equation (3.144). The elements $\underline{\mathbf{X}}_s^{(\pm 1)}$ are updated after obtaining \mathbf{m} in equation (3.149).
14. For this step, the Poynting vector has to be revisited. As stated before, the -1 mode is the only radiating mode. Therefore, the Poynting vector would have the form of equation (3.151).

$$S(\boldsymbol{\rho}) = -\frac{1}{2} \text{Re} \{ \mathbf{J}^{(-1)*} \cdot \mathbf{E}^{(-1)} \} \quad (3.151)$$

Equation (3.151) can be expressed as equation (3.152) by considering the derivation found in the work of Minatti et.al. [37, p. 3901] which states that $\mathbf{J}^{(-1)*} \cdot \mathbf{E}^{(-1)} = \mathbf{J}^{(0)*} \cdot \underline{\mathbf{z}}^{(-1)\dagger} \cdot \mathbf{J}^{(0)}$ where \dagger represents the transpose conjugate. Also, the asymptotic approximation of the Hankel function is used for $\mathbf{J}^{(0)}$.

$$S(\boldsymbol{\rho}) = -\frac{1}{2} \text{Re} \{ \mathbf{J}^{(0)*} \cdot \underline{\mathbf{z}}^{(-1)\dagger} \cdot \mathbf{J}^{(0)} \} = -\frac{1}{2} \text{Re} \{ \mathbf{j}^{(0)*} \cdot \underline{\mathbf{z}}^{(-1)\dagger} \cdot \mathbf{j}^{(0)} \} \frac{2e^{-2} \int_0^\rho \alpha(\rho') d\rho'}{\pi \rho \beta_{sw}} \quad (3.152)$$

On the other side, equations (3.128b) and (3.129) can be used to obtain equation (3.153), which uses the relation between the leakage distribution $\alpha(\boldsymbol{\rho})$ and the radiated power $p_{sw}(0) - p_{sw}(\boldsymbol{\rho})$.

$$S(\rho) = 2\alpha(\rho) \frac{P_{sw}(0)}{2\rho\pi} e^{-2 \int_0^\rho \alpha(\rho') d\rho'} \quad (3.153)$$

Subsequently, equations (3.152) and (3.153) are used to obtain equation (3.154), which can be used to calculate an updated value of $J_\rho^{(0)}$.

$$\alpha(\rho) = -\frac{|J_\rho^{(0)}|^2}{P_{sw}(0)\beta_{sw}} \operatorname{Re} \left\{ \left(\hat{\rho} - \frac{\chi_{\phi\rho}^*}{\chi_{\phi\phi}^*} \hat{\phi} \right) \cdot \underline{\underline{z}}^{(-1)\dagger} \cdot \left(\hat{\rho} - \frac{\chi_{\phi\rho}}{\chi_{\phi\phi}} \hat{\phi} \right) \right\} \quad (3.154)$$

Following, the value of $\tilde{k}^{(0)}$ can be updated by using the obtained value of $\beta_{sw} + \Delta\beta$ in the previous step and replacing it in equation (3.131), and the value of $K_s(\rho)$ can be updated by using equation (3.126).

15. Finally, the obtained value of \mathbf{m} is evaluated with respect to the one obtained previously. If the change in this parameter is consider negligible, then the algorithm can be stopped and the final values of $\underline{\underline{X}}_s$ and \mathbf{J} retrieved. Otherwise, another run can be performed and this evaluated once more.

In the iterative part no update of $\bar{X}_{s,\rho}$, $\bar{X}_{s,\phi}$ nor β_{sw} has been performed. Therefore, it is suggested to update them at the end of the last step by calculating their average value in the metasurface as presented in equation (3.155) using equation (3.121b) and equation (3.121d). Next, β_{sw} can be obtained by solving implicitly equation (3.123) with the updated value of $\bar{X}_{s,\rho}$.

$$\bar{X}_{s,\rho} = \frac{1}{A} \iint_A X_{s,\rho} dA \quad (3.155a) \quad \bar{X}_{s,\phi} = \frac{1}{A} \iint_A X_{s,\phi} dA \quad (3.155b)$$

3.3. FDTD simulations

In this section, the principles of FDTD simulations are explained with special focus on the basic concepts. The intention of this section is not to expand the FDTD theory, but to clarify the basics for electromagnetic modelling of periodic structures. Furthermore, this method is chosen because it is the one used by the software Lumerical, which is the one made available by TNO for this project. Other methods may be suitable for this type of analysis and their applicability should be evaluated for each specific case.

3.3.1. Basic principles

FDTD stands for finite-difference time-domain, which consists namely on discretize the spatial and time domain to solve Maxwell's equation for the given problem. Consider Maxwell's equations in differential form as stated in equation (3.156) where $\mathbf{D} = \epsilon\mathbf{E} = \epsilon_0\epsilon_r\mathbf{E}$ and $\mathbf{B} = \mu\mathbf{H} = \mu_0\mu_r\mathbf{H}$, μ_0 and ϵ_0 are the permeability and permittivity of free-space respectively, and μ_r and ϵ_r are the relative permeability and permittivity respectively. Furthermore, σ is the electric conductivity and σ^* is the equivalent magnetic loss [15, p. 68]

$$\frac{\partial \mathbf{B}}{\partial t} = -\nabla \times \mathbf{E} - \sigma^* \mathbf{H} \quad (3.156a) \quad \frac{\partial \mathbf{D}}{\partial t} = \nabla \times \mathbf{H} - \sigma \mathbf{E} \quad (3.156b)$$

$$\nabla \cdot \mathbf{D} = 0 \quad (3.156c) \quad \nabla \cdot \mathbf{B} = 0 \quad (3.156d)$$

After some manipulations on equation (3.156a) and equation (3.156b), the set contained in equation (3.157) can be derived, which will be used to solve Maxwell's equations in time domain.

$$\frac{\partial H_x}{\partial t} = -\frac{1}{\mu} \left[\frac{\partial E_z}{\partial y} - \frac{\partial E_y}{\partial z} \right] - \frac{\sigma^*}{\mu} H_x \quad (3.157a) \quad \frac{\partial H_y}{\partial t} = -\frac{1}{\mu} \left[\frac{\partial E_x}{\partial z} - \frac{\partial E_z}{\partial x} \right] - \frac{\sigma^*}{\mu} H_y \quad (3.157b)$$

$$\frac{\partial H_z}{\partial t} = -\frac{1}{\mu} \left[\frac{\partial E_y}{\partial x} - \frac{\partial E_x}{\partial y} \right] - \frac{\sigma^*}{\mu} H_z \quad (3.157c) \quad \frac{\partial E_x}{\partial t} = \frac{1}{\epsilon} \left[\frac{\partial H_z}{\partial y} - \frac{\partial H_y}{\partial z} \right] - \frac{\sigma}{\epsilon} E_x \quad (3.157d)$$

$$\frac{\partial E_y}{\partial t} = \frac{1}{\epsilon} \left[\frac{\partial H_x}{\partial z} - \frac{\partial H_z}{\partial x} \right] - \frac{\sigma}{\epsilon} E_y \quad (3.157e) \quad \frac{\partial E_z}{\partial t} = \frac{1}{\epsilon} \left[\frac{\partial H_y}{\partial x} - \frac{\partial H_x}{\partial y} \right] - \frac{\sigma}{\epsilon} E_z \quad (3.157f)$$

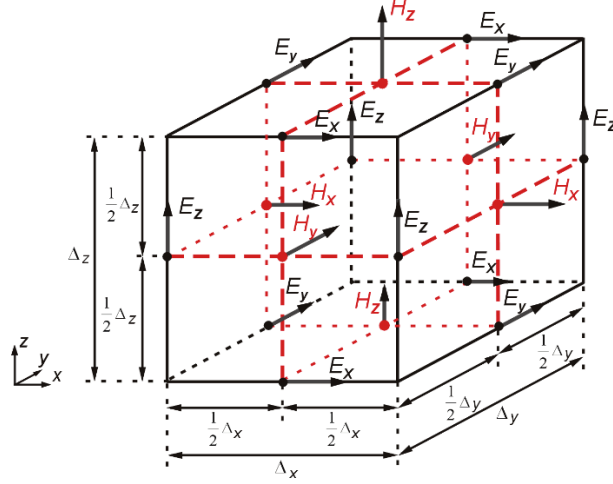


Figure 3.12: Construction of Yee cell in a three-dimensional mesh. Source: [7, p. 748]

3.3.2. Yee cell

To solve these equations, the space coordinates are discretized in blocks called “Yee cells”, which name comes from the author’s last name Kane S. Yee, who in 1966 proposed this method as an approach to solve Maxwell’s equations in the time domain [15]. First, the simulation domain’s length, width and height is discretized in cubes with size Δx , Δy and Δz respectively. Subsequently, consider as an example the representation of the electric field in this mesh such that its x , y , and z components are aligned with the middle of the edges of each cell as described in equation (3.158a), equation (3.158b) and equation (3.158c). In contrast, the magnetic field components have an offset of $(1/2)\Delta x$, $(1/2)\Delta y$ and $(1/2)\Delta z$ in all its elements as shown in equation (3.158d), equation (3.158e) and equation (3.158f). In equation (3.158) the values of p , q and w are integers such that $(\Delta x)p$, $(\Delta y)q$ and $(\Delta z)w$ are contained in the spatial domain of the simulation region. This method is illustrated in figure 3.12 where the arrows and the elements of the electric and magnetic fields are directed and positioned as described in equation (3.158).

$$E_x(x, y, z) = E_x \left[\Delta x \left(p + \frac{1}{2} \right), (\Delta y)q, (\Delta z)w \right] \quad (3.158a)$$

$$E_y(x, y, z) = E_y \left[(\Delta x)p, \Delta y \left(q + \frac{1}{2} \right), (\Delta z)w \right] \quad (3.158b)$$

$$E_z(x, y, z) = E_z \left[(\Delta x)p, (\Delta y)q, \Delta z \left(w + \frac{1}{2} \right) \right] \quad (3.158c)$$

$$H_x(x, y, z) = H_x \left[\Delta x(p + 1), \Delta y \left(q + \frac{1}{2} \right), \Delta z \left(w + \frac{1}{2} \right) \right] \quad (3.158d)$$

$$H_y(x, y, z) = H_y \left[\Delta x \left(p + \frac{1}{2} \right), \Delta y(q + 1), \Delta z \left(w + \frac{1}{2} \right) \right] \quad (3.158e)$$

$$H_z(x, y, z) = H_z \left[\Delta x \left(p + \frac{1}{2} \right), \Delta y \left(q + \frac{1}{2} \right), \Delta z(w + 1) \right] \quad (3.158f)$$

This configuration of the electric and magnetic fields allows to calculate equation (3.157) with more precision because each of the derivatives with respect to time will be a function of the same value and of the adjacent terms of the magnetic or electric field that are oriented in orthogonal directions. Whenever this meshing technique is used, it is necessary to use a second order representation of the partial derivatives as in equation (3.159) where the origin is assumed to be the bottom left corner in figure 3.12.

$$\left. \frac{\partial E_y}{\partial z} \right|_{(0, \frac{\Delta y}{2}, \frac{\Delta z}{2})} = \frac{E_y \left(0, \frac{\Delta y}{2}, \Delta z \right) - E_y \left(0, \frac{\Delta y}{2}, 0 \right)}{\Delta z} + \mathcal{O}(2) \quad (3.159)$$

In the time domain, the electric and magnetic fields are never calculated for the same time step during the simulation. As in the case of the spatial domain, in the time domain there is also an offset of $(\Delta t)/2$ between the electric and magnetic field, which is used to calculate the time derivatives with a second order precision. This integration method is known as “leapfrog method” [15, p. 70]. By considering this approach and the Yee cell arrangement in figure 3.12, the equation needed to calculate H_x in the time step $(t_s + \frac{1}{2})\Delta t$ following equation (3.157a) is given in equation (3.160). This same procedure can be followed for the other elements of the electric and magnetic fields to solve integrate Maxwell’s equations in the time domain.

$$H_x^{(t_s + \frac{1}{2})\Delta t} = \frac{1}{\frac{1}{\Delta t} + \frac{\sigma^*}{2\mu}} \left[\left(\frac{1}{\Delta t} - \frac{\sigma^*}{2\mu} \right) H_x^{(t_s - \frac{1}{2})\Delta t} - \frac{E_{z|+\frac{\Delta y}{2}}^{t_s(\Delta t)} - E_{z|-\frac{\Delta y}{2}}^{t_s(\Delta t)}}{\mu(\Delta y)} + \frac{E_{y|+\frac{\Delta z}{2}}^{t_s(\Delta t)} - E_{y|-\frac{\Delta z}{2}}^{t_s(\Delta t)}}{\mu(\Delta z)} \right] \quad (3.160)$$

Finally, it is important to mention the Courant-Friedrich-Levy stability condition, which uses the wave equation for a plane wave to obtain an upper limit of the time-step and expresses it in terms of the space grid resolution. This is done by considering the wave velocity in the given media and the needed time resolution to represent its propagation in a stable manner. This criteria is stated in equation (3.161) and its derivation can be consulted by the reader in the work of Natalia K. Nikolova [41, p. 19-24].

$$\Delta t \leq \Delta t_{max} = \frac{1}{c \sqrt{\left(\frac{1}{\Delta x}\right)^2 + \left(\frac{1}{\Delta y}\right)^2 + \left(\frac{1}{\Delta z}\right)^2}} \quad (3.161)$$

3.3.3. Boundary conditions

The FDTD method has to perform the simulation in a finite space and time. Therefore, boundary conditions should be used to limit the simulated space considering that a space and time relatively large to the mesh size would consume more computational resources. The most important boundary conditions used for FDTD simulation and particularly for this project are Perfectly Matched Layer (PML) and periodic boundary conditions.

PML boundary conditions are used to absorb ideally all the incident field in the delimited boundaries. The idea behind them is to “replace the infinite space that surrounds a finite computational domain” [2, p. 2] by simulating in the PML boundary a material with anisotropic conductivities that permits transmission in the PML media from a wave with variable incident angle, and no subsequent field reflection due to its absorbing properties. This boundary conditions is usually implemented as multiple material layers to increase gradually the conductivity and minimize reflections [48, p. 186]. In the metasurface unit cell simulation, PML boundary conditions are used to represent free-space in the positive z-direction.

Periodic boundary conditions are used to simulate large structures that have a repeating pattern in one or more axes. These structures are approximated to infinite structures along the axis where the repeating pattern occurs by imposing periodic boundary conditions. This is done because it results computationally cheaper, as only one small part of the structure is simulated. For example, for the case of calculating the average reactance of a metasurface unit cell, periodic boundary conditions are set in x- and y-axes that would simulate an infinite planar structure.

To understand how periodic boundary conditions work, it results helpful to take the example of an infinite propagating plane wave in 2D with periodic boundary conditions along its y-axis as it is shown in figure 3.13. In this case, at some point in time, a plane wave is propagating in negative-y direction close to the simulation region boundary for minimum y-values. Then, in a subsequent point in time, the contribution of this propagating wave is added to the values close to the boundary with maximum-y values as it is shown with the electric field in figure 3.13. This summarizes how the periodic boundary conditions work, which could be easily extrapolated to the 3D metasurface case where the periodic boundary conditions are in the x- and y-axes.

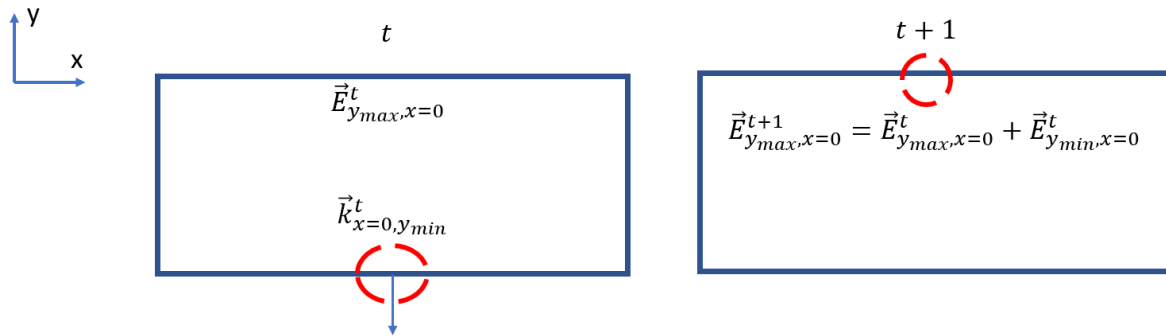
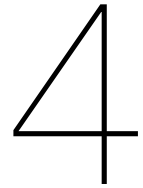


Figure 3.13: Electric field when using periodic boundary conditions in a 2D simulation

When using periodic boundary conditions, it is important to be careful with how the source is injected and what does that imply for the boundary conditions. The most simple case is when a single-frequency plane wave source is injected such that it propagates perpendicular to the boundary condition's plane normal. However, when this plane wave is injected at an angle, a phase shift term has to be applied to the electric and magnetic field values that go through the periodic boundaries, which is proportional to the frequency of the injected wave and to the simulation region dimensions.



Metasurface antenna design

In this chapter, the whole process of the antenna design is specified and applied to the case of the SAR antenna presented in chapter 2. The first section is centred in the unit cell database representation, where a method for obtaining this database is derived. Next, the Adiabatic Floquet analysis explained in section 3.2.4 is applied to this antenna design. Finally, the antenna layout is obtained by associating a patch shape from section 4.1 to the required reactance obtained in section 4.2 with an optimization procedure.

The order proposed for the design methodology in section 3.2.2 is modified. The unit cell database is obtained before the antenna synthesis because the concepts that imply this first part are easier to implement than the second. The author notes that this is not optimal for subsequent designs, but it reduces the implementation effort for the first time this is modelled.

4.1. Unit cell impedance database

As it was presented in section 3.2.3, the reactance database is obtained by performing full-wave simulations of unit cells with periodic boundary conditions. In this section, the motivations for the dimensions common to all unit cell are explained, together with the method used for calculating their reactance.

4.1.1. Physical properties of the unit cell

As it was explained in section 3.2.1, a metasurface antenna is composed of unit cells arranged in a square lattice. Each of these unit cells has a patch in the middle with at least two symmetry planes that can collectively control the propagating surface wave in terms of phase and direction. Furthermore, as one of the requirements of a metasurface antenna is that there has to be a slight variation between adjacent patches, only one particular patch shape is used in each antenna design and the patch's dimensions and orientations are changed slightly in contiguous unit cells.

Patch shape

The patch shape was the first parameter that was chosen because it determines the shape parameters that would be varied in the simulations. This was chosen considering the reported performances in [9], the available literature for verification purposes, and the use of a square mesh to represent the geometry. The performances are reported in figure 4.1 and are shown for five patch shapes. When comparing these, it can be concluded directly that the “coffee bean” shape does not offer any additional benefits compared with the “grain of rice” (or elliptical shape, which is how it is going to be referred from now on). The four patch shapes remaining highlight individually in any of the remaining performance parameters or in their combination, thus they will be evaluated in terms of literature available and its representation in FDTD simulations.

Regarding the presence in literature of the remaining four patches, research articles including how the reactance changes with the shape of these geometries and excitation frequency are considered. The elliptical patches are included in two research papers [32, 35], where particularly the first one treats this geometry in detail, providing information about singularities in their current distribution and quasi-analytical models. The other patch that has been a subject of research in literature is the slotted

	Coffee Bean	Slotted patch	Grain of Rice	Double anchor	Double π
					
# parameters	2	3	3	3	3
Anisotropy Control					 
Range of X_{pp}				 	 
Bandwidth (group velocity)				 	 
Sensitivity to tolerances			 		
Loss in the metal			 		

Figure 4.1: Patch shapes performances in metasurface antennas. Source: [9, p. 4]

patch. There is one research paper that treats the design of a dual circularly polarized broadside beam antenna that contains information that can be used to compare its calculated reactance, where the dispersion is only considered for an elliptical patch instead of the circular patch described in figure 4.1 [50, p. 2950], providing more degrees of freedom that can be varied to contain the whole reactance range that would result from the synthesis process. The other two patch configurations, the double anchor and the double π , do not have an impedance database representation in literature as far as the author knows, so they are discarded from the analysis.

Finally, the geometric representation of the remaining two patches is compared in terms of easiness to represent them in a square mesh such as in FDTD simulations. In the elliptical patches case, its representation would certainly not be exact because a square mesh is used to represent the curvature of these patches. However, by using a fine mesh and high ratio of minor and major axes (a'/b'), these circular shapes can be reasonably represented. In the slotted patch case, the presence of straight elements could decrease the simulation accuracy in the case when these are not parallel to the square mesh used in the simulations. Consequently, there is not a clear favourite between these two geometries after a first round of choices. However, when looking again at figure 4.1, the slotted configuration is superior to the elliptical configuration only in one parameter and by one level, whereas the elliptical configuration is superior in two parameters by two levels in each case. Therefore, the elliptical patch configuration is finally chosen for this metasurface antenna.

Unit cell permittivity and size

The physical parameters common to all the unit cells in the metasurface antenna are the relative permittivity (ϵ_r), thickness (h), and length and width, which are assumed to be equal (d). The relative permittivity is chosen based on the value presented in [32], which is $\epsilon_r = 9.8$. In contrast with [35], the value from [32] is based on the material Arlon AR-1000 accredited for space flight [36].

The thickness and length of the unit cell are chosen so that only the fundamental mode propagates in the periodic unit cell array. Even though the obtained reactance can contain the contribution of higher order modes and still be correct because full-wave simulations are performed, it has been chosen to avoid this because it would not be possible to isolate the value of the transparent reactance, which is needed for the antenna synthesis process and for verification purposes. The method used to make sure that only the fundamental mode propagates in the periodic unit cell array is based on a MoM impedance representation and is summarized in appendix C [32]. From the chosen value of the relative permittivity and using equations (C.9) and (C.10), $h/d > 0.123$ and $\lambda/d > 7.65$.

Some examples of unit cell initial properties have been retrieved from the available literature in table 4.1. The first important aspect is that all of them have the same value of ϵ_r , which makes the analysis easier. Next, the ratio h/d is much bigger than the minimum required value of 0.123. Having a higher thickness than the minimum required increases the range of values that the short circuit reactance spans as shown in equation (3.116), but at the expense of having a heavier antenna. Finally, the

Table 4.1: Literature examples of unit cell physical properties compared with chosen design (grey).

	Minatti et.al. 2012 [36]	Mencagli et.al. 2015 [32]	Martini et.al. 2020 [26]	Current design
ϵ_r [-]	9.8	9.8	9.8	9.8
d [mm]	4	3	1.25	10
h [mm]	1.575	1	0.508	4
λ [mm]	34.86	27.25	11.53	93.69
f [GHz]	8.6	11	26	3.2
Type	Coffee bean	Elliptical	Elliptical	Elliptical
λ/d [-]	8.715	9.083	9.224	9.369
h/d [-]	0.39	0.33	0.4064	0.4

λ/d value is much closer to the minimum of 7.65 in the three cases because, close to that boundary, is the point where the patch anisotropy plays a bigger role in the surface wave propagation without the contribution of the band-gap or higher order modes excitation [28, p. 11]. Being further to the minimum value of λ/d means that a smaller patch with respect to the wavelength is used, locating the unit cells in the low-frequency band where the anisotropic effects are negligible, as explained in section 3.2.3.

For the case of the current metasurface antenna design, $f = 3.2$ GHz and $\lambda = 93.69$ mm. To simplify the units, integer number in the order of millimetres have been chosen due to the longer wavelength, in contrast with the examples in table 4.1. In order to have comparable units to the examples cited in table 4.1 and keeping in the boundaries of h/d and λ/d , the values chosen for d and h are 10 mm and 4 mm respectively, yielding $\lambda/d = 9.369$ and $h/d = 0.4$. These are compared with the literature values in table 4.1.

Varying patch parameters

The parameters that define the elliptical patch configuration in the unit cell are defined in figure 4.2, where a' and b' are the major and minor axes respectively, δ is the angle of the major axis with respect to the x -axis, and ψ is the difference between the surface wave propagation angle α_{sw} and δ .

As it was explained in section 3.2.4, a cylindrical wave is excited on a metasurface antenna, which will be incident to all the unit cells in every angle making $\alpha_{sw} \in [0, 2\pi]$. Subsequently, the reactance response to different values of α_{sw} can be analytically obtained as it was shown in equation (3.118) with rotation matrices. Therefore, the only parameters of the unit cell that are needed to be varied in this configuration are a' , b' and δ , as the reactance response of α_{sw} can be analytically obtained. To simplify the units of a' and b' , a' can be defined as the ratio a'/d and b' as $\eta = b'/a'$. Due to the definition of minor and major axes and to the symmetry of an elliptical patch, $\eta \in (0, 1]$ and $\delta \in [0, \pi]$, but the domain of a'/d cannot be defined so easily. The patch area cannot go beyond the boundaries of the unit cell because then, due to the periodic boundary conditions, the part of the ellipse that exceeds the boundaries would be placed contiguous to the complementary boundary, which makes the patch non-symmetric. Furthermore, the patch cannot touch other adjacent patch because then they would be short circuited, which in terms of reactance represents an abrupt change between contiguous unit cells. For the case in which the patches are either oriented horizontally or vertically, axiom 4.1 can be adopted as the lower boundary of the maximum value that a'/d can take. On the contrary, a'/d can be greater if δ and η are varied, reaching the maximum value of $a'/d(\eta \rightarrow 0^+, \delta = \pi/4) = (\sqrt{2})^-$. These are theoretical values that have the limitation of being subjected to an FDTD simulation, but it is important to recall the dependency of the domain of a'/d on δ and η .

Axiom 4.1 For elliptical patches, the following condition applies:

$$\frac{a'}{d} < 1 \quad \forall \left(\delta = \frac{m\pi}{2} \quad \forall m \in \mathbb{Z} \right)$$

4.1.2. Scattering method

The method adopted to obtain the impedance database is based on the work of Patel and Grbic [42], which has been generalized for an anisotropic unit cell with two symmetry axes. In this subsection

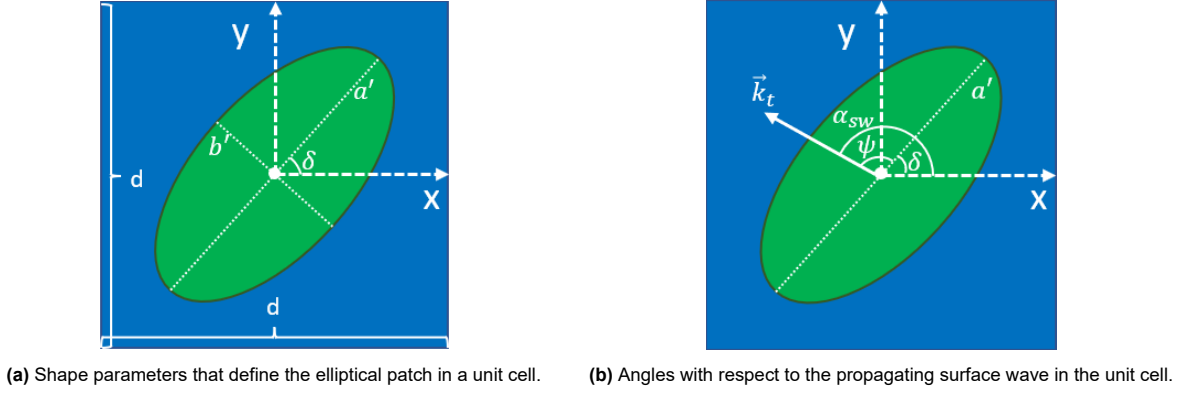


Figure 4.2: Elliptical patch configuration for the unit cell.

the derived method to construct the impedance database is explained, the verification methods and outcomes are presented, and its results for the antenna design introduced in section 2.2.2 are shown.

Method description

This method consists on using scattering simulations of a plane wave normally incident to a periodic array of particular unit cell configurations to obtain the electric field's phase shift, intensity and polarization given in the far-field, which can be used to obtain the input impedance as described by Patel et.al. [42, p. 2091], which is equivalent to the concept of opaque impedance treated in section 3.2.3. As explained in section 4.1.1, there are three shape parameters (η , a'/d and δ) that define the reactance response of a unit cell, which means that a full database must have every possible combination of these parameters. However, to simplify the analysis, the full-domain of a'/d was not included and it was considered only up to 1 to avoid unrealistic patch shapes.

The main idea behind this method is to analyse the unit cell response to an incident plane wave with the same method as the one used to derive the scattering matrix ($\underline{\mathbf{S}}$) of a two-port network, where the two ports represent the two different types of polarized surface waves that the metasurface supports (TM and TE). However, a unit cell array with a ground plane as this type of metasurface does not strictly have a transmission mode to support the S_{12} or S_{21} parameters. Therefore, to avoid any confusion, the scattering matrix is renamed as reflection matrix ($\underline{\mathbf{\Gamma}}$) where the Γ_{11} and Γ_{22} are the reflection coefficients of the TM and TE polarized injected waves respectively, and Γ_{12} and Γ_{21} are the reflection coefficients of the incident TM wave that is reflected as TE and the incident TE wave reflected as TM respectively. It is important to note that this renaming is figurative and used only to avoid confusions because all the concepts of the scattering matrix defined in section 3.1.2 can still be applied to this model. As the metasurface does not have any active elements and higher order modes are avoided, it is modelled with lossless materials, and the network can be considered reciprocal and lossless which makes $\underline{\mathbf{\Gamma}}$ symmetric and unitary.

As it was explained in section 3.2.3, the dyadic model of the reactance assumes that in the TM mode the electric field is aligned with the direction of propagation ($\hat{\mathbf{k}}_t$), whereas in the TE it is perpendicular but still tangent to the surface ($\hat{\mathbf{k}}_t^\perp = \hat{\mathbf{k}}_t \times \hat{\mathbf{z}}$) [28, p. 7]. This definition of polarization can be applied to the scattering model by performing two simulations for each shape configuration. The first one defines the propagation direction $\hat{\mathbf{k}}_t$ parallel to the electric field direction of the injected plane wave (TM mode), whereas the second one is injected with the electric field aligned with $\hat{\mathbf{k}}_t^\perp$ (TE mode). It is important to note that the direction of the TM mode is defined arbitrarily in the simulations, but it is translated to the reactance database by defining α_{sw} as the angle between $\hat{\mathbf{k}}_t$ and the x -axis. Furthermore, rotation matrices can be applied to change the surface wave angle of incidence to the one that will be evaluated.

One important detail that must not be ignored is that the plane wave is injected at broadside direction, meaning that there is no transverse wavevector propagating on the metasurface plane. The simulation then assumes $|\mathbf{k}_t| = k_\rho = 0$, but the unit vector $\hat{\mathbf{k}}_t$ exists because it is defined with the electric field polarization. The assumption of making $k_\rho = 0$ is used because it has been noted in some publications that the spatial dispersion from the patch cladding is negligible in low frequencies and in the transition region when compared to the one of the dielectric slab, which can be expressed analytically as in equations (3.115) and (3.116) [12, 33].

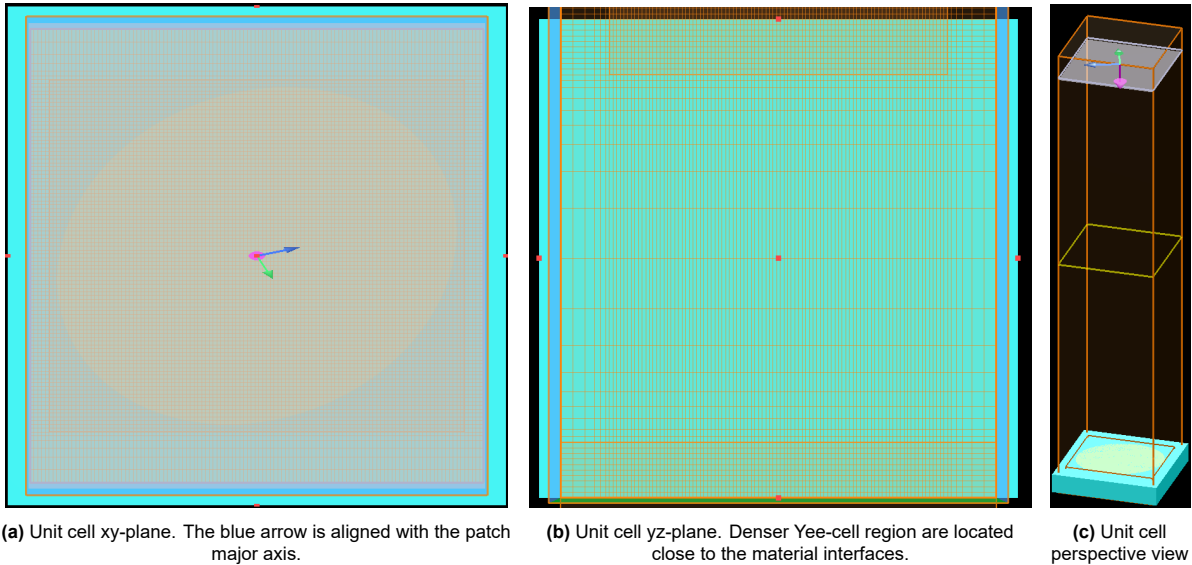


Figure 4.3: Mesh (orange squares) in the unit cell planes for $\eta = 0.8$, $a'/d = 0.9$ and $\delta = 20^\circ$. The green arrow represents the magnetic field, the blue arrow the electric field and the purple the propagation direction. The lightblue region indicates the dielectric substrate slab, the green ellipse the patch and the dark region free-space. The thick orange lines represent the simulation region, the darker blue lines the periodic boundary conditions, the yellow lines the monitor where the data is recorded, and the transparent grey area the plane where the plane wave is injected.

For a particular patch shape, the transparent reactance can be retrieved as follows:

1. **Create the simulation environment:** The program used is Lumerical FDTD, where a plane wave is injected at broadside direction from the unit cell. Periodic boundary conditions in the x - and y -directions are used to simulate an infinite array, which is analogous to the use of the Floquet theorem described in section 3.1.4. In the negative z -direction, a PEC layer is placed in the boundary underneath the lossless dielectric substrate to simulate the ground plane and, in the positive direction, a PML boundary is used to absorb the incident radiation. Subsequently, the measurements are taken between the injected plane wave and the metasurface interface with free-space, at a distance of $z = \lambda/2$ considering $z = 0$ as the interface of the patch cladding with free-space, as it was shown in figure 3.9b. This distance is chosen because the evanescent modes should decay before reaching the measurement monitor so that the far-field projection considers only visible modes. Subsequently, it was chosen to align the polarization of the TM mode with the ellipse major axis because then $\hat{\mathbf{k}}_t$ will be aligned to one of the eigenvectors, which decouples the system in only two transparent reactance terms (X_{1s} and X_{2s}) as it was shown in section 3.2.3. Finally, the mesh is discretized in cubic cells on an FDTD simulation as it was explained in section 3.3.2. In order to represent with greater accuracy the dynamics of the electromagnetic phenomena concerning irregularities that interfere with the propagating waves, a finer mesh is used in the interface between two materials with different electrical properties such as PEC, dielectric and free-space layers as it is shown in figure 4.3 where these are represented with orange lines that are denser close to these regions. Particularly, in figure 4.3b it is shown in the interface of the dielectric with the ground plane (bottom) and with free-space (top).

The patch interface with the dielectric substrate at $z = 0$ has a particular importance because the currents at the ellipse edges exhibit a singularity when they are approximated with Rao-Wilton-Gilsson (RWG) functions [32], which occurs due to stronger field variations than in other simulation regions. Therefore, it would be advantageous in terms of simulation time and precision to use a finer mesh on the area occupied by the patch and in its vicinity than in other parts of the unit cell. This is particularly important for patches with relatively low η value and with δ close to 0° , 90° and 180° , because they occupy a relatively small square area in the unit cell which can be further refined by making coarser its surroundings. Furthermore, as a large number of simulations are made, it would be advantageous to have them last a similar time and consume similar computer resources. These issues made imperative the need of an adaptive algorithm that would keep

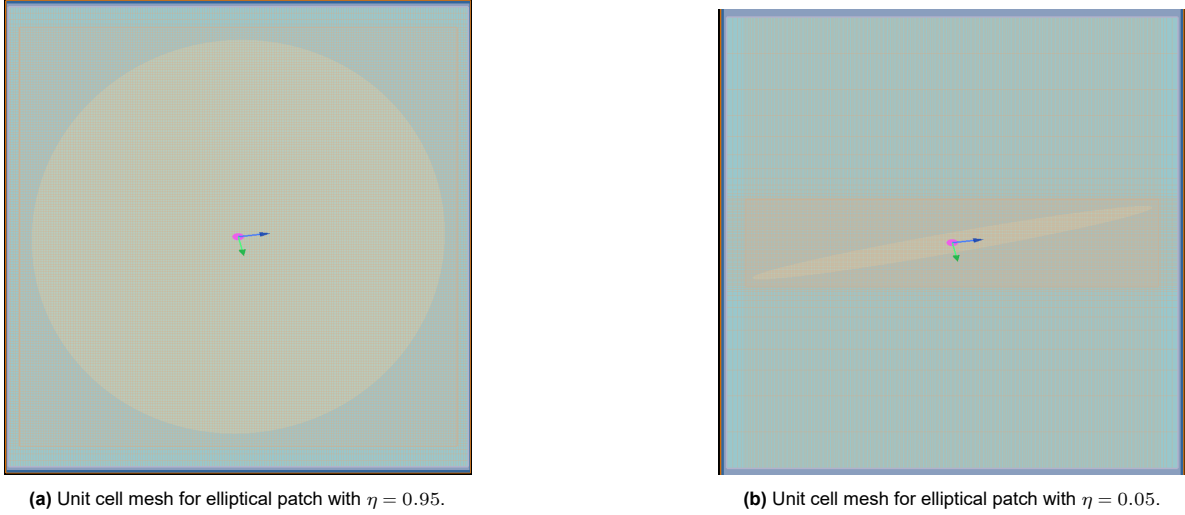


Figure 4.4: Unit cell mesh after implementing the adaptive mesh refinement for two different η values, $\delta = 10^\circ$ and $a/d = 0.9$. Thick orange lines surround the region where the mesh is refined.

constant the number of Yee cells that surround the patch when the shape parameters are changed, so that smaller Yee cells are used when the patch has a highly elongated shape extending through the x- and y-axes, and a coarser mesh is used when the patch occupies a higher square area. The author notes that this would result in a coarser mesh for patches with low values of η which are oriented close to diagonal angles.

Consider Δx_0 and Δy_0 the reference mesh size in x- and y-directions, corresponding to an initial refinement of an arbitrary patch shape. Following, the meshed patch circumference has maximum values in the x- and y-planes denoted as x_{max} and y_{max} respectively. Furthermore, a number of Yee cell layers N_Y are added to the area with finer mesh to account for the interface between the patch and the surrounding dielectric. Equation (4.1) sets equal the number of Yee cells in both cases, the reference mesh and the desired mesh for a particular patch shape, and can be solved for Δx and Δy considering that $\Delta x = \Delta y$ as shown in equation (4.2). An example of the modelling with this adaptive mesh is shown in figure 4.4, where figure 4.4a shows the mesh refinement for a patch with $\eta = 0.95$ and figure 4.4b shows this for $\eta = 0.05$.

$$\frac{d^2}{\Delta x_0 \cdot \Delta y_0} = \frac{4x_{max}y_{max}}{\Delta x \Delta y} + 2 \frac{N_Y \cdot \Delta x \cdot 2 \cdot y_{max}}{\Delta x \Delta y} + 2 \frac{N_Y \cdot \Delta y \cdot 2 \cdot x_{max}}{\Delta x \Delta y} \quad (4.1)$$

$$(\Delta x, \Delta y) = 2 \frac{\Delta x_0 \Delta y_0}{d^2} \left[N_Y (x_{max} + y_{max}) + \sqrt{N_Y^2 (x_{max} + y_{max})^2 + \frac{d^2}{\Delta x_0 \Delta y_0} x_{max} y_{max}} \right] \quad (4.2)$$

2. **Obtain the electric field:** The electric field components are obtained using a normalized far-field projection of the incident and scattered waves. In the simulations, the incident wave is injected in negative z-direction and the scattered field is reflected in positive z-direction. This is not aligned with the definition of incident and reflected fields, which should be in positive and negative directions respectively. Therefore, the complex conjugate has to be taken from the obtained far-field projections. Furthermore, these projections are aligned with the Cartesian coordinate system, but they are injected with polarization angles δ that are aligned with the ellipse major and minor axes. Thus, a rotation matrix has to be applied in the z-axis to the resulting fields to define them in a δ -rotated coordinate system, defined by x' , y' and z' such that the x' - and the y' -axes are aligned with the TM and TE modes respectively. Figure 4.5 shows a schematic of the simulation set-up with the rotated reference frame where the sub-indices \bar{i} and \bar{s} are the incident and reflected fields respectively. Moreover, as the incident field is propagating in negative direction, the correction is performed by rotating the result by δ , whereas for the reflected field is corrected by rotating by $-\delta$ as shown in equation (4.3).

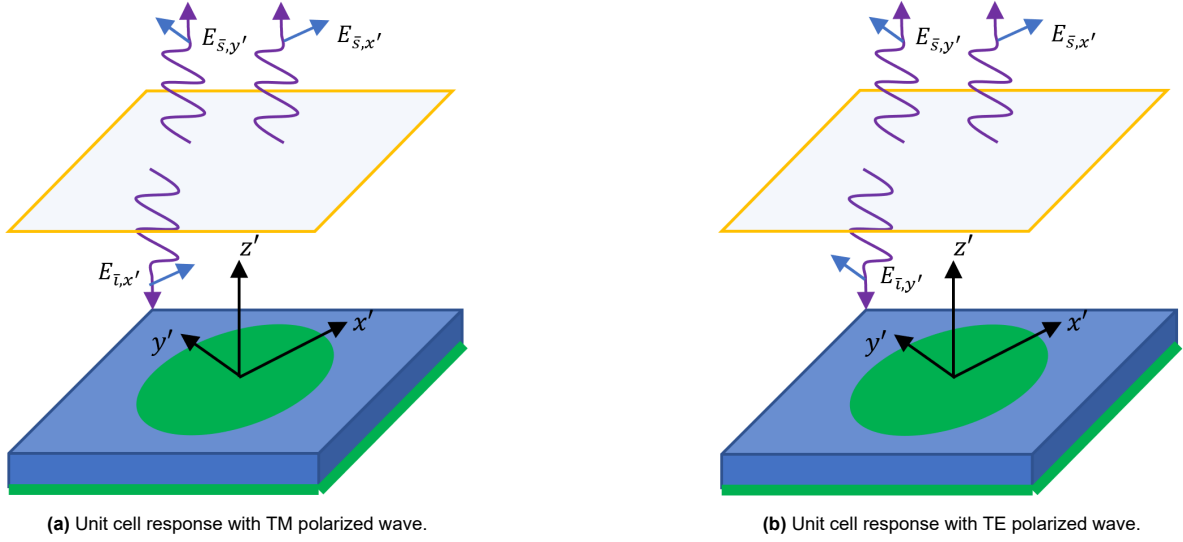


Figure 4.5: Incident and reflected TM and TE plane waves in the rotated unit cell reference system.

$$\mathbf{E}_{\bar{i},x'} = \underline{\underline{\mathbf{R}}}(\delta) \cdot \mathbf{E}_{\bar{i}} \quad (4.3a)$$

$$\mathbf{E}_{\bar{s},y'} = \underline{\underline{\mathbf{R}}}(-\delta) \cdot \mathbf{E}_{\bar{s}} \quad (4.3b)$$

3. **Obtain the reflection matrix:** The reflection matrix $\underline{\underline{\Gamma}}$ can be obtained with the ratio of the scattered and the incident electric field far-field projections as shown in equation (4.4). As it was explained in the previous step, the complex conjugate is obtained to represent an incident and scattered wave propagating in positive and negative directions respectively. Furthermore, the cross-diagonal components are multiplied by $e^{j\pi} = -1$ because the incident field is projected in the negative direction, whereas the scattered in positive direction. Therefore, these two fields have to be placed in a common coordinate system, which is done by applying a phasing term of π to one of these terms. As it was shown in equation (3.49), in a reciprocal network $\Gamma_{12} = \Gamma_{21}$. However, it is important to note that these two values come from two different simulations subjected to different numerical errors. Therefore, even though they should be equal it is expected that they would be slightly different from each other.

$$\Gamma_{11} = \left(\frac{E_{\bar{s},x'}}{E_{\bar{i},x'}} \right)_{TM}^* \quad (4.4a)$$

$$\Gamma_{22} = \left(\frac{E_{\bar{s},y'}}{E_{\bar{i},y'}} \right)_{TE}^* \quad (4.4b)$$

$$\Gamma_{21} = - \left(\frac{E_{\bar{s},y'}}{E_{\bar{i},x'}} \right)_{TM}^* \quad (4.4c)$$

$$\Gamma_{12} = - \left(\frac{E_{\bar{s},x'}}{E_{\bar{i},y'}} \right)_{TE}^* \quad (4.4d)$$

4. **Obtain the impedance matrix:** The impedance matrix $\underline{\underline{\mathbf{Z}}}$ can be obtained with equation (3.50) where Z_0 represents the impedance of free-space ζ , and the reflection matrix is used in place of the scattering matrix. As the unit cell infinite array can be considered as a reciprocal lossless network, it is expected that the resulting matrix $\underline{\underline{\mathbf{Z}}}$ would be purely imaginary and symmetric. Furthermore, the result is a 2×2 dyad which diagonal elements are aligned with $\hat{\mathbf{k}}_t$ and $\hat{\mathbf{k}}_t^\perp$ respectively.
5. **Obtain the opaque reactance matrix:** The opaque reactance matrix can be obtained directly by taking the imaginary values from $\underline{\underline{\mathbf{Z}}}$, such that $\underline{\underline{\mathbf{X}}} = j\underline{\underline{\mathbf{Z}}}$. As it was mentioned in the method's general description, the simulations are made such that the magnitude of the transverse wavenumber is zero. Therefore, the obtained opaque reactance is a function of the polarization direction given by $\hat{\mathbf{k}}$, the transverse wavenumber $k_\rho = 0$, and the radial frequency ω of the free-space plane wave.
6. **Obtain the transparent reactance matrix:** The transparent reactance matrix $\underline{\underline{\mathbf{X}}}_s$ can be obtained by solving equation (4.5) where $\underline{\underline{\mathbf{X}}}_{cc}$ is the short circuit reactance given by equations (3.115) and (3.116) for $k_\rho = 0$. Finally, given the fact that the transparent reactance spatial dispersion is small compared to the short circuit one [12, 33], axiom 4.2 can be formulated, which results in

the transparent reactance for a particular patch configuration.

$$\underline{\underline{\mathbf{X}}}_s(\omega, \hat{\mathbf{k}}_t, k_\rho = 0) = \left[\underline{\underline{\mathbf{X}}}^{-1}(\omega, \hat{\mathbf{k}}_t, k_\rho = 0) - \underline{\underline{\mathbf{X}}}_{cc}^{-1}(\omega, \hat{\mathbf{k}}_t, k_\rho = 0) \right]^{-1} \quad (4.5)$$

Axiom 4.2 *The transparent reactance spatial dispersion can be assumed negligible within the low frequency and transition bands.*

$$\underline{\underline{\mathbf{X}}}_s(\omega, \hat{\mathbf{k}}_t, k_\rho = 0) \approx \underline{\underline{\mathbf{X}}}_s(\omega, \mathbf{k}_t)$$

7. **Iterate for different patch configurations:** The same procedure described above is done for different patch configurations, such as different δ angle with respect to the unit cell, different major axis ratio to the unit cell size a'/d and different minor axis ratio to the major axis η . The author notes that it results easier to perform all simulations in one batch job in a high-performance computer cluster, and then analyse separately the data in multidimensional matrices with iterative loops.

Verification

The presented procedure has been verified mainly by using the unit cell design described in the research paper of Mencagli, Martini and Maci [32] specified in table 4.1 ($\epsilon_r = 9.8$, $d = 3$ mm, $h = 1$ mm, $a'/d = 0.9$ and $f = 11$ GHz), and comparing the obtained reactance with the results of the authors. To this end, 1,406 simulations have been performed by using 2 injected waves orthogonal polarizations, 19 different η values (from 0.05 to 0.95 in steps of 0.05), and 37 different angles (from 0° to 180° in steps of 5°). Other intermediate steps for verification have been done, which will be described next.

The first step was to verify that the simulation set-up was representing accurately the reactance values (step 1). This was done by simulating the shape of $\eta = 0.95$ at $\delta = \alpha_{sw} = 0$, so the anisotropy of the metasurface is still being represented. It was then found that the parameters that influence the most the resulting reactance were the mesh size in all the three axes. The length of a Yee cell in z-direction (Δz_0) is given by the accuracy level in the simulation, which is a parameter defined automatically by the FDTD environment. It has a value from 1 to 8 being 1 the coarser mesh and 8 the finest mesh “ensuring that numerical dispersion is a negligible contribution to errors in virtually all situations”¹. On the other side, the length of the Yee cell in x - and y -directions (Δx_0 and Δy_0) has been changed manually because, as it directly affects the patch geometry, it has a greater influence on the final result than Δz . Furthermore, considering that the patch is being continuously rotated in different simulations, Δx_0 is kept equal to Δy_0 to keep the same influence under different angles. The resulting transparent TM reactance is shown in figure 4.6 for different values of mesh refinement as a ratio of the wavelength. From figure 4.6b it appears that $X_s^{(ee)}$ is close to converge when $\Delta z_0 \approx \lambda/35$, which is the maximum refinement level suggested by the FDTD software. Therefore, this value was used in the simulation for the Δx_0 and Δy_0 mesh components. Figure 4.6a shows the refinement for the components in the elliptical patch plane, which starts to converge at $\Delta(x_0, y_0) \approx \lambda/550$ and fully converges at $\Delta(x_0, y_0) \approx \lambda/1,300$. Even though the obtained values of Δx_0 , Δy_0 and Δz_0 are calculated for only one patch configuration, these are already a good starting point for the following simulations because they offer a realistic view of the required mesh for reasonable accurate results. The effect of using this shape for the mesh calibration will be assessed later in this same subsection. For the following steps, the accuracy of 8 for Δz is used and the accuracy of Δx_0 and Δy_0 will be specified.

The second step is verified, which consisted on obtaining the far-field projections of the electric fields and then rotate them by δ and $-\delta$ so that the resulting field is aligned with the patch eigenvector directed towards the major axis. A good method to verify that this step is done correctly is by obtaining the cross-polarized reflected field for any of the waves injected. If this result is not equal to zero, then the injected wave is not aligned with the eigenvector or numerical errors are affecting the outcome. Figure 4.7a shows $|E_{s,y'}|_{TM}$, which results exhibit a cross-polarized field being reflected from the unit cell infinite array at $\delta \neq \frac{\pi p}{4} \quad \forall p \in \mathbb{Z}$. To discard numerical errors, the same combination of different patch shapes and angles was simulated but with a finer mesh ($\Delta x_0 = \Delta y_0 = \lambda/1,300$). The results of $|E_{s,y'}|_{TM}$ are shown in figure 4.7b, which exhibit a decrease in magnitude of this parameter. However, this is not proportional to the imposed mesh refinement, which suggests that the major axes of the patches are

¹Understanding the non-uniform mesh in FDTD - Ansys optics. <https://optics.ansys.com/hc/en-us/articles/360034382634-Understanding-the-non-uniform-mesh-in-FDTD> Retrieved on 06-10-2022.

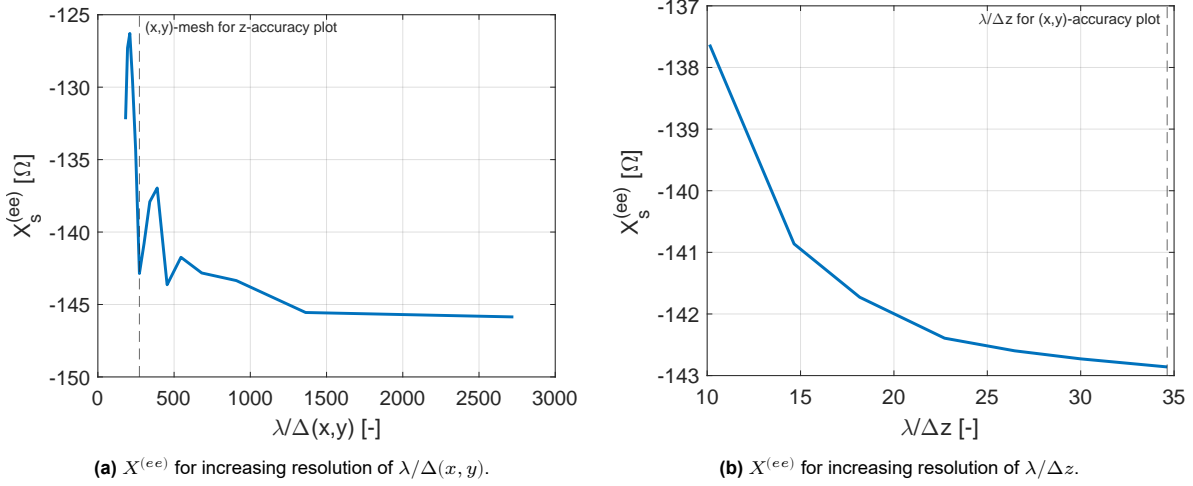


Figure 4.6: Mesh size refinement for $a'/d = 0.9$, $\eta = 0.95$, $\alpha_{sw} = \delta = 0^\circ$, $\epsilon_r = 9.8$, $d = 3$ mm, $h = 1$ mm, and $f = 11$ GHz.

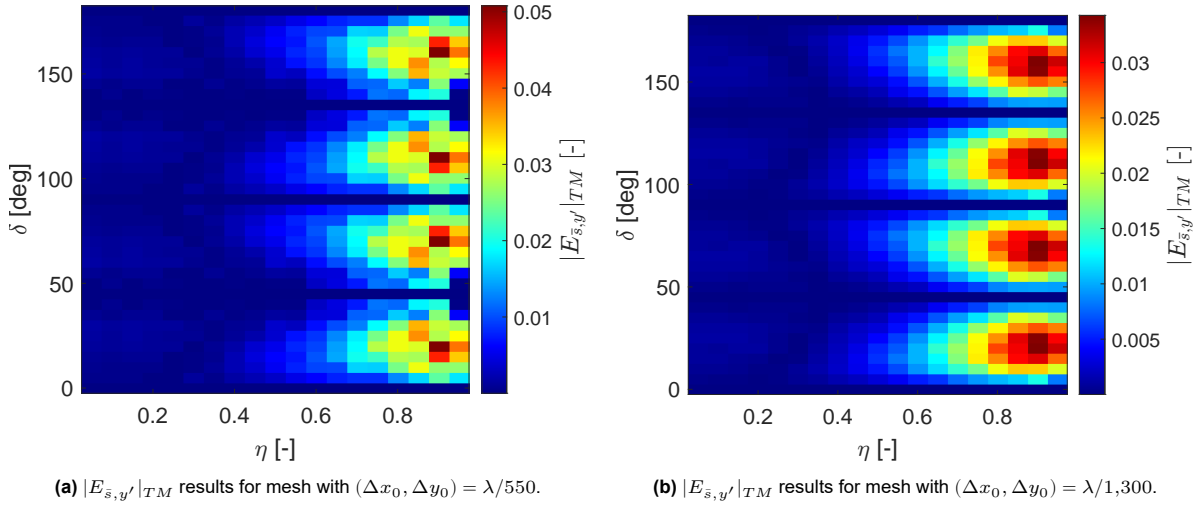


Figure 4.7: Reflected far-field projection of cross-polarized electric field component for different mesh refinements.

actually not aligned with the eigenvectors. Even though the magnitudes suggest a small degree of cross polarization (2% at most), these appear in regular periods for δ and they are maximum when η is close to the unity. One possible cause of this misalignment is the unit cell square lattice. It was reported in [32] that the square lattice clearly affects the surface wave wavenumber in the dynamic band. Therefore, it is possible that its influence is visible in the transition band too, specially in smaller quantities. Figures 4.8a and 4.8b show the case where the wavevectors are aligned with the symmetry axes of the square lattice and of the patch at $\delta = 0^\circ$ and $\delta = 45^\circ$ respectively. In both cases, the wavefront perceives a clear period on the infinite unit cell array in both its propagation and perpendicular direction. However, in figures 4.8c and 4.8d this is not the case, where the wavefront perceives an asymmetry due to the misalignment of the patch and the square lattice, which could cause the appearance of a cross-polarized reflected component as it was seen in figure 4.6.

The third step, which consists on obtaining the reflection matrix, can be verified by looking to its properties in a reciprocal and lossless network. The reciprocal network condition given in equation (3.49), which can be summarized to $\Gamma_{12} = \Gamma_{21}$, is plotted in figure 4.9a for all the analysed unit cell configurations. It is worth noting that Γ_{12} and Γ_{21} were calculated in different simulations, each of them subjected to the same degree of numerical errors. Therefore, when both elements are subtracted, it is expected that the outcome would be subjected to the same degree of numerical error. These are show in relative terms in figure 4.9b suggesting that, even though there are numerical errors in the simulation making the network not perfectly reciprocal, these represent at most 5% of the cross-polarized reflection coef-

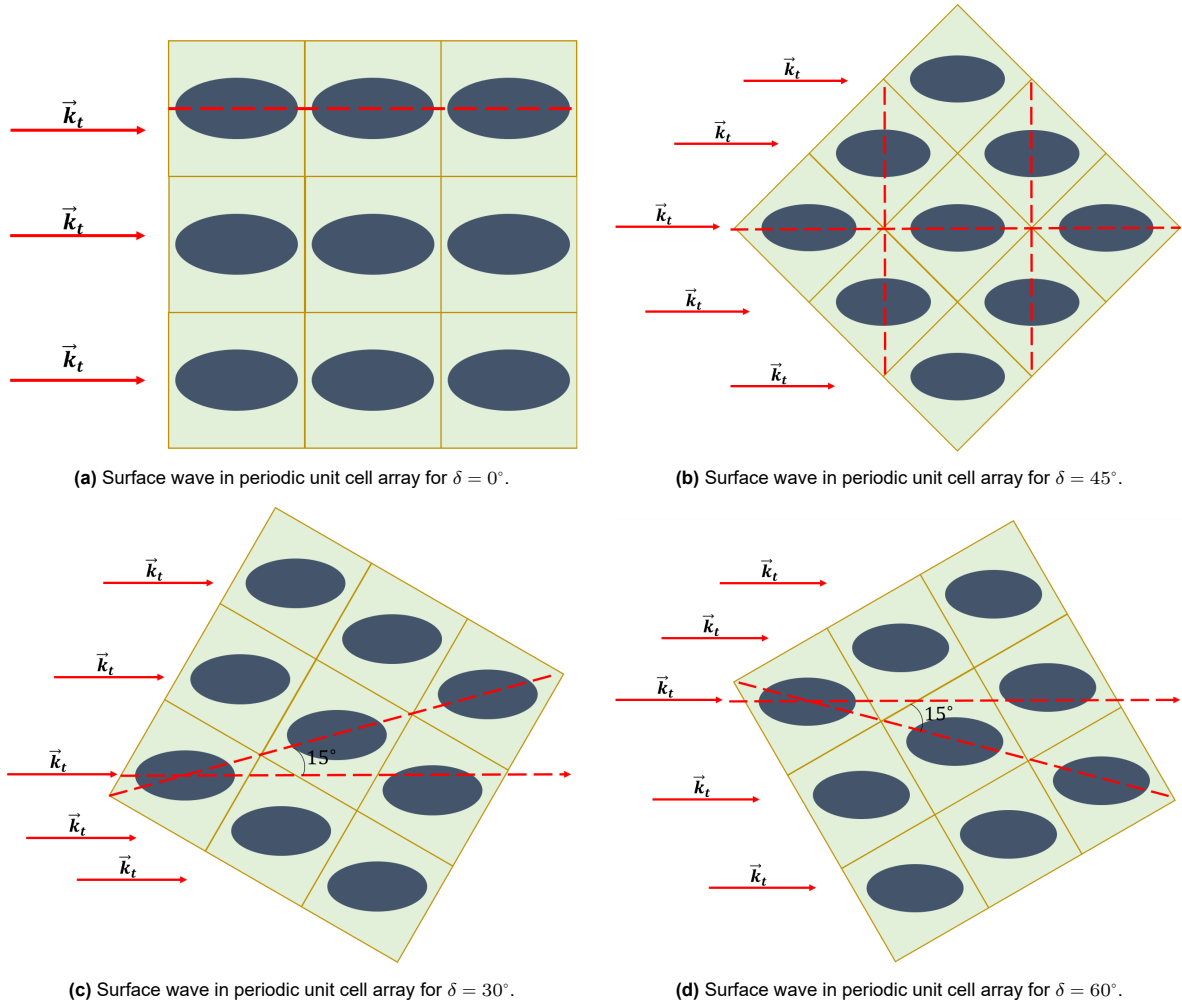


Figure 4.8: Incident surface wave for different δ patch orientations. The smaller angle between the symmetric axis of the square lattice and the patch is shown when this is different than zero.

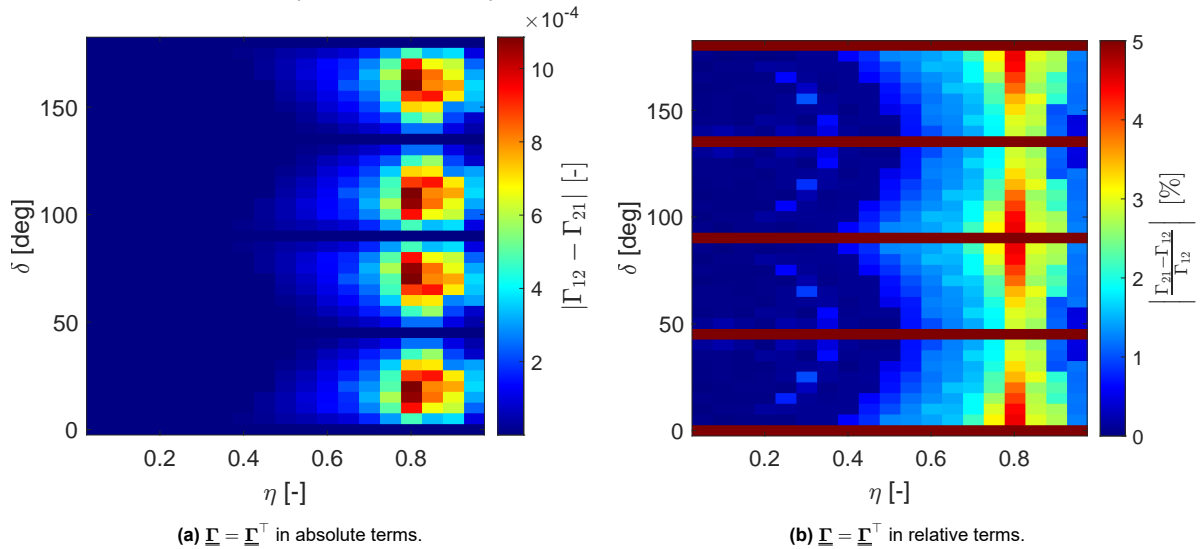


Figure 4.9: Evaluation of the reciprocal network condition ($\Gamma_{12} - \Gamma_{21} = 0$) for $(\Delta x_0, \Delta y_0) = \lambda/1,300$. Thick red lines in figure 4.9b represent δ -values at which the cross-polarization is close to zero.

ficient, which was regarded as an acceptable error to continue with the design. This further confirms that there is cross-polarization when the wave is injected with its electric field parallel to the major and minor axes of the unit cell because both Γ_{12} and Γ_{21} values are consistent with each other.

The condition for a lossless network given in equation (3.57) ($\underline{\Gamma}^\top \cdot \underline{\Gamma}^* = \underline{\mathbf{U}}$) can be verified by subtracting the right side to the left side of equation (3.57) to see how close they are from zero. By expressing the results in terms of the components of $\underline{\Gamma}$, equation (4.6) is obtained and plotted in equation (4.6) where the component 2,1 is not plotted due to redundancy with component 1,2 because they are the complex conjugate of each other. The fact that figures 4.10a and 4.10b are much smaller than figure 4.10c is evident when equation (4.7) is analysed, which expresses each component of equation (4.6) in terms of the simulation output. Equations (4.7a) and (4.7b) are obtained from just one simulation each (either TM or TE respectively), and as the far-field components are already normalized, the ratio between the scattered and incident fields is almost one. The difference, which is a term of nine orders of magnitude smaller than 1 in the worst cases, is caused by the reflection on the PML of the cross-polarized scattered term that is incident to the monitor in negative direction. On the other side, equation (4.7c) depends on both TM and TE simulations, which makes the error term closely proportional to the one of the far-field projections of each simulation, which was already discussed when figure 4.9 was examined.

$$\underline{\Gamma}^\top \cdot \underline{\Gamma}^* - \underline{\mathbf{U}} = \begin{bmatrix} |\Gamma_{11}|^2 + |\Gamma_{21}|^2 - 1 & \Gamma_{12}^* \Gamma_{11} + \Gamma_{21} \Gamma_{22}^* \\ \Gamma_{21}^* \Gamma_{22} + \Gamma_{12} \Gamma_{11}^* & |\Gamma_{22}|^2 + |\Gamma_{12}|^2 - 1 \end{bmatrix} = \underline{\mathbf{0}} \quad (4.6)$$

$$|\Gamma_{11}|^2 + |\Gamma_{21}|^2 = \left(\frac{|\mathbf{E}_{\bar{s},x'}|}{|E_{\bar{i},x'}|} \right)_{TM}^2 \quad (4.7a) \quad |\Gamma_{22}|^2 + |\Gamma_{12}|^2 = \left(\frac{|\mathbf{E}_{\bar{s},y'}|}{|E_{\bar{i},y'}|} \right)_{TE}^2 \quad (4.7b)$$

$$\Gamma_{12}^* \Gamma_{11} + \Gamma_{21} \Gamma_{22}^* = (\Gamma_{21}^* \Gamma_{22} + \Gamma_{12} \Gamma_{11}^*)^* = - \frac{(E_{\bar{s},x'})_{TM} (E_{\bar{s},x'})_{TE}^* + (E_{\bar{s},y'})_{TM} (E_{\bar{s},y'})_{TE}^*}{(E_{\bar{i},x'})_{TM} (E_{\bar{i},y'})_{TE}} \quad (4.7c)$$

To conclude the verification of the third step, the deviations from the lossless and reciprocal networks, even though they exist, they are comparatively small with respect to the ideal conditions and appear mostly due to numerical errors from the simulations. This has been shown in figures 4.9 and 4.10 where the difference with the ideal case is at most in the order of 10^{-3} .

The effects of these numerical errors can be easily evaluated with the impedance matrix, which is the fourth implementation step. This can be calculated directly by using equation (3.50) as it was explained when this step was described. The results for the example case are shown in figure 4.11 where the resistance matrices obtained from the simulations are illustrated for each patch configuration, which ideally should be zero because this is a lossless structure. These results, which are in line with the ones shown previously in figures 4.9 and 4.10, quantify the impact of the simulation errors in terms of losses that the infinite array would have. As in figures 4.7, 4.9 and 4.10, the biggest deviations are focused on shapes around $\eta \approx 0.8$ and at angles multiples of $\delta = 45^\circ$. This can be attributed to the fact the cross-polarization is maximum at those angles (figure 4.7), which increases the differences between Γ_{12} and Γ_{21} , and therefore affects the lossless and reciprocal network conditions.

In order to assess if the magnitude of the obtained resistance could have any important consequence in the rest of the model, figure 4.11 has to be compared against the reactance $\underline{\mathbf{X}}(\omega, \hat{\mathbf{k}}_t, k_\rho = 0)$ which is obtained from the fifth step of the derived method to obtain the transparent reactance database. This consists on obtaining the imaginary term from $\underline{\mathbf{Z}}$ and is plotted in figure 4.12. Apparently, the influence of the resistance in the impedance magnitude can be regarded as small, certainly in the terms Z_{11} and Z_{22} where is at least five orders of magnitude smaller. In the case of the cross-diagonal terms, the ratio of reactance against the impedance magnitude is shown in figure 4.13, where it is clear that this is at most 3% and therefore can be considered to be small. Given the fact that the obtained maximum values of R_{12} are five times greater than R_{21} , the ratio of this value against the impedance magnitude would be greater for the first case, as the reactance does not vary much between both cross-diagonal components, which is illustrated in figure 4.12d.

The sixth and last step consists on obtaining the transparent reactance $\underline{\mathbf{X}}_s(\omega, \mathbf{k}_t)$ from $\underline{\mathbf{X}}(\omega, \hat{\mathbf{k}}_t, k_\rho = 0)$, which spatial dispersion is assumed negligible in the transition band as it was stated in axiom 4.2. The reduced expression of the short circuit reactance for $k_\rho = 0$ is shown in equation (4.8), which has been derived from equation (3.116), and is used in equation (4.5) to accelerate calculations. The final transparent reactance database is shown in figure 4.14 where each of the transparent reactance

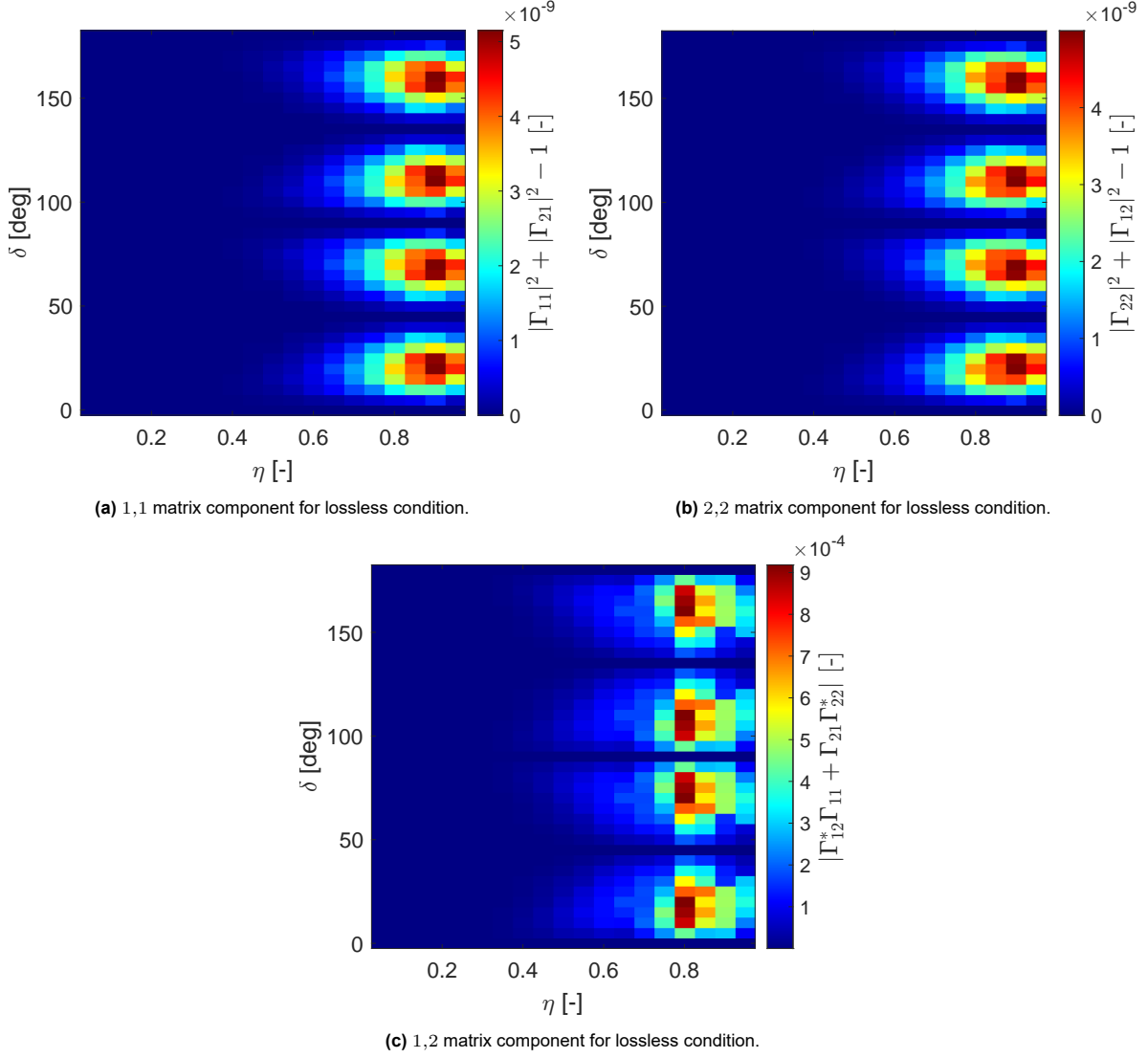


Figure 4.10: Conditions for lossless network obtained from equation (4.6) for $(\Delta x_0, \Delta y_0) = \lambda/1,300$.

components is shown, together with the relative error of the cross-diagonal components, which again does not go beyond 3.5%. One important remark, and consideration to further verify the results, is that in figure 4.14b appears to be a singularity at low values of η . It results particularly useful to analyse this with circuit theory. Consider figure 3.11 where the equivalent circuit model of the metasurface unit cell was presented. As the transparent reactance and the grounded slab are represented with a parallel circuit model, the fact that the first one has a singularity is equivalent to state that is an open circuit, which means that this term would be invisible for the impinging current. As this occurs for the TE case, where the electric field is oriented parallel to the patch minor axis, and it has been assumed in axiom 4.2 that the surface wave propagates in that direction, then this can be interpreted as the case in which a current is propagating perpendicular to metal cables separated by the unit cell size d . This is due to the fact that elliptical patches are becoming thinner, therefore the distance between them in the direction of their major axis decreases and the one in the direction of their minor axis increases. As a consequence, the surface wave tends to encounter an open circuit in the TE mode, which means that the only contribution to the opaque reactance would be the one of the short circuit reactance.

$$\underline{\mathbf{X}}_{cc}(\omega, \hat{\mathbf{k}}_t, k_\rho = 0) = \frac{\zeta}{\sqrt{\epsilon_r}} \tan(kh\sqrt{\epsilon_r}) (\hat{\mathbf{k}}_t \hat{\mathbf{k}}_t + \hat{\mathbf{k}}_t^\perp \hat{\mathbf{k}}_t^\perp) \quad (4.8)$$

As a further verification, the obtained results can be compared with the research article of Mencagli

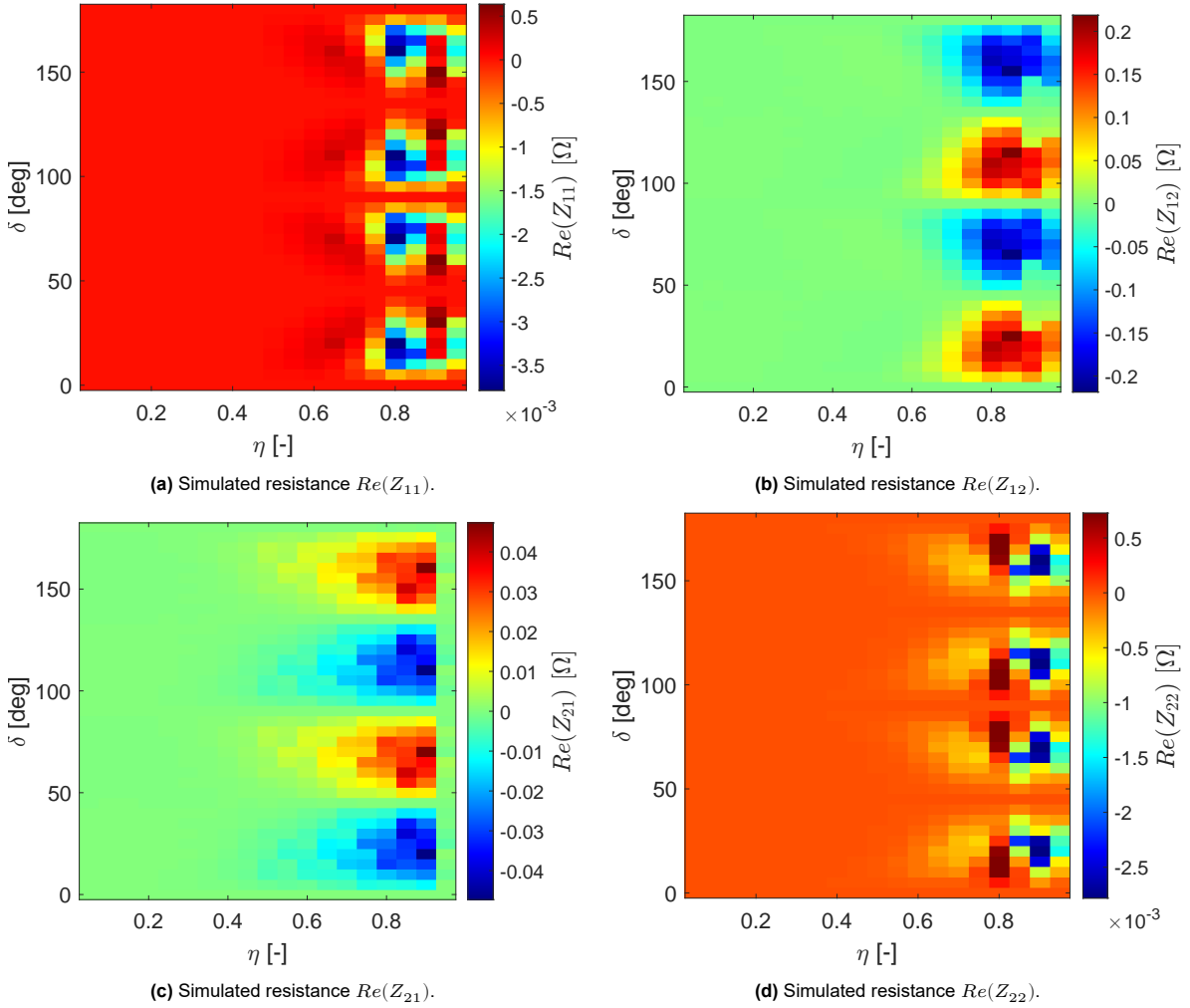


Figure 4.11: Obtained resistance matrix components $Re(\underline{\mathbf{Z}})$ (or $\underline{\mathbf{R}}$) after processing the reflection matrix $\underline{\mathbf{\Gamma}}$ for an incident surface wave with $k_{\rho} = 0$ and the simulation mesh $(\Delta x_0, \Delta y_0) = \lambda/1,300$.

et.al. [32], which initial unit cell parameters were obtained from. The first task was to reproduce the equivalent impenetrable metasurface reactance $X_{s,eq}$, which is equivalent to the reactance in the isotropic case represented by equation (3.107). This is shown in figure 4.15b for a surface wave angle of $\alpha_{sw} = 0$ and varying patch orientations δ , expressing this in terms of ψ . Therefore, the first step was to align the obtained results with this propagation angle by rotating the transparent reactance matrix by $-\delta$ degrees as it was explained in equation (3.118). Next, the surface wave wavenumber $k_{\rho sw}$ is obtained by solving the transverse resonant equation from equation (3.117) for a coupled system, since the cross-diagonal terms in $\underline{\mathbf{X}}_s$ do exist. Following, the equivalent impenetrable metasurface reactance $X_{s,eq}$ is calculated and linearly interpolated in figure 4.15a which visually resembles the one in figure 4.15b.

The next task consisted on verify the robustness of axiom 4.2 for broadband simulations. To this end, the simulations were performed for a broad range of frequencies keeping a similar amount of computation effort, which is an advantage of time-domain simulation methods presented in section 3.3 compared to frequency-domain methods. As it was mentioned before, it is expected that the approximations done with the derived model would work in the low frequency and transition bands. Figure 4.16 shows these results for the cases in which $\delta = 0^\circ$ and α_{sw} varies (figures 4.16a to 4.16c), and in which $\alpha_{sw} = 0$ and δ varies (figure 4.16d). It is important to note that figures 4.16a to 4.16c are the results of two simulations (TE and TM modes for a given shape and orientation), and for each plot the resulting transparent reactance value $\underline{\mathbf{X}}_s$ has been rotated according to the required α_{sw} using equation (3.118), from which the $k_{\rho sw}$ value was finally obtained by solving equation (3.117) and plotted for different

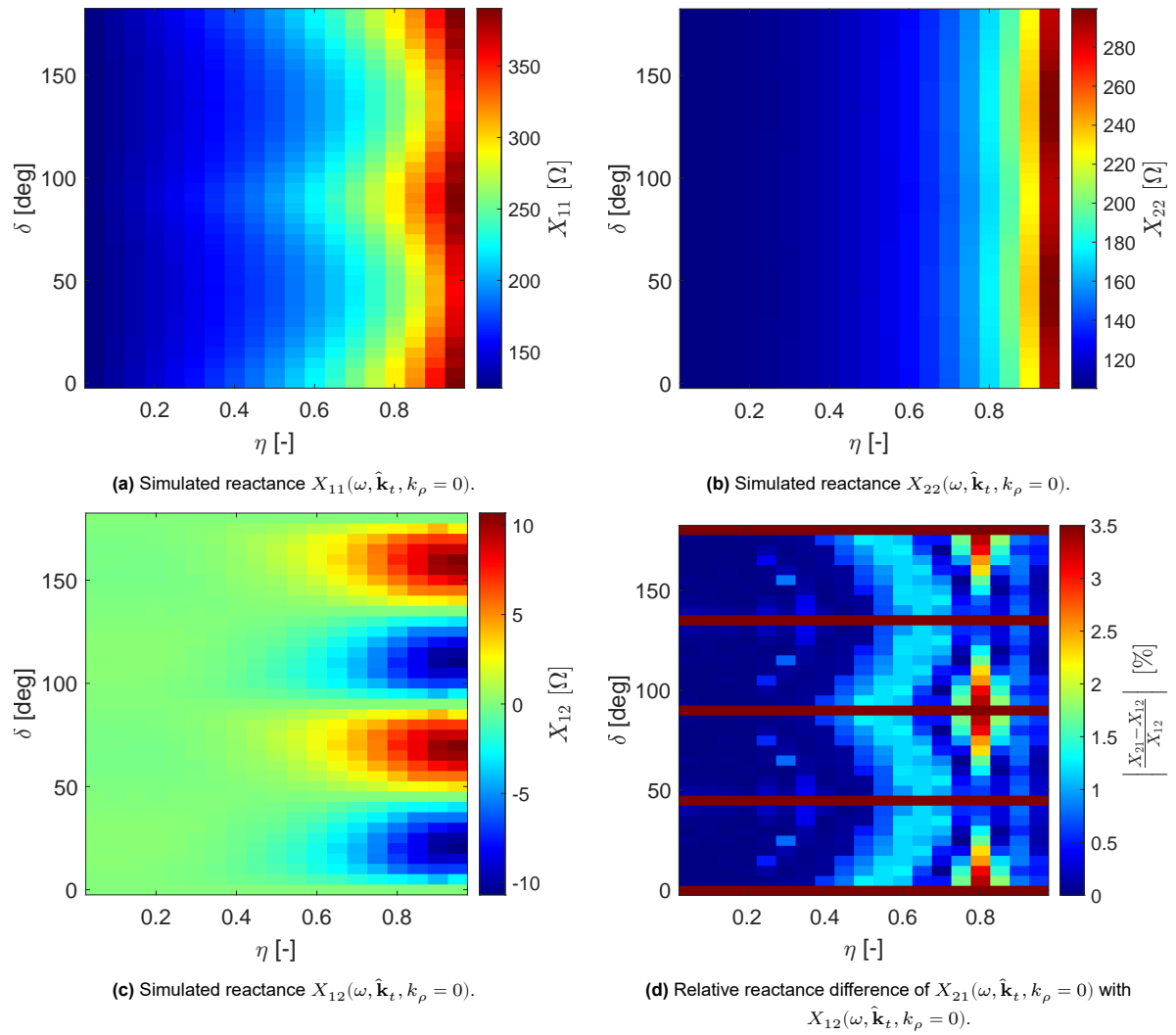


Figure 4.12: Opaque reactance matrix components considering $k_\rho = 0$ obtained from the simulation mesh $(\Delta x_0, \Delta y_0) = \lambda/1,300$.

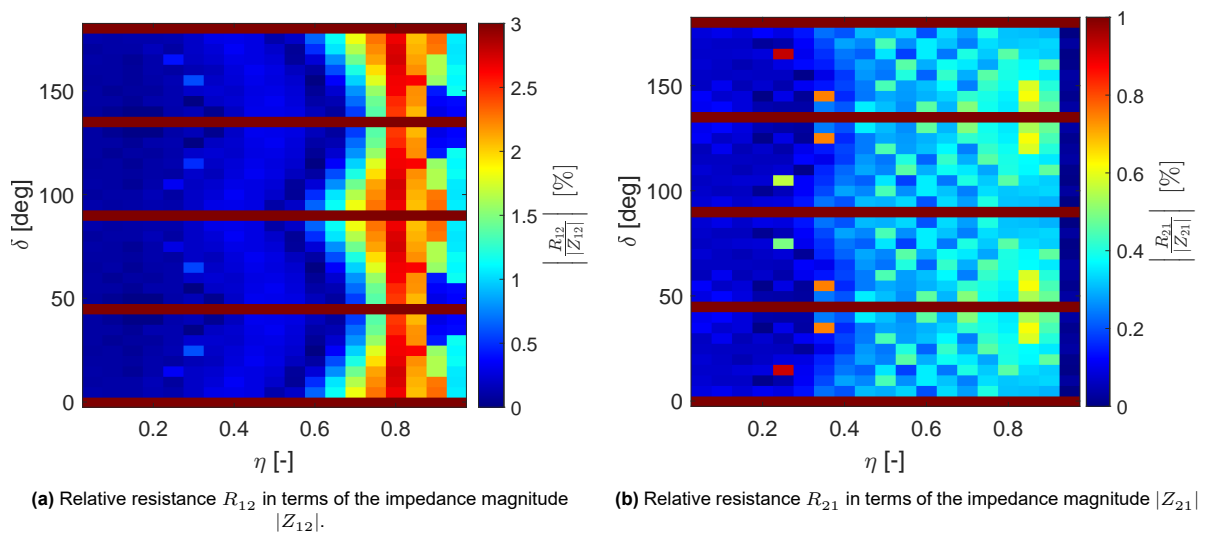


Figure 4.13: Cross-diagonal resistance evaluated in terms of the magnitude of the cross-diagonal impedance for the simulation mesh $(\Delta x_0, \Delta y_0) = \lambda/1,300$.

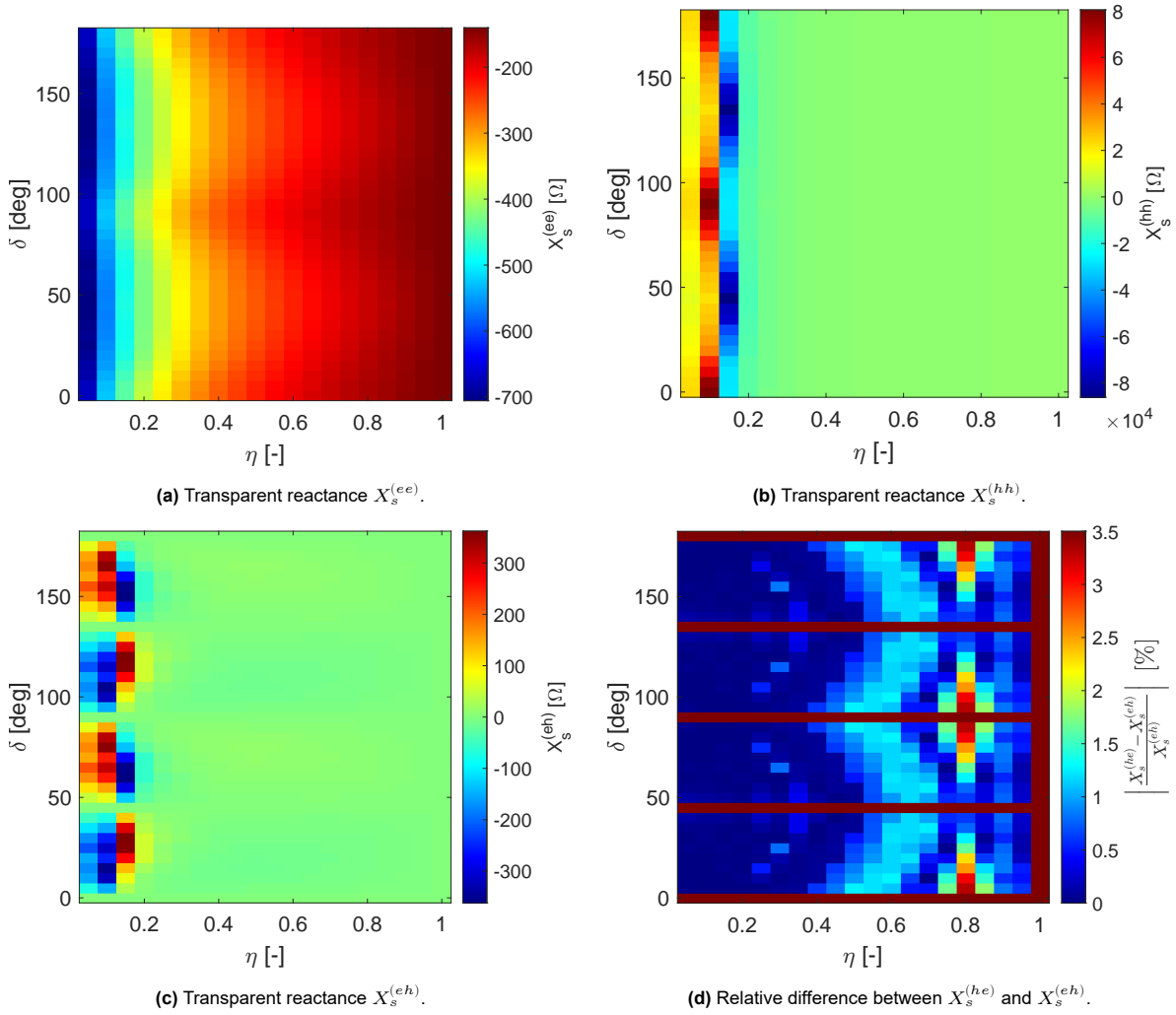


Figure 4.14: Obtained transparent reactance database $\underline{\mathbf{X}}_s$ from the simulation mesh $(\Delta x_0, \Delta y_0) = \lambda/1,300$. The values for $\eta = 1$ have been added.

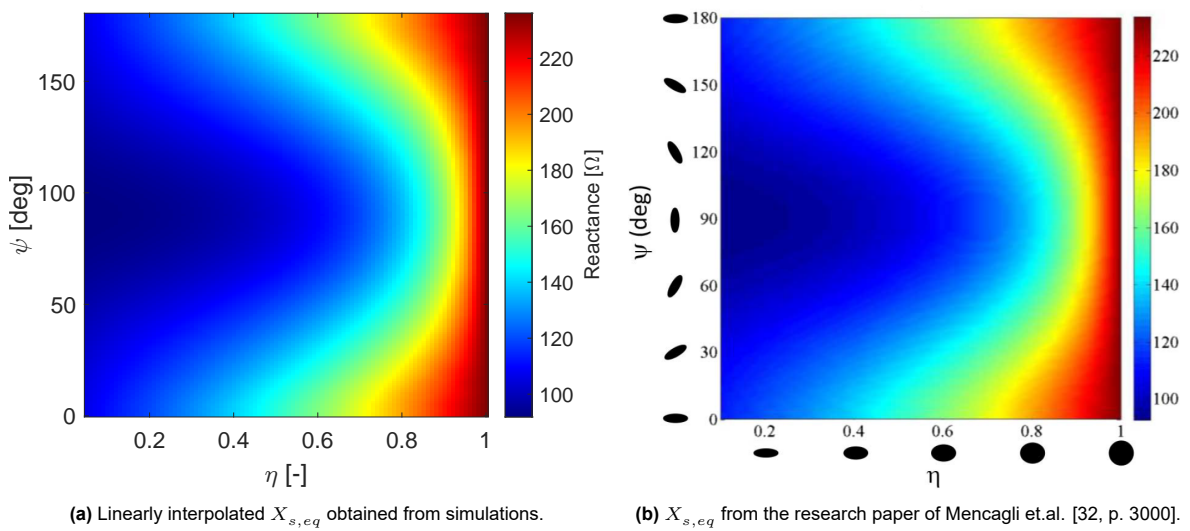


Figure 4.15: Equivalent impenetrable metasurface reactance linearly interpolated from simulations compared to the verification plot. The ψ angle is used in the vertical axis keeping $\alpha_{sw} = 0$ and $\psi = \delta$.

frequencies. When equation (3.117) is solved at high frequencies, a second solution may arise that represents the TE solution which indicates that, for a given excitation frequency, two surface waves can propagate with two different wavenumbers and different polarizations, leading to a dual mode regime. These two solutions appear for $\alpha_{sw} = 70^\circ$ and $\alpha_{sw} = 90^\circ$, and are plotted in figures 4.16b and 4.16c. However, when considering the inaccuracies at higher frequencies due to the role of higher order Floquet modes, which are not considered in the presented model, these results may give only a rough approximation. This is specially visible at frequencies beyond 17 GHz on figures 4.16a and 4.16d, where a clear deviation from the verification example arises.

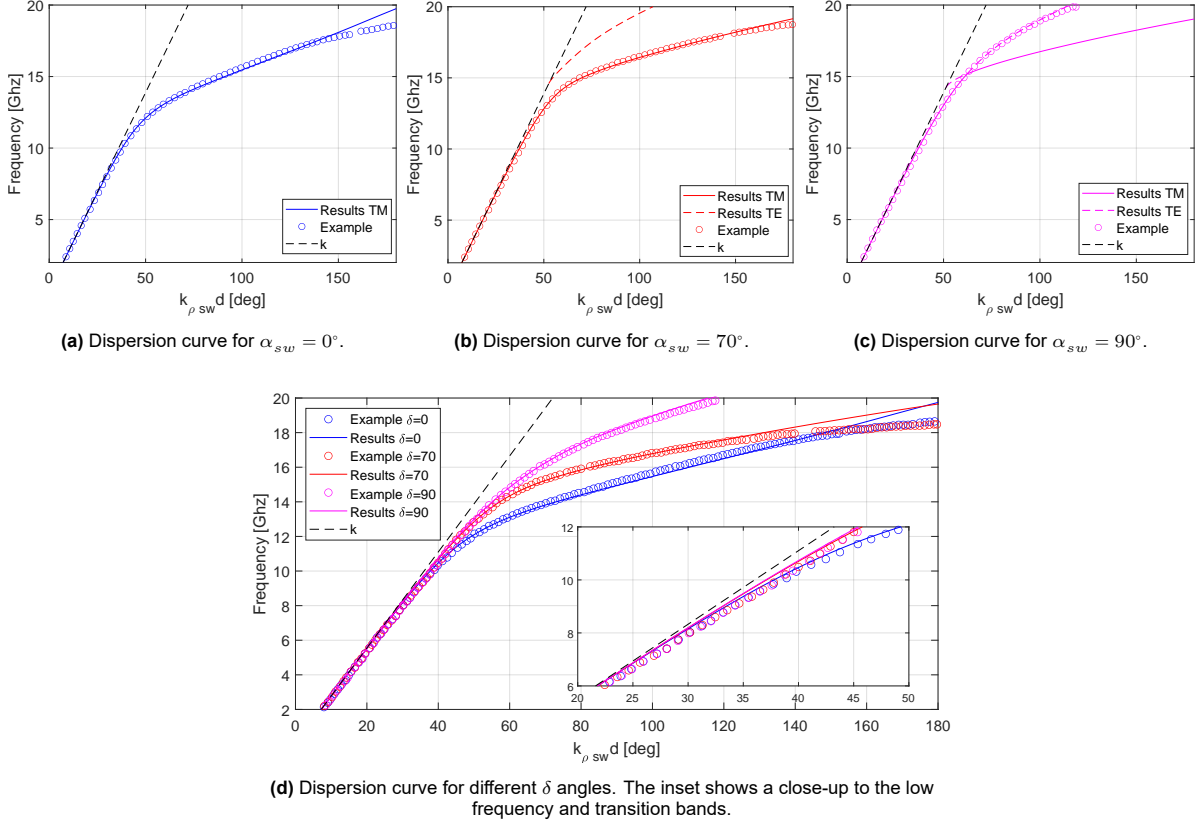


Figure 4.16: Dispersion curves for different values of α_{sw} keeping $\delta = 0^\circ$ (top row), and for different values of δ keeping $\alpha_{sw} = 0$ (bottom plot). For all cases $\eta = 0.5$. Example data used from Mencagli et.al. [32].

The last part in the verification process of the method for deriving the reactance database corresponds to the calculation of the Isofrequency Dispersion Curves (IDC), which shows the frequency and direction at which the dominant surface wave propagates in the spectral plane for a given excitation frequency. The results are shown in figure 4.17 where the results obtained from the simulations are shown on the left-side and the ones from literature on the right-side. The results match with the verification plots up to 17 GHz, which is even beyond the frequency where the TE mode starts appearing. Furthermore, one other form in which the limit of the transition band with the dynamic band can be identified is to obtain the frequency at which the IDC is significantly deformed [28, p. 11], which is according to figures 4.17a and 4.17b at 15 GHz, which also is the same frequency at which the TE mode starts appearing in figure 4.16c. In conclusion, it has been verified that the reactance obtained with the derived method would be reliable up until the boundary of the transition and dynamic bands. After this boundary, these results should be used considering that the further they are from this boundary, the less precise they would be.

Results

The method described previously was applied to the patch configuration specified in table 4.1. Simulations were done for different combinations of $\delta \in [0^\circ, 180^\circ]$ with $\Delta\delta = 5^\circ$, and $\eta \in [0.05, 1]$ with $\Delta\eta = 0.05$. Considering that two simulations for each shape had to be done for TM and TE polarizations, the total

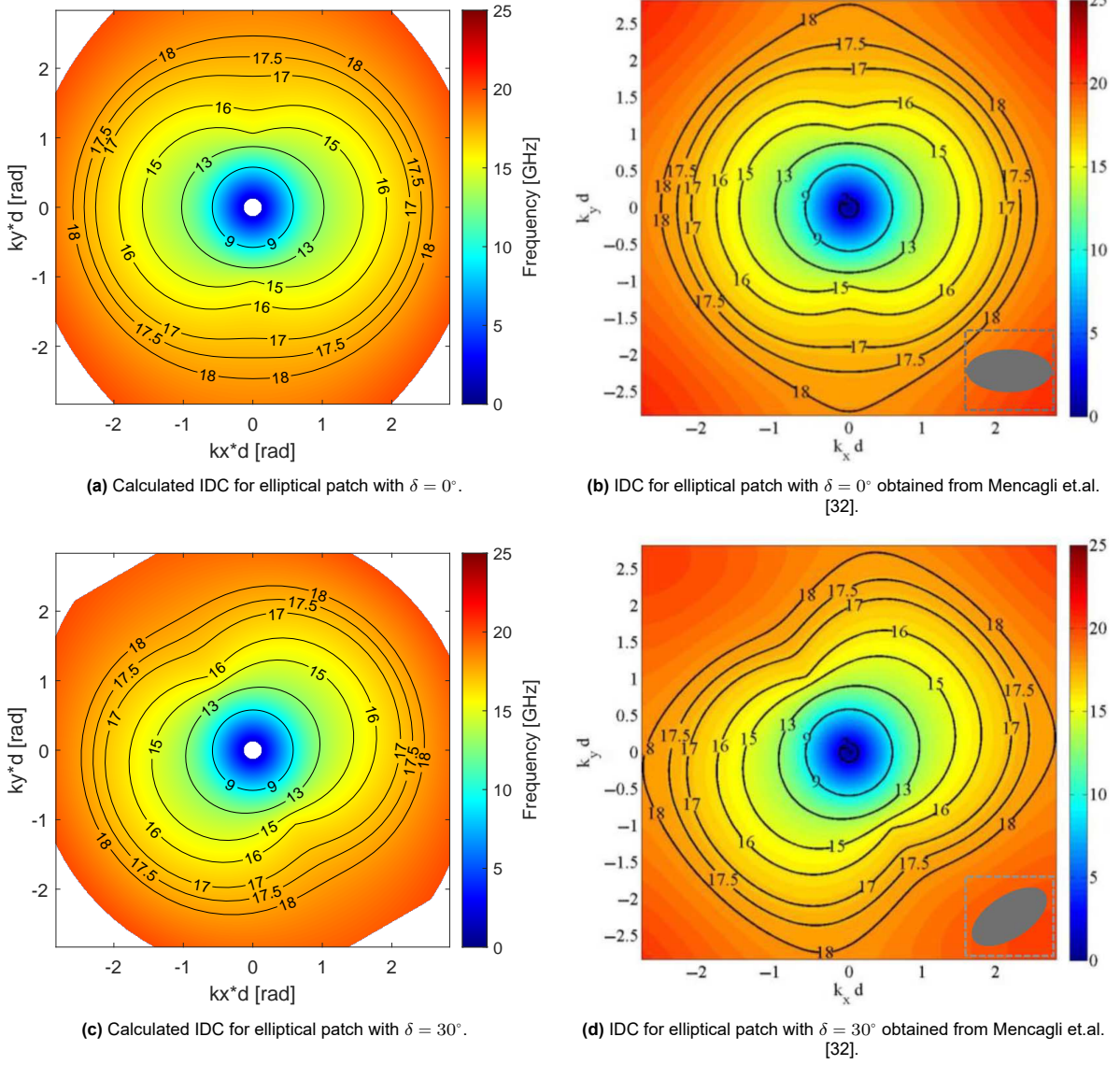


Figure 4.17: IDC for two different patch configurations obtained with the presented simulation method (left) compared against results in literature (right). The color bar on the plots of the right represent the frequency in GHz.

number of simulations was 1,480 with 37 different angles and 20 different shapes. Ultimately, the initial simulation mesh used was of $(\Delta x_0, \Delta y_0) = \lambda/1,500$, which is in a similar order of magnitude as in the verification example. It is important to note that the contribution of a'/d was maintained fixed at $a'/d = 0.9$ because results were not found in the consulted literature that would allow to compare the effects of changing this parameter in the presented model. However, it was later found that varying this parameter allows to have a wider reactance amplitude range that would span all the required values for the antenna synthesis. This topic is treated in more detail in section 4.2.2.

The obtained database is shown in figure 4.18 in terms of $X_s^{(ee)}$, $X_s^{(hh)}$, and $X_s^{(eh)}$ for 3.2 GHz, and the relative difference between the cross-polarized terms. There is a close resemblance with figure 4.14, specially in the $X_s^{(ee)}$ term shown in figure 4.18a. The other reactance matrix terms, $X_s^{(hh)}$ and $X_s^{(eh)}$, are not as similar because in the case of figure 4.14 they go over the singularity that defines these values as open circuits, whereas in figure 4.18 they are just below, in the capacitance region. Furthermore, figure 4.18d shows that the difference between the cross-diagonal reactance term is around 4%, which is a similar value as in figure 4.14d. The only visible difference was in the patches with $\eta = 0.05$, which shows mixed capacitive and inductive behaviours for each 45° segment, together with relatively small $X_s^{(eh)}$ values causing high relative differences for values close to $\delta = 45^\circ$.

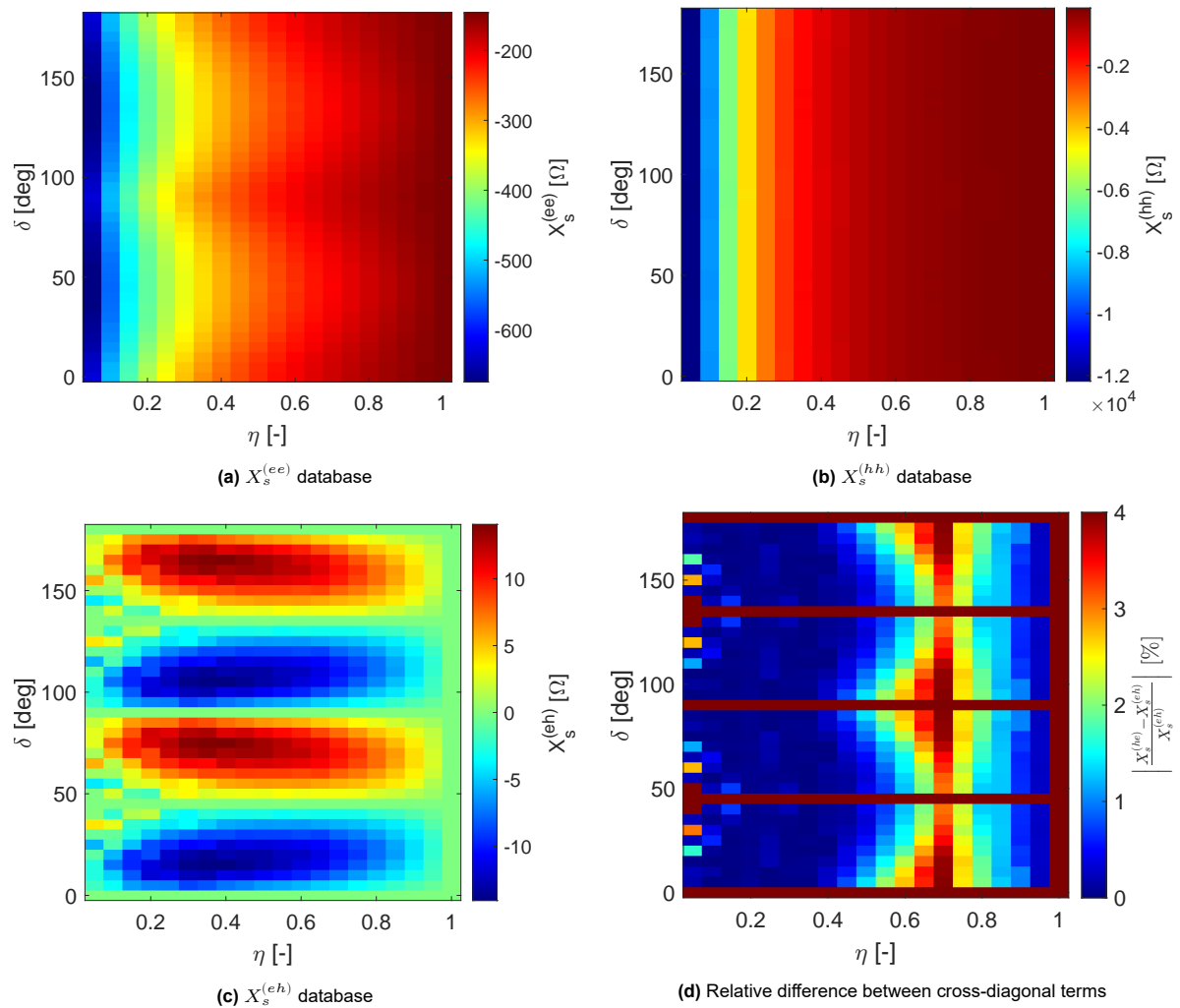


Figure 4.18: Resulting database for the patch configuration specified in table 4.1 for $\alpha_{sw} = \delta$, $a/d = 0.9$ and $f = 3.2$ GHz.

These results were verified by asking to the authors of [27] if they could provide numerical simulations that would replicate the data obtained in figure 4.18 with the method that was developed by one of them in [24], which is based on the MoM approach specified in appendix C. The authors agreed and they sent the required database that was used to verify the results obtained by the previously described method. The transparent reactance database sent by the authors, referred as \underline{X}'_s , is shown in figures 4.19a to 4.19c for each of the matrix components. These are compared with the ones obtained in figure 4.18 (after applying a linear interpolation to match the elements in η and δ) in figures 4.19d to 4.19f. The most important difference is the one illustrated in figure 4.19e where it reaches up to almost 90% for patches with low η . This is because, when the patches have this elongated shape, they approximate to the open circuit boundary which was explained in the verification part of this section when figure 4.14b was described. As there is a singularity, the reactance tends to diverge, causing a loss in precision in the calculated $X_s^{(hh)}$. Therefore, it is advised to avoid using those values for the final antenna unless thorough testing has been done beforehand, assessing the precision close to the open circuit limit. Nevertheless, the bottom inset on figure 4.19e shows that there is a error of the order of 5% for $\eta > 0.7$, which matches the one of figure 4.19d and the error term predicted in figure 4.18. On the contrary, this is not the case for the cross-diagonal term $X_s^{(eh)}$, which absolute difference is shown in figure 4.19f, indicating a deviation of 2.5Ω in a region where the maximum amplitude of $(X'_s)^{(eh)}$ is 10Ω . When looking at the boundaries that separate positive and negative values in this cross-diagonal term, figure 4.18c shows that this is in all cases in values of δ multiples of 45° , whereas in figure 4.19d occurs at 0° and 90° , but tends to vary with the patch shape at around 50° , which is the same angle where the maximum difference of 2.5Ω is found. However, this magnitude represents between 0.5%

and 1% of $(X'_s)^{(ee)}$ and $(X'_s)^{(hh)}$, so its influence in the overall $\underline{\underline{X}}_s$ precision would be marginal.

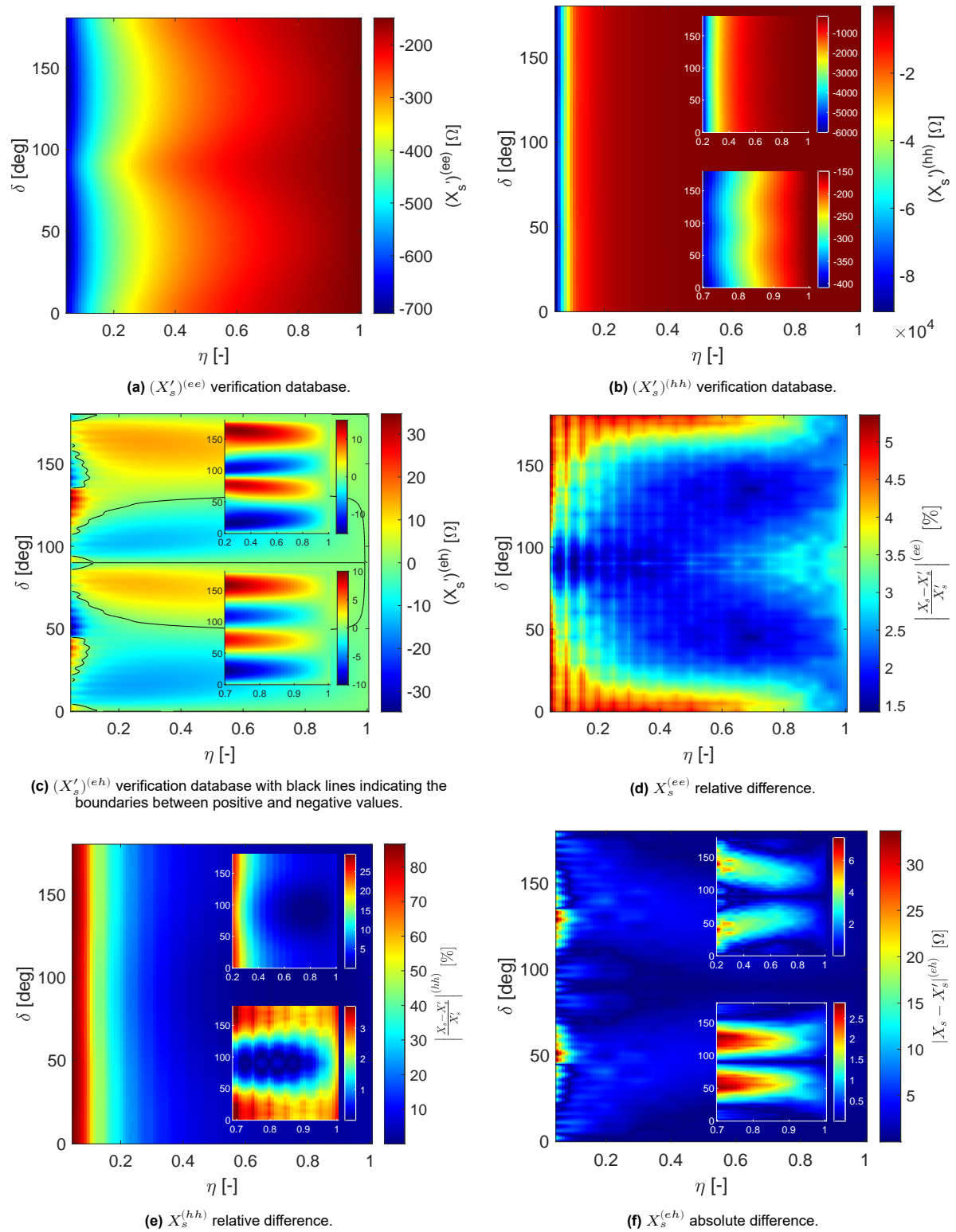


Figure 4.19: Transparent reactance matrix components of the verification dataset for $\alpha_{sw} = 0$, 3.2 GHz, $a/d = 0.9$, and varying δ (figures 4.19a to 4.19c). Next, figures 4.19d to 4.19f show the relative difference between the obtained values in figure 4.18 with the verification database. The insets focus on the ambiguous image sections.

In conclusion, the method used to derive the reactance database using FDTD simulations, which is

available in commercial software, has been described, verified and implemented in the case described on chapter 2. The presented method is an adaptation of the one described in Patel and Grbic in [42] for anisotropic patches, using the properties explained in [28]. The method has been verified for elliptical patches using the plots found in [32], but the underlying principles would apply to any shape with two symmetry axes. The results show a deviation of at most 5% for few shapes that are sufficiently far from the open circuit reactance, which causes a singularity that would require a finer simulation method to accurately predict.

4.2. Antenna synthesis

In this subsection, the antenna synthesis procedure implementation is explained. First, the used target field is presented for the SAR antenna which requirements are specified in chapter 2. Next, the antenna synthesis procedure, which is based on the method presented in section 3.2.4, is verified and implemented.

4.2.1. Target field

In this part, the target field in the antenna aperture is derived. This is represented by \mathbf{E}_A , which elements were explained when equation (3.125) was presented. The antenna requirements from table 2.1 that influence directly the required far-field are the frequency, radius, directivity and HPBW, given the fact that the design will focus on the antenna central frequency. There are no requirements for the sidelobe level or polarization, but they will be still reported for the completeness of the final design and implemented if possible.

The target field of a circular metasurface antenna such as the ones presented in figure 3.5a can be approximated to the one of a circular aperture. From the book of Antenna Theory of Balanis [1, p. 419], three general target distributions can be obtained which performance is reported in table 4.2 for the objective antenna radius and frequency, where FNBW is the first-null beam width, and FSLM is the first side lobe maximum with respect to the main lobe.

Table 4.2: Antenna parameters for different aperture distributions. Formulas obtained from [1].

	Uniform	Radial taper	Radial taper squared
Distribution	E_0	$E_0 \left[1 - \left(\frac{\rho}{a}\right)^2\right]^1$	$E_0 \left[1 - \left(\frac{\rho}{a}\right)^2\right]^2$
HPBW [deg]	2.74	3.41	3.94
FNBW [deg]	6.55	8.75	10.9
FSLM [dB]	-17.6	-24.6	-30.6
Directivity [dB]	36.53	35.28	34.01

The first distribution in table 4.2, the uniform distribution, is an ideal case for a leaky-wave antenna because having a uniform current in the aperture ending abruptly at the boundary implies that all the power is dissipated only there, meaning that there is no leakage and therefore that this distribution cannot be used for this case. The other two, the radial taper and radial taper squared, have a maximum at the antenna centre and then the current decreases as it approaches to the boundaries, which resembles the case of a leaky-wave antenna. Therefore, the radial taper distribution will be used for the final antenna design because, given the directivity requirement of 36 dB and the HPBW of 3.2° , is the distribution that comes closer to these values.

Regarding the polarization, there are no requirements in the available SwarmSAR literature. However, there are multiple advantages that can be traced to polarimetric SAR applications. As examples, van Zyl and Kim report the use of the backscattered vertically and horizontally polarized radiation to measure the soil moisture [51], whereas Zhang, Li, Liang and Tsou report a good performance when using circularly-polarized signals for marine remote sensing applications such as oil spill classification [55]. The inconvenience of using polarimetric SAR is that the antenna must receive the signal in two different polarizations in the basic dual-mode configuration [51], which would require at least two feeding points able to identify them. An approach that would address this topic is using different polarizations in different satellites, but that would be against the requirement of exchangeable nodes in the SwarmSAR mission. Therefore, for the simplicity of this case, it has been decided to use a linearly polarized

antenna because it does not have a phasing term in the aperture [40, p. 3914], which simplifies the design procedure. Furthermore, if a metasurface antenna with polarimetric SAR capabilities is required at any future point in time, this design could be escalated to achieve that objective by using more than one feeding point as it is detailed in [14, 50].

Finally, equation (4.9) can be derived, which shows the required electric field in the aperture to fulfil the far-field requirements for a horizontally-polarized broadside radiation pattern with radial tapering in the aperture. Whereas the first term in brackets show the radial tapering, the second shows the required direction of the electric field in the aperture for a linearly-polarized radiation pattern, which in this case it has been aligned arbitrarily to the x -axis.

$$\mathbf{E}_A = E_0 \left[1 - \left(\frac{\rho}{a} \right)^2 \right] \left[\cos(\phi) \hat{\boldsymbol{\rho}} - \sin(\phi) \hat{\boldsymbol{\phi}} \right] U_A \quad (4.9)$$

4.2.2. Adiabatic Floquet analysis implementation

In this subsection, the verification and implementation of the method presented in section 3.2.4 are explained. First, these two parts are preceded by a brief method description focused on giving more details on the mathematical derivation of the method presented in section 3.2.4. Next, an example case is used for the verification of this method implementation. As the exact distributions used for this example case are not known by the author, a guess of these values was tried, where some deviations can be identified but the main behaviour is similar to the one used by the authors. At the end, the antenna synthesis is applied to the SAR antenna described in chapter 2.

Method description

The method used in this part has already been explained step-by-step in section 3.2.4. However, there are some parts of the derivations that are worth to bring in detail now because they depend on steps that were explained in subsequent points.

One example is step 6, which explanation ended up in equation (3.126). This equation can be derived by rearranging equation (3.148) into the form of equation (4.10). Then, using only the real part of the fast-varying periodic terms which are $-kl(\boldsymbol{\rho})$ from \mathbf{E}_A , $Ks(\boldsymbol{\rho})$ in $\underline{\mathbf{X}}_s^{(-1)}$, and $\beta_{sw}\rho + \int \beta_{\Delta}(\boldsymbol{\rho}')d\rho'$ on $\mathbf{J}^{(0)}$, equation (3.126) is obtained.

$$\left\{ \underline{\mathbf{U}} - j\underline{\mathbf{X}}_s^{(0)} \cdot \left[\underline{\mathbf{Z}}_{GF}^{(-1)} \right]^{-1} \right\} \cdot \mathbf{E}_A(\boldsymbol{\rho}) = j\underline{\mathbf{X}}_s^{(-1)} \cdot \mathbf{J}^{(0)} \quad (4.10)$$

The second case is step 11, particularly the derivation of equation (3.142). This can be demonstrated for a general case by considering negligible all the modes above N and below $-N$. Then, equation (3.141) becomes equation (4.11).

$$\mathbf{E}_t(\boldsymbol{\rho}) = \sum_{q=-N}^N \underline{\mathbf{Z}}_{GF}^{(q)} \cdot \mathbf{J}^{(q)} = j(\underline{\mathbf{X}}_s^{(0)} + \underline{\mathbf{X}}_s^{(-1)} + \underline{\mathbf{X}}_s^{(+1)}) \cdot \mathbf{J}^{(q)} \quad (4.11)$$

From equation (4.11) the terms with the same rapid phase variation $qKs(\boldsymbol{\rho})$ are grouped together, which are related to $\mathbf{E}^{(q)}$ by equation (4.12).

$$\mathbf{E}^{(q)} = j \left[\underline{\mathbf{X}}_s^{(0)} \cdot \mathbf{J}^{(0)} + \underline{\mathbf{X}}_s^{(-1)} \cdot \mathbf{J}^{(q+1)} + \underline{\mathbf{X}}_s^{(+1)} \cdot \mathbf{J}^{(q-1)} \right] \quad (4.12)$$

Following, using equation (3.137) to replace $\mathbf{E}^{(q)}$, equation (4.13) is obtained relating the transparent boundary condition with the Floquet modes and the spectral GF.

$$\left[-\underline{\mathbf{Z}}_{GF}^{(q)} + j\underline{\mathbf{X}}_s^{(0)} \right] \cdot \mathbf{J}^{(q)} + j\underline{\mathbf{X}}_s^{(-1)} \cdot \mathbf{J}^{(q+1)} + j\underline{\mathbf{X}}_s^{(+1)} \cdot \mathbf{J}^{(q-1)} = 0 \quad (4.13)$$

Replacing q by $\pm N$, one of the terms of equation (4.13) can disappear because it would be regarded as negligible, leading to a difference equation for $\mathbf{J}^{\pm N}$ expressed in equation (4.14a) where $\underline{\mathbf{Y}}^{\pm N}$ is defined in equation (4.14b).

$$\mathbf{J}^{(\pm N)} = \underline{\mathbf{Y}}^{(\pm N)} \cdot j\underline{\mathbf{X}}_s^{(\pm 1)} \cdot \mathbf{J}^{(\pm N \mp 1)} \quad (4.14a) \quad \underline{\mathbf{Y}}^{(\pm N)} = \left[\underline{\mathbf{Z}}_{GF}^{(\pm N)} - j\underline{\mathbf{X}}_s^{(0)} \right]^{-1} \quad (4.14b)$$

This difference equation can be obtained for the next term $\mathbf{J}^{\pm N \mp 1}$ as shown in equation (4.15).

$$\mathbf{J}^{(\pm N \mp 1)} = \underline{\mathbf{Y}}^{(\pm N \mp 1)} \cdot j \underline{\mathbf{X}}_s^{(\pm 1)} \cdot \mathbf{J}^{(\pm N \mp 2)} \quad (4.15a)$$

$$\underline{\mathbf{Y}}^{(\pm N \mp 1)} = \left[\underline{\mathbf{Z}}_{GF}^{(\pm N \mp 1)} - j \underline{\mathbf{X}}_s^{(0)} + \underline{\mathbf{X}}_s^{(\mp 1)} \cdot \underline{\mathbf{Y}}^{(\pm N)} \cdot \underline{\mathbf{X}}_s^{(\pm 1)} \right]^{-1} \quad (4.15b)$$

This result can be generalized for the $p - 1$ term, which is shown in equation (4.16).

$$\mathbf{J}^{(\pm N \mp p \pm 1)} = \underline{\mathbf{Y}}^{(\pm N \mp p \pm 1)} \cdot j \underline{\mathbf{X}}_s^{(\pm 1)} \cdot \mathbf{J}^{(\pm N \mp p)} \quad (4.16a)$$

$$\underline{\mathbf{Y}}^{(\pm N \mp p \pm 1)} = \left[\underline{\mathbf{Z}}_{GF}^{(\pm N \mp p \pm 1)} - j \underline{\mathbf{X}}_s^{(0)} + \underline{\mathbf{z}}^{(\pm N \mp p \pm 1)} \right]^{-1} \quad (4.16b)$$

$$\underline{\mathbf{z}}^{(\pm N \mp p \pm 1)} = \underline{\mathbf{X}}_s^{(\mp 1)} \cdot \underline{\mathbf{Y}}^{(\pm N \mp p \pm 2)} \cdot \underline{\mathbf{X}}_s^{(\pm 1)} \quad (4.16c)$$

Setting $p = N$, a closed-form expression for $\mathbf{J}^{(\pm 1)}$ can be obtained as presented in equation (4.17).

$$\mathbf{J}^{(\pm 1)} = j \mathbf{Y}^{(\pm 1)} \cdot \mathbf{X}^{(\pm 1)} \cdot \mathbf{J}^{(0)} \quad (4.17)$$

When using equation (4.17) in equation (4.13) for $q = 0$ and grouping the remaining terms in $\underline{\mathbf{X}}_N$, equation (4.18) is obtained, where $\underline{\mathbf{X}}_N$ is defined in equation (4.19). Equation (4.18) is analogous to equation (3.143), whereas equation (4.19) is to equation (3.144). The only difference is the dependency on N , which is directly related to the number of Floquet modes evaluated. In fact, in the method presented in section 3.2.4, it has been assumed that $N = 1$ because it already gives a good approximation for a reactance range of $\bar{X}/\zeta \in [0.5, 1.5]$ [37, p. 3902]. Equation (4.19), on the other side, includes the dependency on higher-order Floquet modes in $\underline{\mathbf{Y}}^{(\pm 1)}$ because this term is calculated recursively from N to 1 with equation (4.16b).

$$j \underline{\mathbf{X}}_N \cdot \mathbf{J}^{(0)} = 0 \quad (4.18)$$

$$j \underline{\mathbf{X}}_N = \left[\underline{\mathbf{Z}}_{GF}^{(0)} - j \underline{\mathbf{X}}_s^{(0)} \right] + \underline{\mathbf{X}}_s^{(-1)} \cdot \underline{\mathbf{Y}}^{(+1)} \cdot \underline{\mathbf{X}}_s^{(+1)} + \underline{\mathbf{X}}_s^{(+1)} \cdot \underline{\mathbf{Y}}^{(-1)} \cdot \underline{\mathbf{X}}_s^{(-1)} \quad (4.19)$$

Finally, equation (3.146) can be solved for the N terms in the adiabatic Floquet expansion by only including the $\underline{\mathbf{Y}}^{(\pm 1)}$ obtained from considering the higher-order terms. With the obtained results, the higher order terms of \mathbf{J} and \mathbf{E} can be calculated to obtain a more precise final expression.

Other practicalities that are important to mention regarding this method's implementation is that the cylindrical coordinate system is used in the simulations, whereas for plotting a linear interpolation is performed to transform these results to the Cartesian plane. This interpolation is used for illustration purposes only because it makes the results compatible with the plotting functions. Furthermore, to perform step 13, the built-in optimization algorithm function from MATLAB® is used to solve the non-linear system of equation (3.146). Later, in the verification step, the convergence of this algorithm applied to this problem is evaluated. The initial parameter used for β_{sw} in the verification and results parts is $\beta_{sw} = 1.5k$, and the radiation efficiency is of $\eta_{eff} = 0.9$.

Verification

In this section, two verification levels are being carried out for a linearly-polarized antenna with $\epsilon_r = 9.8$, $h = 0.5$ mm, $f = 26.25$ GHz, and $a = 10\lambda$, which is the fourth example in the research publication where this method was derived from [40, p. 3913-3916]:

1. **Verification of single steps:** To this end, a simplified distribution will be used for the verification of steps 8 and 11, which involve numerical integration. This is specified in equation (4.20), which only has a radial component. An example function with only the azimuthal component is not evaluated because most equations at this first stage only deal with integration along the radial direction like equations (3.130) and (3.131). Next, for step 13, an example given in [37, p. 3902] to obtain α and β_Δ for a broadside circularly-polarized beam is reproduced.

$$\mathbf{E}_A(\rho) = E_0 \left[1 - \left(\frac{\rho}{a} \right)^2 \right] \hat{\rho} U_A \quad (4.20)$$

Only these steps are verified because their implementation is more difficult than the rest, which in the majority of cases only require to do simple arithmetic operations. Furthermore, the analytical

derivation could only be obtained up until step 12 because solving equation (3.146) in step 13 requires an equation solving algorithm because of the non-linearity of the problem.

2. **Verification of the complete algorithm:** It is attempted to replicate the example presented in [40], which requires the execution of the complete algorithm. The main inconvenience of using this example is that the distribution used for \mathbf{E}_A is not reported in the source, which makes impossible to obtain a perfect comparison. Hence, multiple distributions were tried to obtain the one that would fit best, which was found to be the radial distribution presented in equation (4.9) with $E_0 = 285 \text{ V/m}$. Furthermore, as the far-field radiation pattern is obtained with the electric field in the aperture, the one obtained from the synthesis process $\mathbf{E}^{(-1)}$ can be compared against the objective \mathbf{E}_A in the far-field as a more precise verification procedure. Whereas in the first case it would be expected to have a similar behaviour between the verification example and the obtained from the synthesis pattern, in the second case the far-field distributions can be used as an actual verification to assess the precision of this algorithm.

To verify step 8, first $S(\rho)$ has to be initially estimated with equation (3.127). Considering that $l(\rho) = 0$, $\mathbf{K}_t = 0$ and $K_z = k$. Therefore, equation (4.21) can be obtained.

$$S(\rho) = \frac{|\mathbf{E}_A|^2}{2\zeta} \quad (4.21)$$

The next step is calculating the radiated power, which is obtained by integrating $S(\rho)$ throughout the metasurface area, which is the first element in the denominator of equation (3.130). The result of this calculation is given in equation (4.22).

$$P_{rad} = \frac{\pi(aE_0)^2}{6\zeta} \quad (4.22)$$

Following, the second element in the denominator of equation (3.130), which represents the azimuthal averaged radiated power, is calculated. This is presented in equation (4.23) where the primes indicate the integration variables.

$$2\pi \int_0^\rho S(\rho')\rho' d\rho' = \frac{\pi E_0^2}{6a^4\zeta} (3a^4\rho^2 - 3a^2\rho^4 + \rho^6) \quad (4.23)$$

To finalize step 8, the initial estimation of the leakage parameter α is calculated analytically in equation (4.24).

$$\alpha(\rho) = \frac{3\eta_{eff}a^4\rho|\mathbf{e}_A|^2}{a^6 - 3\rho^2\eta_{eff}a^4 + 3\rho^2\eta_{eff}a^2 - \rho^6\eta_{eff}} \quad (4.24)$$

The cylindrical coordinate system used required the discretisation of the radial and azimuthal directions, which was set to $a/(\Delta\rho) = 800 \quad \forall \rho \in [10^{-10}, a]$, to avoid a singularity with the zero, and $2\pi/(\Delta\phi) = 361 \quad \forall \phi \in [0, 2\pi]$, to facilitate conversion from radians to degrees. The integration function used was the trapezoidal and its results are shown in figure 4.20 compared to the analytical solution. Given the satisfactory level of agreement between the numerical and analytical results ($< 0.001\%$), it was decided to continue to the next steps.

In step 11, a first estimation of the modulation vector is obtained. The modulation is performed in both $\hat{\rho}$ and $\hat{\phi}$ directions. However, given that there is no azimuthal component of \mathbf{e} in equation (3.150d) because equation (4.20) lacks of it, $m_\phi = 0$ and the modulation vector is reduced to the modulation coefficient $m_\rho \exp(j\Phi_\rho)$. Obtaining this parameter from the retrieved value of α involves integrating once more to obtain $\tilde{k}^{(0)}(\rho)\rho$ in equation (3.131), using this value in a Bessel function to obtain $\tilde{\sigma}$ as described in equation (3.150a), and using the resulting coefficient to obtain the modulation coefficient value. The derivation of the analytical solution of α integral is shown in equation (4.25), which is used in the analytical model. The comparison between the numerical and analytical results of the real and imaginary results are shown in figure 4.21, which illustrates a similar agreement level as in figure 4.20, which suggests that the integration algorithm is performing the calculations at a satisfactory agreement level.

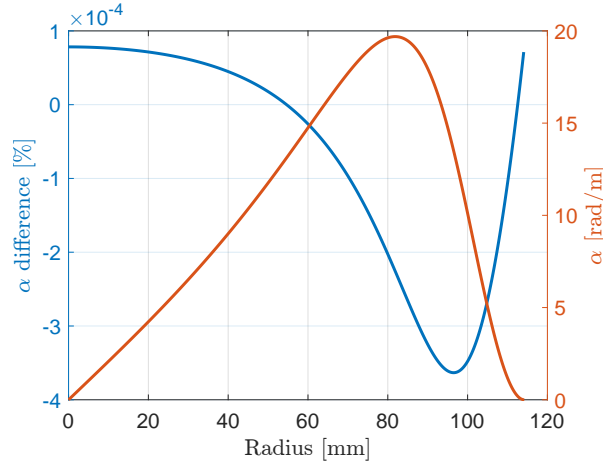


Figure 4.20: Difference between the numerically and analytically obtained α in step 8 of the modulation algorithm.

$$\int_0^\rho \alpha(\rho') d\rho' = 3 \ln(a) - \frac{1}{2} \ln(a^6 - 3\eta_{eff}\rho^2 a^4 + 3\eta_{eff}\rho^4 a^2 - \eta_{eff}\rho^6) \quad (4.25)$$

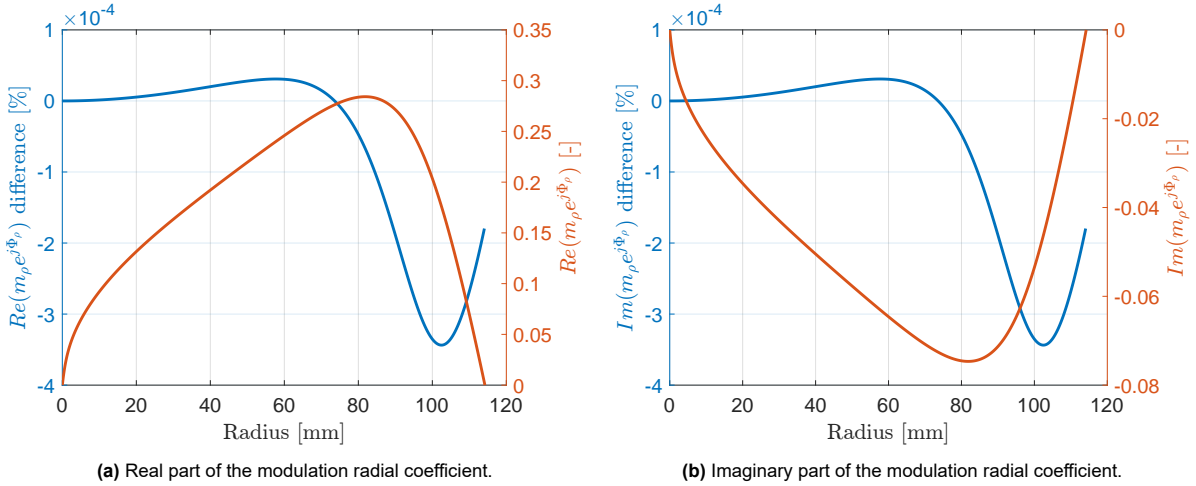


Figure 4.21: Difference between the numerically and analytically obtained radial modulation coefficient in step 13 of the algorithm.

Before performing the verification of the whole algorithm, step 13 can be verified with an example presented in [37, p. 3902]. Equation (4.26) shows the transparent reactance distribution for a circularly-polarized metasurface antenna with a broadside radiation beam. This can be written in terms of the varying phase contributions as in equation (4.27) considering $m_\rho = m_\phi$.

$$X_{s,\rho\rho} = \bar{X}_{s,\rho} [1 \pm m_\rho \cos(\beta_{sw}\rho + \phi)] \quad (4.26a)$$

$$X_{s,\rho\phi} = \bar{X}_{s,\rho} [m_\rho \sin(\beta_{sw}\rho + \phi)] \quad (4.26b)$$

$$\underline{\mathbf{X}}_s^{(0)} = \bar{X}_{s,\rho} \underline{\mathbf{U}} \quad (4.27a)$$

$$\underline{\mathbf{X}}_s^{(\pm 1)} = \frac{m_\rho \bar{X}_{s,\rho}}{2} e^{\mp j(\beta_{sw}\rho + \phi)} [(\hat{\rho}\hat{\rho} - \hat{\phi}\hat{\phi}) + e^{\pm \frac{\pi}{2}} (\hat{\rho}\hat{\phi} + \hat{\phi}\hat{\rho})] \quad (4.27b)$$

Next, as the interest of this example is examining the range of \bar{X}/ζ in which using $N = 1$ in equation (4.18) would be acceptable, the average transparent reactance $\bar{X}_{s,\rho}$ is set in terms of the ratio of the average opaque reactance and the free-space impedance \bar{X}/ζ . To achieve this, it can be assumed

that the propagating surface wave has, on average, a cylindrical wavefront at a sufficient distance of the origin. This aligns the expressions in dyadic form $\hat{\mathbf{k}}_t \hat{\mathbf{k}}_t$ and $\hat{\mathbf{k}}_t^\perp \hat{\mathbf{k}}_t^\perp$ with $\hat{\boldsymbol{\rho}} \hat{\boldsymbol{\rho}}$ and $\hat{\boldsymbol{\phi}} \hat{\boldsymbol{\phi}}$. Next, when the eigenvectors of $\underline{\underline{\mathbf{X}}}_s$ are aligned with the propagation direction, equation (3.117) can be solved for a decoupled system, where the solution corresponding to $\hat{\boldsymbol{\rho}} \hat{\boldsymbol{\rho}}$ represents the one with the TM polarization, which is the dominant propagation mode. Then, given the fact that the current density excited by a dipole source only has a radial component, the current density can be approximated on average to equation (4.28), where the surface wave propagation constant represents the magnitude of the transverse wavevector $\beta_{sw} = k_\rho$. This can be used to obtain the relation between the average opaque reactance and the transverse wavevector, which coincides with the one for an isotropic metasurface presented in equation (3.107). Finally, solving the transverse resonance condition of equation (3.117) for the TM mode, the relation between the average transparent and opaque reactance is obtained in equation (4.29).

$$\mathbf{J}_0 = J_0 H_1^{(2)}(\beta_{sw} \rho) \hat{\boldsymbol{\rho}} \quad (4.28)$$

$$\frac{\bar{X}_{s,\rho}}{\zeta} = \frac{\bar{X}}{\zeta} \left\{ 1 - \frac{\bar{X}}{\zeta} \frac{\epsilon_r \cot \left[kh \sqrt{\epsilon_r - 1 - \left(\frac{\bar{X}}{\zeta}\right)^2} \right]}{\sqrt{\epsilon_r - 1 - \left(\frac{\bar{X}}{\zeta}\right)^2}} \right\}^{-1} \quad (4.29)$$

Next, the wavevectors $\beta^{(q)}$ are obtained considering the N used, where the only radiating mode would be the -1 . Equation (3.134) is used considering that $K_s(\boldsymbol{\rho})$ is defined by comparing equations (3.121) and (4.26), where it can be concluded that $K_s(\boldsymbol{\rho}) = \beta_{sw} \rho$. Furthermore, as this vector is used to solve the non-linear system defined by equation (3.146) for β_Δ and α , the effect of α has to be included in equation (3.134), which results in equation (4.30). This equation is then used instead of equation (3.134) for solving equation (3.146) and obtain $\mathbf{k}^{(0)}$.

$$\mathbf{k}^{(q)} = (\beta_{sw} + \Delta\beta - j\alpha) \hat{\boldsymbol{\rho}} + qK \nabla_t s(\boldsymbol{\rho}) \quad (4.30)$$

Equation (4.30) is used in the spectral GF approximation of the Floquet modes $\underline{\underline{\mathbf{Z}}}_{GF}^{(q)}$, particularly by replacing it with the transverse wavenumber by $[\mathbf{k}^{(q)}]^\top \cdot \mathbf{k}^{(q)} = k_\rho^2$. As $\mathbf{k}^{(q)}$ can be complex, special care has to be taken with the complex square roots that arise from equations (3.113) to (3.116), as the algorithm to calculate them can cause some discontinuities because of angle wrapping effects. The results of this step's verification are shown in figure 4.22 where the obtained calculations are compared against the example data from [37, p. 3902]. The optimization algorithm of MATLAB® was used, showing convergence on every result. A very good agreement is observed between these results, except for $\bar{X}/\zeta = 0.7$ and $\bar{X}/\zeta = 1.3$ corresponding to β_Δ in figure 4.22b which appear to be shifted. This could be a mistake from the source paper, as the results obtained match for all the other cases.

Next, the second verification level is performed, which consists on attempting to reproduce the results of example 4 from [40], which is of a linearly polarized radiation beam in broadside direction with the antenna parameters described at the beginning of the verification part. To this end, the whole algorithm is executed and its similarity with the plots from [40] is evaluated. First, the convergence level is assessed with the change in \mathbf{m} between consecutive iterations as specified in equation (4.31). When this value changes less than a threshold in simulation p , then it can be concluded that the algorithm has converged to a solution for the objective transparent reactance $\underline{\underline{\mathbf{X}}}_s$ and current density \mathbf{J} .

$$(\Delta m)_{avg} = \frac{1}{\pi a^2} \iint_A \frac{|m_{\rho,p}(\boldsymbol{\rho}) - m_{\rho,p-1}(\boldsymbol{\rho})| + |m_{\phi,p}(\boldsymbol{\rho}) - m_{\phi,p-1}(\boldsymbol{\rho})|}{2} dA \quad (4.31)$$

For this case, the threshold has been set empirically to $(\Delta m)_{avg,obj} = 10^{-4}$ which represents the objective average difference of the slow-varying modulation parameter \mathbf{m} between consecutive iterations. The results are shown in figure 4.23, where the convergence is achieved at the eighth step, which is within the boundary of five to ten steps needed for convergence suggested by the authors in [40, p. 3912], and validates the convergence of MATLAB® optimization algorithm.

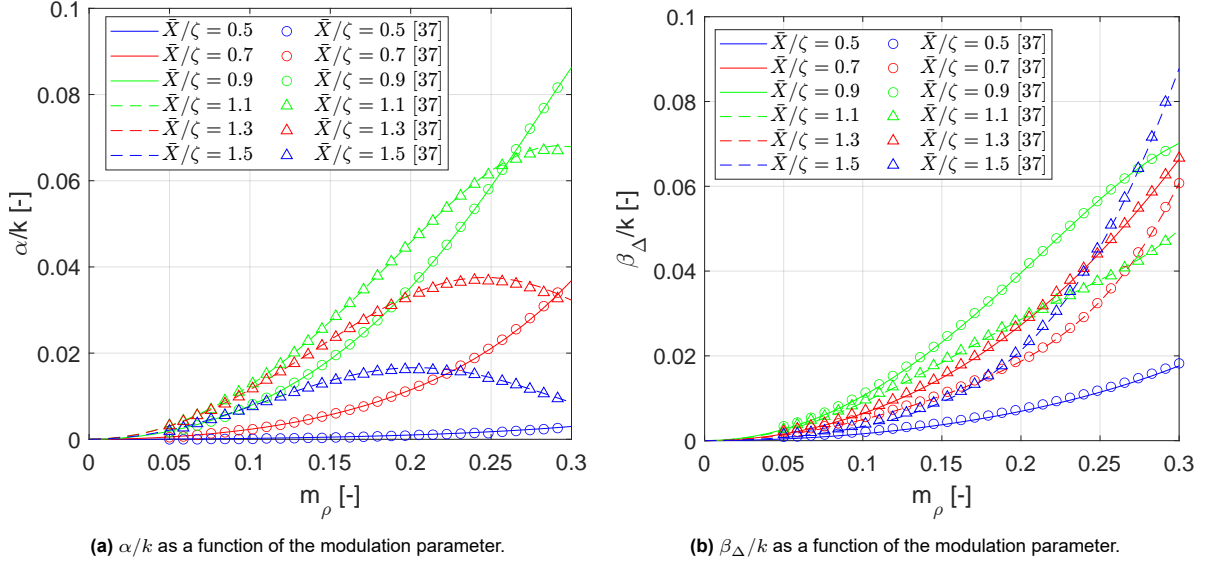


Figure 4.22: α/k and β_{Δ}/k as a function of the modulation parameters for different values of \bar{X}/ζ considering $N = 1$ for a circularly-polarized antenna radiating a broadside beam. Example data obtained from Minatti et.al. [37].

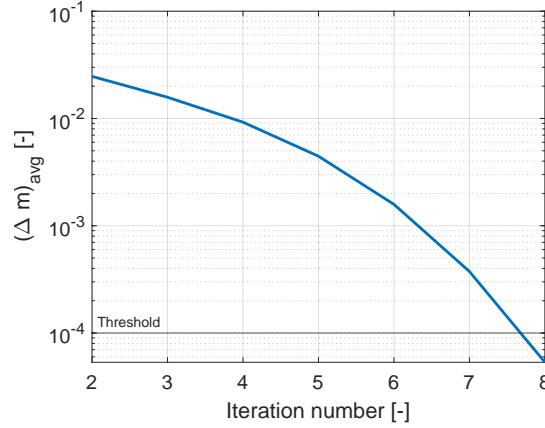


Figure 4.23: Convergence of the modulation index \mathbf{m} as a function of the number of iterations in the algorithm for the verification antenna parameters.

The first results that can be compared are the ones of the Poynting vector magnitude $S(\rho)$ in figures 4.24a and 4.24b, and the leakage parameter $\alpha(\rho)$ in figures 4.24c and 4.24d. When comparing figures 4.24a and 4.24b it can be noted that the verification example (figure 4.24a) has a power distribution that decays to a value close to zero much before than the simulated one (figure 4.24b). Furthermore, as a consequence, the leakage parameter in figure 4.24d spreads over a greater area because the propagating surface wave keeps its energy over a longer radial distance, making its amplitude relatively smaller than the one in figure 4.24c which leaks most of its radiation over a smaller radial distance.

Next, the current density aligned with the x-axis is compared with the verification example. In the verification example, the currents “have been normalized in amplitude to match the average of the MoM currents” [40, p. 3913], which is the method that the authors used to verify their own implementation. For the obtained results, the normalization has been executed by using the average of the currents itself J_{avg} , which is obtained as specified in equation (4.32). The main plot in figure 4.25 shows that the ratio $|J_x/J_{avg}|$ is greater than the one obtained by the authors in almost every case. Nevertheless, the slope is preserved and the obtained oscillatory pattern preserves at least one frequency component of the verification example. This occurs because the number of Floquet modes used by the authors of the verification example is greater than one ($N > 1$), which adds more frequency components in the final \mathbf{J} , and therefore more oscillations. Even though this affects the current distribution, it is not

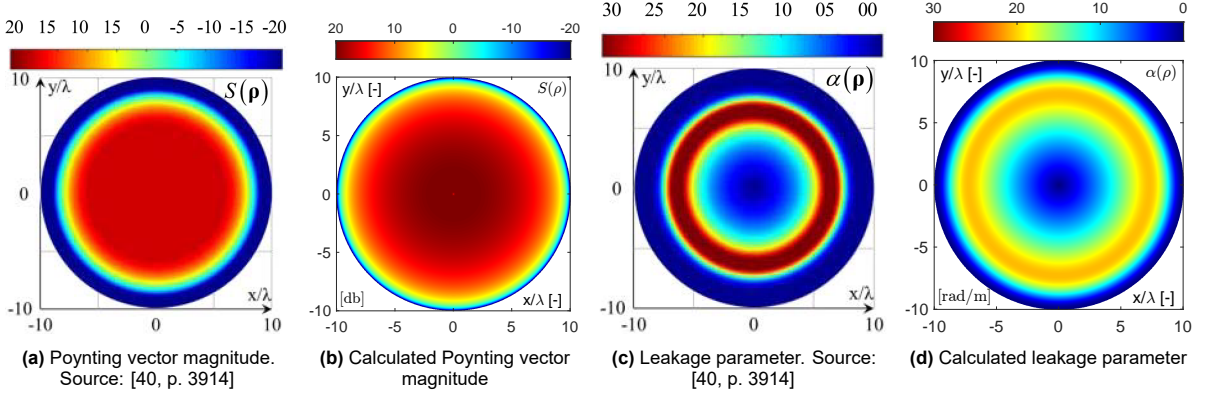


Figure 4.24: Comparison of leakage parameters and Poynting vector magnitudes from the verification research publication [40, p. 3914] and the results after the implementation of this algorithm.

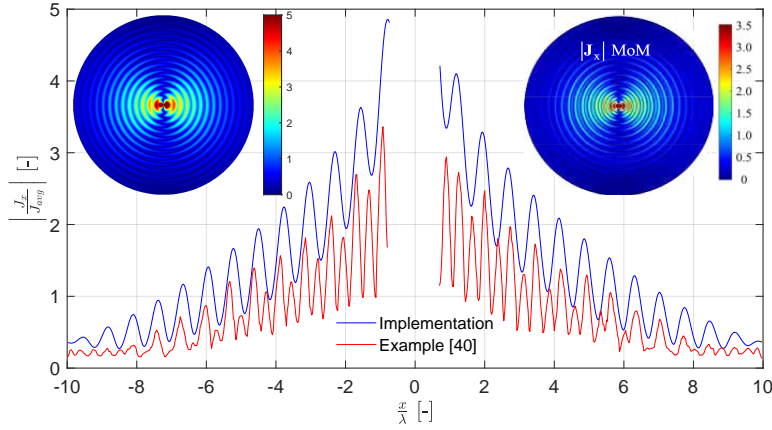


Figure 4.25: Comparison between the normalized total current density aligned with the x-axis $|J_x|$ obtained from the implementation of this algorithm and the one resulting from the implementation of a MoM algorithm in the consulted research publication [40]. Right inset shows the x-aligned current distribution in the verification example, whereas the one on the left shows this same parameter for this implementation.

expected to affect the far-field results because the calculation of these higher-order modes affects only the near-field results, as these decay exponentially in the z-positive direction.

$$J_{avg} = \frac{1}{\pi a^2} \iint_A |\mathbf{J}| dA \quad (4.32)$$

Subsequently, the far-field results are compared with the verification example from [40] and with the initial objective distribution. Given that the only radiating mode is the -1 mode, which was specified when equation (4.30) was described, the far-field contribution is obtained only by evaluating $\mathbf{E}^{(-1)}$ in the results, and \mathbf{E}_A in the target distribution. In the main plot of figure 4.26 the results of the presented CP procedure are compared against the data retrieved from [40] at the diagonal plane $\varphi = 45^\circ$, which is where the XP level is higher. In the first place, this makes evident that a different distribution has been used for the verification example, as the maximum directivity and nulls (local minima between lobes where the directivity tends to zero) are different. This is a direct consequence of what was observed in figures 4.24a and 4.24b, as in the first case the power is radiated in a smaller antenna area than in the second case, resulting in a smaller maximum directivity. In contrast, when the results are compared with the objective distribution (left inset), the maximum difference of -5 dB indicates that the implementation produces the desired aperture patterns within that range, which given the antenna directivity represents a negligible deviation. Furthermore, the XP level is evaluated in the right inset, showing that its level is much smaller compared to the one of the CP radiation pattern.

Finally, the CP directivity is plotted in the (u, v) -plane in figure 4.27b and compared against the results from the verification example in figure 4.27a. It is clearly shown that, in contrast with the ver-

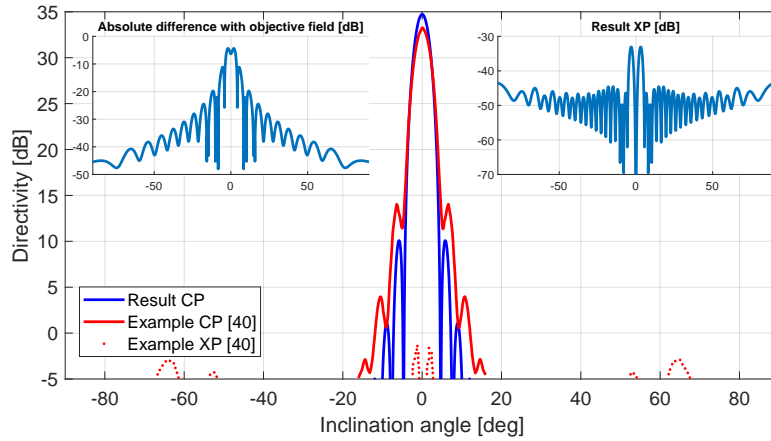


Figure 4.26: Main part: comparison between the resulting far-field CP pattern with the CP verification example (red solid line) and the XP (dotted line), obtained from Minatti et.al. [40, p. 3916]. Left inset: Difference between the resulting and the objective CP far-fields. Right inset: XP results. All the results are in the plane $\varphi = 45^\circ$.

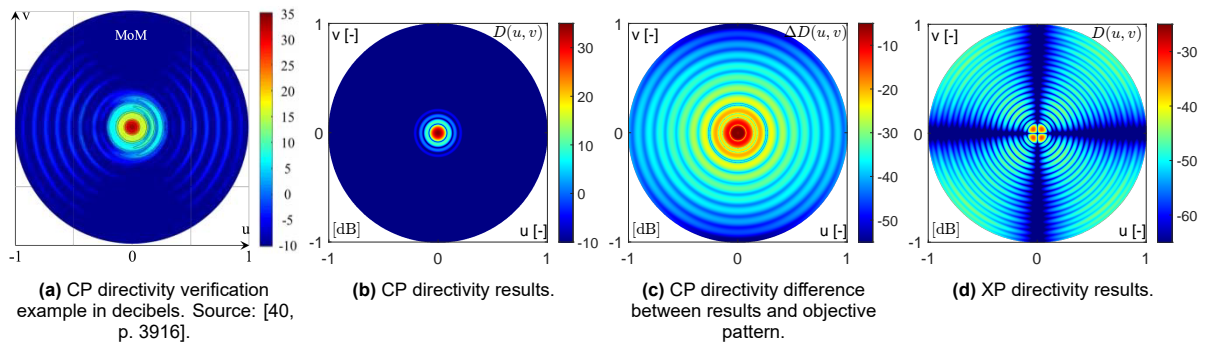


Figure 4.27: Directivity evaluated in the (u, v) -plane for the verification case.

ification example, the side lobe level in the results is underneath -10 dB in most of the (u, v) -plane, which is in agreement with the results obtained in figure 4.26. Next, the difference between the objective pattern and the results is plotted in figure 4.27c, which shows a small difference comparable with the left inset in figure 4.26. The XP directivity is plotted in figure 4.27d, where it is clearly visible that its maximum level is negligible compared with the CP level, and it is achieved in the diagonal plane, at $\varphi = 45^\circ$.

In conclusion, the verification of the antenna synthesis algorithm shows a good agreement between the example from [40] and the obtained results, even though the distributions used are different. This is further verified by comparing the far-field results of the obtained radiation pattern with the objective pattern, where the differences are negligible.

Results

Figure 4.28 shows the far-field results when using equation (4.9) as the aperture field distribution for the metasurface antenna. The maximum achieved directivity reaches 35.28 dB and the HPBW is 3.41° , just as predicted in table 4.2 but not fulfilling the antenna requirements for the SwarmSAR mission in table 2.1 of $D_{CP} = 36$ dB and HPBW= 3.2° . However, the author notes that the difference is relatively small and adjusting the exponent of the first expression between brackets in equation (4.9) to a value between zero and one would be enough to fill the required gap. This is because a bigger part of the aperture would be used, approaching the antenna to a diffraction limited system with uniform electric field distribution. Nevertheless, this would cause a higher side lobe level (FSLM), which requirement was not reported in table 2.1 but it increases the ambiguity level in measurements. The left inset in figure 4.28 shows a similar small negligible with the objective field as in figure 4.26, and the right inset shows the XP level, which is also negligible when compared with the main distribution.

Figure 4.29 shows the far-field CP and XP distributions in the (u, v) -plane, together with the dif-

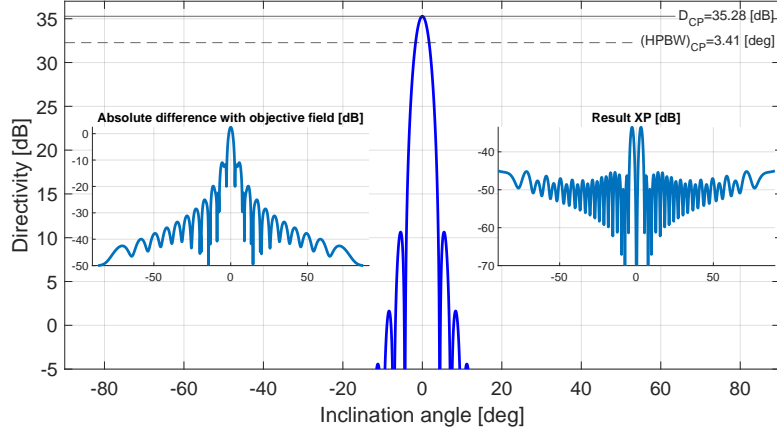


Figure 4.28: Main part: CP far-field radiation pattern of SAR antenna design. Left inset: Difference between the resulting and the objective CP far-fields. Right inset: XP results. All the results are in the plane $\varphi = 45^\circ$.

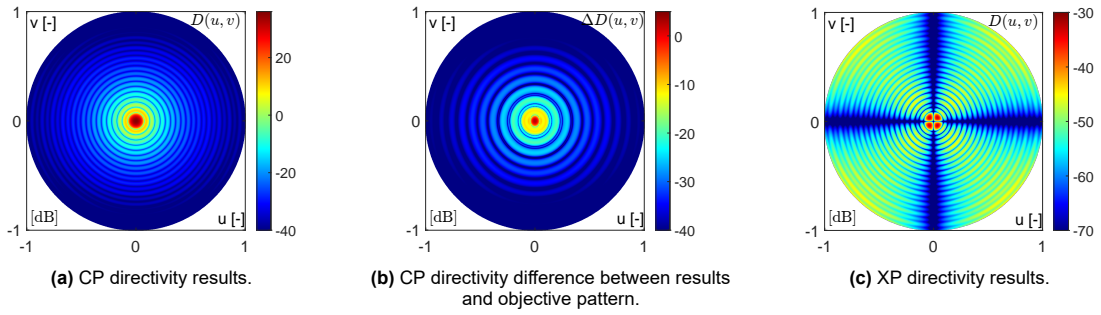


Figure 4.29: Directivity of SAR antenna evaluated in the (u, v) -plane.

ference of the CP with the objective. The resulting CP pattern in figure 4.29a shows an azimuthally symmetric behaviour up to -25 dB and a main beam in broadside direction, which corresponds with figure 4.28. Next, figure 4.29b shows a maximum difference of 5 dB with respect to the objective, which is still a negligible quantity given the beam directivity of 35.28 dB. The XP level in figure 4.29c shows again that its maximum is at the diagonal plane ($\varphi = 45^\circ$) and its magnitude is also relatively small compared to the main beam and the side lobe level.

The final result of this synthesis procedure is the metasurface antenna reactance distribution, shown in figure 4.30. It is evident the periodic nature of this dyadic expression, which arises from the exponential function of $\underline{\mathbf{X}}_s^{(\pm 1)}$ in equation (3.122c), particularly from $K_s(\rho)$ which represents the rapid periodic variation. Furthermore, $\underline{\mathbf{X}}_s$ varies in the azimuthal direction, reaching amplitude maximums at values multiples of $\phi = \pi/2$. At $\phi = 0^\circ$ and $\phi = 180^\circ$, $X_{s,\rho\phi} = 0$ and $X_{s,\rho\rho}$ and $X_{s,\phi\phi}$ have a periodic distribution along ρ with maximum amplitude, whereas at $\phi = 90^\circ$ and $\phi = 270^\circ$, $X_{s,\rho\rho} = X_{s,\phi\phi} = 0$ and $X_{s,\rho\phi}$ has maximum amplitude in radial direction. This is shown in figure 4.31 where figures 4.31a and 4.31b illustrate the first and second case respectively. In these two plots, it can be easily retrieved that the average reactance of $X_{s,\rho,\rho}$ and $X_{s,\phi,\phi}$ is $\bar{X}_{s,\rho} = \bar{X}_{s,\phi} = -146.89 \Omega$, varying $\pm 37.75 \Omega$ for the case where $\phi = 0^\circ$. On the other side, $X_{s,\rho,\phi}$ has an average value of 0° and varies $\pm 37.4 \Omega$ at $\phi = 90^\circ$.

4.3. Patch matching

In this subsection, the resulting transparent reactance of the antenna synthesis procedure obtained in section 4.2.2 is matched with the unit cell database in section 4.1.2 to obtain the final metasurface antenna design.

4.3.1. Method description

It can be easily concluded that the reactance database obtained in figure 4.18 and the verification database from figures 4.19a to 4.19c would not have the required reactance range to provide a solu-

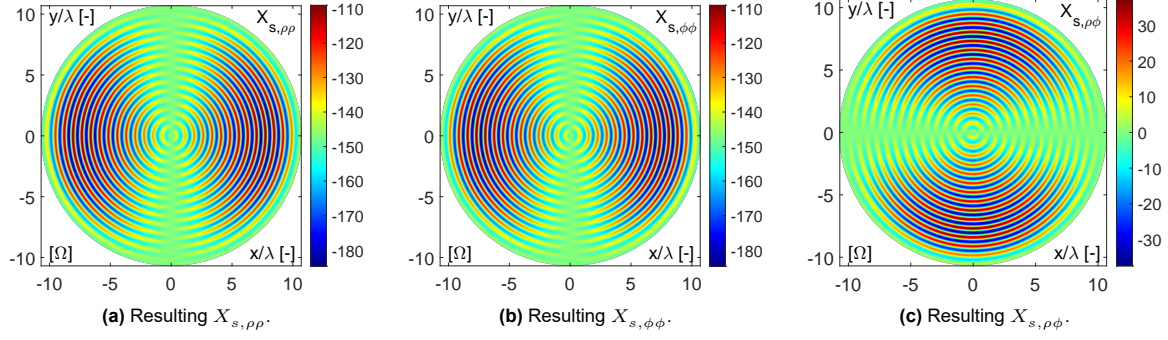


Figure 4.30: Final transparent reactance dyad in the metasurface antenna.

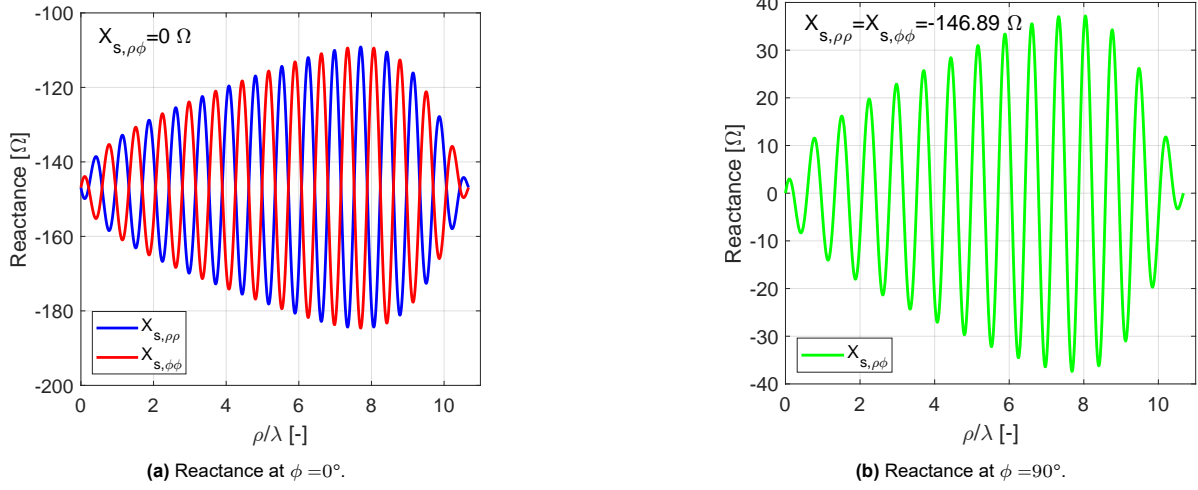


Figure 4.31: Transparent reactance at $\phi = 0^\circ$ and $\phi = 90^\circ$ for the metasurface SAR antenna.

tion for the reactance distribution obtained from the synthesis process in figure 4.31. This is because, from figure 4.31a at $\phi = 0$ (equivalent to having $\alpha_{sw} = 0$), the maximum reactance value is $X_{s,\rho\rho} = X_{s,\phi\phi} = -109.14 \Omega$, which is not contained in any of the reactance databases of $X_s^{(ee)}$ nor $X_s^{(hh)}$ presented in section 4.1.2. Even more, the maximum value of these databases is $X_s^{(ee)} = X_s^{(hh)} \approx -150 \Omega$, which is close to the average reactance value obtained in the synthesis process. Therefore, it is evident that the reactance database needs to be expanded in another dimension to cope with this insufficient amplitude range.

The other ellipse shape parameter that can be varied is the ratio a'/d which represents the patch size in the unit cell. Considering $X_s^{(ee)}$ and $X_s^{(hh)}$ are negative in every case, the transparent reactance, representing the patch cladding at the surface, is a capacitive surface. Therefore, to decrease the capacitive value and obtain the objective reactance range, the patch size must increase towards its short-circuit value of $X_s^{(ee)} = X_s^{(hh)} = 0 \Omega$. To decrease the computation time and facilitate this last part, this new database was provided by the authors of [27] for $\frac{a'}{d} \in [0.9, 1]$, keeping δ and η varying with the same values as in section 4.1.2.

The steps to perform this part are as follows:

1. **Discretise the antenna:** This step is performed in two dimensions considering the antenna radius a and the unit cell width and length d . It is important that all unit cells fit within the antenna, so blank spaces should be left when this condition is not fulfilled. Furthermore, a blank circular space has to be left in the antenna centre for its feeding mechanism, which the author chose arbitrarily to have a radius of $\bar{a} = 5 \text{ cm}$. Next to that, the x - and y -axes pass through the boundaries of neighbouring unit cells, which is convenient to define the antenna surface area in Cartesian coordinates in four quadrants with an equal number of unit cells in each of them, and each unit cell belonging to only one quadrant.

The antenna is then finally discretised in a finite number of elements where each of these corresponds to a unit cell on the antenna surface. These unit cells can be associated to a particular position in the xy -plane, which corresponds to its centre. The surface wave propagation angle α_{sw} , which in this case is the same as the azimuthal angle ϕ as the surface wave propagates in radial direction, can be easily calculated with the `atan2` function, returning the angle $\alpha_{sw} \in [0, 2\pi]$ from a two-dimensional vector. Finally, a transformation from polar to Cartesian coordinates of figure 4.30 is obtained to associate the final reactance requirement to each unit cell. Then, the remaining problem can be summarized as associating an elliptical patch shape to a required transparent reactance dyad $\underline{\underline{\tilde{\mathbf{X}}}}_s(x, y)$ given a propagation angle $\alpha_{sw}(x, y)$ for the whole set of unit cells discretised in the metasurface antenna.

2. **Align α_{sw} with the database:** A propagation angle $\alpha_{sw}(x, y)$ and a reactance dyad $\underline{\underline{\mathbf{X}}}_s(x, y)$ can be associated to each unit cell. In counterpart, the database can be expressed either with a constant α_{sw} as in figure 4.15, or with $\alpha_{sw} = \delta$, which varies in a fixed manner together with the patch orientation angle δ . This is because, as it was mentioned in section 4.1.1, the effect of varying the surface wave propagation angle can be analytically addressed with rotation matrices as shown in equation (3.118) because $\underline{\underline{\mathbf{X}}}_s$ is a diagonalizable matrix. Therefore, two paths can be taken to reconcile the different surface wave propagation angle between each unit cell and the reactance database: either rotate all the dyads in the database by $\alpha_{sw}(x, y)$ for each evaluated unit cell, or rotate all the unit cells to one reference angle which is aligned with the database. Certainly, the first one would be more computationally expensive as the number of rotations equals the number of unit cells times the number of elements in the database, whereas in the second case the number of rotations equals just the number of unit cells. However, the disadvantage in the second approach is that the obtained solution has to be rotated back to the original surface wave propagation angle associated to the unit cell $\alpha_{sw}(x, y)$. This would not pose a problem if the solution would be exactly found. On the contrary, if this is not the case, there would be an error introduced that would expand to the other elements in the transparent reactance dyad when this is rotated back, potentially causing a suboptimal patch distribution in the metasurface antenna. Nevertheless, as it is expected that the reactance database would contain the whole range of the required reactance, this second approach of rotating the unit cell reactance dyads was chosen.

The procedure to perform this step can be summarized as follows. Consider the objective transparent reactance dyad distribution in the metasurface antenna $\underline{\underline{\tilde{\mathbf{X}}}}_s(x, y)$ and the transparent reactance database aligned with $\alpha_{sw} = 0^\circ$. Then, $\underline{\underline{\tilde{\mathbf{X}}}}_s(x, y)$ has to be rotated as described in equation (4.33) so that the resulting objective transparent reactance distribution in the metasurface antenna $\underline{\underline{\tilde{\mathbf{X}}}}_{s,rot}(x, y)$, which is now expressed relatively to the same surface wave propagation angle as the database, can be matched to the transparent reactance of an elliptical patch shape.

$$\underline{\underline{\tilde{\mathbf{X}}}}_{s,rot}(x, y) = \underline{\underline{\mathbf{R}}}^\top [-\alpha_{sw}(x, y)] \cdot \underline{\underline{\tilde{\mathbf{X}}}}_s(x, y) \cdot \underline{\underline{\mathbf{R}}} [-\alpha_{sw}(x, y)] \quad (4.33)$$

3. **Minimize the difference between the required and the chosen shape reactance for each unit cell:** For each unit cell, before starting the optimization itself, an initial patch configuration has to be found to ensure that the optimization algorithm would converge with high probability to the global minimum. Given that the database is sampled relatively finely, each of the dyads contained in it can be subtracted by the objective dyad $\underline{\underline{\tilde{\mathbf{X}}}}_s(x, y)$, and the minimum difference from this operation, together with the corresponding shape variables η , $\frac{a'}{d}$ and ψ , can be subsequently found, serving as a starting point. Then, the optimization algorithm task is just refining this partial solution by using a linear interpolation function that evaluates a continuous range of η , $\frac{a'}{d}$ and ψ in the vicinity of this point. The resulting shape for the unit cell is given by $\eta(x, y)$, $\frac{a'}{d}(x, y)$ and $\psi(x, y)$, which corresponds to the transparent reactance solution found $\underline{\underline{\hat{\mathbf{X}}}}_{s,rot}(\eta, \frac{a'}{d}, \psi)$ in equation (4.34).

$$\eta(x, y), \frac{a'}{d}(x, y), \psi(x, y) = \underset{\substack{\eta \in [0.05, 1] \\ \frac{a'}{d} \in [0.9, 1] \\ \psi \in [0, 2\pi[}}{\text{argmin}} \left[\begin{array}{cc} 1 & 1 \end{array} \right] \cdot \left| \underline{\underline{\tilde{\mathbf{X}}}}_{s,rot}(x, y) - \underline{\underline{\hat{\mathbf{X}}}}_{s,rot} \left[\eta, \frac{a'}{d}, \psi(\alpha_{sw} = 0) \right] \right| \cdot \begin{bmatrix} 1 \\ 1 \end{bmatrix} \quad (4.34)$$

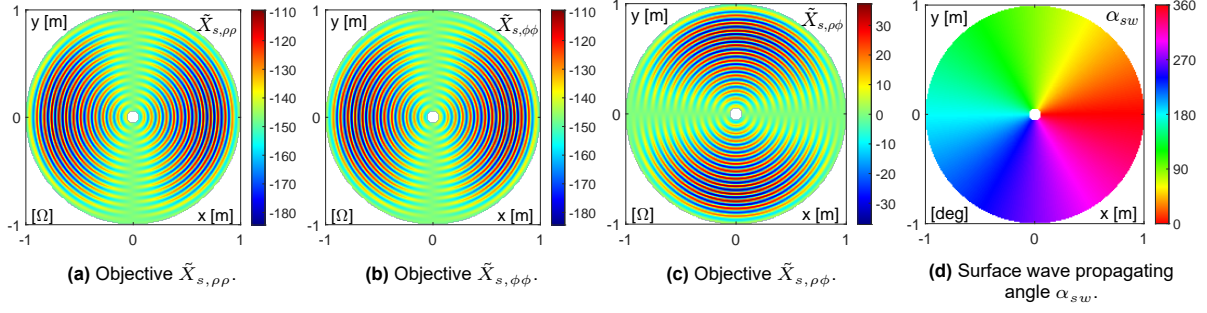


Figure 4.32: Discretisation results of objective transparent reactance and propagating angle of unit cells in the metasurface antenna.

To finalize, the obtained transparent reactance dyad $\hat{\underline{\underline{X}}}_{s,rot}$ is rotated back α_{sw} to obtain $\hat{\underline{\underline{X}}}_s(x, y)$ as in equation (4.35), which represents the final reactance distribution in the antenna.

$$\hat{\underline{\underline{X}}}_s(x, y) = \underline{\underline{\mathbf{R}}}^\top[\alpha_{sw}(x, y)] \cdot \hat{\underline{\underline{X}}}_{s,rot}(x, y) \cdot \underline{\underline{\mathbf{R}}}[\alpha_{sw}(x, y)] \quad (4.35)$$

4.3.2. Verification

As the previously presented method was developed by the author and in literature there is no available example of patch matching with a given reactance database, this cannot be verified with a literature example, making the verification rely only on unit tests. This is useful for step 1 to ensure that the discretisation is done correctly. However, for steps 2 and 3, this can be interpreted as redundant because step 2 involves just a matrix multiplication, and after performing step 3 the result can be found. Therefore, the verification is only centred in step 1 and, in the results part, the outcome of step 3 is evaluated against the objective reactance distribution $\hat{\underline{\underline{X}}}_{s,rot}$.

To verify step 1, figures 4.32a to 4.32c shows the objective reactance distribution, which is the discretised version of figure 4.30 in 30,928 unit cells. It is clearly visible that figures 4.32a to 4.32c resembles precisely figure 4.30. The other argument used is the propagation angle α_{sw} which plot shown in figure 4.32d illustrates the azimuthal angle in the metasurface antenna, which coincides with the incident surface wave angle.

4.3.3. Results

The result of the optimisation function presented in equation (4.34) and rotated back with equation (4.35) is shown in figure 4.33 in absolute and percentage terms, evaluated relatively to the absolute sum of all the dyadic elements. These results show that there is an important deviation from the objective values at angles between $[\pi/4, 3\pi/4]$ and $[5\pi/4, 7\pi/4]$, with maximum deviation at angles close to $\phi = 90^\circ$. To get a better insight on where the problem is, the difference between each element of the transparent reactance dyadic representation is shown in figure 4.34 in absolute and percentage values. It is first interesting to appreciate that the elements $X_{s,\rho\rho}$ and $X_{s,\phi\phi}$ have almost a perfect fit at $\phi = 90^\circ$, which deteriorates rapidly until angles close to $\phi = 45^\circ$. On the contrary, the worst fit in $X_{s,\rho\phi}$ is at $\phi = 90^\circ$, and it improves when this angle changes. The cause of this behaviour can be tracked down to figure 4.31, which shows the two extreme cases for the reactance distribution. The first one in figure 4.31a, when $\phi = 0^\circ$, is matched with the reactance database as the error shown in this region in figure 4.33 is negligible. On the contrary, the second one in figure 4.31b is not matched with the database as that is precisely the region where the error is. When comparing figures 4.31b and 4.34 it is clear that the average reactance values of $\hat{X}_{s,\rho\rho}$ and $\hat{X}_{s,\phi\phi}$ are matched, and the varying part of $\hat{X}_{s,\rho\phi}$ is not. Furthermore, given these results at $\phi = 90^\circ$, the mismatch in $\hat{X}_{s,\rho\rho}$ and $\hat{X}_{s,\phi\phi}$ close to $\phi = 90^\circ$ can be attributed to the effects of rotating back to the real surface wave propagation angle α_{sw} after obtaining the optimisation result because the error, which is initially in $\hat{X}_{s,\rho\phi}$, expands to other dyadic components after this rotation matrix is applied.

The percentage differences in figures 4.34d to 4.34f show that the deviation between $\hat{\underline{\underline{X}}}_s$ and $\tilde{\underline{\underline{X}}}_s$ is not negligible, reaching values up to 40% for the cross-diagonal component at angles close to $\phi = 90^\circ$. A close look at this angle is shown in figure 4.35, where the reactance difference and the shape param-

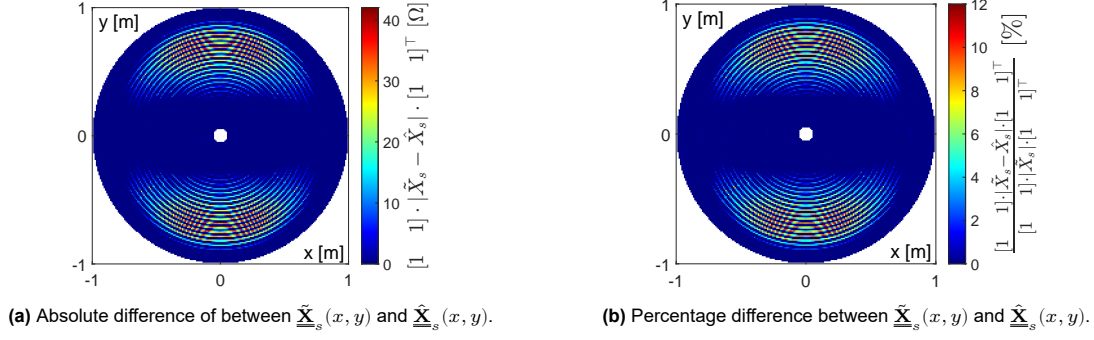


Figure 4.33: Absolute and percentage difference of the partial results between $\tilde{\underline{\underline{X}}}_s(x, y)$ and $\hat{\underline{\underline{X}}}_s(x, y)$ aligned with α_{sw} .

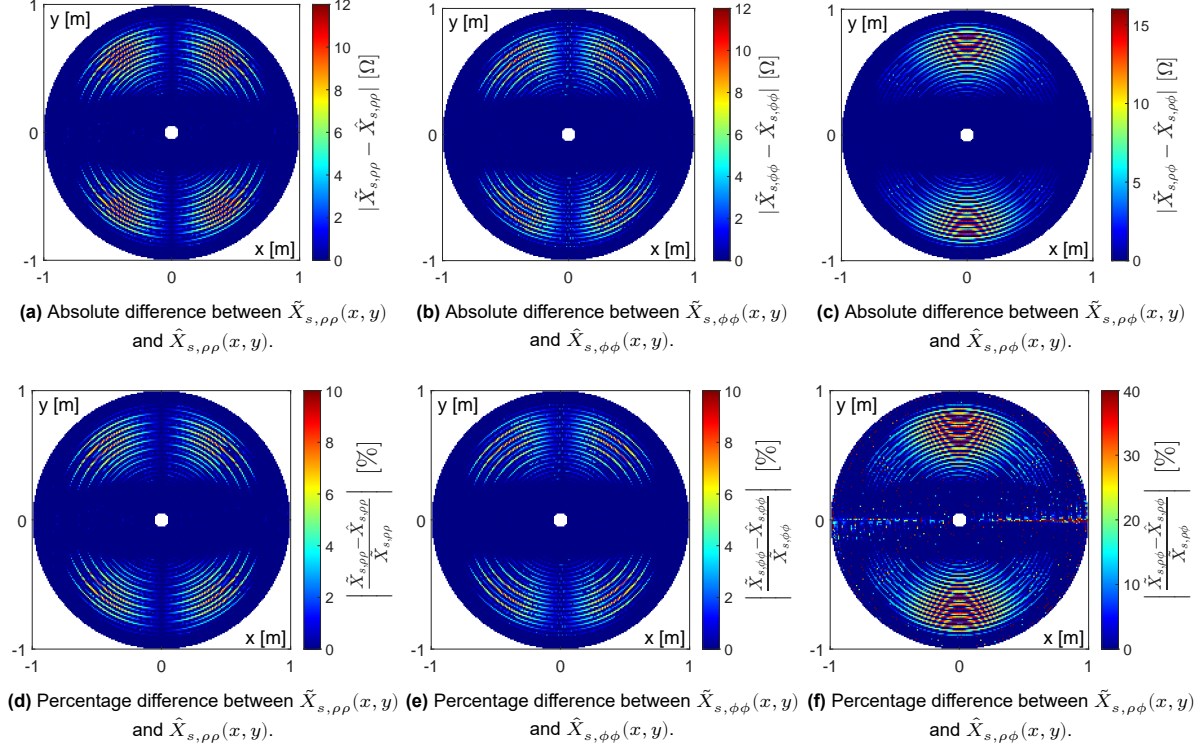


Figure 4.34: Absolute and percentage difference of the partial results between the dyadic components of $\tilde{\underline{\underline{X}}}_s(x, y)$ and $\hat{\underline{\underline{X}}}_s(x, y)$ aligned with α_{sw} .

eters of the unit cells in the first Cartesian quadrant adjacent to the y -axis are plotted. These results show additional insight on what can be done to address the reactance mismatch obtained by comparing per unit cell its shape parameters with the parts where the biggest reactance differences are. As explained before, the biggest differences are caused by the cross-diagonal component and these are where $\eta \approx 0.82$ and $\frac{a'}{d} \approx 1$. As $\eta \in [0.05, 1]$ and $\frac{a'}{d} \in [0.9, 1]$, the results in figure 4.35 suggest that increasing the value of $\frac{a'}{d}$ beyond one could decrease the reactance difference obtained. This is further confirmed by examining figure 4.36, which shows the reactance database as a function of η and $\frac{a'}{d}$ for $\psi = 45^\circ$, where the black lines indicate the required reactance values for maximum amplitude at $\phi = 90^\circ$. The shape parameters values obtained from the optimization algorithm for $\phi = 90^\circ$ at maximum amplitude coincide with the intersection point of the black lines in figures 4.36a and 4.36b with $\frac{a'}{d} = 1$, showing that the algorithm was obtaining the ideal values for $\tilde{X}_{s,\rho\rho}$ and $\tilde{X}_{s,\phi\phi}$, as it was already shown in figure 4.35. However, as the black lines in figure 4.36 do not intersect in any single point, then there is no solution in the database that could match the required reactance. Given that the line of maximum amplitude in figure 4.36c has a bigger slope than the ones in figures 4.36a and 4.36b and is situated at lower values of η , it would be expected that, for a sufficiently large value of $\frac{a'}{d}$, these two lines of maximum amplitude would intersect each other, reaching then a solution that would match the required

Table 4.3: Elliptical patch shapes simulated for the database expansion. Gray cells show the shape simulated as a function of δ (rows) and $\frac{a'}{d}$ (columns) for $\eta \in [0.72, 0.8]$.

	1.01	1.02	1.03	1.04		1.01	1.02	1.03	1.04
20°	Gray				110°	Gray			
25°	Gray	Gray			115°	Gray	Gray		
30°	Gray	Gray	Gray		120°	Gray	Gray	Gray	
35°	Gray	Gray	Gray	Gray	125°	Gray	Gray	Gray	Gray
40°	Gray	Gray	Gray	Gray	130°	Gray	Gray	Gray	Gray
45°	Gray	Gray	Gray	Gray	135°	Gray	Gray	Gray	Gray
50°	Gray	Gray	Gray	Gray	140°	Gray	Gray	Gray	Gray
55°	Gray	Gray	Gray	Gray	145°	Gray	Gray	Gray	Gray
60°	Gray	Gray	Gray	Gray	150°	Gray	Gray	Gray	Gray
65°	Gray	Gray	Gray	Gray	65°	Gray	Gray	Gray	Gray
70°	Gray	Gray	Gray	Gray	70°	Gray	Gray	Gray	Gray

reactance at maximum amplitude directed along $\phi = 90^\circ$.

Considering axiom 4.1 presented in section 4.1.1, $\frac{a'}{d}$ can only be increased beyond one if the major axis of the elliptical patch is not aligned neither with the unit cell x - or y -axes. When examining δ in figure 4.37, which represents the major axis angle with the x -axis, it can be concluded that when the surface wave propagates parallel to the y -axis, the patch is oriented at angles of $\delta = 45^\circ$ and $\delta = 135^\circ$, which are the angles at which $\frac{a'}{d}$ can be increased the most, up to $\sqrt{2}$ for $\eta \rightarrow 0^+$. Therefore, it can be concluded that an increase in $\frac{a'}{d}$ is possible and necessary to obtain a better fit between $\tilde{\mathbf{X}}_s$ and $\hat{\mathbf{X}}_s$.

More entries were added to the database to increase the range of $\frac{a'}{d}$ for a range of δ and η that could still fit in a unit cell. By extrapolating the black lines for values of $\frac{a'}{d}$ greater than one in figure 4.36, it was estimated that their intersection point would be at around $\frac{a'}{d} = 1.04$ and $\eta = 0.72$. This was taken as a reference point for $\delta = 45^\circ$ and $\delta = 135^\circ$, which was then scaled down in terms of $\frac{a'}{d}$ for angles further away from the unit cell diagonal. The additional performed unit cell simulations are shown in table 4.3, where the gray cells indicate that the given shape was added to the database. Table 4.3 is shown as a function of δ (rows) and $\frac{a'}{d}$ (columns) where $\Delta\delta = 5^\circ$, $\Delta\frac{a'}{d} = 0.01$, $\eta \in [0.72, 0.8]$, and $\Delta\eta = 0.02$.

The results after repeating the previously presented methodology are shown in figure 4.38 where the maximum error between $\tilde{\mathbf{X}}_{s,\rho\rho}$ and $\hat{\mathbf{X}}_{s,\rho\rho}$ has decreased from 12% in figure 4.33 to 5%. Furthermore, when comparing these two plots, a less dense error distribution is observed in figure 4.38, indicating that the error is present in less regions within the antenna. However, an error term is still present again close to $\phi = 90^\circ$, which is worth analysing in detail.

Figure 4.39 shows the reactance error distribution in absolute and in percentage terms for all the elements of the transparent reactance dyad. As in figure 4.34, the biggest contribution to the error is caused by the cross diagonal term $X_{s,\rho\phi}$ at angles close to $\phi = 90^\circ$, and a small contribution at $\phi = 20^\circ$. However, the percentage error in this same term has been reduced from 40% to 12%, and in the diagonal elements from 12% to 5%. Therefore, it can be concluded that there is an improvement in the antenna performance after adding the elliptical patch shapes from table 4.3.

To obtain a more clear impression on what has to be done to improve the results from figure 4.39, figure 4.40 was obtained, which is analogous to figure 4.35 which compares the error in reactance per dyadic element with η and $\frac{a'}{d}$ from the optimisation results. It results clear from this plot that again the outliers of the cross-diagonal reactance error are caused by a the range of $\frac{a'}{d}$, which reaches its maximum at the limit of the database, that is at $\frac{a'}{d} = 1.04$. Therefore, to further improve the fit the range of $\frac{a'}{d}$ has to be further increased to greater values. However, as this has already been done with positive results, it will not be performed again because of redundancy.

For completeness, the final shape parameters are reported in figure 4.41. Figure 4.41a shows the patch angle with the x -axis, which behave as expected. When the surface wave propagates horizontally ($\phi = 0^\circ$ or $\phi = 180^\circ$) there is no cross-diagonal reactance term, as it was shown in figure 4.31a. Therefore, the patch at these angles has either an orientation angle of $\delta = 0^\circ$ or $\delta = 90^\circ$. On the contrary,

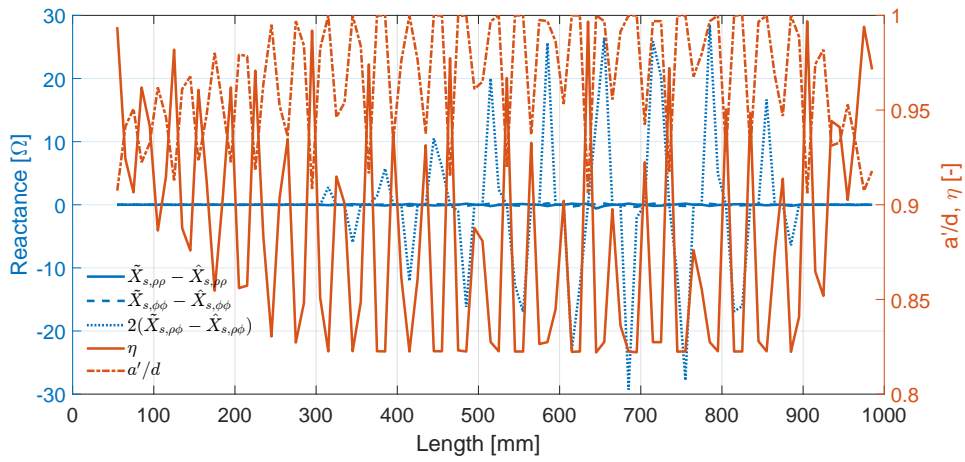
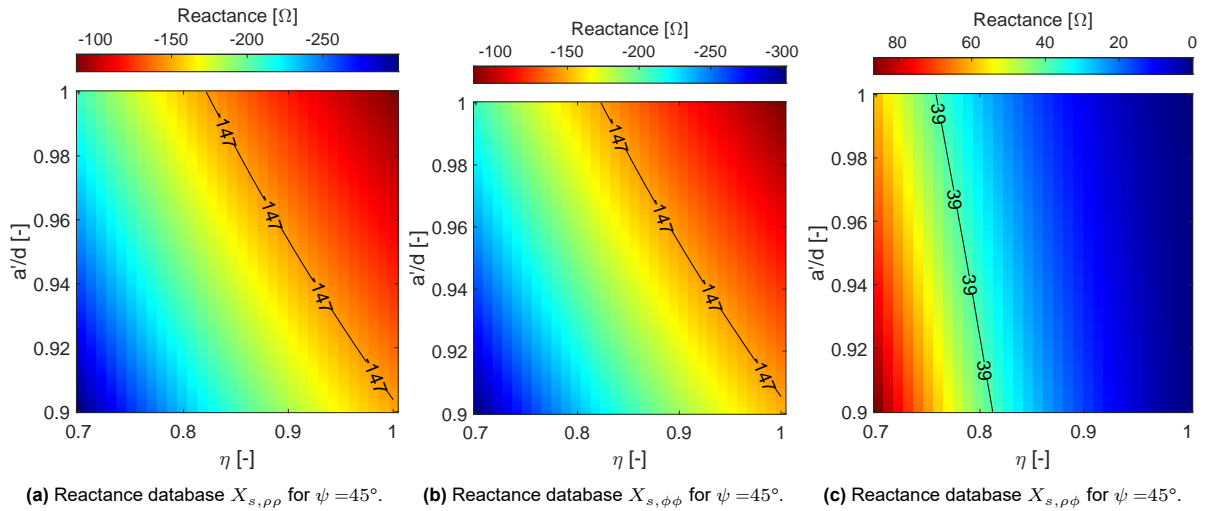


Figure 4.35: Reactance difference per dyadic component of the partial results compared with shape parameters η and $\frac{a'}{d}$ for a surface wave propagating approximately in vertical direction.



(a) Reactance database $X_{s,\rho\rho}$ for $\psi = 45^\circ$. **(b)** Reactance database $X_{s,\phi\phi}$ for $\psi = 45^\circ$. **(c)** Reactance database $X_{s,\rho\phi}$ for $\psi = 45^\circ$.

Figure 4.36: Reactance database $\underline{\underline{X}}_s$ for $\psi = 45^\circ$. The black lines indicate the reactance values for maximum amplitude at $\phi = 90^\circ$.

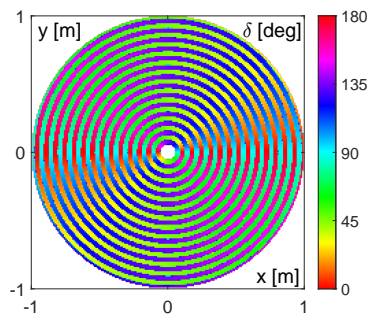
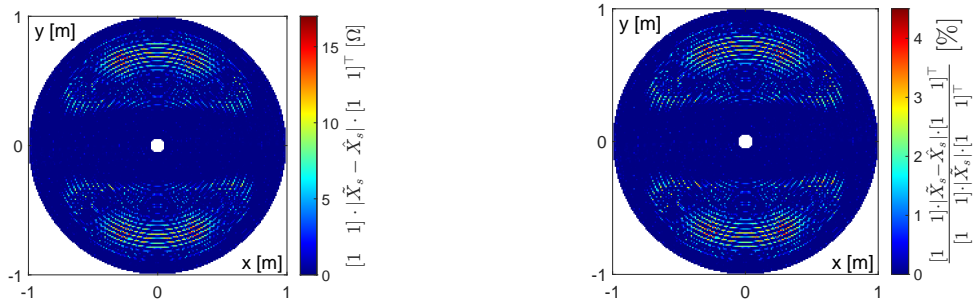
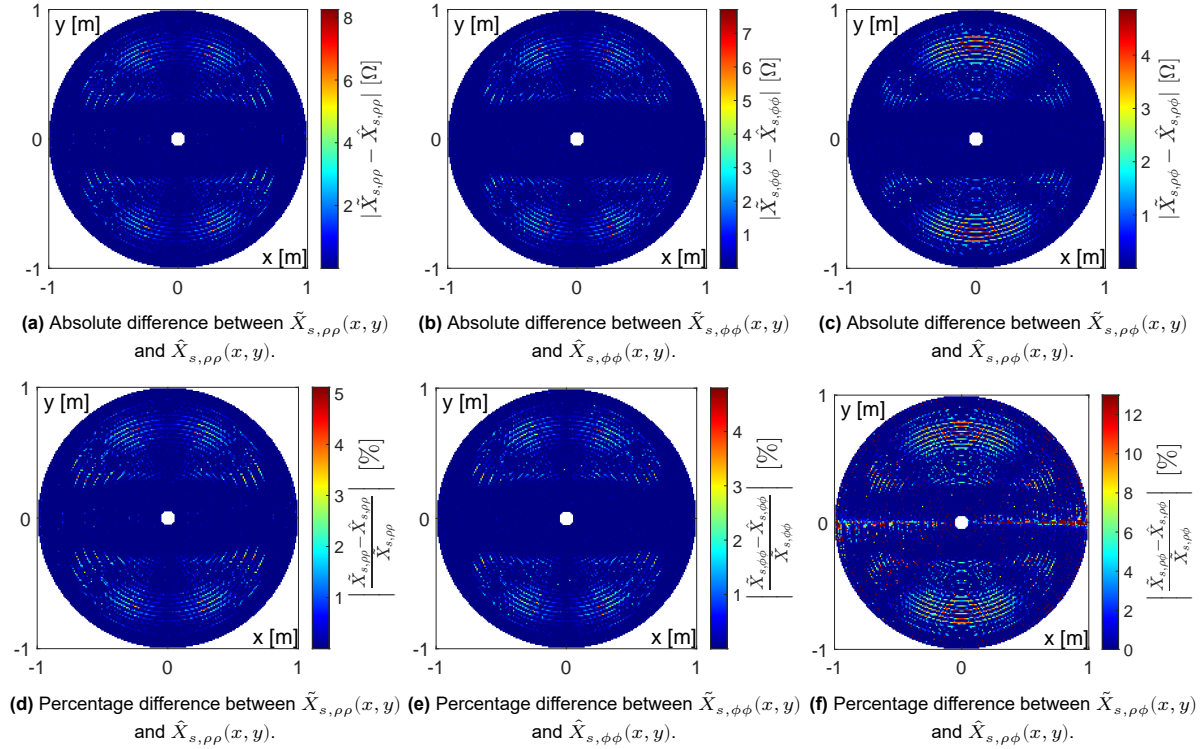
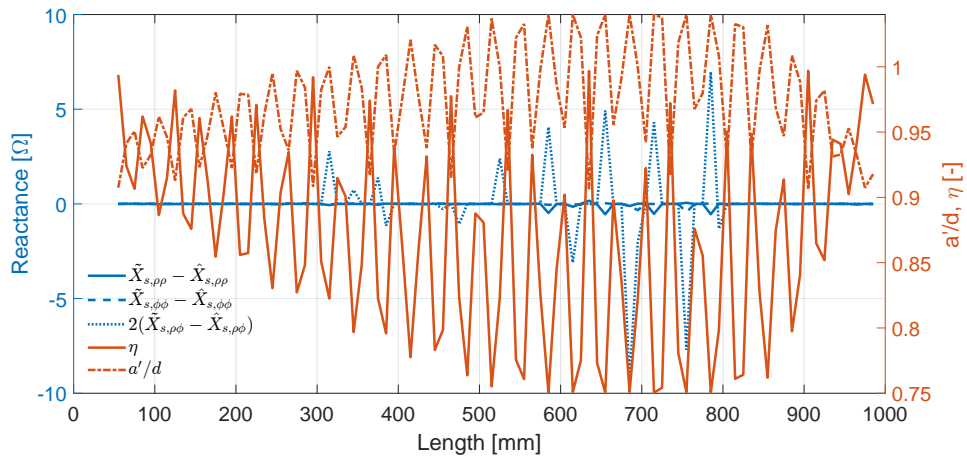


Figure 4.37: Patch orientation angle δ of the partial results with respect to the x -axis in the metasurface antenna.

(a) Absolute difference between $\tilde{\mathbf{X}}_s(x, y)$ and $\hat{\mathbf{X}}_s(x, y)$.(b) Percentage difference between $\tilde{\mathbf{X}}_s(x, y)$ and $\hat{\mathbf{X}}_s(x, y)$.**Figure 4.38:** Absolute and percentage difference of final results between $\tilde{\mathbf{X}}_s(x, y)$ and $\hat{\mathbf{X}}_s(x, y)$ aligned with α_{sw} .(a) Absolute difference between $\tilde{X}_{s,\rho\rho}(x, y)$ and $\hat{X}_{s,\rho\rho}(x, y)$.(b) Absolute difference between $\tilde{X}_{s,\phi\phi}(x, y)$ and $\hat{X}_{s,\phi\phi}(x, y)$.(c) Absolute difference between $\tilde{X}_{s,\rho\phi}(x, y)$ and $\hat{X}_{s,\rho\phi}(x, y)$.(d) Percentage difference between $\tilde{X}_{s,\rho\rho}(x, y)$ and $\hat{X}_{s,\rho\rho}(x, y)$.(e) Percentage difference between $\tilde{X}_{s,\phi\phi}(x, y)$ and $\hat{X}_{s,\phi\phi}(x, y)$.(f) Percentage difference between $\tilde{X}_{s,\rho\phi}(x, y)$ and $\hat{X}_{s,\rho\phi}(x, y)$.**Figure 4.39:** Absolute and percentage difference of final results between the dyadic components of $\tilde{\mathbf{X}}_s(x, y)$ and $\hat{\mathbf{X}}_s(x, y)$ aligned with α_{sw} .**Figure 4.40:** Reactance difference per dyadic component of final results compared with shape parameters η and $\frac{a'}{d}$ for a surface wave propagating approximately in vertical direction.

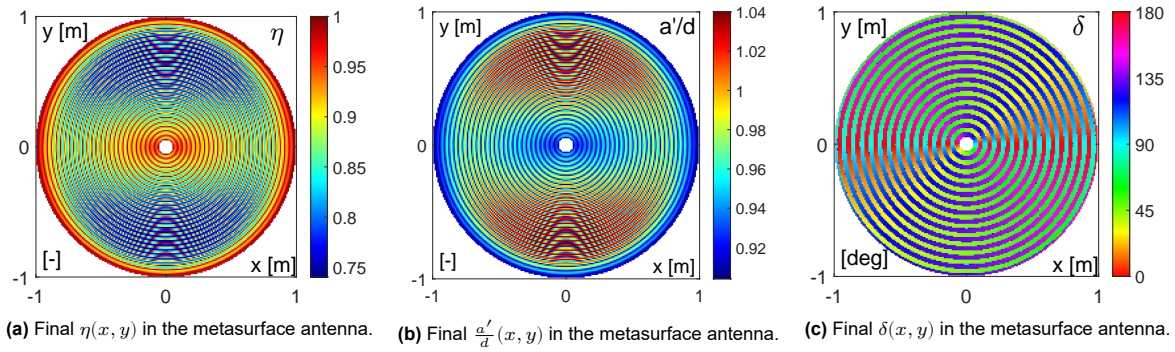


Figure 4.41: Final shape parameters in the metasurface antenna.

when the surface wave propagates vertically ($\phi = 90^\circ$ or $\phi = 270^\circ$), the patch is oriented at either $\delta = 45^\circ$ or $\delta = 135^\circ$ to obtain maximum cross-diagonal reactance. In the case of η and $\frac{a'}{d}$ not much more extra analysis can be made, only that η has high values and $\frac{a'}{d}$ low when the surface wave is close to the radial boundaries because the reactance amplitude tends to be low, which approximates the patch to have a circular shape with a relatively high reactance, which makes $\frac{a'}{d}$ relatively low.

Finally, the shape parameter distributions can be used to obtain the final antenna layout by using the data from figure 4.41 and the definition of each one of the shape parameters mentioned in figure 4.2. This results in the antenna design, which is shown in figure 4.42 and have been plotted in the xy -plane to illustrate the patch distribution. A detailed view of the patches that surround $\phi = 0^\circ$ and $\phi = 90^\circ$ is shown in figure 4.43, which illustrates the different elliptical shapes that correspond to the reactance of figure 4.31a and figure 4.31b respectively.

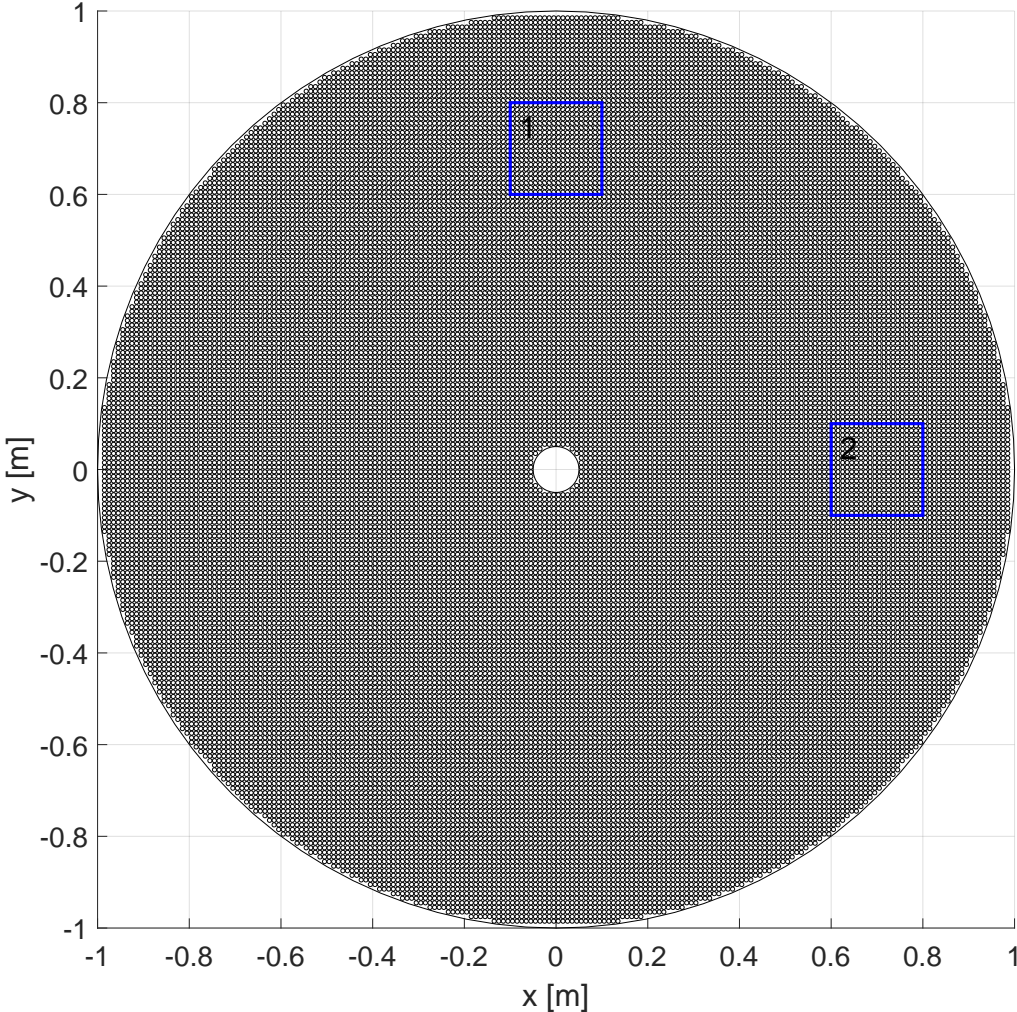


Figure 4.42: Final SAR metasurface antenna layout in the xy -plane. Areas 1 and 2 are shown in more detail in figure 4.43.

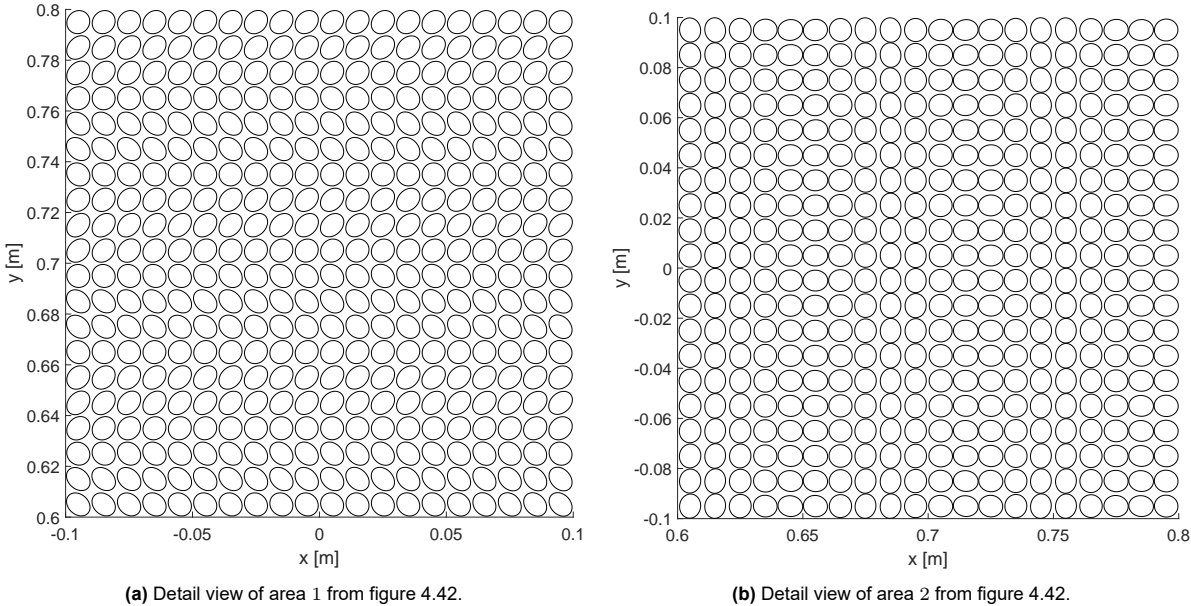


Figure 4.43: Metasurface SAR antenna detail views of figure 4.42.

5

Results and discussion

The outline of this chapter is as follows. In the first section, a first-level mass estimation is performed, which is followed by the comparison of the design results of the SAR metasurface antenna obtained in chapter 4 with the requirements for an individual SwarmSAR node stated in chapter 2. Next, to also finalize the report, the conclusions and recommendations are stated.

5.1. Design results

The last required figure of merit is the antenna mass. The first step is obtaining the dielectric mass, which is shown in equation (5.1) where $V = \pi/250$ represents the antenna volume for a circular area of 1 m radius and a thickness of 4 mm, and $\bar{\rho}_\epsilon = 2840 \text{ kg m}^{-3}$ is the density of the dielectric AR-1000¹.

$$\bar{m}_\epsilon = \bar{\rho}_\epsilon V = 2840 \frac{\pi}{250} \approx 36 \text{ kg} \quad (5.1)$$

Next, the mass of the remaining elements can be estimated. These are composed by the patch cladding in the dielectric surface, the ground plane and the structural parts that would keep the antenna fixed. A design concept has been proposed by Minatti et.al. where the metasurface is mounted over a multilayer structure composed of a top and a bottom layer of carbon fibre and a quartz honeycomb layer in between [38]. This sketch is shown in figure 5.1, which has been reported to have a total mass of 2.26 kg for an antenna of 27 cm radius, and 1.575 mm dielectric thickness, using the Roger TMM10i dielectric which has a density of $2761.69 \text{ kg m}^{-3}$ [38]². From this reported antenna, the mass of 1 kg representing the contribution of the dielectric substrate can be subtracted, which results in 1.26 kg as the remaining mass of the patch cladding, the ground plane and the antenna support structure. Using these results, a lower and an upper bound for a first weight estimation of the synthesized antenna is obtained as follows:

- **Lower bound:** This can be interpreted as extending the dimensions of the ground plane, the support structure and the patch cladding from the example in [38] to the final design obtained in chapter 4. The surface density can be extracted from this example, which results in $\bar{\rho}_r = 5.5 \text{ kg m}^{-2}$. Subsequently, this is multiplied by the antenna area of $A = 3.14 \text{ m}^2$, which results in an added mass of 17 kg and a total mass of 53 kg. This is considered to be an underestimation because the mass is increasing only considering the increase in area, ignoring the additional weight of the dielectric, which now is thicker (4 mm) and therefore concentrates more mass per squared meter.
- **Upper bound:** This value can be calculated by extrapolating the ratio 1.26 obtained by dividing the structure mass (1.26 kg) by the dielectric mass (1 kg) from the example antenna to the one obtained in chapter 4. This results in an added mass of 45 kg and a total mass of 81 kg.

A summary of the presented antenna capabilities is shown in table 5.1, which can be compared against the antenna requirements presented in section 2.2.2 as follows:

¹Typical Properties: AR-1000. <http://www.agssales.com/ar1000.pdf> Retrieved on 04-11-2022.

²TMM® 10i Laminates - Rogers Corporation. <https://www.rogerscorp.com/advanced-electronics-solutions/tmm-laminates/tmm-10i-laminates> Retrieved on 04-11-2022.

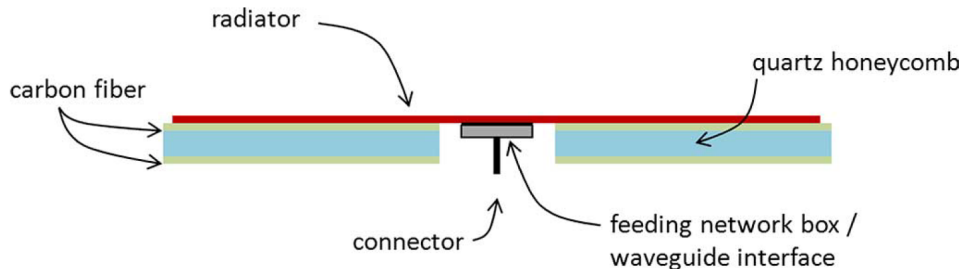


Figure 5.1: Metasurface antenna mounting configuration. Source: [38]

Table 5.1: Metasurface SAR antenna design main characteristics.

Parameter	Value
Frequency	3.2 GHz
Surface area	3.1 m ²
Directivity	35.28 dB
XP level	-30 dB
HPBW	3.41°
Side lobe level	11 dB
Polarization	Linear
Dielectric mass	36 kg
Total mass	53 kg - 81 kg
Surface weight ratio	0.04 m ² /kg - 0.06 m ² /kg

- *SwarmSAR-SYS-Sub-PL-Ant-01*, which fixes the central antenna frequency, is fulfilled but the broadband response has still to be evaluated.
- *SwarmSAR-SYS-Sub-PL-Ant-02*, which sets the bandwidth size, can only be evaluated when obtaining the antenna broadband response.
- *SwarmSAR-SYS-Sub-PL-Ant-03*, which limits the maximum antenna size, is fulfilled as this restriction has been considered in the first part of the modulation.
- *SwarmSAR-SYS-Sub-PL-Ant-04*, which indicates the target directivity, is not yet fulfilled because the target value is 36 dB and the one obtained is 35.28 dB. The author notes that this difference requires one more iteration to be fulfilled because the exponent of the first expression in brackets in equation (4.9), which defines the electric field amplitude in the aperture, has to be adjusted to reach the objective value.
- *SwarmSAR-SYS-Sub-PL-Ant-05*, which shows the target value of 3.2° of the HPBW, as in the previous requirement is not yet fulfilled because the HPBW that the designed antenna reaches is just above it, with 3.41°. As in the previous case, this just requires one more iteration that adjusts the amplitude of the electric field in the aperture.
- *SwarmSAR-SYS-Sub-PL-Ant-06*, which proposes a minimum transmitted power, has not yet been evaluated as the feeding design is not included in this methodology.
- The same applies to *SwarmSAR-SYS-Sub-PL-Ant-07*, which sets a maximum variation of the pulse length, as it is part of the feeding system.
- *SwarmSAR-SYS-Sub-PL-Ant-08*, which indicates the antenna's maximum mass, is not met as this requirement aims for a value of 1 m²/kg and the one that is obtained with this design is between 0.04 m²/kg and 0.06 m²/kg. This cannot be easily solved without changing other requirements because the difference is approximately a factor of twenty.

The comparison between the antenna requirements and the final result from applying the proposed methodology shows that, even though these requirements for the single-frequency case are mostly met (or require one more iteration), the mass is still an important restriction for the implementation of these type of structures when it is so constrained as in this case. For such cases, structures as the reference case presented in section 2.3 could perform better because they achieve easily *SwarmSAR-SYS-Sub-PL-Ant-08*. When this requirement is mentioned in the original research of Iannini et.al. [17],

the authors acknowledge that it is a challenging requirement for large antennas in mini satellites and that their baseline is a “reflector-based antenna with a circular dish, illuminated by a single feed” [17]. If it would be needed to fulfil *SwarmSAR-SYS-Sub-PL-Ant-08* independently from the other requirements with a metasurface antenna, the value of $1 \text{ m}^2/\text{kg}$ can be achieved by shifting to a higher frequency where $h\bar{\rho}_\epsilon < 1 \text{ m}^2/\text{kg}$, only considering the mass of the dielectric substrate. This demands a thickness, for the AR-1000 dielectric substrate, of 0.35 mm, which can be achieved with the presented method only by using a higher central frequency to avoid higher-order mode propagation. Another form to come closer to the required mass value is by using a different material for the dielectric layer, which has to be less dense and suitable for the production of printed circuit boards, which is the method used to fabricate metasurface antennas. For this exercise, the material AR-1000 has been used because it is cited in the metasurface antenna literature as being similar to others used for space [36, 12]. However, a better option could be looked for with a smaller mass density value.

On the other side, this does not exclude metasurface antennas from space applications. The fact that the final structure has only one feeding point, whereas the antenna presented for comparison has 256 radiating elements, makes this methodology suitable when only one radiating mode is required as it reduces the system complexity and possible failure points. Applications are not only limited to SAR, but also can be used for satellite communications in the K_a -band as presented in the work of Minatti et.al. [38]. It is important to recall that nowadays laser satellite communication is being intensively developed for all type of satellites. However, given its obvious advantages of high bandwidth and low possibility of intercepting and jamming a signal, there are still challenging obstacles such as the weather interference [52], the dispersive effect of the atmosphere [49], and the high accuracy needed for the attitude determination and control subsystem, which are not a problem for communication in the radio spectrum. In the case where laser satellite communication would replace traditional communication antennas, they can be added to a platform for redundancy if there is a problem with the optical link between the transmitter and the receiver optical terminals. Furthermore, different radiation patterns can be obtained with the presented modulation procedure that could be used to communicate to more than one terminal at the same time, which is not achievable with one laser satellite communication transmitter. To obtain these different radiation patterns it is precise to change only the patch cladding in the interface, which simplifies the qualification and acceptance procedures for the antenna design [38]. There are other methods that could be integrated in the developed methodology in case it is needed to expand the number of radiating modes. One of them uses multiple feeding points to receive from multiple areas in the spherical plane [14], whereas another transmits and receives in both right-hand and left-hand circular polarizations [50].

Another interesting comparison is the one of the metasurface antenna with a reflector dish antenna, as the second one is characterized by a more simple design for a pencil-beam radiation pattern as it consists of a curved metallic dish with a horn antenna used as a feeding point. However, when a different radiation pattern is used, the reflector dish needs to be shaped such that the desired radiation characteristics are obtained, which ends up slowing down the spacecraft design, qualification and acceptance processes. In contrast, a metasurface antenna has a rather standard printing circuit board procedure to obtain different radiation patterns saves time in these processes. Next to that, having a planar antenna helps to its deployment in comparison with a curved dish, which ends up occupying more volume in the satellite. Therefore, a metasurface antenna can be regarded as a trade-off between a phased-array antenna, which can generate many radiation patterns but it is more complex and generally heavier, and a reflector dish antenna, which is generally simpler and applied for high-gain radiation patterns.

5.2. Conclusion and recommended further work

A procedure to design a metasurface antenna has been presented in this thesis report, which used as starting point the work of previous authors and adapted it to available commercial tools for EM simulation to reduce the implementation time. This work has been presented in the context of the design of an antenna for space-based SAR in the S-band (*SwarmSAR* constellation) which, even though its mass cannot fit within the design requirements, its central frequency performance satisfies them. To answer the first research question formulated in chapter 1, the proposed methodology starts by obtaining a reactance database for a particular patch shape, followed by obtaining the reactance distribution in the antenna, and finally matching both distributions to end up with an antenna layout for a predetermined

radiation pattern. The reactance database has been derived using scattering data obtained from full-wave simulations performed with the commercial software Lumerical® FDTD. It has been shown that these values have negligible deviations when compared to the verification examples. Next, the antenna synthesis has been performed using adiabatic Floquet analysis with satisfactory results. Finally, the result of these two parts are matched using an optimization algorithm that minimizes the deviation between the objective reactance and the one from the database to find the best possible shape for a particular unit cell. In the SAR case, the antenna is composed out of 30,928 unit cells, which is the aggregate result of scattering simulations and optimization procedures to deliver a device that can generate a given radiation pattern. The reader then can use this methodology to design printed circuit boards masks that, when connected to a feeding point at its centre that launches azimuthally symmetric surface waves (e.g. monopole), would work as an antenna with a predefined radiation pattern.

It is important to note that a non-conventional and very advanced antenna design was used to answer the second research question. This design, specified in section 2.3, consists of a low-mass blanket with multiple patch antennas that effectively work as a phased-array antenna. Even though it has been shown that in terms of mass, the reference case outperforms the metasurface antenna, in terms of complexity it does not. The metasurface antenna has only one feeding point, whereas the phased-array used in the example has 256, which are additional possible failure points. Furthermore, to have different radiation patterns in a metasurface antenna, only the patch distribution on its surface would have to change to achieve this functionality, consequently saving design, qualification and acceptance times. Next to that, the weight estimation has been done considering the standard material AR-1000, widely cited in literature for being used for metasurface antenna fabrication. However, a different material with similar electrical properties and lower mass density could be used to reduce the antenna mass.

There are multiple parts in the design that have not been addressed and are encouraged for future work. The first one and most important is to perform a full-wave simulation of the antenna to verify that the actual patch distribution produces the adequate far-field radiation pattern in the intended broadband frequency range. This can be performed by relying in a MoM formulation that uses an adequate set of basis functions to evaluate the patch distribution over the antenna. Next, an expression to represent the distance between the elliptical patches in adjacent unit cells, dependent on the patch inclination angle and the minor axis ratio with the major axis, should be derived. In the presented work, this was represented with the ratio of major axis against unit cell size, which was restricted to a maximum value of 1 because in the worst case scenario this was the value that would make the minimum distance between adjacent patches equal to zero. However, it was shown in section 4.3.3 that extending this beyond one for some inclination angle and minor axis ratio combinations could increase the reactance range of the database, meeting the requirements for the antenna synthesis. Next, a method to obtain the exact dimensions of the feeding system should be implemented, which can rely in iterative optimization to avoid reflections between the waveguide that launches the surface wave and the metasurface antenna. Subsequently, an assessment on the losses in the antenna should be performed, which could be integrated in the full-wave simulation by considering actual material losses. Finally, the manufacturability of the antenna has to be addressed by integrating the tolerances of the printed circuit manufacturing technology into a statistical process to obtain the error distribution in the far-field pattern after the antenna is manufactured. The author suggests using a Montecarlo scheme with the full-wave antenna simulation.

The next step to make this technology accessible and more attractive for more types of missions is making the antenna deployable. As this antenna is planar and can be easily manufactured, it would be attractive for CubeSat missions operating in a higher frequency range where the dielectric does not contribute much to the whole antenna mass. As a deployable concept would imply dividing the antenna in segments, further studies should be performed to address how the discontinuities in the structure would impact the antenna performance, and how to reduce them.

Another interesting application is using these antennas for compressive sensing applications. The idea would consist on taking advantage of the metasurface dispersive nature to generate pseudo-random radiation patterns with a high degree of orthogonality between each other in a narrow frequency range. Then, sampling a wide field of view at these different frequencies would generate orthogonal responses, which could be used to reconstruct it with a sub-Nyquist sampling scheme avoiding aliasing effects. Some comparisons of using metasurface antennas in compressive sensing with other sampling schemes can be found in [45, 46].

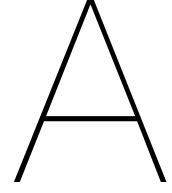
References

- [1] Constantine A. Balanis. *Antenna Theory - Analysis and Design (4th Edition)*. John Wiley & Sons, 2016. ISBN: 978-1-118-64206-1. URL: <https://app.knovel.com/hotlink/toc/id:kpATADE01N/antenna-theory-analysis/antenna-theory-analysis>.
- [2] Jean-Pierre Berenger. *Perfectly Matched Layer (PML) for Computational Electromagnetics*. Morgan & Claypool, 2007.
- [3] Arun K. Bhattacharyya. *Phased Array Antennas: Floquet Analysis, Synthesis, BFNs, and Active Array Systems*. John Wiley & Sons, Ltd, 2005.
- [4] Michael Boyarsky et al. "Synthetic aperture radar with dynamic metasurface antennas: a conceptual development". In: *J. Opt. Soc. Am. A* 34.5 (May 2017), A22–A36. DOI: 10.1364/JOSAA.34.000A22. URL: <http://opg.optica.org/josaa/abstract.cfm?URI=josaa-34-5-A22>.
- [5] Ovidio Mario Bucci et al. "Intersection approach to array pattern synthesis". In: *IEE Proceedings H (Microwaves, Antennas and Propagation)*. Vol. 137. 6. IET, 1990, pp. 349–357.
- [6] Daniele Cavallo. "Connected array antennas : analysis and design". English. PhD thesis. Electrical Engineering, 2011. ISBN: 978-94-6191-035-6. DOI: 10.6100/IR719461.
- [7] Agnieszka Choroszucho. "Analysis of the influence of the complex structure of clay hollow bricks on the values of electric field intensity by using the FDTD method". In: *Archives of Electrical Engineering* vol. 65.No 4 December (2016), pp. 745–759. DOI: 10.1515/aee-2016-0052. URL: <http://journals.pan.pl/Content/102171/PDF/DOI%5C%2010.1515aee-2016-0052.pdf>.
- [8] Marco Faenzi, David González-Ovejero, and Stefano Maci. "Flat Gain Broadband Metasurface Antennas". In: *IEEE Transactions on Antennas and Propagation* 69.4 (2021), pp. 1942–1951. DOI: 10.1109/TAP.2020.3026476.
- [9] Marco Faenzi et al. "Metasurface Antennas: New Models, Applications and Realizations". In: *Scientific Reports* 9.1 (2019). DOI: 10.1038/s41598-019-46522-z.
- [10] Tom G. Farr et al. "The Shuttle Radar Topography Mission". In: *Reviews of Geophysics* 45.2 (2007). DOI: <https://doi.org/10.1029/2005RG000183>. eprint: <https://agupubs.onlinelibrary.wiley.com/doi/pdf/10.1029/2005RG000183>. URL: <https://agupubs.onlinelibrary.wiley.com/doi/abs/10.1029/2005RG000183>.
- [11] Bryan H. Fong et al. "Scalar and Tensor Holographic Artificial Impedance Surfaces". In: *IEEE Transactions on Antennas and Propagation* 58.10 (2010), pp. 3212–3221. DOI: 10.1109/TAP.2010.2055812.
- [12] Matteo Alessandro Francavilla et al. "On the Numerical Simulation of Metasurfaces With Impedance Boundary Condition Integral Equations". In: *IEEE Transactions on Antennas and Propagation* 63.5 (2015), pp. 2153–2161. DOI: 10.1109/TAP.2015.2407372.
- [13] David González-Ovejero and Stefano Maci. "Gaussian Ring Basis Functions for the Analysis of Modulated Metasurface Antennas". In: *IEEE Transactions on Antennas and Propagation* 63.9 (2015), pp. 3982–3993. DOI: 10.1109/TAP.2015.2442585.
- [14] David González-Ovejero et al. "Multibeam by Metasurface Antennas". In: *IEEE Transactions on Antennas and Propagation* 65.6 (2017), pp. 2923–2930. DOI: 10.1109/TAP.2017.2670622.
- [15] Yang Hao and Mittra Raj. *FDTD Modeling of Metamaterials : Theory and Applications*. Artech House, 2008.
- [16] Roger F. Harrington. *Time-Harmonic Electromagnetic Fields*. IEEE Press Series on Electromagnetic Wave Theory. Wiley, 2001. ISBN: 9780471208068. URL: <https://books.google.nl/books?id=4-6kNAEACAAJ>.

- [17] Lorenzo Iannini, Paco Lopez-Dekker, and Peter Hoogeboom. "A Highly Flexible and Scalable S-band SwarmSAR from Very Simple Nodes". In: *2020 IEEE Radar Conference (RadarConf20)*. 2020, pp. 1–6. DOI: 10.1109/RadarConf2043947.2020.9266527.
- [18] David R. Jackson. *Transverse resonance method*. Consulted on 11-02-2022 <http://courses.egr.uh.edu/ECE/ECE5317/Class%20Notes/Notes%2015%205317-6351%20Transverse%20Resonance%20Method.pdf>. 2019.
- [19] Aobo Li, Shreya Singh, and Dan Sievenpiper. "Metasurfaces and their applications". In: *Nanophotonics* 7.6 (2018), pp. 989–1011. DOI: doi:10.1515/nanoph-2017-0120. URL: <https://doi.org/10.1515/nanoph-2017-0120>.
- [20] Guy Lipworth et al. "Metamaterial apertures for coherent computational imaging on the physical layer". In: *J. Opt. Soc. Am. A* 30.8 (Aug. 2013), pp. 1603–1612. DOI: 10.1364/JOSAA.30.001603. URL: <http://www.osapublishing.org/josaa/abstract.cfm?URI=josaa-30-8-1603>.
- [21] Yu Liu, Yijun He, and Biao Zhang. "Ocean wave parameters retrieved directly from compact Polarimetric SAR data". In: *Acta Oceanologica Sinica* 41.4 (2022). DOI: 10.1007/s13131-021-1855-6.
- [22] Art Ludwig. "The definition of cross polarization". In: *IEEE Transactions on Antennas and Propagation* 21.1 (1973), pp. 116–119. DOI: 10.1109/TAP.1973.1140406.
- [23] Stefano Maci. "Metasurfaces: from Numerical Models to EM devices". In: *2019 13th European Conference on Antennas and Propagation (EuCAP)*. 2019, pp. 1–3.
- [24] Stefano Maci and Alessio Cucini. "FSS-Based EBG Surfaces". In: *Metamaterials: Physics and Engineering Explorations*. Ed. by Nader Engheta and Richard W Ziolkowski. 2006, pp. 351–376. DOI: 10.1002/0471784192.ch13.
- [25] Stefano Maci et al. "Metasurfing: Addressing Waves on Impenetrable Metasurfaces". In: *IEEE Antennas and Wireless Propagation Letters* 10 (2011), pp. 1499–1502. DOI: 10.1109/LAWP.2012.2183631.
- [26] Enrica Martini, Francesco Caminita, and Stefano Maci. "Double-scale homogenized impedance models for periodically modulated metasurfaces". In: *EPJ Appl. Metamat.* 7 (2020), p. 12. DOI: 10.1051/epjam/2020010. URL: <https://doi.org/10.1051/epjam/2020010>.
- [27] Enrica Martini and Stefano Maci. "Metasurface Transformation Theory". In: *Transformation Electromagnetics and Metamaterials: Fundamental Principles and Applications*. Ed. by Douglas H. Werner and Do-Hoon Kwon. London: Springer London, 2014, pp. 83–116. ISBN: 978-1-4471-4996-5. DOI: 10.1007/978-1-4471-4996-5_3. URL: https://doi.org/10.1007/978-1-4471-4996-5_3.
- [28] Enrica Martini, Mario Mencagli, and Stefano Maci. "Metasurface transformation for surface wave control". In: *Philosophical Transactions of the Royal Society A: Mathematical, Physical and Engineering Sciences* 373.2049 (2015), p. 20140355. DOI: 10.1098/rsta.2014.0355. eprint: <https://royalsocietypublishing.org/doi/pdf/10.1098/rsta.2014.0355>. URL: <https://royalsocietypublishing.org/doi/abs/10.1098/rsta.2014.0355>.
- [29] Enrica Martini et al. "Flat Optics for Surface Waves". In: *IEEE Transactions on Antennas and Propagation* 64.1 (2016), pp. 155–166. DOI: 10.1109/TAP.2015.2500259.
- [30] Ladislau Matekovits, Valeriu Adrian Laza, and Giuseppe Vecchi. "Analysis of Large Complex Structures With the Synthetic-Functions Approach". In: *IEEE Transactions on Antennas and Propagation* 55.9 (2007), pp. 2509–2521. DOI: 10.1109/TAP.2007.904073.
- [31] Ross C. McPhedran et al. "Metamaterials and metaoptics". In: *NPG Asia Materials* (2011). <https://doi.org/10.1038/asiamat.2011.146>.
- [32] Mario Mencagli, Enrica Martini, and Stefano Maci. "Surface Wave Dispersion for Anisotropic Metasurfaces Constituted by Elliptical Patches". In: *IEEE Transactions on Antennas and Propagation* 63.7 (2015), pp. 2992–3003. DOI: 10.1109/TAP.2015.2422352.
- [33] Mario Mencagli, Enrica Martini, and Stefano Maci. "Transition Function for Closed-Form Representation of Metasurface Reactance". In: *IEEE Transactions on Antennas and Propagation* 64.1 (2016), pp. 136–145. DOI: 10.1109/TAP.2015.2500264.

- [34] Gabriele Minatti, Enrica Martini, and Stefano Maci. "Efficiency of Metasurface Antennas". In: *IEEE Transactions on Antennas and Propagation* 65.4 (2017), pp. 1532–1541. DOI: 10.1109/TAP.2017.2669728.
- [35] Gabriele Minatti, Marco Sabbadini, and Stefano Maci. "Anisotropic surface boundary conditions and their implementations". In: *2013 International Symposium on Electromagnetic Theory*. 2013, pp. 660–663.
- [36] Gabriele Minatti et al. "A Circularly-Polarized Isoflux Antenna Based on Anisotropic Metasurface". In: *IEEE Transactions on Antennas and Propagation* 60.11 (2012), pp. 4998–5009. DOI: 10.1109/TAP.2012.2208614.
- [37] Gabriele Minatti et al. "Flat Optics for Leaky-Waves on Modulated Metasurfaces: Adiabatic Floquet-Wave Analysis". In: *IEEE Transactions on Antennas and Propagation* 64.9 (2016), pp. 3896–3906. DOI: 10.1109/TAP.2016.2590559.
- [38] Gabriele Minatti et al. "Modulated Metasurface Antennas for Space: Synthesis, Analysis and Realizations". In: *IEEE Transactions on Antennas and Propagation* 63.4 (2015), pp. 1288–1300. DOI: 10.1109/TAP.2014.2377718.
- [39] Gabriele Minatti et al. "Spiral Leaky-Wave Antennas Based on Modulated Surface Impedance". In: *IEEE Transactions on Antennas and Propagation* 59.12 (2011), pp. 4436–4444. DOI: 10.1109/TAP.2011.2165691.
- [40] Gabriele Minatti et al. "Synthesis of Modulated-Metasurface Antennas With Amplitude, Phase, and Polarization Control". In: *IEEE Transactions on Antennas and Propagation* 64.9 (2016), pp. 3907–3919. DOI: 10.1109/TAP.2016.2589969.
- [41] Natalia K. Nikolova. *The Finite-Difference Time-Domain (FDTD) Method - Part I*. Available online. <https://www.ece.mcmaster.ca/faculty/bakr/ECE757/FDTD-I.pdf>. 2011.
- [42] Amit M. Patel and Anthony Grbic. "A Printed Leaky-Wave Antenna Based on a Sinusoidally-Modulated Reactance Surface". In: *IEEE Transactions on Antennas and Propagation* 59.6 (2011), pp. 2087–2096. DOI: 10.1109/TAP.2011.2143668.
- [43] Amit M. Patel and Anthony Grbic. "Effective Surface Impedance of a Printed-Circuit Tensor Impedance Surface (PCTIS)". In: *IEEE Transactions on Microwave Theory and Techniques* 61.4 (2013), pp. 1403–1413. DOI: 10.1109/TMTT.2013.2252362.
- [44] David M. Pozar. *Microwave Engineering*. Wiley, 2012.
- [45] Radmila Pribić. "Information-based Analysis of Compressive Data Acquisition". In: *2019 IEEE Radar Conference (RadarConf)*. 2019, pp. 1–6. DOI: 10.1109/RADAR.2019.8835738.
- [46] Radmila Pribić, Geert Leus, and Christos Tzotzadonis. "Signal-to-Noise-Ratio Analysis of Compressive Data Acquisition". In: *2018 IEEE Statistical Signal Processing Workshop (SSP)*. 2018, pp. 603–607. DOI: 10.1109/SSP.2018.8450796.
- [47] John A. Richards. *Remote Sensing with Imaging Radar*. Signals and Communication Technology. Springer Berlin Heidelberg, 2009. ISBN: 9783642020209. URL: <https://books.google.nl/books?id=DAsz9ZwkGXcC>.
- [48] Matthew N.O. Sadiku. *Numerical Techniques in Electromagnetics*. 2nd edition. CRC press, 2000. DOI: [\url{https://doi.org/10.1201/9781420058277}](https://doi.org/10.1201/9781420058277).
- [49] Christopher Schmidt et al. "DLR's Optical Communication Terminals for CubeSats". In: *2022 IEEE International Conference on Space Optical Systems and Applications (ICSOS)*. 2022, pp. 175–180. DOI: 10.1109/ICSOS53063.2022.9749735.
- [50] Amagoia Tellechea Pereda et al. "Dual Circularly Polarized Broadside Beam Metasurface Antenna". In: *IEEE Transactions on Antennas and Propagation* 64.7 (2016), pp. 2944–2953. DOI: 10.1109/TAP.2016.2562662.
- [51] Jakob J Van Zyl and Yunijn Kim. *Synthetic aperture radar polarimetry*. John Wiley & Sons, 2011.
- [52] Alexander Vavoulas, Harilaos G. Sandalidis, and Dimitris Varoutas. "Weather effects on FSO network connectivity". In: *Journal of Optical Communications and Networking* 4.10 (2012), pp. 734–740. DOI: 10.1364/JOCN.4.000734.

-
- [53] Piet Verschuren and Hans Doorewaard. *Designing a Research Project*. second. Amsterdam: Eleven International Publishing, 2013.
- [54] Peter A. Warren et al. "Large, Deployable S-Band Antenna for a 6U Cubesat". In: *Proceedings of the AIAA/USU Conference on Small Satellites*. Vol. 41. <https://digitalcommons.usu.edu/smallsat/2015/all2015/41/>. 2015.
- [55] Yuanzhi Zhang et al. "Comparison of Oil Spill Classifications Using Fully and Compact Polarimetric SAR Images". In: *Applied Sciences* 7.2 (2017). ISSN: 2076-3417. DOI: 10.3390/app7020193. URL: <https://www.mdpi.com/2076-3417/7/2/193>.



Reciprocity theorem

This section contains Pozar's derivation of the reciprocity theorem [44, p. 41] and is used to give more details in the derivation of the impedance for reciprocal networks in section 3.1. Considering Faraday's and Ampere-Maxwell's equations in equation (3.1c) and equation (3.1d) respectively, they can be used to represent two independent sources (1 and 2) in a volume V enclosed by surface s .

$$\nabla \times \mathbf{E}_1 = -j\omega\mu\mathbf{H}_1 - \mathbf{M}_1 \quad (\text{A.1a}) \quad \nabla \times \mathbf{H}_1 = -j\omega\epsilon\mathbf{E}_1 - \mathbf{J}_1 \quad (\text{A.1b})$$

$$\nabla \times \mathbf{E}_2 = -j\omega\mu\mathbf{H}_2 - \mathbf{M}_2 \quad (\text{A.1c}) \quad \nabla \times \mathbf{H}_2 = -j\omega\epsilon\mathbf{E}_2 - \mathbf{J}_2 \quad (\text{A.1d})$$

Consider for the equations above $\nabla \cdot (\mathbf{E}_1 \times \mathbf{H}_2 - \mathbf{E}_2 \times \mathbf{H}_1)^\top$ which can be reduced with vector identities to the expression in equation (A.2).

$$\begin{aligned} \nabla^\top \cdot (\mathbf{E}_1 \times \mathbf{H}_2 - \mathbf{E}_2 \times \mathbf{H}_1) &= (\nabla \times \mathbf{E}_1)^\top \cdot \mathbf{H}_2 - (\nabla \times \mathbf{H}_2)^\top \cdot \mathbf{E}_1 - (\nabla \times \mathbf{E}_2)^\top \cdot \mathbf{H}_1 + (\nabla \times \mathbf{H}_1)^\top \cdot \mathbf{E}_2 \\ &= \mathbf{J}_1^\top \cdot \mathbf{E}_2 - \mathbf{J}_2^\top \cdot \mathbf{E}_1 + \mathbf{M}_2^\top \cdot \mathbf{H}_1 - \mathbf{M}_1^\top \cdot \mathbf{H}_2 \end{aligned} \quad (\text{A.2})$$

Furthermore, integrating both sides over the volume V and using the divergence theorem results in equation (A.3), which is the general form of the reciprocity theorem.

$$\begin{aligned} \iiint_{V'} \nabla^\top \cdot (\mathbf{E}_1 \times \mathbf{H}_2 - \mathbf{E}_2 \times \mathbf{H}_1) dV &= \oiint_A (\mathbf{E}_1 \times \mathbf{H}_2 - \mathbf{E}_2 \times \mathbf{H}_1)^\top \cdot d\mathbf{A} \\ &= \iiint_{V'} (\mathbf{J}_1^\top \cdot \mathbf{E}_2 - \mathbf{J}_2^\top \cdot \mathbf{E}_1 + \mathbf{M}_2^\top \cdot \mathbf{H}_1 - \mathbf{M}_1^\top \cdot \mathbf{H}_2) dV \end{aligned} \quad (\text{A.3})$$

Considering the case where no sources or active devices are in volume V , equation (A.3) becomes equation (A.4) because $\mathbf{J}_1 = \mathbf{J}_2 = \mathbf{M}_1 = \mathbf{M}_2 = 0$.

$$\oiint_A (\mathbf{E}_1 \times \mathbf{H}_2)^\top \cdot d\mathbf{A} = \oiint_A (\mathbf{E}_2 \times \mathbf{H}_1)^\top \cdot d\mathbf{A} \quad (\text{A.4})$$

B

Method of stationary phase

The method of stationary phase is used to make an asymptotic approximation of the values of k_x and k_y in the evaluation of the far-field radiation pattern. The detailed explanation of this method can be found in the book of Balanis [1] and is summarized in this section.

Consider the problem of calculating $I(k)$ such as in equation (B.1) with k and $f(x, y)$ real, and $F(x, y)$ that may be complex. Obtaining a final result for $I(k)$ can be a complicated task for rapidly oscillating values of the exponential term between -1 and $+1$. Therefore, the function $f(x, y)$ is evaluated only near its stationary points (x_s, y_s) given by equation (B.2).

$$I(k) = \int_a^b \int_c^d F(x, y) e^{jkf(x, y)} dx dy \quad (\text{B.1})$$

$$\left. \frac{\partial f}{\partial x} \right|_{\substack{x=x_s \\ y=y_s}} = f'_x(x_s, y_s) = 0 \quad (\text{B.2a}) \quad \left. \frac{\partial f}{\partial y} \right|_{\substack{x=x_s \\ y=y_s}} = f'_y(x_s, y_s) = 0 \quad (\text{B.2b})$$

It is assumed that $F(x, y)$ varies much more slowly than $f(x, y)$, making negligible its contributions to the fast-varying parts of equation (B.1). Therefore, this term can be taken out of the integral as in equation (B.3).

$$I(k) \approx F(x_s, y_s) \int_{-\infty}^{+\infty} \int_{-\infty}^{+\infty} e^{jkf(x, y)} dx dy \quad (\text{B.3})$$

Next, a second degree Taylor expansion of $f(x, y)$ at its stationary points (x_s, y_s) is done in equation (B.4) considering that $f'_x(x_s, y_s) = f'_y(x_s, y_s) = 0$. The elements that define this expansion are then replaced by $\bar{A} = \frac{1}{2} f''_{xx}(x_s, y_s)$, $\bar{B} = \frac{1}{2} f''_{yy}(x_s, y_s)$, $\bar{C} = f''_{xy}(x_s, y_s)$, $\xi = x - x_s$, and $\kappa = y - y_s$. The resulting expression is then replaced in equation (B.3), where the exponential function is defined by the second degree polynomial expansion of $f(x, y)$.

$$f(x, y) \approx f(x_s, y_s) + \frac{1}{2}(x - x_s)^2 f''_{xx}(x_s, y_s) + \frac{1}{2}(y - y_s)^2 f''_{yy}(x_s, y_s) + (x - x_s)(y - y_s) f''_{xy}(x_s, y_s) \quad (\text{B.4})$$

$$f(x, y) \approx f(x_s, y_s) + \bar{A}\xi^2 + \bar{B}\kappa^2 + \bar{C}\xi\kappa$$

$$I(k) \approx F(x_s, y_s) e^{jkf(x_s, y_s)} \int_{-\infty}^{+\infty} \int_{-\infty}^{+\infty} e^{jk(\bar{A}\xi^2 + \bar{B}\kappa^2 + \bar{C}\xi\kappa)} d\xi d\kappa \quad (\text{B.5})$$

Next, the polynomial expansion defined in equation (B.4) can be diagonalized to the expression aligned with its eigenvectors. This can be done by defining its eigenvalues as \bar{A}' and \bar{B}' and solving for them as in equation (B.6). Finally, the quadratic equation is now a function of ϑ and ι , and is aligned with its eigenvectors.

$$\left| \begin{array}{cc} \bar{A} - (\bar{A}', \bar{B}') & \bar{C}/2 \\ \bar{C}/2 & \bar{B} - (\bar{A}', \bar{B}') \end{array} \right| = 0$$

$$(\bar{A}', \bar{B}') = \frac{1}{2} \left[(\bar{A} + \bar{B}) \pm \sqrt{(\bar{A} + \bar{B})^2 - (4\bar{A}\bar{B} - \bar{C}^2)} \right] \quad (\text{B.6})$$

$$\bar{A}\xi^2 + \bar{B}\kappa^2 + \bar{C}\xi\kappa = \bar{A}'\vartheta^2 + \bar{B}'\iota^2$$

Equation (B.6) can be used to decouple the exponential part of equation (B.5) as in equation (B.7) where the coefficients \bar{A}' and \bar{B}' are placed within absolute values because the effect of their sign is expressed explicitly in the \pm term at the beginning of the exponential function.

$$I(k) \approx F(x_s, y_s) e^{jkf(x_s, y_s)} \int_{-\infty}^{+\infty} \int_{-\infty}^{+\infty} e^{jk(\bar{A}'\vartheta^2 + \bar{B}'\iota^2)} d\vartheta d\iota \quad (\text{B.7})$$

$$I(k) \approx F(x_s, y_s) e^{jkf(x_s, y_s)} \int_{-\infty}^{+\infty} e^{\pm jk|\bar{A}'|\vartheta^2} d\vartheta \int_{-\infty}^{+\infty} e^{\pm jk|\bar{B}'|\iota^2} d\iota$$

The integral of equation (B.7), now defined as $I''(k)$, can be simplified with its symmetry properties as shown in equation (B.8), where the coefficients \bar{A}' , \bar{B}' and the quadratic terms ϑ , ι are expressed explicitly and can be interchanged with each other.

$$I''(k) = \int_{-\infty}^{+\infty} e^{\pm jk|\bar{A}', \bar{B}'|(\vartheta, \iota)^2} d(\vartheta, \iota) = 2 \int_0^{+\infty} e^{\pm jk|\bar{A}', \bar{B}'|(\vartheta, \iota)^2} d(\vartheta, \iota) \quad (\text{B.8})$$

Next, the variable τ is used to simplify equation (B.8) by replacing the exponential part with the expression defined in equation (B.9a). Next, this element and its derivative in equation (B.9b) are used to replace equation (B.8), resulting in equation (B.10) which contains an integral element, called the Fresnel integral, with a well-known closed-form representation.

$$k|\bar{A}', \bar{B}'|(\vartheta, \iota)^2 = \frac{\pi}{2}\tau^2 \quad (\text{B.9a}) \quad d(\vartheta, \iota) = \sqrt{\frac{\pi}{2k|\bar{A}', \bar{B}'|}} d\tau \quad (\text{B.9b})$$

$$I''(k) = 2 \sqrt{\frac{\pi}{2k|\bar{A}', \bar{B}'|}} \int_0^{\infty} e^{\pm j\frac{\pi}{2}\tau^2} d\tau = \sqrt{\frac{\pi}{k|\bar{A}', \bar{B}'|}} e^{\pm j\frac{\pi}{4}} \quad (\text{B.10})$$

Subsequently, equation (B.10) is used to replace equation (B.7), resulting in equation (B.11) in which the signs of the exponential functions at its end are defined by the signs of \bar{A}' and \bar{B}' as shown by δ_c .

$$I(k) \approx F(x_s, y_s) e^{jkf(x_s, y_s)} \frac{\pi}{k\sqrt{|\bar{A}'||\bar{B}'|}} e^{\pm j\frac{\pi}{4}} e^{\pm j\frac{\pi}{4}} = F(x_s, y_s) e^{jkf(x_s, y_s)} \frac{j\pi\delta_c}{k\sqrt{|\bar{A}'||\bar{B}'|}} \quad (\text{B.11})$$

$$\text{where } \delta_c = \begin{cases} +1 & \bar{A}' > 0 \vee \bar{B}' > 0 \\ -1 & \bar{A}' < 0 \vee \bar{B}' < 0 \\ -j & \bar{A}'\bar{B}' < 0 \end{cases}$$

The coefficients \bar{A}' and \bar{B}' in equation (B.11) can be expressed as \bar{A} and \bar{B} by obtaining $\bar{A}'\bar{B}'$ from the second line of equation (B.6), resulting in equation (B.12a) which can be replaced in equation (B.11) to obtain equation (B.13). Next, considering equation (B.12b), table B.1 can be elaborated by relating the signs of each coefficient with equation (B.12), which results in defining δ_c for \bar{A} and \bar{B} . The final result is shown in equation (B.13), which represents the approximation of equation (B.1).

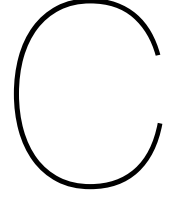
$$\bar{A}'\bar{B}' = \frac{4\bar{A}\bar{B} - \bar{C}^2}{4} \quad (\text{B.12a}) \quad \bar{A}' + \bar{B}' = \bar{A} + \bar{B} \quad (\text{B.12b})$$

Table B.1: Sign of \bar{A}' and \bar{B}' considering the values of \bar{A} and \bar{B} .

	$4\bar{A}\bar{B} > \bar{C}^2$		$4\bar{A}\bar{B} < \bar{C}^2$	
	$\bar{B} > 0$	$\bar{B} < 0$	$\bar{B} > 0$	$\bar{B} < 0$
$\bar{A} > 0$	$\bar{A}' > 0 \vee \bar{B}' > 0$			$\bar{A}'\bar{B}' < 0$
$\bar{A} < 0$		$\bar{A}' < 0 \vee \bar{B}' < 0$	$\bar{A}'\bar{B}' < 0$	

$$I(k) \approx F(x_s, y_s) e^{jkf(x_s, y_s)} \frac{j2\pi\delta_c}{k\sqrt{|4\bar{A}\bar{B} - \bar{C}^2|}}$$

$$\text{where } \delta_c = \begin{cases} +1 & 4\bar{A}\bar{B} > \bar{C}^2 \vee \bar{A} > 0 \\ -1 & 4\bar{A}\bar{B} > \bar{C}^2 \vee \bar{A} < 0 \\ -j & 4\bar{A}\bar{B} < \bar{C}^2 \end{cases} \quad (\text{B.13})$$



Method of Moments (MoM) impedance representation

Many derivations and calculations presented in this report are based on an impedance representation using the Method of Moments (MoM). The approach presented in this appendix is a summary based on the method presented in [32]. The reader is encouraged to consult that article if further doubts remain.

A spectral Galerkin MoM approach is used to obtain the impedance MoM matrix $\underline{\underline{Z}}^{MoM}$ as a function of the fundamental Floquet mode \mathbf{k}_t and of the excitation frequency $f = kc/(2\pi)$ in terms of N Floquet modes \bar{q} . Such representation is possible because an infinite array of identical unit cells is assumed in the simulation region, which ultimately can be expressed as a single unit cell with periodic boundary conditions. The Floquet wavevectors $\mathbf{k}_{\bar{q}}$ are defined as in equation (3.105) in a reciprocal lattice of the form of figure 3.4 with N nodes centred in the fundamental wavevector \mathbf{k}_t . M basis functions are used to represent the equivalent currents in the spectral domain given by J_p^{TM} , which is the basis function p aligned with $\mathbf{k}_{\bar{q}}$, and J_q^{TE} , which is the basis function q aligned to $\hat{z} \times \hat{\mathbf{k}}_{\bar{q}}$. The components of the MoM matrix are given in equation (C.1) [32], which results in $\underline{\underline{Z}}^{MoM}$ having a size of $M \times M$. The elements $Z_{GF}(\omega, \mathbf{k}_{\bar{q}})$ are specified in equation (C.2) [32] and are spectral representations of the GF aligned either with the TM or TE modes at a given excitation frequency and at the \bar{q} Floquet mode. X_0 and Z_1 can be traced back to equation (3.113) and equation (3.115) respectively, with the difference that the expressions in section 3.2.3 are applied only to the fundamental Floquet mode, whereas the ones presented here are generalized to all the Floquet modes.

$$Z_{pq}^{MoM}(\omega, \mathbf{k}_{\bar{q}}) = \sum_{\bar{q}=0}^N [Z_{GF}^{TM}(\omega, \mathbf{k}_{\bar{q}}) J_p^{TM}(\mathbf{k}_{\bar{q}}) J_q^{TM*}(\mathbf{k}_{\bar{q}}) + Z_{GF}^{TE}(\omega, \mathbf{k}_{\bar{q}}) J_p^{TE}(\mathbf{k}_{\bar{q}}) J_q^{TE*}(\mathbf{k}_{\bar{q}})] \quad (C.1)$$

$$Z_{GF}^{TM}(\omega, \mathbf{k}_{\bar{q}}) = jX_{GF}^{TM}(\omega, \mathbf{k}_{\bar{q}}) = j \left\{ [X_0^{TM}(\omega, \mathbf{k}_{\bar{q}})]^{-1} + [Z_1^{TM}(\omega, \mathbf{k}_{\bar{q}})]^{-1} \cot \left(h \sqrt{\epsilon_r k^2 - \mathbf{k}_{\bar{q}}^T \cdot \mathbf{k}_{\bar{q}}} \right) \right\}^{-1} \quad (C.2a)$$

$$Z_{GF}^{TE}(\omega, \mathbf{k}_{\bar{q}}) = jX_{GF}^{TE}(\omega, \mathbf{k}_{\bar{q}}) = j \left\{ [-X_0^{TE}(\omega, \mathbf{k}_{\bar{q}})]^{-1} + [Z_1^{TE}(\omega, \mathbf{k}_{\bar{q}})]^{-1} \cot \left(h \sqrt{\epsilon_r k^2 - \mathbf{k}_{\bar{q}}^T \cdot \mathbf{k}_{\bar{q}}} \right) \right\}^{-1} \quad (C.2b)$$

Consider the asymptotic case for higher-order Floquet modes where $\mathbf{k}_{\bar{q}}^T \cdot \mathbf{k}_{\bar{q}} \gg \epsilon_r k$, and $\epsilon_r > 1$ for practical applications. The asymptotic GF impedance is given by $Z_{\infty}^{TM, TE}$ in equation (C.3) after approximating $\sqrt{k^2 - \mathbf{k}_{\bar{q}}^T \cdot \mathbf{k}_{\bar{q}}} \rightarrow -j\sqrt{\mathbf{k}_{\bar{q}}^T \cdot \mathbf{k}_{\bar{q}}}$ and $\sqrt{\epsilon_r k^2 - \mathbf{k}_{\bar{q}}^T \cdot \mathbf{k}_{\bar{q}}} \rightarrow -j\sqrt{\mathbf{k}_{\bar{q}}^T \cdot \mathbf{k}_{\bar{q}}}$ [32].

$$Z_{\infty}^{TM}(\omega, \mathbf{k}_{\bar{q}}) = \frac{\zeta \sqrt{\mathbf{k}_{\bar{q}}^T \cdot \mathbf{k}_{\bar{q}}}}{jk(\epsilon_r + 1)} \quad (C.3a) \quad Z_{\infty}^{TE}(\omega, \mathbf{k}_{\bar{q}}) = \frac{j\zeta k}{2\sqrt{\mathbf{k}_{\bar{q}}^T \cdot \mathbf{k}_{\bar{q}}}} \quad (C.3b)$$

Next, the MoM impedance can be represented by the sum of three terms as in equation (C.4): the one related to the zero-order Floquet mode $\underline{\underline{Z}}_{slab}$, equation (C.5), the low-frequency contribution that

represents the spectral asymptotic GF $\underline{\underline{Z}}_{LF}$, equation (C.6), and the one related to the dynamic band $\underline{\underline{Z}}_{dyn}$, equation (C.7) [32].

$$\underline{\underline{Z}}_{MoM} = \underline{\underline{Z}}_{slab} + \underline{\underline{Z}}_{dyn} + \underline{\underline{Z}}_{LF} \quad (C.4)$$

$$\left(\underline{\underline{Z}}_{slab}\right)_{pq} = Z_{GF}^{TM}(\omega, \mathbf{k}_t) J_p^{TM}(\mathbf{k}_t) J_q^{TM*}(\mathbf{k}_t) + Z_{GF}^{TE}(\omega, \mathbf{k}_t) J_p^{TE}(\mathbf{k}_t) J_q^{TE*}(\mathbf{k}_t) \quad (C.5)$$

$$\left(\underline{\underline{Z}}_{LF}\right)_{pq} = \sum_{q=1}^N \left\{ Z_{\infty}^{TM}(\omega, \mathbf{k}_{\bar{q}}) J_p^{TM}(\mathbf{k}_{\bar{q}}) J_q^{TM*}(\mathbf{k}_{\bar{q}}) + Z_{\infty}^{TE}(\omega, \mathbf{k}_{\bar{q}}) J_p^{TE}(\mathbf{k}_{\bar{q}}) J_q^{TE*}(\mathbf{k}_{\bar{q}}) \right\} \quad (C.6)$$

$$\begin{aligned} \left(\underline{\underline{Z}}_{dyn}\right)_{pq} &= \sum_{q=1}^N \left\{ [Z_{GF}^{TM}(\omega, \mathbf{k}_{\bar{q}}) - Z_{\infty}^{TM}(\omega, \mathbf{k}_{\bar{q}})] J_p^{TM}(\mathbf{k}_{\bar{q}}) J_q^{TM*}(\mathbf{k}_{\bar{q}}) \right. \\ &\quad \left. + [Z_{GF}^{TE}(\omega, \mathbf{k}_{\bar{q}}) - Z_{\infty}^{TE}(\omega, \mathbf{k}_{\bar{q}})] J_p^{TE}(\mathbf{k}_{\bar{q}}) J_q^{TE*}(\mathbf{k}_{\bar{q}}) \right\} \end{aligned} \quad (C.7)$$

When considering the condition of accessibility of only the dominant Floquet mode to the ground slab, $|\underline{\underline{Z}}_{LF}|_{pq} \gg |\underline{\underline{Z}}_{dyn}|_{pq}$ because the low-frequency contribution can be approximated by the asymptotic GF impedance. The condition is fulfilled if equation (C.8) is satisfied for the closest higher-order Floquet mode to the fundamental Floquet mode, which is given by the expression of $\sqrt{\mathbf{k}^T \cdot \mathbf{k}}$ [32].

$$\left| \frac{Z_{GF}^{TM,TE}(\mathbf{k}, \omega) - Z_{\infty}^{TM,TE}(\mathbf{k}, \omega)}{Z_{GF}^{TM,TE}(\mathbf{k}, \omega)} \right| \ll 1 \quad \text{for} \quad \sqrt{\mathbf{k}^T \cdot \mathbf{k}} = \left| \sqrt{\mathbf{k}_t^T \cdot \mathbf{k}_t} - \frac{2\pi}{d} \right| \quad (C.8)$$

Considering the application to practical cases where $\lambda/2 < \lambda_{sw} < \lambda$ and $\epsilon_r > 1$, a second-order approximation of equation (C.8) can be obtained, leading to the results in equation (C.9). The first condition equation (C.9a) is more restrictive when $h/d > \tau$, and the second equation (C.9b) when $h/d < \tau$. τ is specified in equation (C.10) [32].

$$\pi \sqrt{\frac{\epsilon_r^2 + 1}{2(\epsilon_r + 1)}} + 1 < \frac{\lambda}{d} \quad (C.9a) \quad d < \frac{h}{0.23 + \frac{2h}{\lambda}} \quad (C.9b)$$

$$\tau = 0.23 \frac{\sqrt{2(\epsilon_r + 1)} + \pi \sqrt{\epsilon_r^2 + 1}}{\sqrt{2(\epsilon_r + 1)} + 2\pi \sqrt{\epsilon_r^2 + 1}} \quad (C.10)$$